A study of the mechanical properties of liquid crystal polymer fibres and their adhesion to epoxy resin using Laser Raman Spectroscopy

Cosmas Vlattas

Materials Department
Queen Mary and Westfield College

Thesis presented for the degree of Doctor of Philosophy
in the Faculty of Engineering of the University of London.

June 1995

Στον πατερα μου Παντελη

Στην μητερα μου Αρετη

ΤΩΝ ΔΕ ΠΑΡΑΜΕΙΝΑΝΤΩΝ ΕΝ ΤΗ ΝΑΥΜΑΧΙΗ ΠΕΡΙΕΦΟΝΗΣΑΝ
ΤΡΗΧΥΤΑΤΟΙ ΧΙΟΙ ΩΣ ΑΠΟΔΕΙΚΝΥΜΕΝΟΙ ΤΕ ΕΡΓΑ ΛΑΜΠΡΑ
ΚΑΙ ΟΥΚ ΕΘΕΛΟΚΑΚΕΟΝΤΕΣ

ΗΡΟΔΟΤΟΣ VI 15

"Of those that stood their ground in the sea fight, most roughly handled were the Chians, for they would not be cravens but achieved deeds of renown"

Herodotus VI 15

ABSTRACT

A number of high performance fibres (*aramid, PBZT* and *PBO*) spun from liquid crystal polymer solutions were examined in this work. In particular, a thorough investigation of the mechanical response of these fibres under tensile and compressive deformations was carried out. The major experimental tool employed was the technique of Laser Raman Spectroscopy. It was found that stress-induced changes of these fibres at molecular level are proportional to the macroscopic deformation applied. This correlation is unique for the fibres. A method for converting spectroscopic data to predicted stress-strain curves in tension and compression was proposed. An estimation of their compressive strength was derived and an understanding of the nature of their compressive failure was discussed.

The adhesion of these fibres to epoxy resin was also investigated by monitoring *in situ* the interfacial stresses developed along the *interface/interphase* of model single fibre composite coupons. The strength of the interfacial bond was measured. The effect of various parameters such as fibre modulus, fibre diameter and fibre nature upon the interfacial strength of the various systems was evaluated. The mechanisms of stress transfer along with the nature of interfacial damage was examined accurately. It was found that the major parameter controlling the above mechanisms was interfacial yielding in shear. A numerical appoximation (using Finite Element Analysis) was employed in order to evaluate the experimental results. Finally, general conclusions concerning the performance of these fibres were drawn.

ACKNOWLEDGEMENTS

I would like to thank my supervisor Dr. Costas Galiotis for his guidance and endless assistance throughout this project. I would also like to thank Professor Craig K.L. Davies for his encouragement during my years in the Department of Materials.

I am grateful to the 'Pateras Foundation of Scholarship' for the financial support without which this work could not have been completed.

A big thank you is also due to Brenda Keneghan for her patience, tireless encouragement and useful comments about the thesis during the 'writing up' period.

The support from the technical and secretarial staff of the Materials Department on the 'good' days and encouragement on the 'bad' days during the writing of the thesis is also very much appreciated.

I would also like to mention all my friends in the Department and particularly Alkiviadis Paipetis for valuable discussions and ideas, along with Ata Yoosefinejad for his help in the production of this volume.

I feel it is meaningless to thank my beloved parents, because a simple thank you is not enough to express my gratitude.

CONTENTS

CHAPTER 3

CHAPTER 4

CHAPTER 5

LIST OF TABLES

CHAPTER 1

CHAPTER 2

CHAPTER 3

CHAPTER 4

CHAPTER 5

LIST OF FIGURES

CHAPTER 1

CHAPTER 2

CHAPTER 3

CHAPTER 4

CHAPTER 5

CONCLUSIONS AND FEATURE WORK

APPENDICES

INTRODUCTION

It would be impossible to imagine today's world without the innovative technology of high-performance polymers and fibres i.e. graphite, glass, boron, polymeric filaments, etc. The superior mechanical properties and unique flexibility of design and fabrication of systems reinforced with these materials has put them at the forefront of a wide range of applications e.g. automobiles, aircraft, space vehicles, off-shore structures, containers, piping, sporting goods, prostheses, electronics and numerous other appliances.

The synthetic fibre industry began in 1935 with the invention of *nylon*. It has developed dramatically since then. New man made fibres were introduced, such as polyacrylic fibre in 1949, polyester fibre in 1953, polypropylene fibre in 1957. After 1960 second generation fibres were developed and commercially produced. In the late 1960's, the discovery of the liquid crystalline behaviour of rigid, rod-like aromatic polyamides was made. This led to the development of high-strength, high-modulus *aramid* fibres. This heralded a new era in the history of synthetic fibres and their composites, with new products and applications appearing on the market in the 1970's, 1980's and 1990's.

A brief description of the structure, morphology and applications of the materials is given in chapter 1. A review of the mechanical properties of these fibres is also given along with an attempt to correlate them with their molecular structure.

The fundamental principles of the spectroscopic technique used and the results obtained are given in chapter 2. Some observations associated with the spectroscopic studies are presented.

The dependence of the molecular deformation with its resulting changes in the Raman spectrum, on external deformation is outlined in chapter 3. Tensile deformations result in distinct frequencies in the Raman spectrum to shift to lower values. This unique optomechanical correlation, characteristic for the material has been used for the study of these fibres subjected to tensile deformations. Very important observations concerning the molecular structure of these fibres and their response to external tensile strain or stress are made.

Compressive deformations in these materials, result in shift of vibrational frequencies in the Raman spectrum to higher values. In chapter 3, modified versions of the *cantilever* and *four-point bending beam method* are employed in order to study the behaviour of these fibres under axial compressive load. A method for converting spectroscopic data to predicted stress-strain curves and an estimation of the compressive strength of these fibres is proposed. Evidence of the nature of compressive failure and the mechanisms associated with it is given.

In chapter 5, a model composite coupon geometry is employed for the evaluation of the strength of the interface between these fibres and epoxy resin matrices. A simple mathematical model based on the balance of forces at the interface is employed for transforming strain measurements in the fibre to shear stress distributions along the interface. A finite element analysis model is also considered in order to model the experimental results. Regardless of the difficulties due to *mathematical singularities* existing at the fibre tip, results compatible to the experimental were produced.

Finally, in the epilogue section, the conclusions and overall remarks of this work are summarised and certain suggestions for further work are presented.

CHAPTER 1:

STRUCTURE, MORPHOLOGY AND APPLICATIONS OF LIQUID CRYSTAL POLYMER FIBRES

1.1. Introduction.

The measured strengths of most conventional materials are found to be much smaller than their theoretical strengths. An explanation for this discrepancy is the presence of imperfections or inherent flaws in the material. Man made filaments or fibres, on the other hand, exhibit much higher strengths along their lengths because imperfections or flaws are minimized due to the small cross-sectional dimensions of the fibre and/or the orientation of the molecular structure (in the case of the synthetic fibres). Therefore, structure-property relationships can be developed according to the neccesary requirements, depending on the specific applications of these materials.

In figure 1.1 [**Yang 1989**] the *specific strength* (strength per unit density) of a wide range of materials including synthetic fibres as a function of the *specific tensile modulus* (tensile modulus per unit density), is presented. This relation is of prime importance when maintenance of strength is required with minimum weight. The conventional materials appear in the left hand corner quite close to the x-axis in contrast with the polymeric and non-polymeric fibres, which exhibit high specific strength to specific modulus correlation. These *high performance* fibres offer high strength, high modulus, thermal stability at very high temperatures, chemical and solvent resistance, low weight and a number of other useful properties. These fibres are rapidly entering into new materials markets, such as automobile, sport, military, aerospace, civil and other industries.

These fibres are embedded in matrix materials to form *fibrous composites*. The matrix serves as a good binder for the fibres, transfers successfully the load

to the fibres and protects them against any enviromental attack or damage. The outstanding features of fibre reinforced composites and especially oriented fibrous composites are their high specific moduli and strengths. These two features make the fibrous composites very attractive structural materials and their utilization is continuously increasing.

The development of modern reinforcing fibres is the result of several technological discoveries. These have yielded a number of fibre types such as *aromatic high-strength fibres, gel-spun polyethylene fibre, graphite(carbon) fibres* and *inorganic fibres*.

High strength, high modulus fibres prepared from aromatic polymers are of prime concern in this work. Certain details of the fabrication, the properties and the applications of fibres produced from liquid crystalline polymer solutions (LCP fibres) are presented in this chapter. Industrial activities dealing with different kinds of LCP fibres are taking place mainly in the United States, Europe, Russia and Japan. From a technical point of view, the process mechanisms related to the formation of LCP fibres are very complex. The methods vary from polymer to polymer. In principle, the process of fibre preparation begins with polymer synthesis, followed by polymer isolation and polymer recovery, preparation of spin solution and finally, fibre formation by *spinning*. Other processes such as *heat treatment* lead to further molecular alignment and higher crystallinity. By controlling these parameters, maximum alignment of molecular chains and a high degree of crystallinity, can be achieved. As a result, maximum fibre strength and modulus can be obtained.

1.2. LCP fibres : Structure, fabrication and applications.

Nylon was the first man-made fibre commercially produced in the 1930's. Since then, the *polyacrylic fibre* was developed in 1949 and the *polyester fibre* in 1953. Soon after, in 1957, the *polypropylene fibre* was introduced. These four types

of fibres made a major impact on the textile industry with applications in apparel, home furnishing and carpets production. The use of natural fibres such as cotton and wool was sharply diminished. The development of synthetic fibres has soared even more throughout the last 20 years. The crucial points in the history of the synthetic fibre industry are given in table 1.1 **[Yang 1989]**:

FIBRE TYPE	YEAR
Nylon	1935
Nylon 66	1938
Polyacrylonitrile	1949
Polyvinyl alcohol	1950
Polyester	1953
Polypropylene	1957
Non-wovens	1960
Polyaramide	1962
Polyhydrazide	1964
Aromatic polymer fibres	1972

Table 1.1. *The history of the synthetic fibre development* **[Yang 1989]**.

The discovery of the liquid crystalline behaviour of rigid rod aromatic polyamides in the late 1960's by du Pont de Nemours Co, led to the development of high-strength, high modulus aromatic polymer fibres in the early 1970's **[Kwolek 1972,1974]**. These so called high-performance fibres offer thermal stability at very high temperatures, chemical and solvent resistance, and low densities, making them suitable for applications where weight saving is a primary objective. Generally speaking, fibres which can be classified as high-performance fibres (certain acceptable performance under extraordinary conditions) are the following:

- **Aromatic polymer fibres**
  - *aromatic polyamides*
  - *aromatic polyesters*
  - *aromatic polyimides*
  - *aromatic heterocyclic polymers*
- **Polyolefin fibres**
- **Carbon fibres**
  - *rayon*
  - *polyacrylonitrile (PAN)*
  - *pitch*
- **Inorganic fibres**
  - *boron*
  - *silicon carbide*
  - *fibre FP*
  - *alumina-boria-silica fibre*
- **Poly(phenylene sulfide) fibre**

This study is concerned mainly with one category of aromatic polymer fibres, the aromatic polyamide fibres. In particular, three different types will be examined: (i) poly(*p*-phenylene terephthalamide), under the abbreviated name 'P*p*PTA', produced by du Pont de Nemours Co. under the trademark Kevlar®, (ii) poly[(benzo-bisthiazole)-*p*-phenylene], under the abbreviated name 'PBZT', produced by US Air-Force and supplied by RAe (currently DRA-Farnborough) and (iii) poly[(dihydrobenzo-bisoxazole)-*p*-phenylene], under the abbreviated name 'PBO', produced by Dow Chemicals Co.

1.2.1. Aromatic polyamide fibres (aramids).

Aromatic polyamides are called 'aramids' in order to be distinguished from conventional aliphatic and cycloaliphatic polyamides, such as nylon. Fibres produced from these polymers show high anisotropic mechanical properties due to their high axial molecular chain orientation and demonstrate excellent resistance to severe thermo-chemical environments. The most widely known

fibres of this family are Kevlar®, produced by du Pont de Nemours Co.(USA), Technora® produced by Teijin Ltd, Japan and Twaron® produced by Akzo-Nobel, Netherlands. A brief review of the polymer and fibre preparation, properties, crystal structure and morphology of Kevlar® and other aramid products is given below.

(i) Polymer and fibre preparation.

Aromatic polyamides are prepared from various aromatic diamines and diacids. The simplest form of all is poly(*p*-phenylene terephthalamide), usually abbreviated as *Pp*PTA or PPD-T. This polymer can be prepared by the low temperature polycondensation of *p*-phenylene diamine and terephthaloyl chloride in dialkyl amide solvent (only one *repeat unit* shown in the reaction below) :

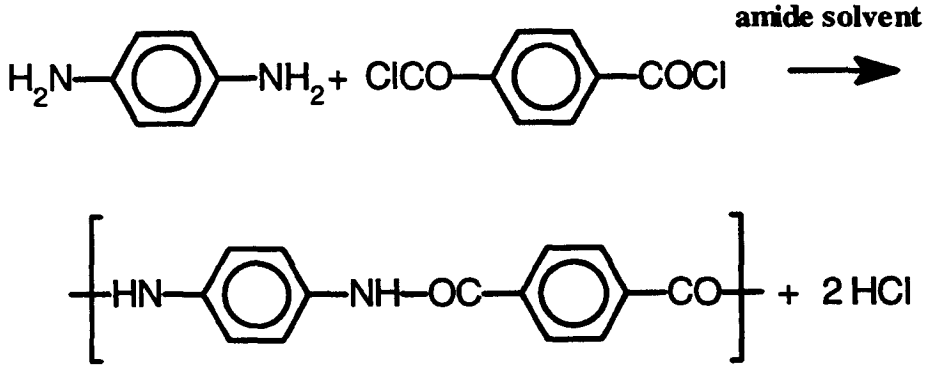

poly(*p*-phenylene terephthalamide)

In general, the basic aim in polymer fibre technology is the development of formation processes which will give rise to almost perfect orientation of extended molecular chains in the solid state and, hence, tensile strength and modulus approaching the theoretical values. This technology includes spinning and heat treatment methods. There are three major methods of spinning: (i) *melt spinning,* (ii) *dry spinning* and (iii) *wet spinning.*

The melt spinning process is employed widely for polymers that can be extruded in a molten state. The polymer melt is ejected from small capillary

holes to form fibres, attenuated by an external force, and cooled to its solid state. The dry spinning process is used for polymer solutions of volatile solvents. In this case, the solvent is recovered from the extruded filaments by flash vaporization with hot gases. The wet spinning process, so called because water or aqueous solutions are often used as the coagulating agent, is employed mostly for polymer solutions that must undergo coagulation and extraction for solvent recovery.

Kevlar® fibres are prepared from the polymer solution by two main combinations of spinning: *wet-jet wet spinning* **[Kwolek 1974]**, **[Bair 1974]** or *dry-jet wet spinning* **[Blades 1975]** followed by heat treatment of the spun fibres. During spinning, the polymer solutions are spun from spinnerets and coagulated by water or dilute solutions of solvents and salts. The resulting fibres are then washed and dried. The as-spun fibres may be heat-treated above ~300°C under tension. Such heat treatment increases the fibre strength and modulus to very high levels. In the wet-jet spinning process, solution and coagulation take place simultaneously. In the dry-jet spinning process (figure 1.2a,b) fibre spinning occurs in an air space and is followed by coagulation. The process mechanisms during spinning and heat treatment lead to high molecular alignment and crystallinity. These give rise to significantly improved fibre properties. In figure 1.3, the fibre fabrication processes along with the corresponding chemical and physical structures that result from these processes are illustrated **[Morgan 1989]**.

(ii) Types of Kevlar® fibre products.

Du Pont produces several types of Kevlar® filament yarns: Kevlar®, Kevlar®29, Kevlar®49, Kevlar®68, Kevlar®149, and more recently the second generation of aramid filaments such as Kevlar®119 Kevlar®129 and others. All these products come basically from the same polymer but serve in different applications, depending on their thermomechanical and physical properties

which vary within a broad range. The major types of Kevlar® filament yarns currently available in the market are the following:

FIBRE CODE	TYPE
Kevlar®	Tyre yarn
Kevlar®29	All-purpose yarn
Kevlar®49	High modulus yarn
Kevlar®68	Moderate modulus yarn
Kevlar®100	Coloured yarn
Kevlar®119	High elongation yarn
Kevlar®129	High tenacity yarn
Kevlar®149	Ultra-high modulus yarn

Table 1.2. *Various Kevlar® fibre yarns by the du Pont Co* **[Yang 1993]**.

Kevlar® fibre products also include new different product forms other than continuous filament yarns such as staples, fabrics, pulps, M/B elastomeric masterbatch, 'Wearforce' composites and others **[Yang 1993]**. Various product forms of Kevlar® **[du Pont 1989]** are shown in figure 1.4.

In the present study three types of commercial fibres of low (Kevlar®29), medium (Kevlar®49) and high (Kevlar®149) Young's modulus along with two experimental heat treated fibres **[Termonia 1989]** were tested and their properties examined:

FIBRE	DENIER	FINISH
Kevlar®29	1500d denier	none
Kevlar®49	1500d denier	none
Kevlar®49 ht1	1420d denier	none
Kevlar®49 ht2	2160d denier	none
Kevlar®149	1500d denier	surface finish

Table 1.3. *Various Kevlar® fibres examined in this work.*

(iii) Typical fibre properties.

In general, Kevlar® fibre is an outstanding high-strength, high-modulus fibre. Its properties can be altered by using solvent additives, varying the spinning conditions, and using post-spinning processes usually referred as heat treatment. This process, always takes place after the fibre formation. Usually, the fibre undergoes crystallization upon cooling or coagulation. The crystalline structure and the degree of crystallinity of the fibre are highly dependent upon the rate and temperature of cooling and the spinning stress. *Hot stretching* (drawing) is generally the method used for increasing the molecular orientation in the fibre and thus the fibre strength and modulus. The degree of drawing depends on the plasticity of the fibre. A wet fibre with high solvent content may be drawn considerably more than a dry fibre with low residual solvent. Dry fibres are therefore drawn at elevated temperatures in very short exposures to affect the molecular orientation and crystal growth. Results **[Bair 1977]**, **[Kaneda 1979]** have shown that there is a general trend of increase of fibre strength and modulus with the heat treatment temperature, up to a critical temperature. The fibre tensile stress during heat treatment appeared to be very critical. These phenomena are generally true for most high performance aromatic fibres. The post-spinning treatment is not limited to dry fibres. Stretching of polyamide

fibres with high solvent or water content has been performed and fibres of excellent tensile properties have also been reported in the literature [**Asahi 1977**].

Instead of drawing, other processes such as *annealing* can be used. Annealing induces post-crystallization and inter-molecular stress relaxation in the fibre. This is often done by allowing a fibre to shrink lengthwise at very low process tensions or with prolonged exposure to elevated temperatures. It can often lead to changes in the crystalline form and crystalline imperfections. As a result, such a process would give fibres with low tensile properties. Two heat treated Kevlar®49 fibres are included in these studies. More details about fibre properties will be discussed in a later chapter.

(iv) Crystal structure and morphology of Kevlar® fibres.

Kevlar® fibre contains several levels of superimposed microscopic and macroscopic structures. They include the *crystalline structure, pleat structure, fibrillar structure* and *skin-core structure.* Several structural models have been proposed to describe these fine structures and morphological features. A brief review of the above follows in the paragraphs below.

A. *Crystalline structure.* Kevlar® fibre has a highly crystalline, highly ordered molecular structure which has been determined by X-ray diffraction techniques. Several researchers ([**Northolt 1973**], [**Hasegawa 1973**], [**Tashiro 1977**]), have assigned the structure of Kevlar®49 crystal unit to a monoclinic system (figure 1.5a). The orientation angles of the molecular chains with respect to the c-axis are approximately 6° for the *p*-diaminophenylene segment and approximately 14° for the terephthaloyl segment. The amide groups are assumed to be coplanar and oriented nearly (4° mismatch) parallel to the [1 0 0] planes. The characteristic distance between the amide and carbonyl end groups of adjacent polymer chains is 3Å and the angle NH···O is 160°. Such close proximity of NH···O enhances relatively strong hydrogen bonding which links the adjacent

chains into hydrogen-bonded sheets forming the [2 0 0] lattice planes. The orientation angle between the amide plane and the phenylene plane of the terephthaloyl segment is estimated to be 30°. The angle between the amide plane and the phenylene plane of the diaminophenylene segment is 38°. The absence of appreciable free rotation around the phenylcarbonyl bond and the phenylamide bond imparts to the polymer chain a rodlike character. In contrast with the previous crystal structure reported as *Modification I* **[Chatzi 1987]** it was found that films cast from H_2SO_4 solutions of Kevlar® fibres coagulated with water indicate the existence of an alternate crystal lattice termed as *Modification II* **[Haraguchi 1979]**, which is shown in figure 1.5b. The polymer molecules in this structure are ordered along the a-axis with a fairly regular intermolecular spacing under van der Waals forces. At the same time, the ordering of the molecules along the hydrogen bond direction is hindered by the bound water molecules in amide linkages through hydrogen bonds.

Results from X-ray analysis reveal important information in terms of crystallinity, crystallite size, crystal defects and crystal orientation. It is estimated that crystallinity of Kevlar®29 is of the order of 80-85% and that of Kevlar®49 of the order of 90-95% **[Panar 1983]**. It was also found that the crystallite size along the fibre axis is higher for Kevlar®29 compared with Kevlar®49 **[Hindeleh 1984]**.

Because of its anisotropic nature, Kevlar® fibres have a high level of axial crystal order. The average angle of orientation between crystallites and fibre axis measured with diffraction techniques is of a 'bulk average' nature and is more likely to be twice the angle of a given crystallite in the fibre. The orientation angle is numerically smaller for higher degrees of axial crystal orientation. Experimental results agree with the above. Kevlar® and Kevlar®29 fibres give orientation angles in the range of 12-20° and Kevlar®49 in the order of 12° or less with even lower values for Kevlar®149.

Small Angle X-ray Scattering (SAXS) [**Herglotz 1984**] and Transmission Electron Microscopy [**Panar 1983**] techniques revealed a *crystalline defect structure* for Kevlar®. A series of bands spaced by 30-40nm were observed. It was suggested [**Panar 1983**] that these bands represent stacks of crystalline layers perpendicular to the fibre axis which are separated by defect layers. A crystalline structure model demonstrated in figure 1.6a was proposed. The vertical lines in this model represent molecular chains. Highly extended chains pass through consecutive crystalline layers, while chain bends and possibly half the chain ends are contained in alternating defect layers. While the defect layers represent weak links in the axial fibre structure, they are successfully bridged by straight-through polymer chains which enhance the fibre strength.

In a different approach [**Pruneda 1981**], a defect structure model illustrated in figure 1.6b was proposed. An assumption based on experimental observations was made: The polymer chain ends congregate in a defect plane where fibre fracture may occur. The periodicity of the defect planes was assumed to be equal to the polymer chain length of 200-250nm. These assumptions are inaccurate in terms of the tensile fracture mechanisms of Kevlar® fibres and in that Kevlar® polymer chain lengths are of the order of 100nm.

(B) *Fibrillar Structure.* Kevlar® fibres fibrillate upon abrasion because they contain a highly ordered fibrillar structure. The tendency for fibrillation can be attributed to the lack of lateral forces, except for the van der Waals and the hydrogen bond forces between macromolecules which are very weak. In figure 1.6c, a proposed model of the fibrillar structure of Kevlar® fibre is shown [**Panar 1983**]. These fibrils are oriented along the fibre axis and are about 600nm wide and up to several centimeters long. They also show the crystalline defect layers at 35nm spacing. The highly crystalline, highly oriented fibrils constitute the basic elements of a fibre for load bearing applications. Such a 'microcomposite' arrangement imparts high strength and high modulus to the fibre.

(C) *Pleat Structure*. Kevlar® fibres exhibit a radially oriented crystalline organization with a uniform distribution of ordered crystalline material throughout the fibre [**Hagege 1979**]. Radial/transverse bands with some tangential splitting are observable by optical microscopy. As can be seen in figure 1.7a, these bands are visible in a cross-polarized light field. It is quite impressive, that by applying a tensile deformation, these bands disappear, figure 1.7b [**Panar 1983**]. It has been reported that the spacing between these bands is 500-600nm [**Dobb 1977**], [**Hagege 1979**], [**Panar 1983**], measured with electron diffraction and dark-field image electron microscopy methods. A model of radial pleated sheets based on these observations was suggested and is schematically shown in figure 1.7c. Experimental data have shown axial banding at 500 and 250nm periodicities in longitudinal fibre sections. The 250nm spacing is just one-half of the 500nm perodicity resulting from changes in crystalline orientation. The [2 0 0] crystalline planes form two alternating bands along the fibre axis at a small angle to each other. These bands in each sheet are aranged at approximately equal but opposite angles to form the pleats. The pleat angle is estimated to be 170°. A narrow transition region exists between the alternating bands, where the P*p*PTA molecules are parallel to the plane of the fibre section. In this region, the hydrogen-bonded sheet must incorporate a bend of about 10° which can only be accomplished by an identical rotation of molecular segments. The pleated sheet structure is also morphologically superimposed on the fibrillar structure.

Both Kevlar®29 and Kevlar®49 fibres exhibit the pleat structure, with Kevlar®49 showing a pleat structure of less intensity and more uniformity. In contrast, Kevlar®149 fibre with ultra-high tensile modulus, higher crystalline orientation and a larger crystallite size than Kevlar®49, lacks the pleat structure [**Krause 1989**]. Clearly, the presence of a pleat structure imparts a small amount of elasticity which tends to depress the tensile modulus of Kevlar® fibre.

(D) *Skin-core structure*. Skin-core differentiation has also been observed in Kevlar® fibres [**Provost 1977**], [**Pruneda 1981**], [**Morgan 1983**]. It was observed that partially fractured fibre skins and stepwise transverse core ruptures occur in the tensile deformation of Kevlar®49 fibres. The fracturing of fibre skins was considered to result from the splitting of a highly ordered fibrillar structure in the skin region. The transverse rupture of fibre cores, however, was attributed to the partial transverse skin fracture at two points which are connected by longitudinal crack propagation and cause the core failure at both points. These considerations suggest a skin-core profile in density and fibrillar orientation resulting from the fibre coagulation process. Such skin-core differentiation is illustrated in figure 1.8a. As can be clearly seen, a highly oriented fibrillar structure in the skin and a poorly oriented fibrillar structure in the core exists in an acid-swollen Kevlar® filament. A proposed model is shown in figure 1.8b [**Panar 1983**]. This model considers uniform axial orientation of the fibrils in the fibre skin, while the fibrils in the fibre core are imperfectly packed and ordered.

Some more evidence from SAXS also suggests the presence of microvoids in Kevlar® fibre. Indeed, elongated voids with their long axes approximately parallel to the fibre axis have been observed in the fibre core. These voids give greater accessibility to dyeing and plasma etching. Also, they must play a very important role in the deformation and fracture characteristics of Kevlar® fibre.

1.2.2. Aromatic heterocyclic polymer fibres.

Aromatic heterocyclic polymers include *polybenzimidazoles, polybenzothiazoles, polybenzoxazoles* and *polyoxadiazoles*. Many of these polymers have been reported in the literature and few of them have industrial potential for high performance fibre production. These polymers contain fused rings in rigid-rod type configuration. They are generally known for their excellent thermal and chemical resistance. However, they are difficult to process due to their

unmeltable behaviour and poor solubility in conventional solvents. Representative polymer fibres spun from this family have been studied and characterised in this work, abbreviated as PBZT and PBO (a *polybenzobisthiazole* and a *polybenzobisoxazole* fibre respectively). The only PBZT fibre examined, (denoted as Z1) was produced by US Air-Force and supplied by Royal Aerospace Establishment (currently DRA Farnborough) and the four grades of different PBO fibres (denoted as B1, B2, B3 and B4) were supplied by Dow Chemicals Co.

Fibres derived from polybenzothiazole polymers are a relatively recent development. Synthesis of a polybenzobisthiazole polymer from the reaction of 2,5-diamino-1,4-benzenedithiol and terephthalic acid is presented below (only one repeat unit for the polymer is shown in the reaction) **[Helminiak 1977]**, **[Wolfe 1978,1980]**:

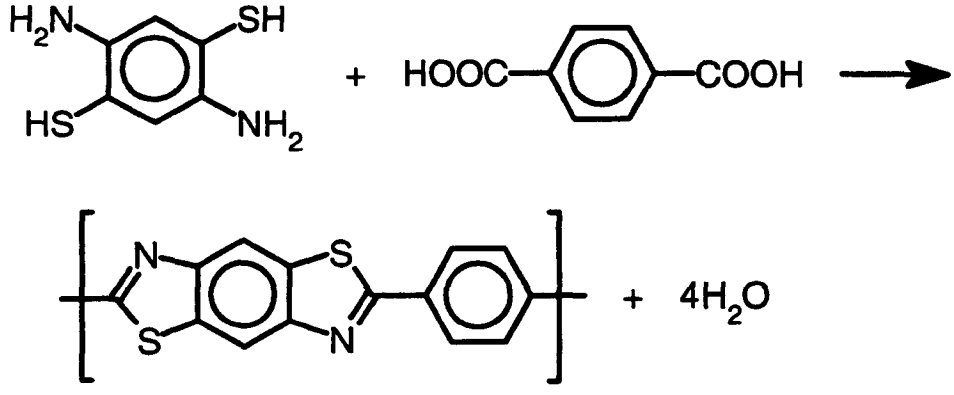

Poly(*p*-phenylene benzobisthiazole)

It can be seen that the thiazoles in the PBZT molecular unit are in *trans* configuration (*t*-PBZT) while the oxazoles of PBO are in *cis* configuration (*c*-PBO). Crystal structure of model compounds has confirmed that the *trans* isomer of PBZT is linear while the *cis* isomer is slightly bowed **[Allen 1983]**.

Fibre preparation from PBZT-acid solutions is achieved by wet spinning and dry-jet wet spinning processes **[Allen 1981a,b]**, similar to those for Kevlar® (figure 1.9). The spun filaments are coagulated in water and dried (as-spun

fibres). A hot drawing can follow in a nitrogen atmosphere through a tubular oven (heat treated fibres). The stress-strain behaviour of the as spun fibres is non-linear, while the heat treated fibres exhibit an essentially linear behaviour with significantly higher tensile properties. Other workers **[Uy 1990]** improved the fibre spinning process and obtained higher tensile properties for their fibres and excellent environmental stability. At the present time, the high cost of polymer ingredients, polymerization and fibre spinning processes make this fibre extremely expensive.

(A) Fibre structure and morphology of PBZT. Electron and X-ray diffraction techniques have been used extensively for the study of the PBZT chain molecule **[Adams 1980]**, **[Roche 1980]**, **[Wellman 1981]**. There are two planar segments in the molecular structure: the benzobisthiazole domain and the associated phenylene rings. Although the structure is rodlike, there is still some degree of mobility for segmental rotation. It has been proven that the fibre repeat unit contains only one molecular chain repeat unit. As a result, molecular orientation can be achieved.

Since PBZT molecules do not contain co-planar end groups, they lack extensive intermolecular hydrogen bonding and hence longitudinal registry along the fibre axis. Only limited evidence of crystallites with lateral and longitudinal periodicities was found by TEM lattice image analysis. PBZT fibre has largely a 2-dimensional lateral order **[Thomas 1982]** as compared to the 3-dimensional hydrogen-bonded sheet structure of Kevlar®. Its crystallites are well oriented and developed in a skin-core structure. As can be expected, heat treatment of PBZT fibre under tension improves further its crystal orientation. A basic micro-fibrillar structure has also been suggested **[Cohen 1988]**, with microfibrils being in the order of 100Å wide. This scheme implies poor compressive behaviour due to the micro-fibril buckling.

Fibres derived from polybenzoxazole polymer solutions were also developed in the 1980's. Their molecular structure is similar to the

polybenzothiazoles with the sulphur atoms replaced by nitrogen atoms in the *cis* configuration. Poly(*p*-phenylene benzobisoxazole) is synthesized according to the following scheme [**Choe 1983**] involving the polycondensation of 4,6-dihydroxy-*m*-phenylenediamine and terephthalic acid in polyphosphoric acid environment at 130-200°C for several hours (only one repeat unit of the polymer is shown in the reaction below):

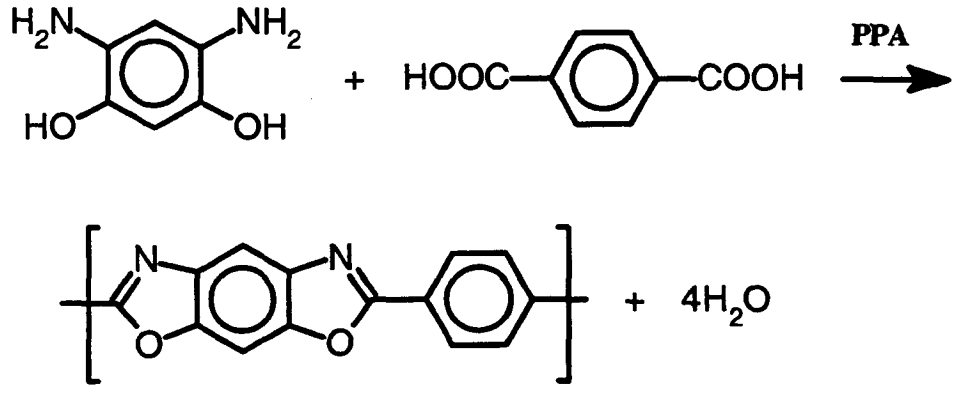

Poly(*p*-phenylene benzobisoxazole)

Fibres can be prepared by dry-jet wet spinning of the polymer solution at 60-90°C. The solution concentration and temperature are varied to accommodate the polymer and facilitate the extrusion process. The spin solutions are concentrated enough to be in the liquid crystalline state. The resulting as spun PBO fibres can be heat treated at 450-500°C in air or nitrogen atmosphere. The heat-treated fibres show high tensile stiffness and strength.

(B) Fibre structure and morphology of PBO. The structure and morphology of PBO fibres has been reported in the literature [**Bhaumik 1981**], [**Fratini 1985,1986**], [**Krause 1988**]. The two segments of the molecular structure (the benzobisoxazole domain and the phenylene ring) are coplanar. PBO molecules are highly oriented, forming a fibrillar structure composed with 200nm ribbon-like fibrils. PBO molecules and crystallites form a 3-D crystalline arrangement with limited long-range order.

In the following table **[Yang 1989]** a review of the structural data for the three basic fibres examined in this work is given:

	Kevlar®		PBZT		PBO	
	as	ht	as	ht	as	ht
Crystal unit cell	Monoclinic		Monoclinic		Monoclinic	
a (Å)	7.87		7.10		5.65	
b (Å)	5.18		6.65		3.58	
c (Å)	12.9		12.35		11.74	
Mean *c* axis (Å)					11.96	12.01
Paracrystalline analysis						
g (%)	1.7			0.55	1.22	1.07
D (nm)	70.0			22.8	15.9	19.5
HT/AS crystallite size ratio						
a axis					1.9	
b axis					1.4	
c axis					1.2	
Crystallite sizes						
Axial (nm)	17.7		19.0		5.2	5.7
Transverse (nm)	4.5		9.0		5.4	10.6
Axial / Transverse	2.7		2.1		0.96	0.54
Density (g/cm^3)						
Calculated	1.49		1.69		-	
Measured	1.44		1.40		1.50	

Table 1.4. *Structural data for PpPTA, PBZT, PBO fibres* **[Yang 1989]**.

1.3. Mechanical properties of LCP fibres - a review.

In the previous paragraphs of this chapter a brief description of the fabrication, structure, morphology and general properties of the LCP fibres examined in this work, was given. In this section, more information focussed on the key mechanical properties of these fibres, is presented. In general, fibre properties are controlled by many parameters such as polymer composition, molecular weight distribution, solution behaviour, spinning and drawing conditions etc. A more detailed account of the mechanical properties of the fibres examined in this work will follow. Results reported in the literature are directly compared with experimental data obtained in this work.

1.3.1. Aromatic polyamide fibres (aramids).

Kevlar® aramid fibre products have been used in industrial applications since their introduction in 1972 by du Pont. A broad spectrum of industrial, aerospace, military and civilian applications is covered. These applications include ballistic and fire protective apparel, hard armours, reinforced tyres and rubber goods, various forms of composites, filament wound pressure vessels, marine ropes, optical cables, industrial gloves and more. While each application has its specific requirements, almost all of them utilize the high strength, high modulus, high toughness, low creep and low weight of Kevlar® fibres.

In general, the mechanical properties of aramid fibres are very much dependent on their microstructure, i.e. the polymer chain conformation and rigidity, the intermolecular hydrogen bonding, crystalline orientation and crystallinity, issues which have already been discussed in detail. Nonlinear chain conformation, reduced chain rigidity and crystalline defects impose some adverse effect on fibre properties. The degree of crystal orientation governs the elastic modulus of aramid fibres. The importance of this parameter is presented in figure 1.10 where the initial Young's modulus is plotted versus orientation

angle [**Kwolek 1974**]. It is obvious that the modulus increases hyperbolically with the minimization of the crystal misorientation. High orientation in aramid fibres is usually achieved by a process already referred as heat treatment. The spun fibre is often stretched simultaneously with or in sequence to post-spinning processess such as washing and drying. The degree of drawing depends largely on the plasticity of the fibre. A wet fibre with high solvent content may be drawn considerably more than a dry fibre with low residual solvent. Dry fibres which are therefore, drawn at elevated temperatures in very short exposures encourage the molecular orientation and crystal growth. The presence of hydrogen bonding in aramid fibres also exerts a significant effect on the spontaneous orientation of polymer chain during heating under tension for a short period of time. The above procedure has been applied succesfully to enhance the mechanical properties of aromatic polyamide fibres. All fibres examined in this work exhibit tensile moduli which correspond to orientation angles of the 0°-10° region according to the correlation shown in figure 1.10.

The tensile properties of Kevlar® yarns are measured after drying at $140^{\circ}C$ and then conditioning at $20^{\circ}C$, 55% relative humidity for 16 hours. The test specimen is twisted at a twist multiplier to a value of 1.1 which is optimal for Kevlar® yarns because the maximum tensile strength is obtained at this twist level as can be seen in figure 1.11a [**du Pont, 1978**]. Kevlar yarn has a break tenacity (strength) of given size yarn with units of *grams of breaking force per denier*, of about 22gpd, which is more than five times that of steel wire and twice that of nylon, polyester or glass fibres. Kevlar® yarn also has high initial specific modulus which is about twice that of steel wire or fibreglass, four times that of high tenacity polyester and nine times that of high tenacity nylon. On the other hand, Kevlar® exhibits 50% loss of its tensile strength and 20% loss of its Young's modulus at elevated temperatures ($300^{\circ}C$).For comparison, the mechanical properties of the various products are given in the following table [**Yang, 1989**]:

Property / Fibre	Density / g/cm³	Strength / MPa	Modulus / GPa	Elong. / %	Spec. Strength / MPa m³ /10³ kg	Spec. Modulus / MPa m³ /10⁶ kg
Kevlar® 29	1.43	2900	70	3.6	2027	49
Kevlar® 49	1.45	2900	135	2.8	2000	93
Kevlar® 149	1.47	2300	143	1.5	1564	97
Nomex®	1.38	600	17	22.0	434	12
Technora®	1.39	3300	70	4.3	2374	50
Vectran®	1.47	3200	91	-	2177	61
PET	1.38	1000	5-12	-	724	3-9
Nylon 66	1.14	1000	12.5	17.0	877	10
Dacron	1.38	1120	13.8	14.5	812	10
Boron	2.50	2550	400	1.0	1020	160
SiC	2.80	4000	420	0.6	1428	150
Alumina	3.25	1800	210	1.2	554	65
Nextel	2.50	1720	152	2.0	688	61
S-glass	2.48	4800	85	5.3	1935	34
E-glass	2.55	2600	72	3.0	1020	28
Steel	7.80	7600	150	4.8	974	19
HS Carbon	2.00	2700	270	0.8	1384	138

Table 1.5. *Comparison of tensile properties of high performance fibres* [**Yang 1989**].

In conclusion, the tensile strength of Kevlar® 49 is more than twice that of Dacron and nylon, and almost 15% greater than that of E-glass. Its Young's modulus is more than 20 times that of nylon, almost 10 times that of Dacron and almost twice that of E-glass. However, inorganic reinforcing fibres such as graphite and boron give higher modulus than Kevlar®49. For comparative purposes, the stress-strain curves of various filaments are given in figure 1.11b.

Twaron® aramid fibre is very similar to Kevlar®. Technora® aramid fibres differ from Kevlar® fibre in its polymer composition and method of preparation. Their mechanical properties along with chemical and impact resistance are quite similar. Technora® is a wholly aromatic copolyamide highly modified with a crankshaft shaped co-ingredient. The highly modified copolymer fibre has a fine structure with randomly distributed amorphous regions and modest crystallinity but fully extended chain structure. Technora® has an equilibrium moisture content significanty lower compared with Kevlar®29 and Kevlar®49 with strong chemical resistance which has been associated with its high drawn fibre morphology.

1.3.2. Aromatic heterocyclic polymer fibres (PBZT and PBO).

PBZT, PBO and AB PBO fibres belong to a group of rigid-rod like chain LCP fibres. They are more recent developments than aramid fibres. They were first produced and investigated by SRI Research International under the U.S. Air Force Ordered Polymer Program. Dow Chemical Co. has acquired a license from Commtech International Management to develop PBO fibres which they recently sold. In the previous paragraphs a description of the dry-jet wet spinning process of the fibre production was given. The as-spun fibres give moderate tensile properties. Considerable efforts have been made in order to improve the fibre properties by heat treatment (PBZT, PBO) or by using very high molecular weight polymers and liquid crystalline solutions **[Wolfe 1987]**. The solution

concentration and temperature were varied to accommodate the polymers and facilitate the extrusion process. The heat treatment conducted under tension gave impressive results, shown in table 1.6:

Property / Fibre	Density / g/cm^3	Strength / MPa	Modulus / GPa	Elong. / %	Spec. Strength / MPa m^3 /10^6 kg	Spec. Modulus / MPa m^3 /10^6 kg
PBZT						
as	1.4	865	86	3.0	617	61
ht	1.4	2500	259	1.5	1785	185
PBO						
as	1.5	2960-3120	90-303	4.2-6.0	1973-2080	60-202
ht	1.5	3070-3450	317-410		2046-2300	211-273
AB PBO						
as	1.6	2570-2830	41-79	4.6-4.8	1606-1768	26-49
ht	1.6	2620-3340	115-144	2.5-3.6	1637-2087	72-90

Table 1.6. *Comparison of tensile properties of heterocyclic polymer fibres* [**Yang 1989**].

It can be seen from the above that the development of synthetic fibres has resulted from technological advances in polymer synthesis and fibre preparation. Some fibres may have the most desirable extended chain conformation, but not necessarily the best mechanical properties because of structural defects arising from fibre forming processes. Some other fibres may have some very attractive mechanical properties but lack chemical and solvent resistance because of chemical composition or morphological defects.

1.4. Summary.

Many different approaches to high performance organic fibres have been developed and all yield the production of various fibres suitable for composite reinforcement. While their properties may differ, all these fibres exhibit low density, very high specific tensile properties, high toughness and relative chemical and electromagnetic inertness. As a result of their high structural anisotropy, they exhibit low compressive and shear properties and negative axial coefficients of thermal expansion. Finally, their use temperatures cover a broad range from low melting (140°C) polyethylene to 300°C for some aramids and heterocyclic polymer fibres.

High performance polymeric fibres have the potential to be used in a number of advanced engineering applications. The present challenge to the synthetic fibre manufacturers and consumers is to facilitate this transition in a controlled, sustainable and commercially successful fashion.

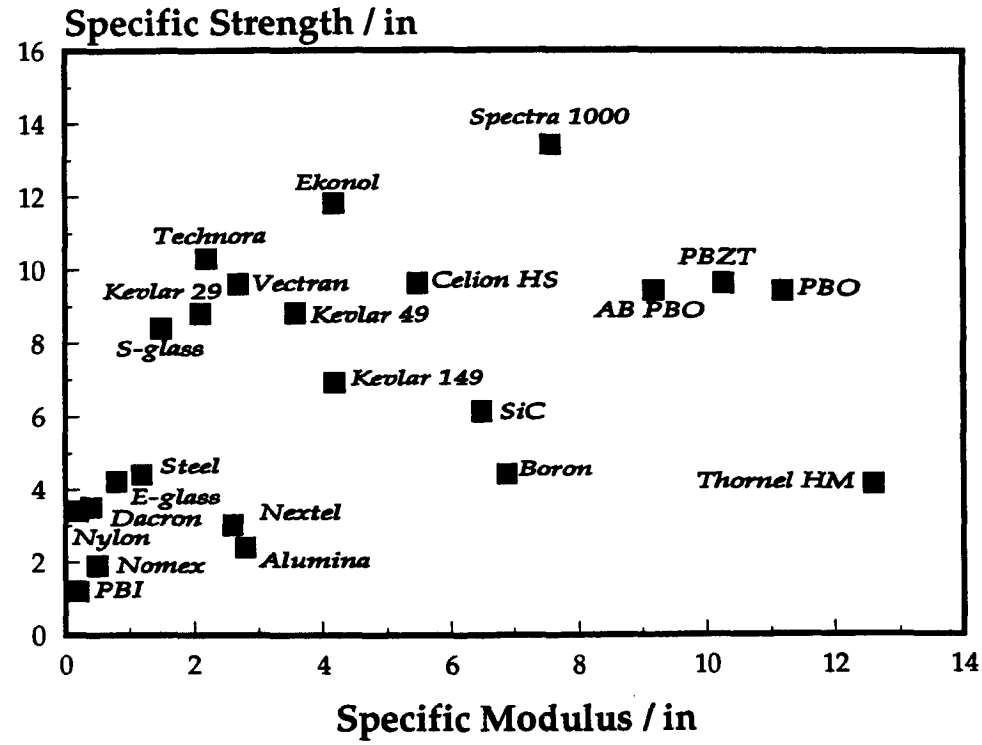

Figure 1.1. Specific tensile strength-modulus for various fibres [**Yang 1989**].

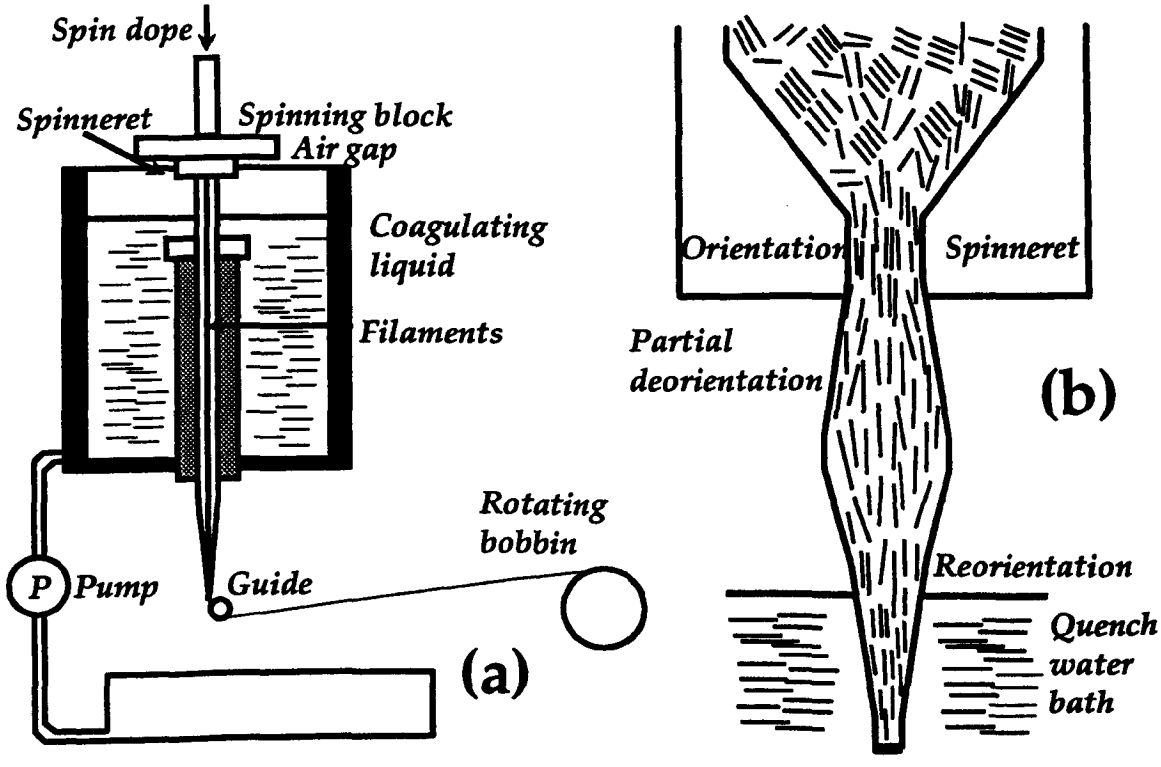

Figure 1.2. (a) Dry-jet wet spinning process for Kevlar® fibre [**Blades 1975**].
(b) Kevlar® fibre structure development during dry-jet wet spinning process.

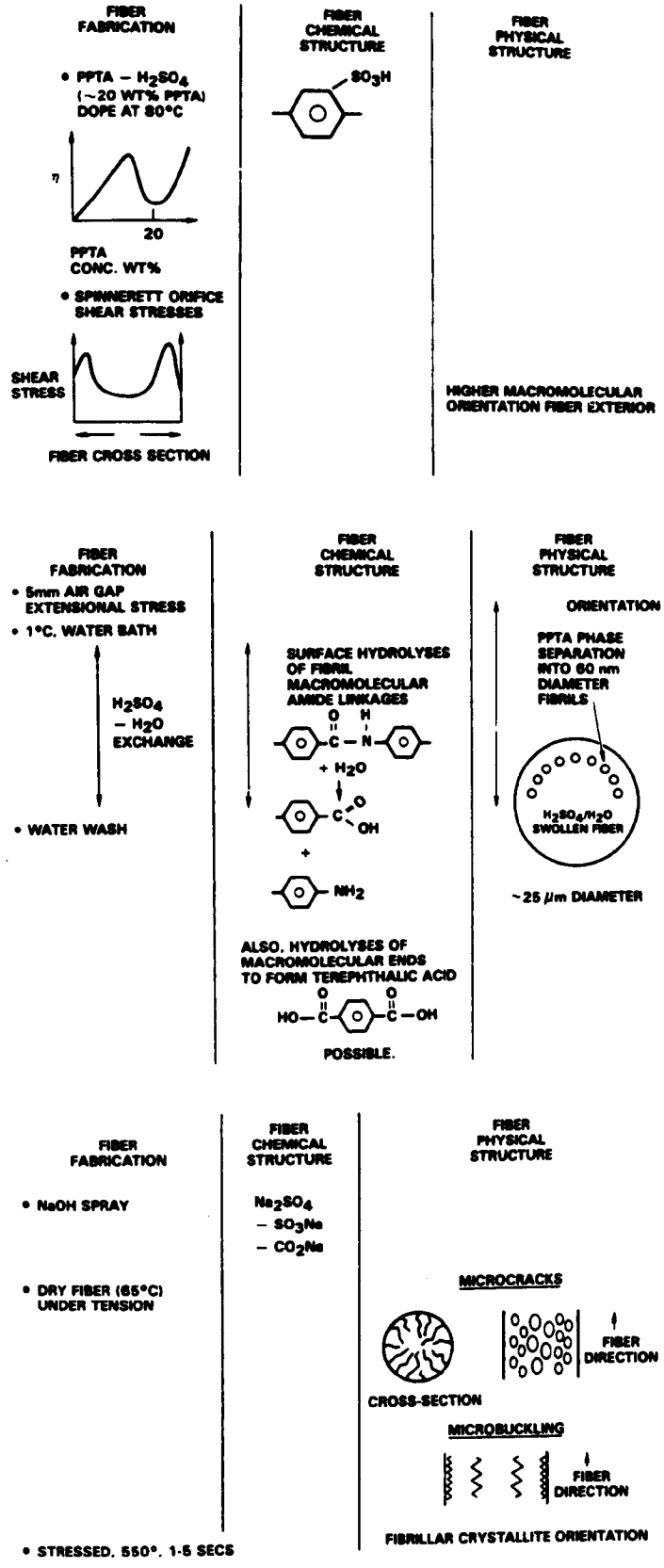

Figure 1.3. Kevlar® fibre chemical & physical structures during fabrication [Morgan 1989].

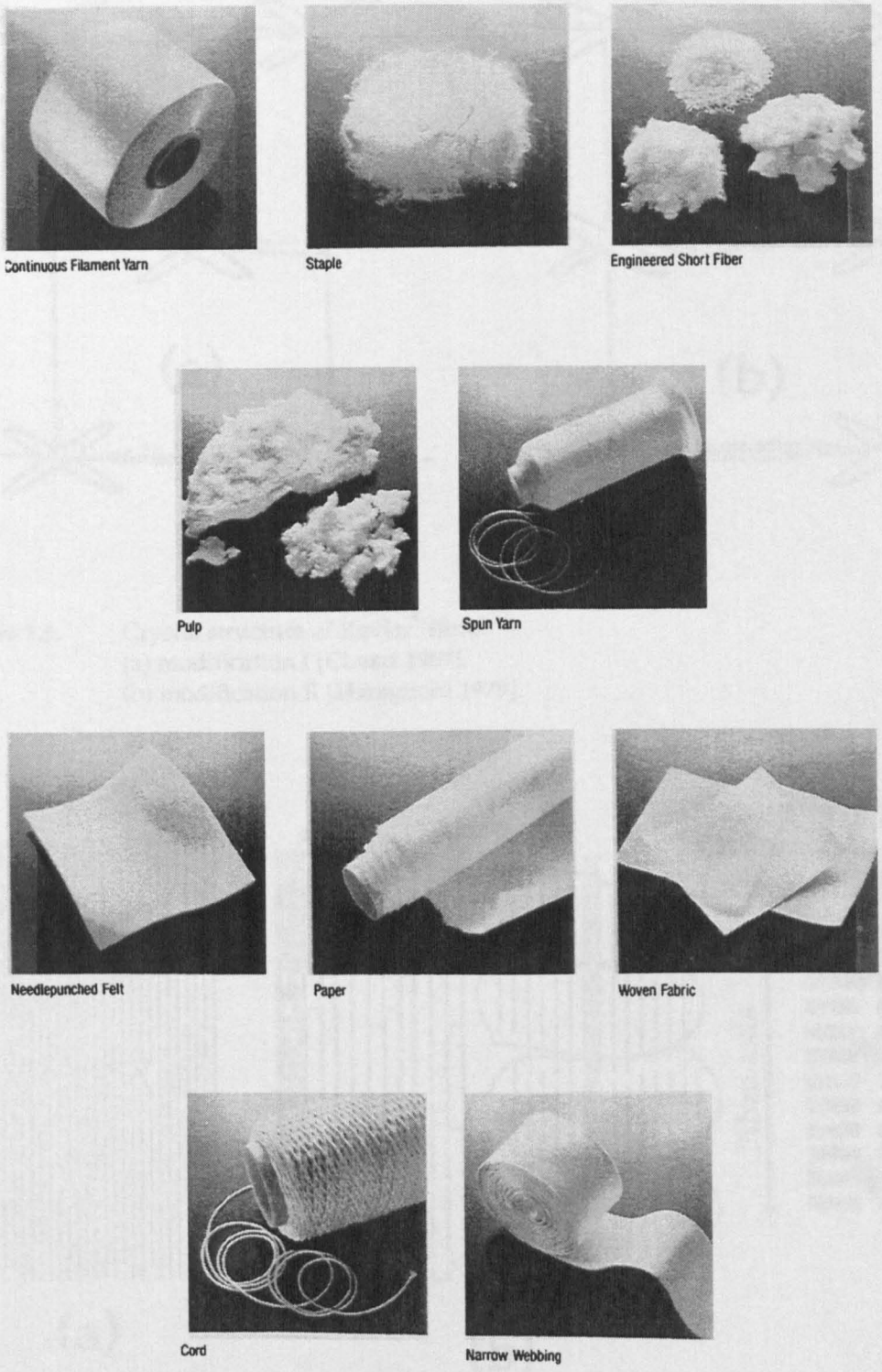

Figure 1.4. Various product forms of Kevlar® **[du Pont 1989].**

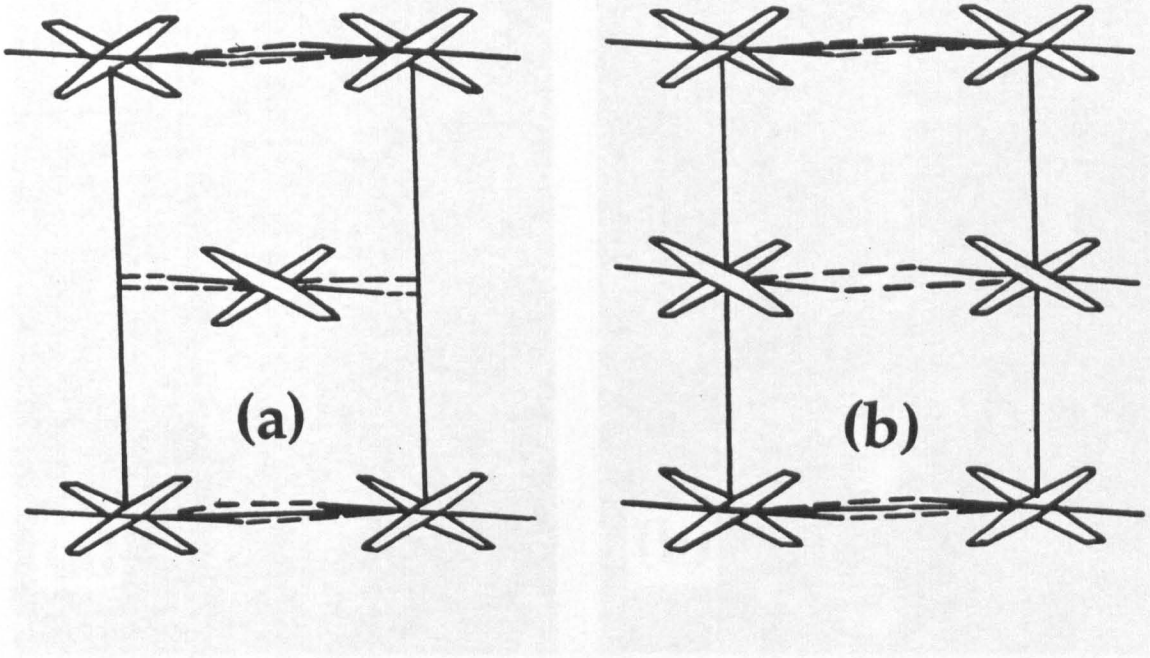

Figure 1.5. Crystal structure of Kevlar® fibre:
(a) modification I [**Chatzi 1987**].
(b) modification II [**Haraguchi 1979**].

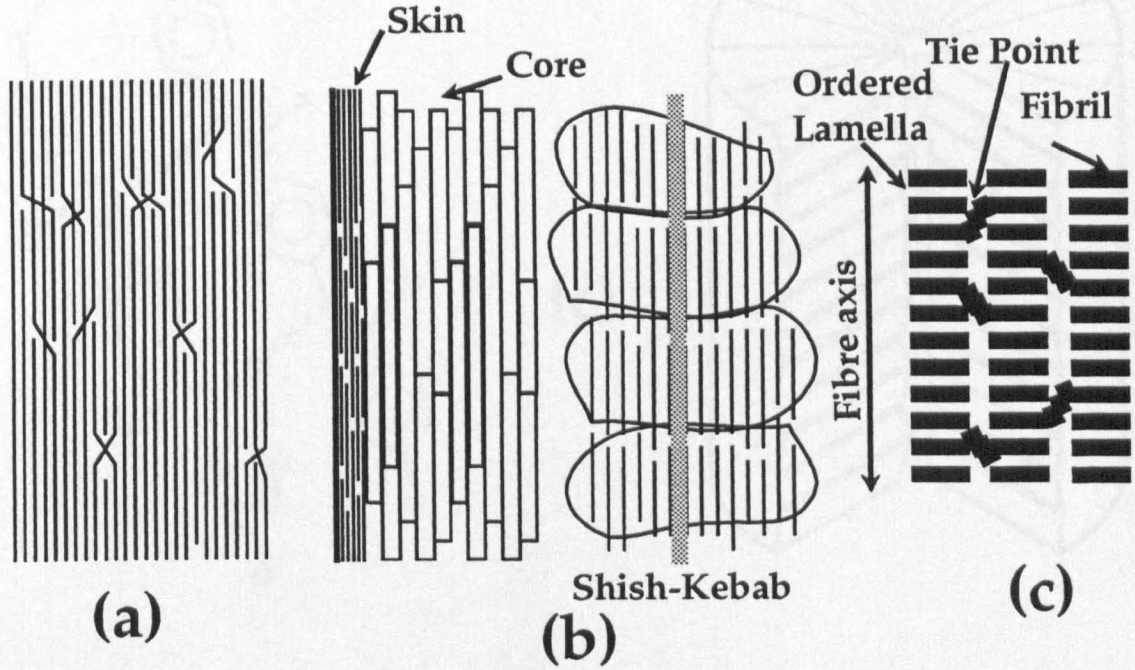

Figure 1.6. (a) Crystalline structure model of Kevlar® fibre [**Panar 1983**].
(b) Crystalline structure model of Kevlar® fibre [**Pruneda 1981**].
(c) Fibrillar structure model of Kevlar® fibre [**Panar 1983**].

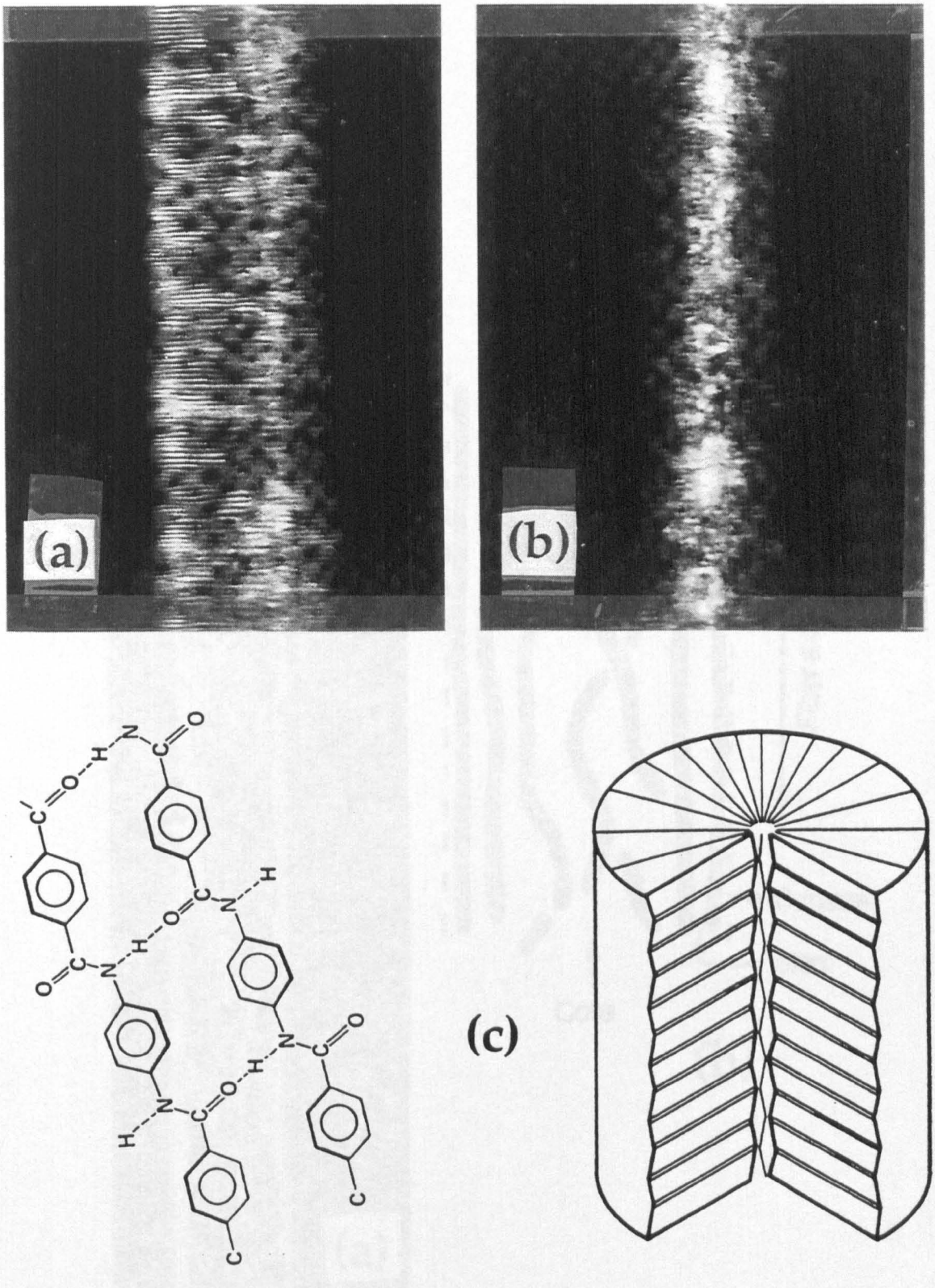

Figure 1.7. (a) Pleat structure of Kevlar® fibre **[Panar 1983]**.
(b) Diminished pleat structure of Kevlar® under tension **[Panar 1983]**.
(c) Schematic model of pleat structure and hydrogen bonding in Kevlar® fibre **[Dobb 1977]**.

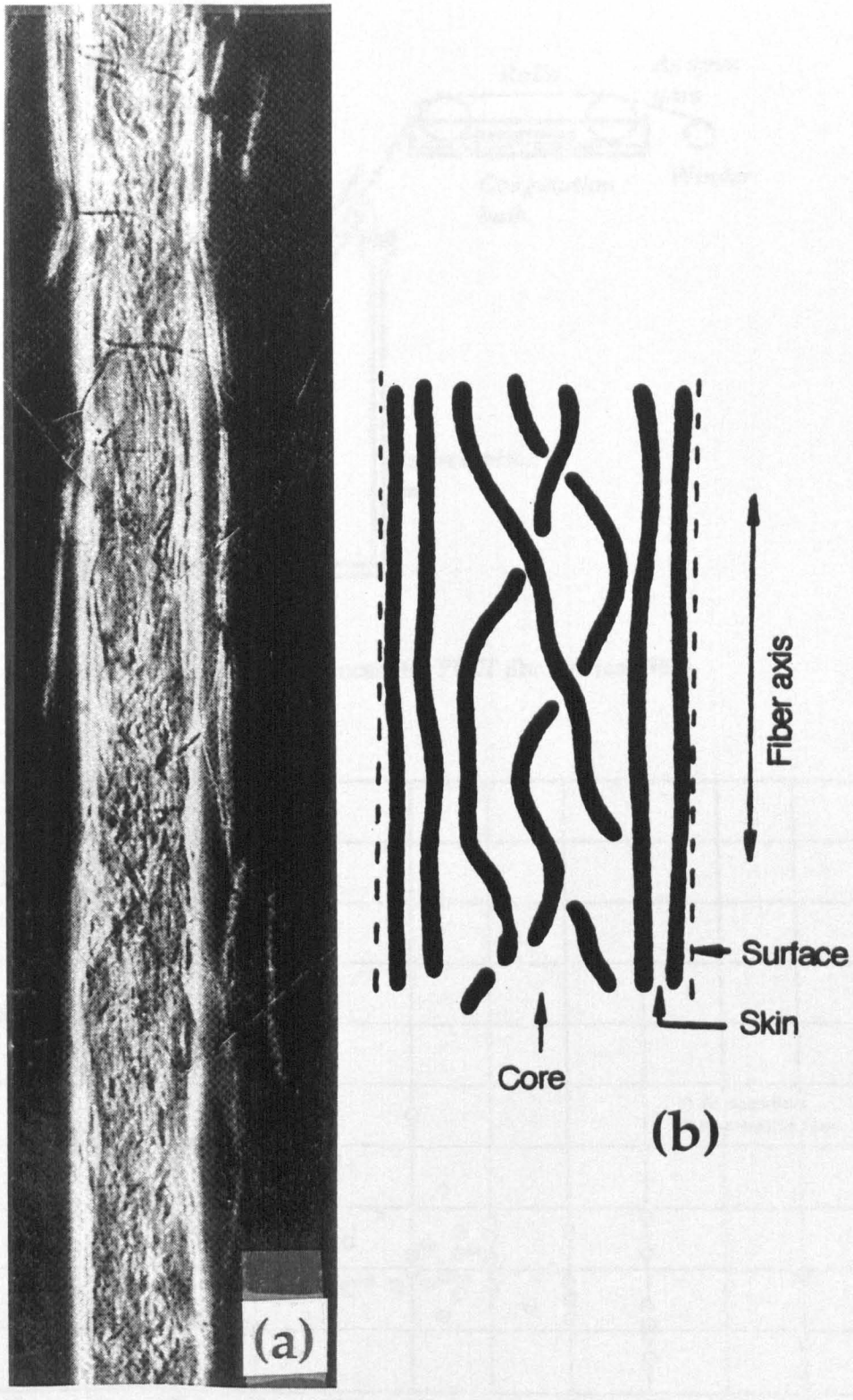

Figure 1.8. (a) Skin structure of Kevlar® fibre **[Pruneda 1981]**.
(b) Schematic representation of skin-core structure of Kevlar® fibre.

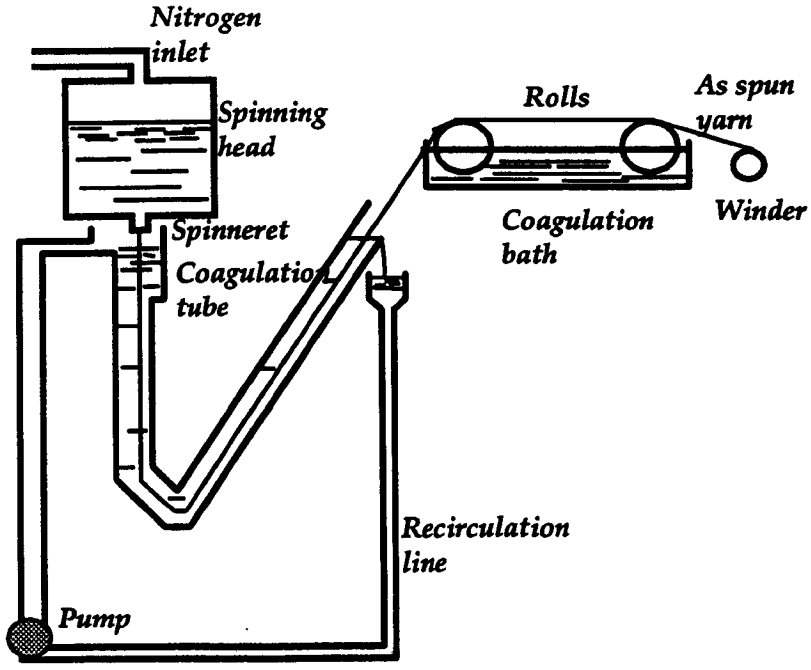

Figure 1.9. (a) Dry-jet wet spinning process for PBZT fibre [Allen 1981].

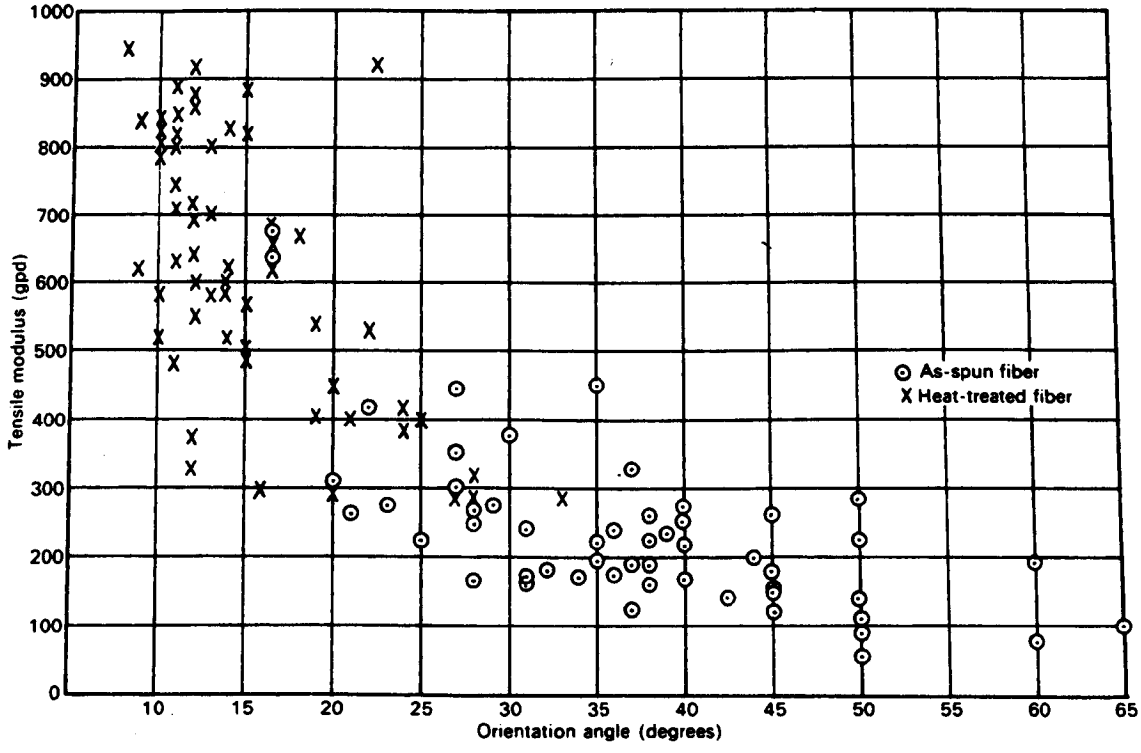

Figure 1.10. Initial Young's modulus vs orientation angle for various experimental aramid fibres [Kwolek 1974].

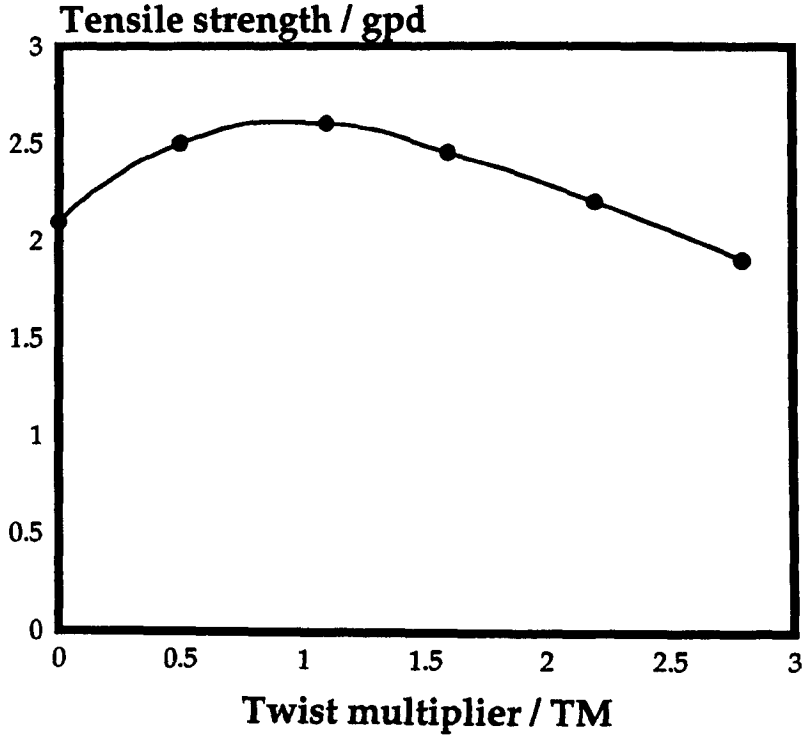

(a)

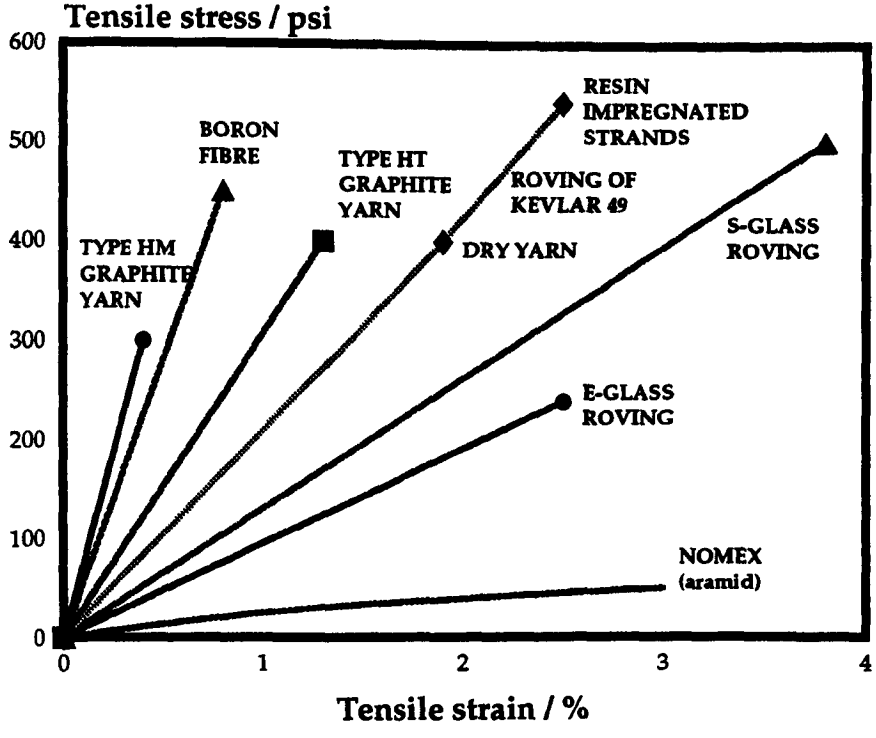

(b)

Figure 1.11. (a) Tensile strength vs twist multiplier of Kevlar fibre **[du Pont 1978]**.
(b) Stress-strain curves for various reinforcing filaments **[Yang 1989]**.

CHAPTER 2:
LASER RAMAN SPECTROSCOPIC STUDIES ON LIQUID CRYSTAL POLYMER FIBRES

2.1. Fundamental principles of Laser Raman Spectroscopy.

2.1.1. The Raman effect.

Visible light is a form of *electromagnetic radiation* and can be viewed as a simple harmonic wave propagating in straight lines. Light can interact with matter in a number of different ways. Interactions between light and matter involve changes of energy before and after the interaction. Reflection or transmission for instance occur with little or no change in the radiant energy, so the reflected or transmitted light has the same frequency as the incident one.

In a similar manner, when light is passed through a transparent substance, *light scattering* occurs, almost entirely without gain or loss of energy. This is termed as *Rayleigh scattering* (elastic scattering). However, a very small amount of the light scattered exhibits constant frequency differences from the incident light, indicating energy transfer to or from the scattering medium. This is called the *Raman effect* **[Raman 1928]** which is schematically shown in figure 2.1a. The frequency differences which represent the differences in energy between the incident and the scattered *photon* are associated with transitions between rotational or vibrational states of the scattering *molecule* **[Long 1977]**. The Raman frequency 'shifts' are termed as *Raman lines* or *bands* and collectively constitute a *Raman spectrum.*

At this stage it is important to mention Max Planck's discovery from the beginning of this century which shows that, the energy of an 'oscillator' (such as

a molecule) is discontinuous and any change in its energy content can occur only by means of a jump between two distinct 'energy states'. Rayleigh and Raman scattering can be easily understood in terms of these principles.

Let us consider the incident radiation as consisting of a stream of particles (*photons*) having energy $\hbar\nu_0$, where $\hbar$ is the Planck's constant and ν_0 the frequency of radiation. Photons can be imagined to undergo collisions with the molecule and, if the collision is perfectly 'elastic', they will be deflected unchanged. A schematic representation of this is given in figure 2.1c, where the molecule undergoes a transition from the *ground energy state* E_0 to a *virtual energy state* E_v and returns back to the ground energy level E_0. In this case, no energy is exchanged between the molecule and the photon and hence, the frequency of the photon remains unchanged. This is called *Rayleigh scattering*.

However, it may happen that energy is exchanged between photon and molecule during the collision: such collisions are called 'inelastic'. The molecule can gain or lose amounts of energy only in accordance with Planck's laws, i.e. its energy change must correspond to the difference in energy between two 'allowed' energy levels. If the molecule gains energy ΔE, the photon will be scattered with energy $\hbar\nu_0 - \Delta E$ and the scattered radiation will have a frequency $\nu_0 - \nu_k$ where $\nu_k = \frac{\Delta E}{\hbar}$. Schematically, this is demonstrated in figure 2.2d, where the molecule undergoes a transition from the ground energy state E_0 to a virtual energy state E_v and finishes at a *stationary energy state* E_1. On the other hand, if the molecule loses energy ΔE, the photon will be scattered with energy $\hbar\nu_0 + \Delta E$ and the scattered radiation will have a frequency $\nu_0 + \nu_k$ where again $\nu_k = \frac{\Delta E}{\hbar}$. This is demonstrated schematically in figure 2.2b, where the molecule is already at a stationary energy state E_1, undergoes a transition to a virtual state E_v and returns to the ground energy state E_0.

Radiation scattered with a frequency lower than that of the incident is referred to as *Stokes scattering* and results in an increase in molecular energy.

Radiation scattered with a frequency higher than of the incident is referred to as *anti-Stokes scattering* and results in a decrease in molecular energy [**Banwell 1983**]. This can only occur if the molecule is originally in an excited energy level. It must be noted at this point that anti-Stokes radiation is of lower intensity than Stokes radiation because at equilibrium temperature the population of molecules of a higher energy level is less than that of a lower level and decays exponentially with energy.

2.1.2. Molecular vibrations and molecular symmetry.

In order to interpret Raman spectra of polyatomic molecular systems, we need to derive a model for the motion of the molecular system in space. This is a very complex problem because it involves simultaneous *translations, rotations* and *vibrations* of the molecular system. As a simplified approach only with the vibrational motions are considered [**Califano 1976**], [**Long 1977**].

Let us consider a molecular system consisting of **N** atoms. We assume that the atomic nuclei **1,2,...,N** vibrate with a small amplitude about their equilibrium positions. In this case, there are **3N** degrees of freedom for the entire molecular system. In the simplest case, only **n=3N-6** degrees of freedom exist, associated with changes in the lengths of the chemical bonds and angles between bonds (*natural vibrational coordinates*). Three degrees of freedom associated with translation of the molecular gravity centre and three associated with overall rotation have been neglected. In linear molecular systems there are **n=3N-5** degrees of freedom because only two coordinates are necessary to specify the molecular orientations. To each vibrational degree of freedom $\mathbf{k}\,(\mathbf{k}=1,2,\ldots\mathbf{n})$ there corresponds a certain vibrational mode of the molecular system with a definite frequency $\omega_k\,(k=1,2,\ldots n)$. Therefore, the vibrational state of the molecular system is characterised by **n** independent (harmonic approximation) *normal vibrational coordinates* $q_k\,(k=1,2,\ldots n)$, which are directly related to the

Cartesian vibrational coordinates x_k $(k = 1,2,...n)$ of the atomic nuclei, representing displacements from their equilibrium positions. For each normal vibrational coordinate, the molecular system undergoes a simple motion in which all the nuclei move in phase with the same frequency but with different amplitudes. A mode of motion of this kind is called a *normal vibrational mode* and the associated frequency is called *normal* or *fundamental vibrational frequency* **[Long 1977]**.

In some cases it can happen that two or more solutions coincide. The two or more corresponding normal vibrations will therefore have the same frequency. In such a case, the two or more vibrations are said to be *degenerate.* The occurrence of degenerate vibrations is directly related to the existence of *symmetry* in the molecular system. By symmetry of a molecular system we mean the symmetry of the nuclear arrangement in the equilibrium configuration. A molecular system is considered to be symmetric if some transformation of its normal coordinates $q_1, q_2, ..., q_n$ carries it from one configuration to another absolutely equivalent configuration. These coordinate transformations are called *symmetry operations* and their geometrical representations are known as *symmetry elements*. A symmetry element is thus defined through the symmetry operations associated with it.

For any molecular symmetry, the normal vibrational modes are classified into various categories :

- vibrational modes whose normal vibrational coordinates are invariable under *all* the symmetry operations. These vibrations preserve the symmetry of the system and they are called *totally symmetric modes.*
- vibrational modes whose normal vibrational coordinates are not affected by symmetry operations. These are called *symmetric modes.*
- vibrational modes whose normal vibrational coordinates reverse their sign under symmetry operations. These are called *anti-symmetric modes.*

It has been found that in the (vibrational) Raman effect the Raman frequency bands are equal to the normal vibrational frequencies of the scattering

systems. In the following two sections a classical and a quantum -mechanical treatment of Rayleigh and Raman scattering is presented. The *selection rules* controlling which transitions participate in the Raman scattering, are also discussed for both treatments.

2.1.3. A classical treatment of Rayleigh and Raman scattering.

Let us return to the molecular system interacting with the (harmonic oscillating) electromagnetic field $\vec{E}(t)$. We assume that the molecular system (scattering system) is free to vibrate but not to rotate, i.e. the nuclei may vibrate about the their equilibrium positions and $q_1, q_2, \ldots, q_n$ are normal coordinates of these vibrations. The *induced dipole moment* $\vec{P}(t, q_1, q_2, \ldots, q_n)$ in the molecule can be expressed by the series [**Long 1977**]:

$$\vec{P}(t, q_1, q_2, \ldots, q_n) = \vec{P}^{(\alpha)} + \vec{P}^{(\beta)} + \vec{P}^{(\gamma)} \qquad (2.1)$$

where the first component, $\vec{P}^{(\alpha)}$, corresponds to Rayleigh and Raman (vibrational) scattering phenomena and the other two to higher order (i.e. rotational) transitions.

The correlation between the induced dipole moment $\vec{P}^{(\alpha)}$ (associated only with vibrational transitions) and the electromagnetic field $\vec{E}(t)$ is as follows:

$$\vec{P}^{(\alpha)} = \tilde{\alpha} * \vec{E}(t) \qquad (2.2)$$

In the above equation $\vec{P}^{(\alpha)}$, $\vec{E}(t)$ are vectors and $\tilde{\alpha}$ is a tensor with components α_{ij}, $i, j = 1,2,\ldots,n$. In general, the direction of the induced dipole moment is not the same as that of the electromagnetic field. For the majority of the molecular systems it involves a real symmetric tensor $\tilde{\alpha}$ which is referred to as the

polarizability tensor. The polarizability tensor $\tilde{\alpha}$ is a function of the normal coordinates of the molecule $q_1, q_2, \ldots, q_n$ at any given time. Due to the fact that $q_1, q_2, \ldots, q_n$ are small relative to the size of the molecule, each component α_{ij}, $i, j = 1,2,\ldots,n$ of the polarizability tensor can be expressed in a Taylor series with respect to the normal coordinates of vibration around their equilibrium values. If we neglect the terms which involve powers of q higher than the first (harmonic approximation) and introduce the time dependence of the electromagnetic radiation $\vec{E}$, $\vec{E}(t) = \cos(\omega_0 t)$ and simple harmonic motion for the normal vibrational mode q_k, $q_k(t) = q_{k0}\cos(\omega_0 t + \delta_k)$, equation 2.2 can be simplified to:

$$\vec{P}^{(\alpha)} = \vec{P}^{(\alpha)}(\omega_0) + \vec{P}^{(\alpha)}(\omega_0 - \omega_k) + \vec{P}^{(\alpha)}(\omega_0 + \omega_k) \qquad (2.3)$$

where the first term represents the Rayleigh scattering component, the second term represents the Stokes Raman scattering component and the third term represents the anti-Stokes Raman scattering component.

In order for a particular molecular frequency ω_k to be Raman active, it is necessary for at least one of the components of the *derived polarizability tensor* (tensor with components $\left(\frac{\partial \alpha_{ij}}{\partial q_k}\right)_0$, the '0' subscript represents equilibrium position) not to be zero. In other words, the induced dipole moment responsible for Raman scattering associated with the normal vibrational coordinate q_k will not be zero if the gradient of at least one component of the derived polarizability tensor against the normal vibrational coordinate q_k is not zero at the equilibrium position. This is the *selection rule* which governs whether a molecular vibrational frequency will be permitted or forbidden in the Raman effect.

If a molecule has little or no symmetry, it is usually correct to assume that all its vibrational modes are Raman active (i.e. fulfil the above selection rule) [**Banwell 1983**]. However, when the molecule has considerable symmetry, it is

not clear whether or not the derived polarizability tensor changes during the vibration. An example of a Raman active mode ($(\frac{\partial\alpha}{\partial q}|_{q=0} \neq 0)$ is shown in figure 2.2a. In contrast, the vibrational modes in figures 2.2b,c are not Raman active $(\frac{\partial\alpha}{\partial q}|_{q=0} = 0)$.

2.1.4. A quantum mechanical treatment of Rayleigh and Raman scattering.

In the previous paragraph scattering phenomena associated with electromagnetic radiation and a molecular system were treated classically. A different approach is introduced here based on the following two considerations:

- the incident radiation is treated with classic principles.
- the molecular system is treated with quantum mechanics principles.

This approach assumes that 'quantized' energy may be transferred between the radiation and the molecular system during the interaction. This is due to downward or upward transitions between specific energy states of the molecular system. The *induced transition moment* associated with the initial and the final energy states is defined by [**Szymanski 1967**]:

$$\mathbf{P_{nm}} = \int \Psi_m * \vec{P}(t) \Psi_n dt \qquad (2.4)$$

The symbols **n**, **m** represent the initial and the final energy state for the molecular system and Ψ_m, Ψ_n the time independent wave functions associated with these energy states which cannot be zero. Taking again a linear approximation for the induced dipole moment, $\vec{P}^{(\alpha)} = \tilde{\alpha} * \vec{E}(t)$, the induced transition moment can be derived.

The *general selection rule* for the Raman activity of a fundamental vibrational transition is as follows: a transition between two states characterised

by the wave functions Ψ_m, Ψ_n is Raman forbidden unless at least one of the products of the type $\Psi_m * \tilde{\alpha} \Psi_n$ belongs to a representation whose structure belongs to the totally symmetric species (i.e. the two wave functions are either both symmetric or both antisymmetric).

2.2. LCP Fibres and Laser Raman Spectroscopy.

As we have already mentioned, Raman Spectroscopy is a type of vibrational spectroscopy dealing with the interaction between an electromagnetic wave (light) and matter (molecule). Information concerning the structure of matter at molecular level may be obtained. Thus, Raman Spectroscopy is a tool for studying the molecular structure of various materials: Organic and inorganic compounds, biochemicals and medicines, polymers and polymer fibres. The very simple instrumentation used by Raman and Khrisnan in 1928 for the observation of the scattered light from various dust-free liquids and gases has since been improved dramatically.

The information provided by Laser Raman Spectroscopy is qualitative and quantitative. The technique has successfully been applied to the field of polymer science for the investigation of different polymer structures. One important advantage of this technique is that there is no limitation to the form of the material to be examined. Fibres, films, powders, gels, blends and crystalline solids may be studied.

In this work, the high performance, highly crystalline polymer fibres described in the 1st chapter have been characterised via this technique. Useful information about their molecular structure has been obtained. The alterations occurring in the Raman spectra of these materials due to macroscopic mechanical deformation have also been monitored and explained.

It has been demonstrated in the previous chapter that the attractive mechanical properties of high performance polymer fibres are due to their

superior structural characteristics. The main aspects controlling the macroscopic behaviour of these fibres are very much dependent on the processing procedure. Alterations to this procedure may lead to dramatic changes in fibre performance. Therefore, a good understanding of the entire molecular structure is essential for a thorough investigation of the existing materials and the design of new ones.

2.3. Literature review.

2.3.1. PpPTA and aramid fibres.

Vibrational spectroscopic measurements (infrared or Raman) have been extensively used for the study of polyethylene terephthalate (PET) and poly(*p*-phenylene terephthalamide) (P*p*PTA). With respect to the PET molecular system, it has been confirmed that the bands forming its spectrum change with crystallinity ([**Ward 1956,1957**]). Nevertheless, several attempts at the assignment of the vibrational modes associated with the above molecular system have been made ([**Boitsov 1963**], [**Bahl 1974**]). In general, these attempts are based on considerations concerning the force constants of the bonds and angles between bonds, along with simplifications based on the entire molecular symmetry. Table 2.1 provides the information (frequency and assignment) for the vibrational modes of P*p*PTA, which has the following molecular structure [**Penn 1979**], [**Kim 1986**] :

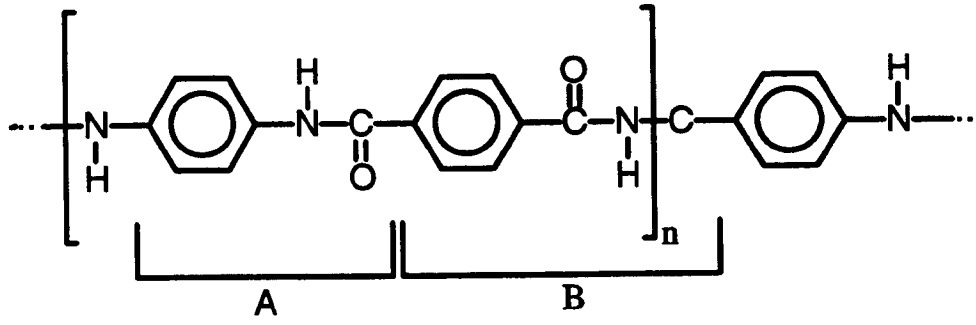

ν_{calc}/cm^{-1} [Kim 1986]	ν_{obs}/cm^{-1} [Penn 1979]	Assignment
646	632w	ring asymmetric deformation (B)
694	698vw	
725	734vw	
773	789vw	
853	851vw	
	919vw	
1106	1104vw	
1187+1188	1187m+1192m	ring C-H in-plane bending (A,B)
1283	1279s	N-H in plane bending (B)
1332	1331s	ring C-H in-plane bending (B)
1400	1409vw	
1516	1518vm	ring C-H in-plane bending (A)
1567	1570w	ring C-C stretching (B)
1615	1615vs	ring C-C stretching (A)
1649	1649m	C'=O stretching (B)

Table 2.1. *Observed and calculated frequencies of* PpPTA *and their assignments (C' represents the carbon atom in C=O).*

2.3.2. PBZT and PBO fibres.

Vibrational spectroscopic studies have been reported in the literature for these rather complex molecular systems **[Venkatesh 1981]**, **[Shen 1982a,1982b]**, **[Day 1987]**. The complexity of the molecular geometry makes it difficult to analyse the vibrational modes in the infrared or Raman spectrum of these polymers. The vibrational assignments for the Raman spectrum and the features observed are given in table 2.2. Various attempts at the spectroscopic characterisation of these molecular systems have been carried out. In table 2.3 the Raman bands observed above 1200 cm^{-1} are listed.

PBZT		PBO	
ν_{obs} / cm^{-1}	Assignment	ν_{obs} / cm^{-1}	Assignment
1203s		1207vw	
1228m		1275vs	C-C stretching
1245s		1302s	
1279s		1314s	
1295w		1334vvw	
1310w		1451m	
1440vs		1491m	
1462vvw		1559vs	C=N stretching
1474vs	heterocyclic ring stretching	1587w	
1503vvs	C=N stretching	1603vs	central ring stretching
1508wsh		1624vvs	phenyl ring stretching
1517.5vw			
1593vs	phenyl ring stretching		
1602s			

Table 2.2. *Raman vibrational assignments for PBZT and PBO fibres.*

2.4. Experimental.

2.4.1. The conventional Laser Raman Spectroscopy setup.

The experimental equipment employed for all Raman spectroscopic studies is schematically presented in figure 2.3. All the individual components of the above system are placed on a vibration-free optical table and are as follows:

The source of excitation light which is a water-cooled Ar^+ laser unit which can provide maximum power of 250 mW for the 514.5 nm line. Although it is tuneable to lower frequencies (up to 458 nm) only the strong 514.5 nm line was used in the current study. The 1.1mm in diameter laser beam is directed via a set of good quality mirrors and a plasma line filter to a specially modified Raman microscope. The design of the microscope is based on the optics arrangement presented graphically in figure 2.4. The incident beam is reflected at 90° on the surface of a dichroic beamsplitter. The beam, is focused onto the specimen via a long working distance objective (x20 or x50). The beam is converged to an approximately 2μm focal spot on the specimen.

The backscattered light is collected by the same objective and transmitted through the dichroic beamsplitter on the 45° surface of a prism which reflects it onto the entrance slit of the spectrographic device via a confocal aperture. This is a triple monochromator type of spectrometer with a three gratings turret for *low* (300gr/mm), *medium* (600gr/mm) and *high* (1800gr/mm) Raman resolution. The total spectral range is from 185 nm to 1000 nm with wavelength *accuracy* of ±0.5 nm and *resettability* of ±0.2nm.

An extremely sensitive light detector is coupled to the spectrometer for the dispersed light collection. The device is equipped with a 600x400 pixels imaging chip which is kept at low temperatures by liquid nitrogen. The Raman signal delivered to the detector is converted to an electrical signal. An appropriately designed interface links the detector with an IBM-compatible Personal Computer

(PC) unit. The whole procedure, i.e. the spectrum acquisition, demonstration and storage is controlled via the computer software provided with the detector. This allows the operator to: (a) view the spectra instantly and (b) carry out the examination and analysis at a later date.

2.4.2. Raman spectra collection.

Individual fibre filaments are separated from the yarn and chopped by means of a pair of ceramic scissors to avoid fibre splitting. The samples are then mounted on the surface of a dust free glass slide which is positioned on the experimental stage of the Raman microscope. The power of the incident beam is kept well below 1mW on the sample to avoid overheating and/or radiation damage. The fibre axis is kept parallel to the polarisation direction of the incident beam. Raman spectra from all fibres with the fibre axis perpendicular to the polarisation direction of the incident beam are also recorded for comparison purposes. The focusing on the specimen is achieved by maximising the light illumination from the focal spot on the fibre by means of a CCTV camera and a monitor connected to it.

2.4.3. The remote Laser Raman Spectroscopy set-up.

The experimental set-up described above has a distinctive and in some cases very important limitation: the Raman microscope is physically attached to the spectrometer and therefore has no freedom of movement relative to the specimen. In a new arrangement developed in our laboratory **[Galiotis 1994]**, **[Paipetis 1995]** a set of optical fibre waveguides was employed to deliver the incident light to the specimen and collect the Raman signal for further analysis. This arrangement provided the flexibility for monitoring stress-induced alterations in the Raman spectrum of LCP fibres examined in this work.

2.4.4. Analysis of the spectroscopic data.

Any spectrum generated by the operation described above can be recorded as a two dimensional set of data: The 1st dimension (x-axis) represents the Raman frequency (cm^{-1}) or wavelength (nm). In fact, this corresponds to a specially selected area of the detector's chip which has been 'binned' in one direction. A conversion factor is employed to convert pixel number to Raman frequency or wavelength. The conversion factor depends on the Raman signal dispersion controlled by the grating used. For this work, the conversion factor is 0.020nm/pixel for the high resolution grating (1800gr/mm) and 0.125 nm/pixel for the low resolution grating (300gr/mm). The 2nd dimension (y-axis) represents 'intensity' (i.e. the number of photons detected) and also 'spatial position'.

For each set of data constituting a spectrum, the 'background' or 'baseline' and one curve for each feature (band) in the spectrum can be calculated by means of standard mathematical routines. The background is assumed to have a quadratic form and the band functions have either a *Lorentzian* (L) distribution form or a *Gaussian* (G) distribution form (see Appendix 1).

For the Lorentzian or the Gaussian distribution the intensity **I** of the band, the position of the band in the Raman spectrum **ν** and the full width of the band at the half of the maximum intensity, FWHM, can be obtained. The quality of the fit can be improved by the minimisation of the *correlation coefficient*, which represents the square root of the sum of the squares of the residuals. When this is the case, the fitting obtained is the optimum.

2.5. Results / Discussion.

2.5.1. Spectroscopic data of aramid fibres.

In this work, Raman spectra of all fibres investigated were obtained by means of an Ar^+ laser unit operating at 514.5nm. Special care was taken to keep laser power focused on the filaments in the range of 0.5-1.0mW so that damage of the fibre due to overheating is avoided. In fact, it was observed that Raman spectra were not reproducible if laser power over 3-5mW is focused on the filament. Under these extreme conditions, physical visible damage ('burning') is observed. Other workers ([**Robinson 1987**], [**Day 1987**], [**Jahankhani 1990**]) have used the 488nm or 632nm lines and have obtained similar Raman spectra.

The Raman spectra of three representative fibres from the three different families of fibres (aramids, PBZT and PBO) examined in this work are shown in figures 2.5 and 2.6 for *low* ($500cm^{-1}$ to $1100cm^{-1}$) and *high* ($1100cm^{-1}$ to $1800cm^{-1}$) frequency ranges, respectively. As can be seen, all major bands reported in the literature have been observed with very high spatial resolution.

(i) Spectroscopic data for Kevlar® fibres.

Raman spectra for all Kevlar® fibres are given in figures 2.7 and 2.8 for low and high frequency regions respectively. The spectroscopic data for Kevlar® fibres are summarised in table 2.3. In this table, the positions of all bands observed in the Raman spectrum are given along with the symmetric distribution employed (Lorentzian or Gaussian) for curve fitting of the raw data. The full width at half maximum (FWHM) data given below concern only the major bands. As expected, the Raman frequencies and FWHM for all grades of aramid fibres examined in this work have similar values.

ν / cm^{-1}	Distribution	FWHM / cm^{-1}
635vw	L	3.8
701*vw	L	
739vw	L	
793w	L	3.1
851*vw	L	
919w	L	
1109vw	L	
1187+1192s**	L+G	3.8+4.0
1265+1279s**	L+L	12.6+7.7
1332s	L	7.1
1411vw	L	4.0
1520s	L	10.0
1573w	L	12.5
1615vs	**G**	**11.5**
1650s	L	7.4

**triplet feature* ***doublet feature*

Table 2.3. *Spectroscopic data for Kevlar® fibres.*

In this project, the emphasis is on the frequency range between 1450-1700cm^{-1} of the Raman spectrum, particularly the 1615cm^{-1} band which is the strongest feature in the Raman spectrum for all Kevlar® fibres. This band has been well examined and fully assigned in the literature: it is primarily attributed to the aromatic ring C-C stretching vibrational mode (see previous section).

In order to calculate accurately the position of this band, a Gaussian distribution was used for the 1615cm^{-1} band and Lorentzian distributions for all the other bands in the spectrum. This combination gave the optimum result although only Lorentzian distributions have been reported in the literature as appropriate for mathematical calculations **[Fina 1988]**. The above procedure was employed for all calculations involving Kevlar® fibres. A typical Raman spectrum of Kevlar®, curve-fitted in the region 1450-1700cm^{-1} is shown in figure A1.1a, in the Appendix 1. The correlation coefficients for different combinations of symmetric distributions are given for comparison purposes for all Kevlar® fibres in table A1.2 also in the Appendix 1.

2.5.2. Spectroscopic data of PBZT and PBO fibres.

The Raman spectrum of PBZT-Z1 fibre examined in this work is given in figure 2.9a (low frequency region) and figure 2.10a (high frequency region). The very high background due to fluorescence in the spectrum should be noted. The band used for optical-mechanical characterisation of the fibre is the 1480cm^{-1} vibrational mode, which is the strongest in the Raman spectrum. This band has been assigned in the literature as due to the heterocyclic ring stretching vibrational mode **[Shen 1982]**. The second strongest band in the spectrum, (1602cm^{-1}) has been assigned to the phenyl ring stretching mode but may also contain contributions from other vibrational modes **[Venkatesh 1981]**. Lorentzian or Gaussian distributions were employed for band assignment, but the former gave the optimum fit in the region of interest (see also Appendix 1, figure A1.1b and table A1.3). The spectroscopic data concerning band position and width are given in the following table:

ν / cm^{-1}	Distribution	FWHM / cm^{-1}
1180w	L	2.8
1212vw	L	14.6
1245vw	L	
1284vw	L	
1480vs	L	15.8
1602m	L	9.5

Table 2.4. *Spectroscopic data for PBZT-Z1 fibre.*

The Raman spectra of all PBO fibres for low and high frequency regions are given in figures 2.9b and 2.10b respectively. The spectra are very similar to each other. The only significant difference between them is the very high background of the B4 grade. The 1620cm^{-1} band, related to stretching vibrational mode of the phenyl ring was the band employed for all measurements in this work. All spectroscopic data are given in the following table:

ν / cm^{-1}	Distribution	FWHM / cm^{-1}
732vw	L	
933m	L	2.8
1176m	L	9.4
1278s	L	5.7
1310m	L	14.6
1556*m	L	-
1620vs	L	9.5

Table 2.5. *Spectroscopic data for PBO fibres (*doublet feature).*

A very important observation concerning Raman spectra of all LCP fibres examined in this work, is the effect of the incident laser light polarisation upon the Raman spectrum. In figures 2.11 and 2.12, Raman spectra taken with the incident laser light polarised parallel to the laser axis (black line, figure 211 & 2.12) are compared with spectra taken under identical conditions but with the incident light polarised perpendicular to the fibre axis (grey line, figure 2.11 & 2.12). As can be seen, for all samples examined, a dramatic drop in intensities of all bands in the Raman spectrum is observed. This drop is so great, that all the bands are almost impossible to trace in the Raman spectrum. This result confirms the high molecular anisotropy existing in these fibres (high level of molecular orientation in the fibre axis).

2.6. Summary.

The Laser Raman Spectroscopy set-up which was employed for spectroscopic analysis of the materials examined in this work enabled us to perform fast data acquisition of high resolution spectra. In general, all Kevlar® fibres exhibit similar spectra with major bands found to agree with experimental or calculated results from the literature. One major observation was the high background for Kevlar®149. A combination of Lorentzian and Gaussian distributions was found to be the most appropriate approximation to the spectroscopic data.

As far as PBZT and PBO spectra are concerned, a very high fluorescent background was observed for Z1 (PBZT) and B4 (PBO) fibres. Lorentzian distributions were employed successfully to calculate the spectroscopic characteristics of all bands in the area of interest of the Raman spectra.

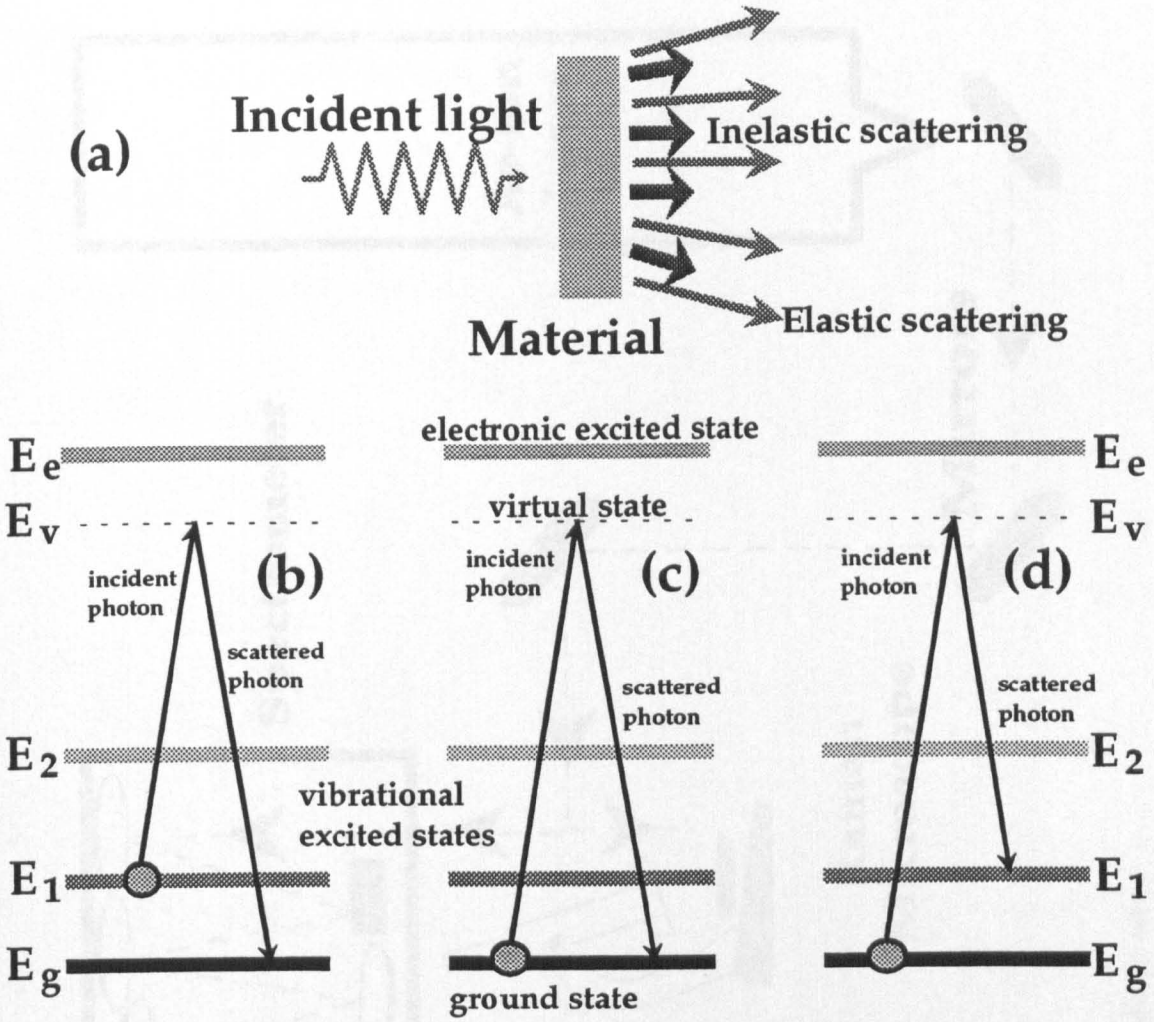

Figure 2.1. Schematic representation of (a) the Raman effect and its mechanisms: (b) anti-Stokes, (c) Rayleigh and (d) Stokes scattering.

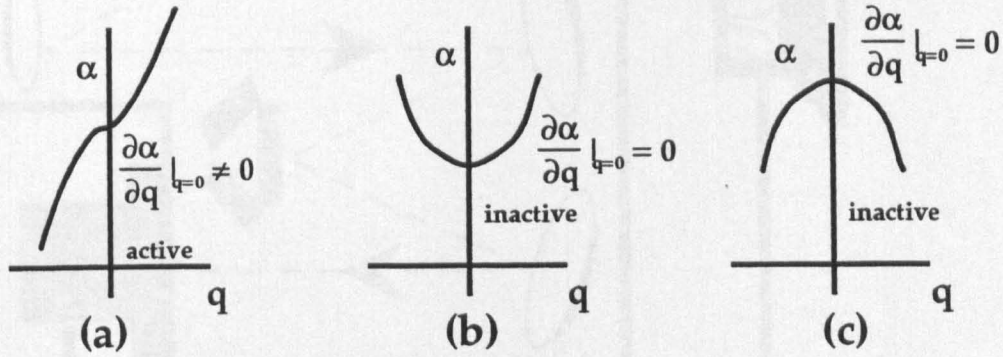

Figure 2.2. The variation of polarisability tensor with respect to the normal vibrational coordinate for three different vibrational modes.

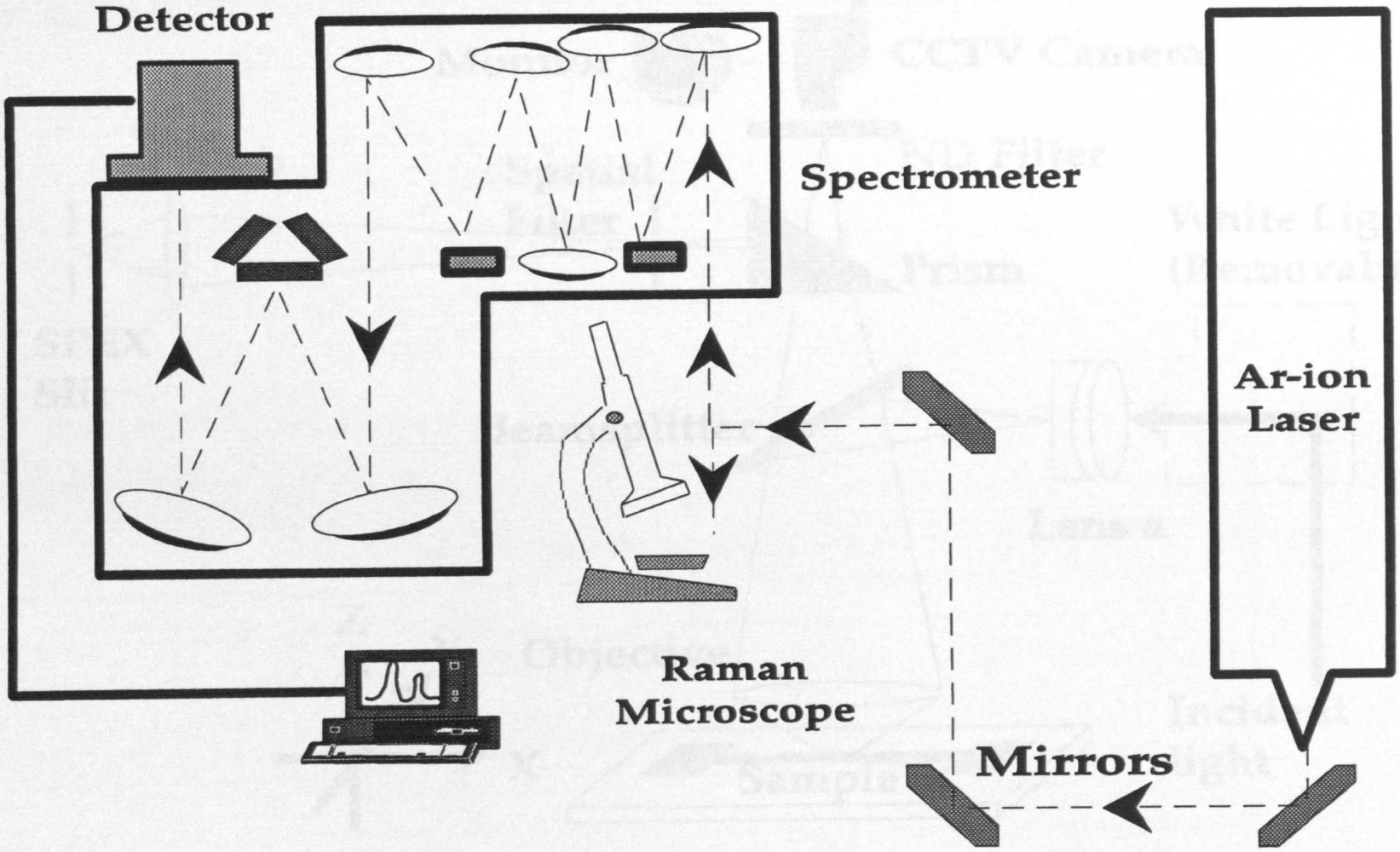

Figure 2.3. Conventional Laser Raman Spectroscopy set-up.

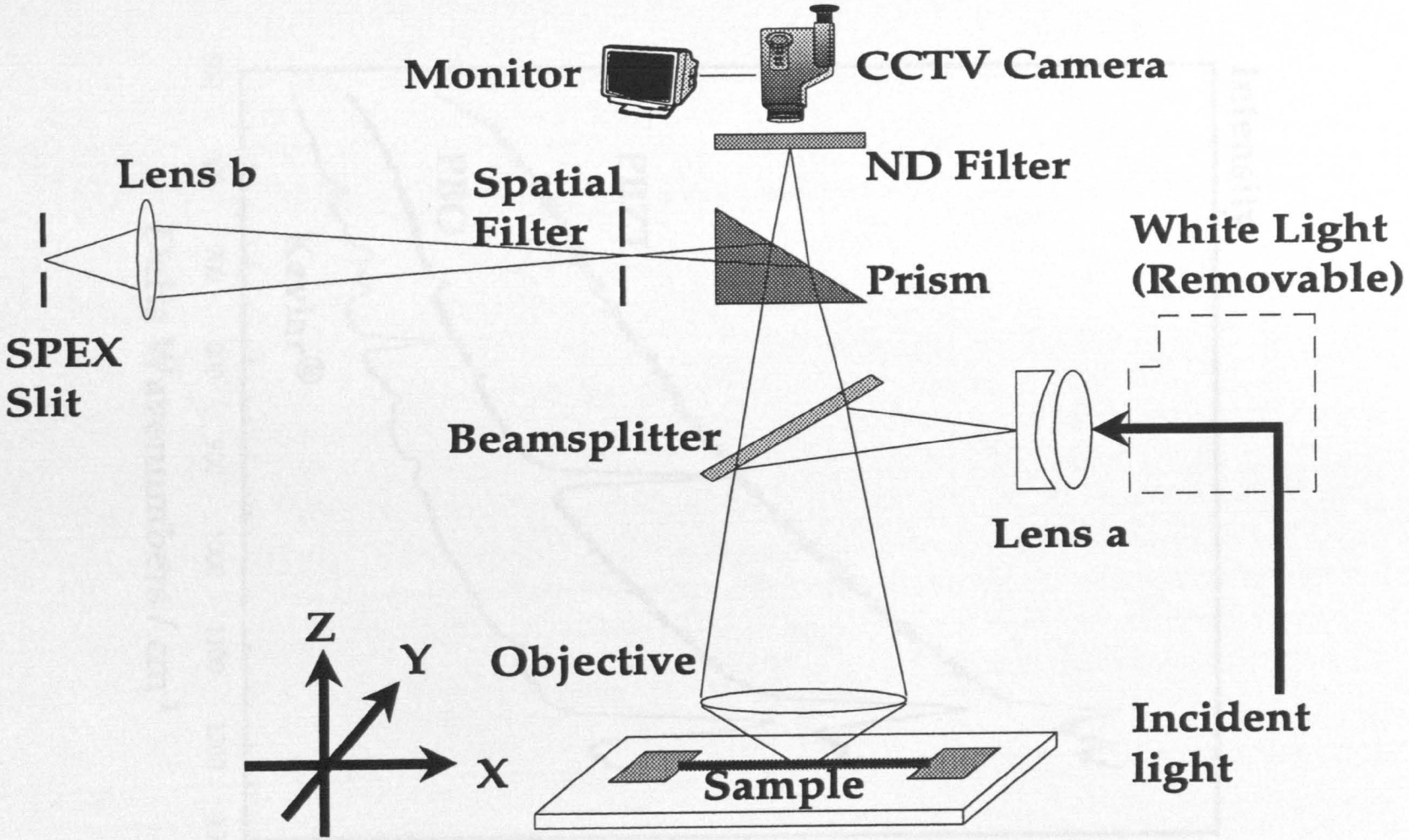

Figure 2.4. Raman microscope components and optical path during Raman spectra collection.

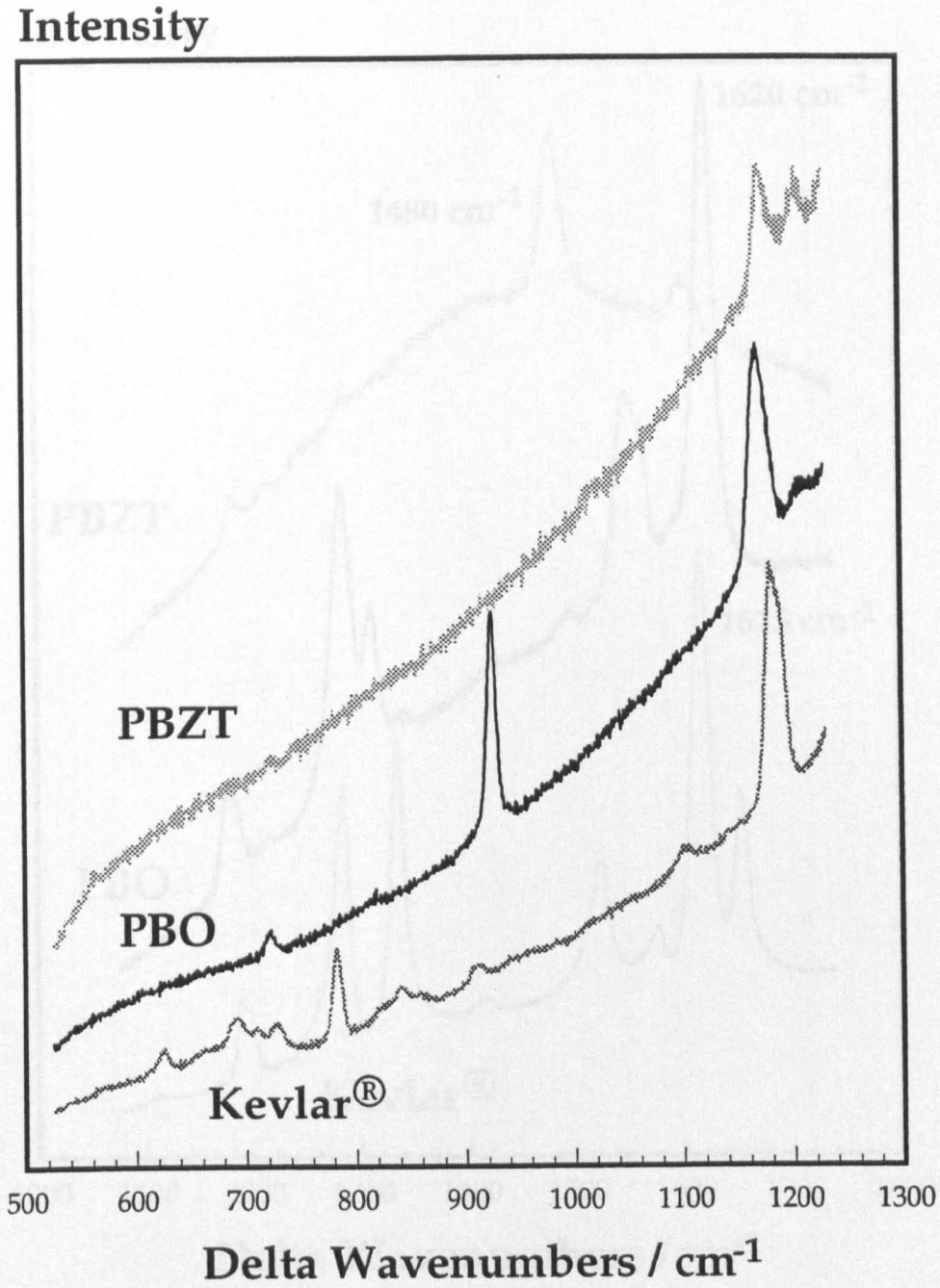

Figure 2.5. Representative Raman spectra of fibres:
Low frequencies region (Kevlar®, PBZT and PBO).

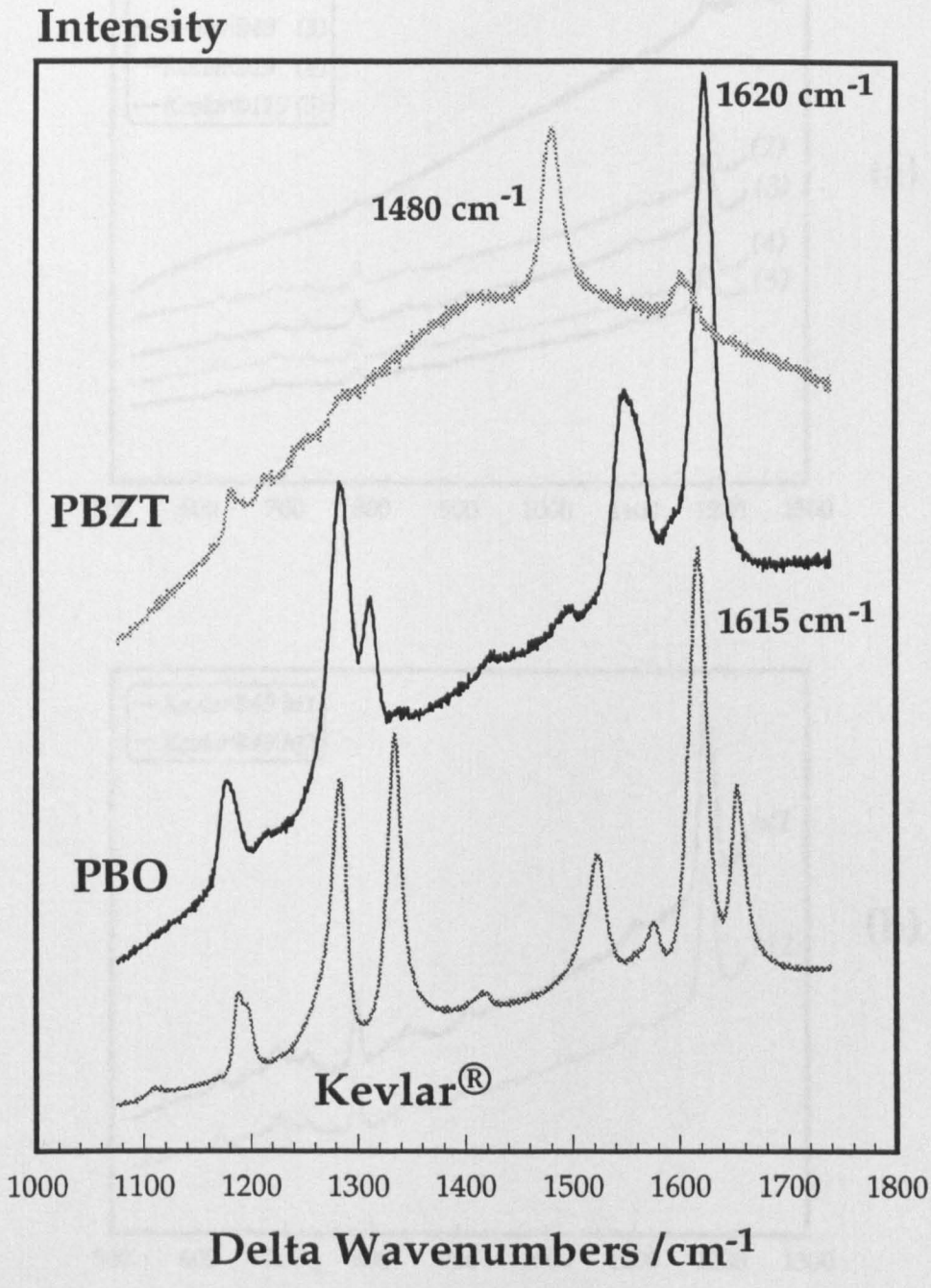

Figure 2.6. Representative Raman spectra of fibres:
High frequencies region (Kevlar®, PBZT and PBO).

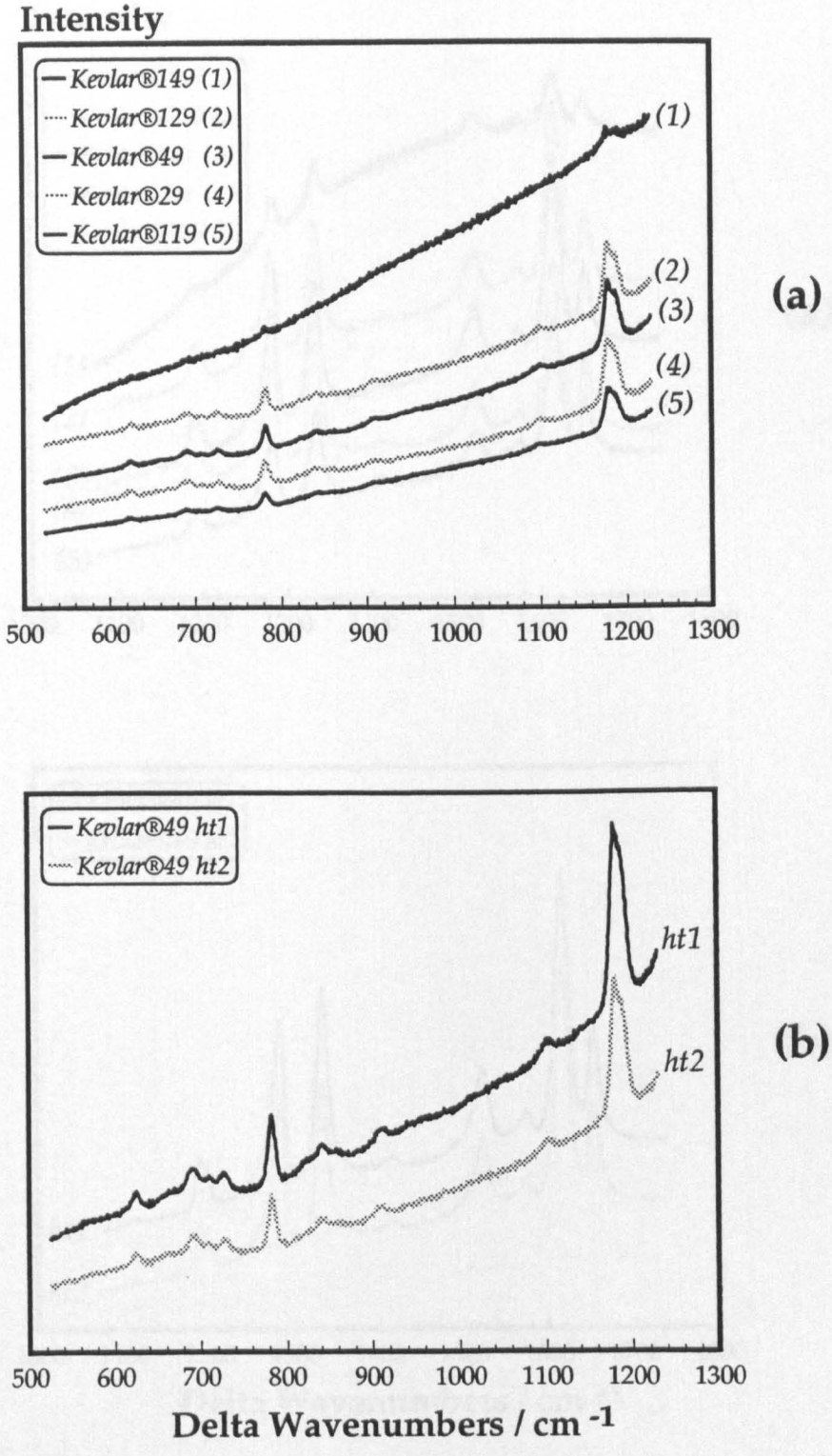

Figure 2.7. Raman spectra of Kevlar® fibres, low frequencies region: (a) non heat treated and (b) heat treated fibres.

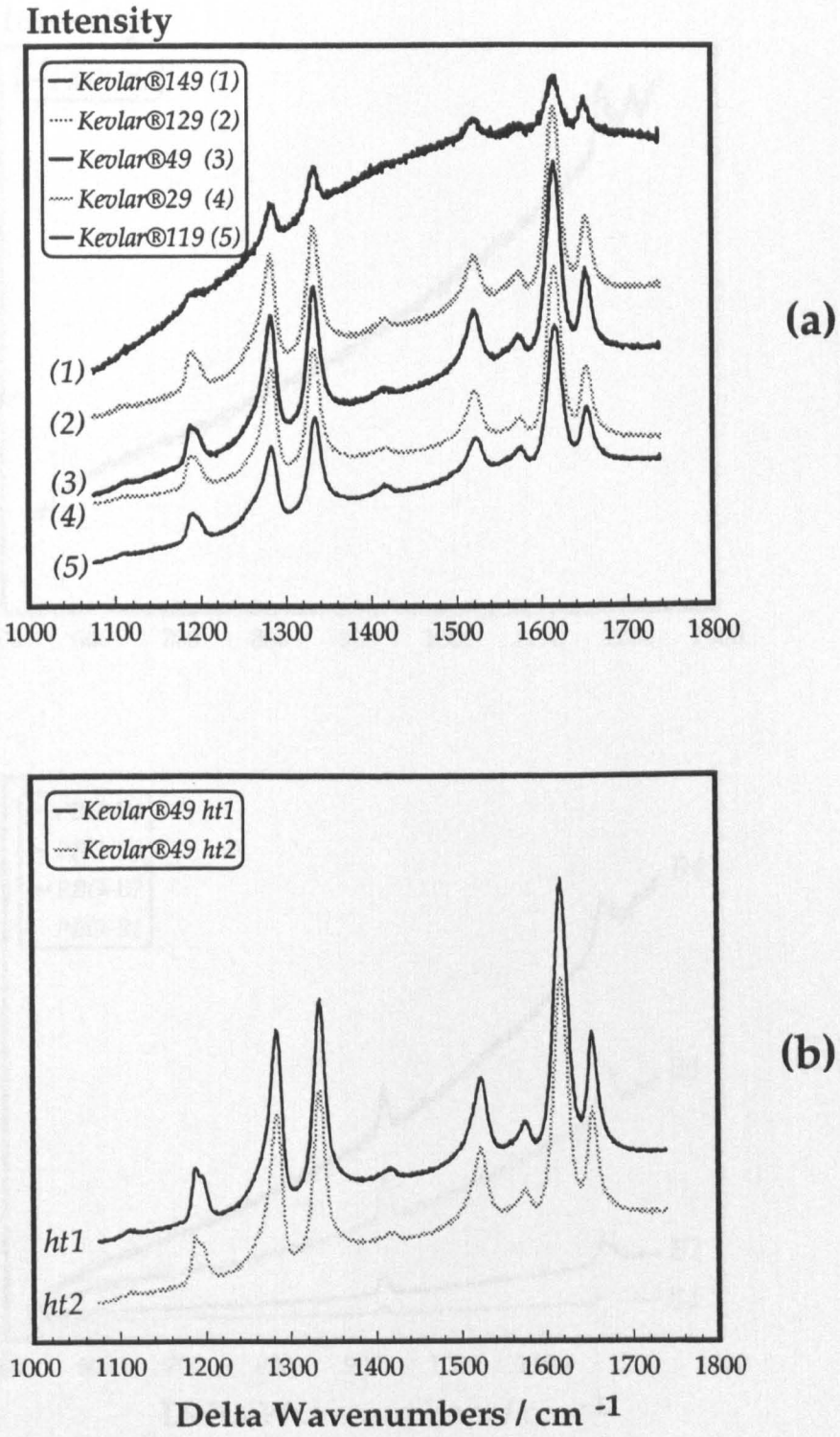

Figure 2.8. Raman spectra of Kevlar® fibres, high frequencies region: (a) non heat treated and (b) heat treated fibres.

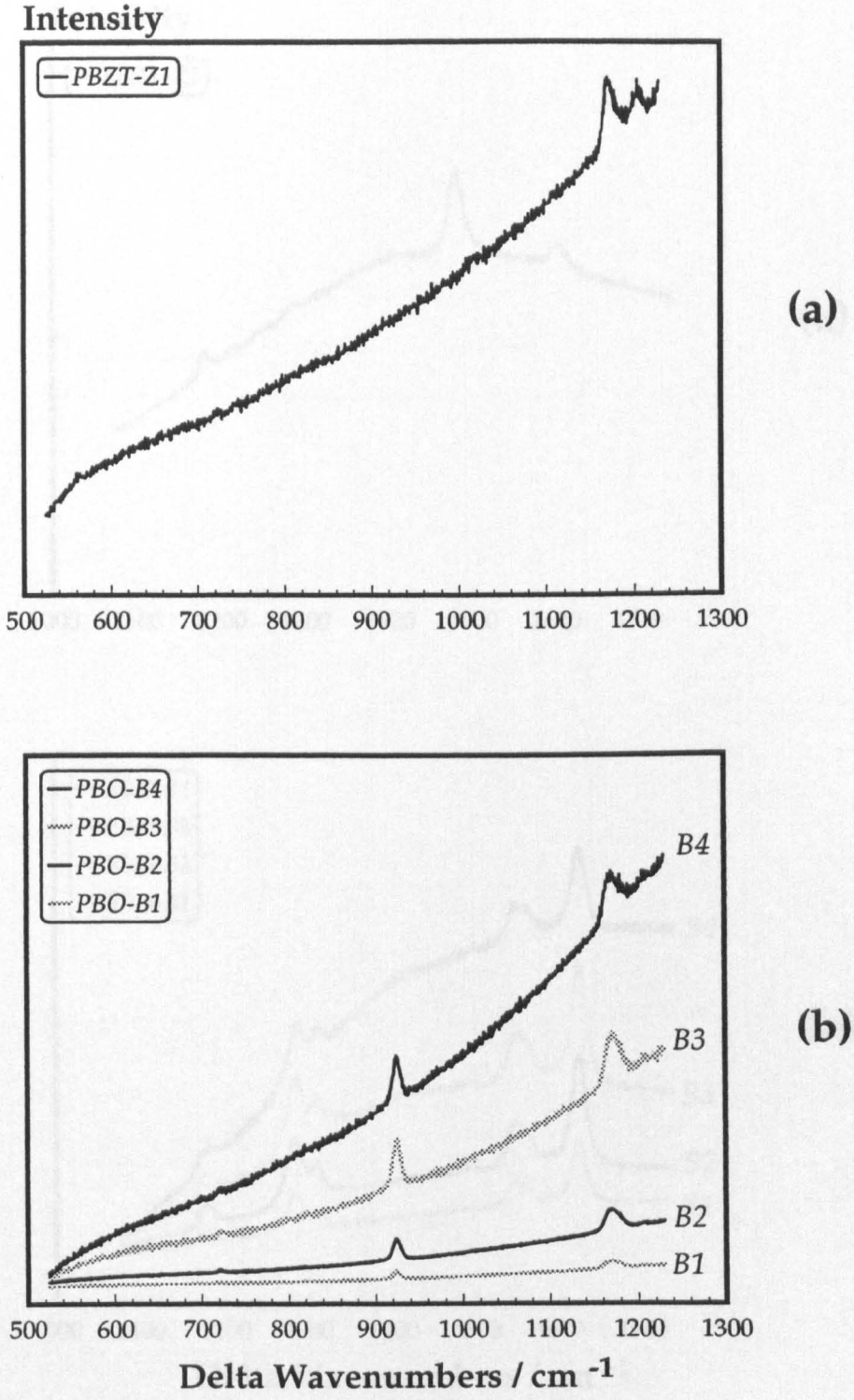

Figure 2.9. Raman spectra of (a) PBZT and (b) PBO fibres - low frequencies region.

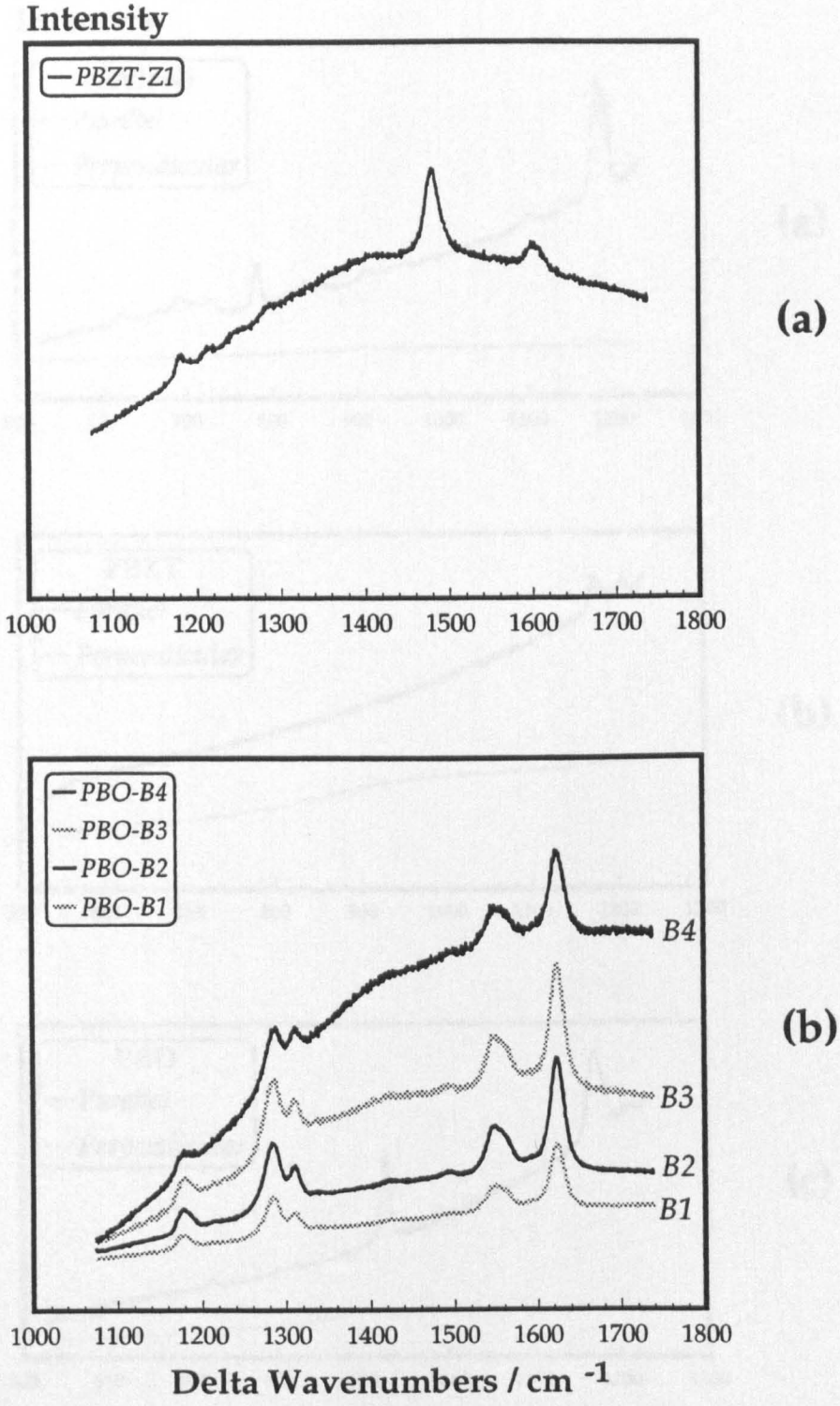

Figure 2.10. Raman spectra of (a) PBZT and (b) PBO fibres - high frequencies region.

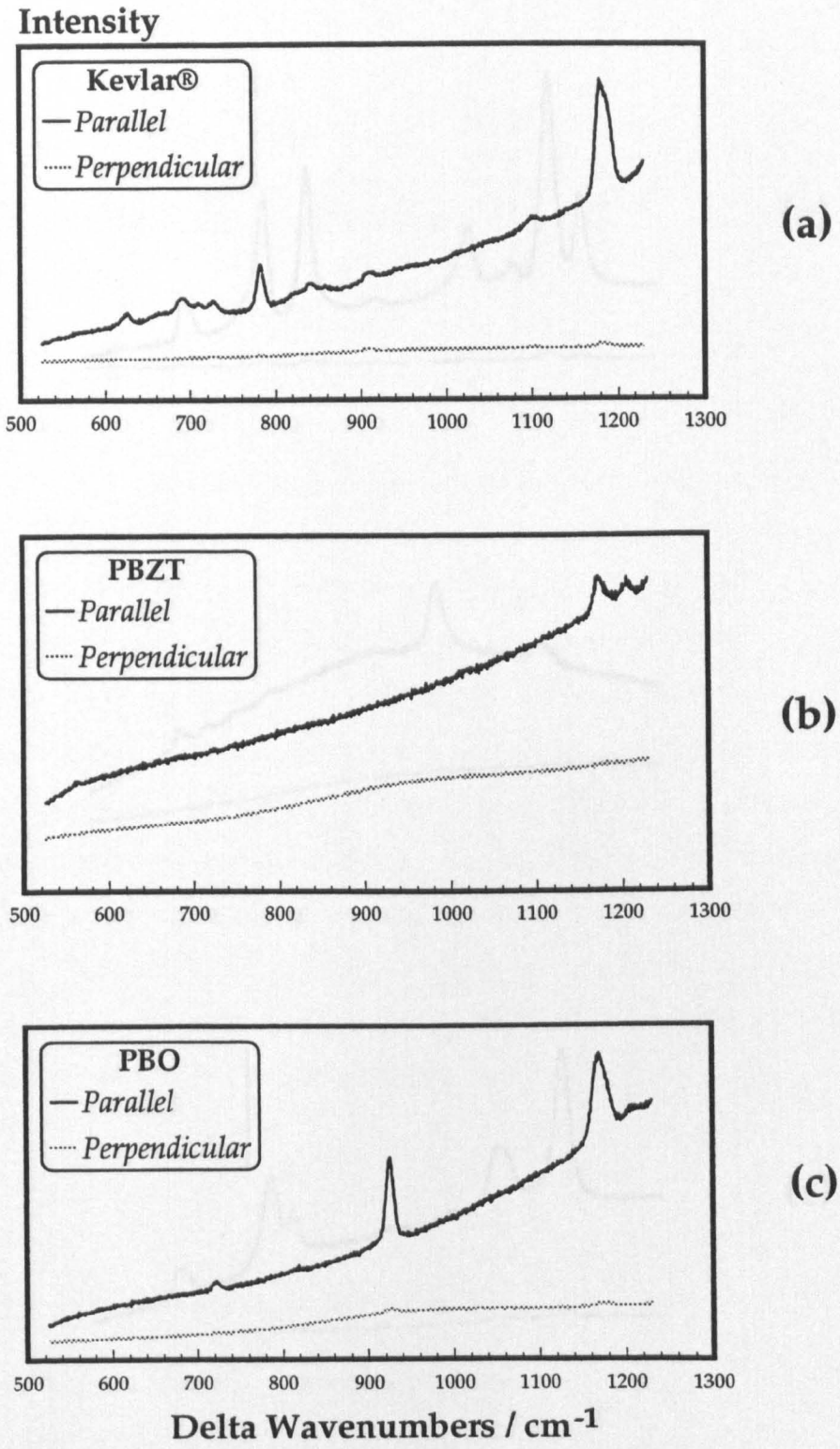

Figure 2.11. Raman spectra of fibres - effect of polarisation.
Low frequencies region: (a) Kevlar®, (b) PBZT and (c) PBO fibres.

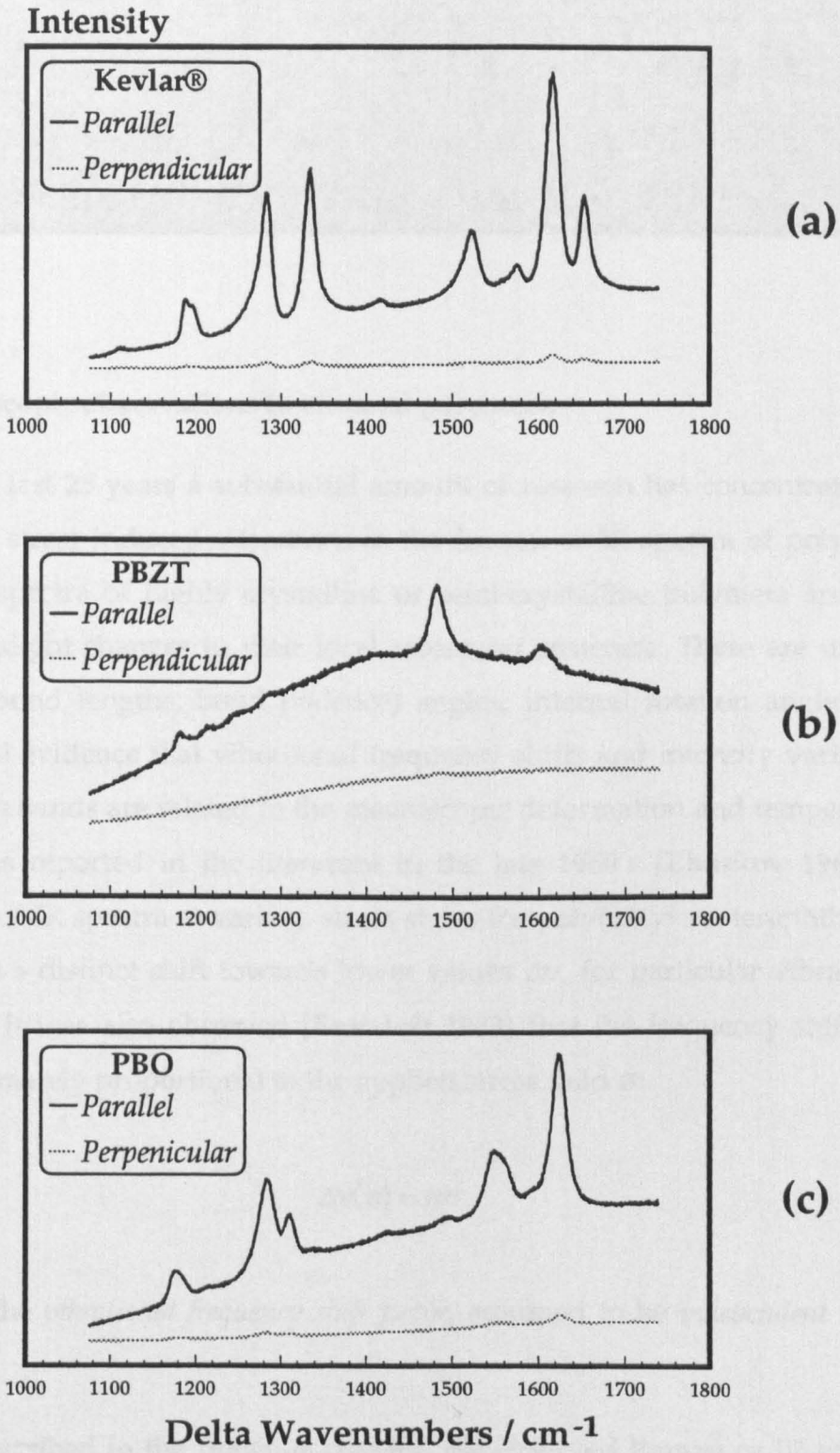

Figure 2.12. Raman spectra of fibres - the effect of polarisation.
High frequencies region: (a) Kevlar®, (b) PBZT and (c) PBO fibres.

CHAPTER 3:
STRESS-INDUCED CHANGES IN THE RAMAN SPECTRA OF LIQUID CRYSTAL POLYMER FIBRES

3.1. Spectroscopic observations in stressed polymers.

For the last 25 years a substantial amount of research has concentrated on the study of stress induced alterations in the Raman or IR spectra of polymers. Vibrational spectra of highly crystalline or semi-crystalline polymers are very sensitive to slight changes in their local molecular structure. These are usually changes in bond lengths, bond (valence) angles, internal rotation angles, etc. Experimental evidence that vibrational frequency shifts and intensity variations of absorption bands are related to the macroscopic deformation and temperature changes, was reported in the literature in the late 1960's [**Zhurkov 1969**]. A comparison of IR spectra at various stress states for poly(ethylene terephthalate) (PET) shows a distinct shift towards lower values $\Delta\nu$, for particular vibrational frequencies. It was also observed [**Bretzlaff 1983**] that the frequency shift, $\Delta\nu$, was approximately proportional to the applied stress field σ:

$$\Delta\nu(\sigma) = \alpha\sigma \tag{3.1}$$

where α is the *vibrational frequency shift factor*, assumed to be *independent* of the stress σ.

As described in the previous chapter, the observed Raman or IR spectral bands of crystalline materials are due to well defined vibrational modes of the scattering (Raman) or absorbing (IR) oscillator species of these materials. In general, the above frequencies are combinations of two or more components. The

vibrational modes of stress-sensitive bands usually consist of at least one component which is involved in a load-bearing action in the skeleton of the molecular chain. This explains why these frequencies are stress-sensitive: any alteration in the geometry of the molecular chain due to the influence of an external macroscopic field (mechanical deformation, pressure or heat) will cause changes in the Raman or IR spectrum of the material.

Experimental evidence for stress or strain sensitive bands (Raman or IR) has been provided for various polymeric materials such as nylon [**Vettegren 1973**], polypropylene [**Wool 1975**], polycarbonate and polystyrene [**Evans 1976**], polydiacetylene [**Batchelder 1979**], [**Galiotis 1983**], Kevlar® [**Galiotis 1985**], polybenzobisthiazole (PBZT) [**Shen 1982a**], [**Day 1987**], polybenzobisoxazole (PBO) [**Young 1990**].

Theoretical models based on conformational energy minimisation methods were applied to simple molecular systems such as polyethylene in order to calculate the vibrational frequencies of stressed chains [**Wool 1986**]. Valence force fields were considered which involve both *harmonic* and *anharmonic potential energy functions* for the skeletal stretching oscillators. Only the latter models could give some theoretical explanation of the experimentally observed stress dependence of frequencies related to the backbone of the structure. Using such a model [**Gubanov 1967**] derived the equations of stress-induced vibrational frequency changes for polyethylene (PE) and polyoxymethylene (POM) chains on the basis of the so-called *equation of helical parameters*. Such an approach is very complicated and it is very difficult to apply to more complex polymer chains [**Tashiro 1990**].

A more recent approach [**Tashiro 1990,1992,1993**], based on the so-called *lattice dynamical theory* developed in the 1950's [**Born 1954**] was applied to highly crystalline molecular systems of arbitrary complexity. The lattice dynamical theory is a powerful tool for understanding the macroscopic physical properties from the microscopic point of view on the basis of crystal structure and

interatomic interactions. The principles of the method which has been adapted to the problem of stress-induced vibrational frequency shifts of polymer crystals under the *quasiharmonic* approximation, will be described briefly in the following section. Initially, though, a simple model of the stress dependence of vibrational frequencies based on a molecular oscillator consisting of two atoms (*molecular dipole*) is presented.

3.2. Modelling the spectro-mechanical correlation in stressed polymers.

The *mechanical energy* **V** during deformation of a molecular system (only the *potential energy* component, kinetical energy is zero in this case) can be expressed as the sum of energy contributions from changes of bonds, valence angles, internal rotation angles and non-bonded interaction distances. If, for simplicity reasons we introduce a diatomic molecule, the force field is only related to the changes in the bond length of the molecule. In this case, a *harmonic* approximation of the (mechanical) energy function (which in this case is only of potential energy nature) can be written in the following form:

$$V(\Delta R) = \frac{1}{2} k_0 (\Delta R)^2 \tag{3.2}$$

where k_0 is a constant parameter, $\Delta R = R - R_0$, R_0 is the bond length at the undeformed state and R is the length of the deformed bond. The contributions from the changes of valence angles, internal rotation angles and non-bonded interaction distances have been ignored. If we define the *molecular strain* ζ of the dipole using the following expression:

$$\zeta = \frac{\Delta R}{R_0} \tag{3.3}$$

then the equation for the potential can be rewritten as follows:

$$V(\zeta) = \frac{1}{2}\frac{k_0}{R_0}\zeta^2 \tag{3.4}$$

In the above approximation (diatomic molecule with harmonic potential energy function), the *force constant* related to the bond coupling of the two atoms is independent of any alteration of the interatomic distance (and therefore, the molecular strain ζ) between the atoms involved induced by any external deformation:

$$F_c(\zeta) = \frac{\partial^2 V(\zeta)}{\partial \zeta^2} = k_0 \tag{3.5}$$

The above approximation, based on an harmonic function for the potential energy, cannot account for the stress or strain dependence of the vibrational modes associated with that bond. The harmonic function approximation of the mechanical energy and the force constant are presented in figures 3.1a,b as a function of the interatomic separation (distance) ΔR respectively. On the other hand, if the energy is expressed with an *anharmonic* approximation (Morse potential function):

$$V(\zeta) = D_0\{1 - \exp(-\eta_a R_0 \zeta)\}^2 \tag{3.6}$$

where D_0 is the *dissociation energy* of the bond, η_a is the *anharmonicity factor*, the force constant can be expressed in the form:

$$F_c(\zeta) = \frac{\partial^2 V(\zeta)}{\partial \zeta^2} = 2D_0\eta_a^2\{2\exp(-2\eta_a R_0\zeta) - \exp(-\eta_a R_0\zeta)\} \tag{3.7}$$

The anharmonic function approximation of the energy function and the force constant $F_c(\Delta R)$ are also presented in figures 3.1a,b as a function of the interatomic separation (distance) ΔR respectively.

It is quite obvious in this approximation that the force 'constant' F_c is not a constant parameter but dependent on the interatomic deformation ΔR. In other words, any increase in the interatomic distance ΔR (which corresponds to a tensile molecular strain, i.e. $\zeta > 0$) will cause a decrease in the value of the force constant F_c. On the other hand, a decrease in the interatomic deformation ΔR (which corresponds to a compressive molecular strain, i.e. $\zeta < 0$) will cause an increase in the value of the force constant F_c. A diagram of this model focussing on the force constant molecular strain dependence at small molecular strains ζ is given in figure 3.1c. Since the vibrational frequency ν is proportional to $\sqrt{F_c}$ [**Tashiro 1990**], any tensile bond length deformation will result in a decrease of the vibrational frequency value and any compressive bond length deformation in an increase of the vibrational frequency value. On the basis of this principle, vibrational frequency shifts for linear and nonlinear model triatomic molecular systems were calculated [**Wool 1975**]. The same method was used for one-dimensional series of anharmonic diatomic oscillators [**Bretzlaff 1981,1983**].

The above approach to deformation induced alterations in Raman or IR spectra of highly crystalline polymers was based on a simplistic interpretation. In the real world of rather complicated molecular systems things are not as simple. A model sufficient for dealing with more complex molecules involves a quasi-harmonic approximation [**Tashiro 1990,1992,1993**]. Some elements of this approach will be described here briefly. Experimental results obtained in this work will be compared with calculated values of the vibrational frequency-mechanical stress correlation predicted with these mathematical approximations.

The vibrational frequencies associated with polymers can be obtained by solving complicated dynamical equations as described in the previous chapter. These equations are functions of force constants, molecular structure and atomic

masses. In this approximation it is assumed that external macroscopic deformations cause molecular structural deformations. These deformations at molecular level affect the intra- and inter-molecular force fields and therefore the vibrational frequencies. Only very small changes in bond lengths, valence angles between bonds, internal rotation angles and non-bonded interatomic distances are considered. It should be mentioned at this stage that the *internal displacement coordinates* are different from the *normal vibrational coordinates* (discussed in the previous chapter) representing the vibrationally caused displacements of bond lengths, valence angles, internal rotation angles etc.

If that is the case, the force constant is only stress or temperature dependent. The mechanical energy of a complex molecular system can be expanded as a Taylor series in internal displacement coordinates from an equilibrium configuration in the following formula:

$$V = V_0 + \sum_i \left(\frac{\partial V}{\partial R_i}\right)_0 \Delta R_i + \frac{1}{2}\sum_{ij}\left(\frac{\partial^2 V}{\partial R_i \partial R_j}\right)_0 \Delta R_i \Delta R_j + \frac{1}{3!}\sum_{ijk}\left(\frac{\partial^3 V}{\partial R_i \partial R_j \partial R_k}\right)_0 \Delta R_i \Delta R_j \Delta R_k + \ldots \quad (3.8)$$

where ΔR_i represents *bond length change*, ΔR_j represents *valence angle change* and ΔR_k represents *internal rotation angle change*, etc.

If we assume that $V_0 = 0$ and employ the condition $\left(\frac{\partial V}{\partial R_i}\right)_0 = 0$, equation 3.8 can be rewritten as follows:

$$V = \frac{1}{2}\sum_{ij}\left[\left(\frac{\partial^2 V}{\partial R_i \partial R_j}\right)_0 + \frac{1}{3}\sum_{k}\left(\frac{\partial^3 V}{\partial R_i \partial R_j \partial R_k}\right)_0 \Delta R_k + \ldots\right]\Delta R_i \Delta R_j + \ldots \quad (3.9)$$

By ignoring all the terms higher than k-th order, the mechanical energy is:

$$V \approx \frac{1}{2}\sum_{ij}\left[\left(\frac{\partial^2 V}{\partial R_i \partial R_j}\right)_0 + \frac{1}{3}\sum_k\left(\frac{\partial^3 V}{\partial R_i \partial R_j \partial R_k}\right)_0 \Delta R_k\right]\Delta R_i \Delta R_j = \frac{1}{2}\sum_{ij} F_{ij}\,\Delta R_i \Delta R_j \qquad (3.10)$$

where:

$$F_{ij} = \left(\frac{\partial^2 V}{\partial R_i \partial R_j}\right)_0 + \frac{1}{3}\sum_k\left(\frac{\partial^3 V}{\partial R_i \partial R_j \partial R_k}\right)_0 \Delta R_k \qquad (3.11)$$

By introducing the following notation:

$$F_{ij}^0 = \left(\frac{\partial^2 V}{\partial R_i \partial R_j}\right)_0 \qquad (3.12a)$$

$$F_{ijk}' = \left(\frac{1}{3}\right)\left(\frac{\partial^3 V}{\partial R_i \partial R_j \partial R_k}\right)_0 \qquad (3.12b)$$

the force constants can be expressed in the following form:

$$F_{ij} = F_{ij}^0 + \sum_k F_{ijk}'\,\Delta R_k \qquad (3.13)$$

Equation 3.10 corresponds to the expression of the harmonic potential energy with the force constant F_{ij}, but the F_{ij} is affected by the change in the internal coordinates. This kind of approach is only valid for infinitesimally small changes of **R** and has already been termed as a 'quasiharmonic approximation' [**Tashiro 1990**]. The force constant equation can be simplifed even further by the approximation that only the diagonal terms F_{ii} exhibit large anharmonicity relative to ΔR_i and are not affected by changes in the other internal coordinates ΔR_j. This can be mathematically expressed as follows:

$$\begin{aligned} F_{ii} &= F_{ii}^{0} + F_{iii}' \Delta R_i, \quad \text{for } i = j \\ F_{ij} &= F_{ij}^{0}, \quad \text{for } i \neq j \end{aligned} \tag{3.14}$$

Therefore, the dependence of the normal vibrational frequencies upon stress or strain can be calculated by deriving equations of the internal displacement coordinates ΔR as a function of stress or strain. These functions can be substituted in equations 3.13 or 3.14 and the force constants determined as functions of stress or strain. Summarised results concerning calculated and observed α factors for polyethylene (PE), polyoxymethylyne (POM) and poly(*p*-phenylene terephthalamide) (P*p*PTA) are given in the following table for comparative purposes [**Tashiro 1988,1990**]:

TYPE	POLYMER	MODE	α / cm^{-1}/GPa [calc.]	α / cm^{-1}/GPa [obs.]
Planar zig-zag	PE	ν_s(CC)	-4.5	-4.3
		ν_{as}(CC)	-6.0	-5.6
Helix	POM	δ(COC)	-19.0	
		τ(CO)	-15.0	
		ν(CO)	-6.0	
Rigid-rod chain	P*p*PTA	ν(ring)	-10.0	-5.5 to -3.5
		ν(CN)	-7.0	
		ν(ϕ-C)	-7.0	

*ν_s: symmetric stretching, ν_{as}: antisymmetric stretching, δ: bending, τ: torsional modes.

Table 3.1. *Vibrational frequency shift factor α for various polymers* [**Tashiro 1990**].

3.3. Experimental.

3.3.1. Conventional tensile testing.

A universal mechanical testing apparatus manufactured by *Hounsfield Testing Equipment* was employed for tensile testing purposes. The machine is supplied with a wide range of load cells (20N-20kN) operating from as low as 5% of their capacity up to full range. The smallest load cell (20N) was used at its smallest sensitivity (1N) for testing single filaments. The fibres were mounted on specifically made grips supplied by the manufacturers of the machine. A minimum of 20 samples per fibre were tested in tension in accordance with the ASTM procedure (ASTM D3379). The filaments were mounted across elliptical holes 25 or 50mm in length which had been previously punched on rectangular paper tabs (figure 3.2a). The fibres were bonded to the paper tabs with CN* or Araldite** adhesive and carefully positioned at the jaws of the microtester. The diameters of the specimen were measured individually using a 'Watson Image-Shearing Eyepiece' device coupled with a conventional microscope (figure 3.2b). This detailed procedure eliminated the error in stress measurements. The average diameter reading for each specimen was used for the estimation of the cross sectional area of each specimen before testing. Special care was taken during the handling and bonding of the fibres and of specimen gripping in order to minimize end effects and misorientation phenomena. The fibres were deformed at very small strain rates (0.05-0.10 min^{-1}) up to fracture. A personal computer with appropriate software was used for data aquisition (2000 data points/test) and further data analysis. This includes accurate stress-strain curves, tangent Young's modulus calculation, specific energy calculation etc. Pure tungsten wire of standard size (25μm in diameter) and properties was used for measuring the compliance of the equipment.

* Cyano-acrylate adhesive, TkN® Trademark.
** Ciba Composites® Trademark.

3.3.2. Mechanical deformation of liquid crystal polymer fibres.

A number of microdevices have been constructed for tensile, compressive, torsional and cycling testing purposes. These devices are specially designed for testing single filaments on the experimental stage under the Raman microscope. This enables us to monitor simultaneously the Raman spectrum of the sample and record any changes occurring in it due to the external applied deformation.

In the table below the mechanical micro-devices employed for loading the single filaments are listed:

Method	Test	Fibre
Microextensometer (MET)	Tension	in air
Cantilever Bending Beam (CBB)	Tension / Compression	in film
Torsion (TRT)	Shear	in air
Four-point Bending Beam (FBB)	Tension / Compression	in film

Table 3.2. *Various methods for spectro-mechanical testing of fibres.*

A small microextensometer (MET) device is used for applying axial tensile strain on single filaments. The device is shown schematically in figure 3.2c. Indvidual filaments are separated from the yarn and carefully mounted on the jaws of the tensometer. A CN-adhesive is used for gluing the sample straight on to the metallic surface of the jaws. The gauge length of the specimens is measured with an accuracy of the order of 0.01mm by means of a micrometer attached to the moving jaw of the tensometer. In order to avoid end effects, high *aspect ratios* L_0/d_f (L_0=gauge length, d_f=diameter of the fibre) were used. Usually, for experimental consistency, a gauge length of 10mm is chosen. This gives aspect ratios varying from 600-1500, depending on the fibre diameter. The separation L between the jaws is recorded during the experiment. The applied macroscopic strain on the fibre can be calculated from the equation:

$$\varepsilon = \frac{\Delta L}{L_0} \tag{3.15}$$

where:

$\Delta L = L - L_0$ is the applied macroscopic elongation of the sample,

L_0 is the initial gauge length of the sample.

The fibres are normally loaded at increments of 0.10 or 0.05%. The fibre is kept fixed in position and Raman spectra at various points along the fibre gauge length are obtained at each strain level. All Raman frequencies associated with vibrational modes of the backbone of the basic molecular unit were found to be sensitive to strain. The most intense of these vibrations and their fundamental assignment are listed in the following table:

Fibre	Frequency	Assignment
Kevlar®	1615 cm^{-1}	phenyl ring stretching
PBZT	1480 cm^{-1}	heterocyclic ring stretching
PBO	1610 cm^{-1}	phenyl ring stretching

Table 3.3. *Raman frequencies used for the characterisation of fibres.*

3.4. Results.

3.4.1. Stress-strain curves of LCP fibres.

The experimental procedure for testing single filaments in tension has been given earlier in the previous section. Two of the most important parameters to be taken into consideration for tensile testing are:

- Strain rate (controlled by machine's cross-head speed).
- Aspect ratio (controlled by specimen's gauge length).

The experiments undertaken for measuring the stress-strain behaviour of all LCP fibres in this work were performed with small strain rates (0.05-0.10 min^{-1}) and large aspect ratios (1500-5000).

The experimental results concerning the tensile behaviour of all fibres examined in this work are demonstrated in figures 3.3 and 3.4. In figure 3.3a typical stress-strain curves for Kevlar®29, Kevlar®49 and Kevlar®149 are presented. Similar curves for the heat treated Kevlar®49 fibres are given in figure 3.3b. The deviation from linearity is quite significant for Kevlar®29, much less for Kevlar®49 and almost negligible for Kevlar®149. The non-linear response of these fibres to external deformation is more easily observed by differentiation of the stress-strain curves which yields Young's modulus-strain curves, shown in figures 3.3c,d. As can be seen from these curves, a decrease of Young's modulus with strain is observed initially for Kevlar®29 and 49. This behaviour is followed by Young's modulus increase with strain. However, in contrast to Kevlar®49 and Kevlar®29, in the higher modulus Kevlar®149, the Young's modulus increases with strain continually, even at the low-strain region [**Allen 1989**]. Similar behaviour to Kevlar®149 is observed for the two experimental (ht1&2) Kevlar®49 fibres, as shown in figure 3.3d. They differ significantly to Kevlar®49 exhibiting no softening effects in the low-strain region.

The stress-strain behaviour of PBZT and PBO fibres are given in figures 3.4a,b respectively. The B2 and B3 type PBO fibres are as spun fibres of two different diameters and the B1 and B4 are heat treated fibres. The Z1 type of PBZT fibre is also a heat treated fibre. The non-linear character of the as spun fibres is attributed to residual stresses arising in the coagulation stage during the dry-jet wet spinning process of fibre production **[Allen 1981a]**. These stresses can be relieved by heat treatment in order to achieve essentially linear behaviour.

The Young's modulus-strain behaviour of the PBZT-Z1 fibre is shown in figure 3.4c. as can be seen, *Strain hardening* is evident. Similar curves for all PBO fibres are demonstrated in figure 3.4d. The nonlinear behaviour of the as-spun fibres (B2 and B3 samples) is very noticable, characteristic for as spun fibres derived from heterocyclic polymers **[Allen 1981b]**, **[Young 1992]**. As expected, strain softening can be relieved by heat treatment to give an essentially linear or parabolic behaviour (B1 and B4 grades). The correlation between the crystalline orientation and modulus follows a similar pattern for the heterocyclic polymer fibres and therefore governs the fibre properties in the same fashion.

The results concerning the (tensile) mechanical behaviour of all LCP fibres examined in this work are summarized in the following table:

FIBRE TYPE	Diameter d / μm	Modulus* E_0 / GPa	Fract. Strain ε_t / %	Strength σ_t / MPa
Kevlar®				
Kevlar® 29	12.0±0.2	70±10	3.2±0.3	2500±150
Kevlar® 49	12.0±0.2	110±10	2.5±0.2	2800±150
Kevlar® 149	12.5±0.2	140±15	1.4±0.1	2700±100
Kevlar® 49 ht1	11.9±0.3	110±10	2.1±0.2	2600±150
Kevlar® 49 ht2	14.6±0.3	110±10	2.4±0.2	2650±150
PBZT				
Z1	16.5±0.3	240±20	1.4±0.1	3500±100
PBO				
PBO - B1	11.5±0.2	205±10	2.5±0.2	5300±200
PBO - B2	12.3±0.2	155±15	3.4±0.3	4400±200
PBO - B3	6.8±0.3	150±15	2.9±0.3	3400±200
PBO - B4	11.7±0.2	220±15	2.1±0.2	4900±200

*Initial Young's modulus.

Table 3.4. *Tensile mechanical data of LCP fibres.*

A number of models have been developed in the past which attempt to describe the strain hardening phenomena observed at high strains in aramid fibres. None of them, however, predict strain softening in the low strain region. It is well documented that Kevlar® fibres consist of identical fibrils built up in a parallel array [**Northolt 1980,1985**]. Experimental work based on X-ray and electron diffraction studies has confirmed that each fibril consists of a series of

crystallites [**Dobb 1977**], [**Northolt 1973,1974**] interconnected by domains containing loosely packed chain segments, ends and chain folds [**Northolt 1977**]. The stress-strain behaviour of Kevlar® fibres is directly dependent on the *crystallite orientation distribution* and the *chain orientation distribution* of the macromolecules which make up the crystallites. The mechanical deformation of these fibres is largely brought about initially by the irreversible rotation of the crystallites and secondly by the elongation of the crystallite lattice through valence angle deformation and bond stretching of the polymer chains. It has been proven experimentally that higher crystalline disorder (i.e. wider crystalline orientation distribution) results in lower tensile modulus [**Kwolek 1972,1974**]. In figure 1.10 (see chapter 1) the initial modulus was plotted vs *orientation angle* $\overline{\varphi}$ (i.e. the mean value of the crystallite orientation distribution) for as spun and heat-treated aramid fibres from the literature [**Yang 1989**]. The hyperbolic correlation between the two parameters explains to a certain extent the variation in stiffness of the stress-strain curves obtained for the aramid fibres shown in figure 3.3.

3.4.2. Monitoring the Raman frequency strain sensitivity of LCP fibres in tension.

As has already been mentioned in the previous section, the areas of interest in the Raman spectra of LCP fibres examined in this work are as follows:

- for Kevlar® is 1475cm^{-1} to 1700cm^{-1},
- for PBZT is 1375cm^{-1} to 1575cm^{-1} and
- for PBO is 1475cm^{-1} to 1675cm^{-1}.

The alterations occurring in the above areas of the Raman spectra due to external macroscopic deformation, are shown in figures 3.5a,b (Kevlar®49), 3.5c,d (PBO-B1) and 3.5e,f (PBZT-Z1) respectively. As can be seen, extreme distortion of the bands is observed prior to fracture for all fibres. In each graph the black line

represents the Raman spectrum of the completely unstretched fibre and the grey line the Raman spectrum of the stretched fibre. It is quite clear that all frequencies related to skeletal vibrational modes (i.e. vibrational modes associated with the polymer backbone) shift towards lower values. Another important observation is that the spreads of the bands (FWHM) at the stretched state are broader compared to those in the unstretched state.

A detailed monitoring of the above changes confirmed experimentally the strain dependence of all these frequencies. The results are presented in figures 3.6, 3,7, 3.8a,b and 3.9a,b for all Kevlar® fibres, figures 3.8c and 3.9c for PBZT-Z1 fibre and figures 3.10 and 3.11 for all PBO fibres. The Raman frequencies and FWHM were plotted as a function of the applied tensile strain. In Appendix 1 the statistical distributions employed for calculations concerning band positions, band intensities and FWHM for all fibres types are given. In a first approximation the Raman frequency versus tensile strain behaviour appears to be linear or nearly linear for all frequencies. The least-squares fit to the raw data has been calculated for all strong features in the Raman spectrum of the three different groups of LCP fibres (Kevlar®, PBZT and PBO) studied in this work. The slope of the fitted line, a characteristic parameter for each fibre and universal for each Raman frequency is defined as the *Raman Frequency Strain Dependence*, α^{ε}. The offset (intercept) of the fitted line represents the Raman frequency of the undeformed fibre. Therefore, at a first approximation:

$$\nu(\varepsilon) = \nu(0) + \alpha^{\varepsilon} \cdot \varepsilon \tag{3.16}$$

or similarly to equation 3.1:

$$\Delta\nu(\varepsilon) = \alpha^{\varepsilon} \cdot \varepsilon \tag{3.17}$$

where $\nu(0)$ is the offset, $\Delta\nu(\varepsilon)$ is the absolute value of the Raman frequency change or shift arising due to the applied tensile strain.

A summary of all the results concerning the Raman Frequency Strain Dependence α^{ε} for all frequencies and the standard error of the first approximation fit for all fibres is displayed in the following tables:

Raman Frequency / cm^{-1}	α^{ε} / $cm^{-1}/\%$	R^2
Kevlar® 49		
1515	-4.61±0.09	0.996
1615	-4.13±0.04	0.999
1655	-1.91±0.07	0.986
PBZT-Z1		
1175	-1.30±0.50*	-
1480	-13.13±0.13	0.998
1605	-8.00±1.00*	-
PBO-B1		
1160	-1.20±0.24	0.975
1280	-7.74±0.05	0.998
1320	-3.14±0.06	0.996
1620	-6.09±0.17	0.985

* from [Day 1987].

Table 3.5. *Spectro-mechanical characterization of all major bands for fibres in tension.*

As described earlier, all studies in this work concentrated on the Raman frequencies assigned in table 3.3. The Raman Frequency Strain Dependence of these frequencies only is given in the following table for all LCP fibres examined:

Raman Frequency / cm^{-1}	α^{ε} / $cm^{-1}/\%$	R^2
Kevlar® (1615 cm^{-1})		
Kevlar® 49	-4.13±0.04	0.999
Kevlar® 29	-3.02±0.04	0.994
Kevlar® 149	-5.06±0.14	0.992
Kevlar® 49 ht1	-4.08±0.03	0.999
Kevlar® 49 ht2	-3.43±0.04	0.998
PBZT (1480 cm^{-1})		
Z1	-13.13±0.13	0.998
PBO (1620 cm^{-1})		
B1	-6.09±0.17	0.985
B2	-3.35±0.06	0.992
B3	-3.42±0.28	0.984
B4	-6.98±0.21	0.982

Table 3.6. *Summary of spectro-mechanical characterization of LCP fibres in tension.*

3.5. Discussion.

3.5.1. Tensile deformation of LCP fibres.

Several attempts have been made in the last 20 years to provide an understanding of the relationship between the physical structure and the macroscopic deformation and failure processes of LCP fibres. The *aggregate structure model* **[Ward 1962]** has been analyzed and expanded **[Northolt 1977,1980,1985]** or used in a modified form as *pleated structure model* **[Ballou 1976]**, **[Dobb 1977]**, **[Avakian 1980]**, **[Allen 1989]** to describe the deformation characteristics of aramid fibres. The fibre according to the first approach is regarded as being built up of parallel aligned fibrils in which cylindrical crystallites have a narrow orientation distribution (*crystallite orientation distribution*) relative to the fibre axis and are linked end-to-end. Each individual crystallite consists of long chains of rodlike P*p*PTA macromolecules. These macromolecules are arranged almost parallel to the fibre axis, having also a narrow orientation distribution (*chain orientation distribution*). A simplified sketch of this model is presented in figure 3.12a **[Morgan 1983]**.

Another important parameter in this approach is the *chain end distribution* within the vicinity of the fibre, given in figure 3.12b **[Morgan 1983]** which controls the tensile deformation and failure of aramid fibres. On the basis of information from the previous reference it is assumed that the chain end distribution in the fibre skin is essentially random but becomes progressively more clustered in the fibre core, resulting in periodic weak planes transverse to the fibre axis.

Significant amounts of work based on electron and optical microscopy, small and wide angle x-ray diffraction studies and chemical degradation studies have been undertaken in order to examine the morphology of P*p*PTA fibres. This was briefly presented in the 1st chapter. It was found that the crystallites have dimensions of up to 40nm in length and 20nm in width **[Northolt 1977,1980]**. On

a larger scale, regular periodicities of 200nm to 300nm in size along the fibre axis have been observed [**Dobb 1977**], [**Morgan 1983**].

The morphology of PBZT fibres has also been studied extensively (see chapter 1). As spun PBZT fibres contain 2nm crystallites which, upon heat treatment grow into axially elongated crystallites 10nm-20nm in size [**Thomas 1982**]. A similar observation has been made for PBO fibres [**Allen 1981a**].

A simplified approach to the tensile deformation of such a fibre model is based on the assumption that the total axial deformation ε_{total} induced by a macroscopic stress σ is given by:

$$\varepsilon_{total} = \varepsilon_{stretch}^{elastoplastic} + \varepsilon_{rotation}^{plastic} = [\varepsilon_{sr} + \varepsilon_{si}] + \varepsilon_{ri} \qquad (3.18)$$

where $\varepsilon_{stretch}^{elastoplastic}$ represents longitudinal extension of the crystallites due to stretching (made up by a reversible ε_{sr} and an irreversible ε_{si} component) and $\varepsilon_{rotation}^{plastic}$ represents rotation of the crystallites due to shear deformation, which is irreversible. The Raman frequency shift $\Delta\nu(\varepsilon)$ for a given (skeletal) vibrational mode is due only to the deformation of covalent bonds along the molecular chain and therefore is due only to the stretching component $\varepsilon_{stretch}^{elastoplastic}$ and is not affected by the rotational component $\varepsilon_{rotation}^{plastic}$. In fact, the irreversible chain extension component ε_{si} can be clearly seen in figure 3.13 where a typical Raman frequency shift $\Delta\nu(\varepsilon)$ versus strain set of data is demonstrated for 'loading' and 'unloading' (up to four complete 'cycles'). Hysteresis is clearly observed and plastic deformation of ~0.40% is detected.

Northolt derived an analytical formula for the stretching component as a function of the initial (i.e. at $\sigma = 0$) crystalline orientation distribution (average), $\langle \sin^2 \varphi_0 \rangle$, the theoretical modulus of the polymer chain e and the force constant governing the rotation of the crystallites. Due to molecular anisotropy of aramid fibres it was considered that the force constant is directly related to the shear

modulus in the plane containing the symmetry axis of the crystallite. This approximation can be written as follows (*aggregate structure model*):

$$\varepsilon(\sigma) \equiv \frac{\sigma}{e_N} + \frac{1}{2}\langle \sin^2 \varphi_0 \rangle \left[1 - \exp\left(-\frac{\sigma}{g}\right)\right] \tag{3.19}$$

where e_N=220 GPa [**Northolt 1980**].

The approach proposed by Allen (*pleated structure model*) was based on measurements which demonstrate that any macroscopic deformation applied in the fibre will result at a microscopic level in a progressive opening of the fibre's pleated sheet structure. This behaviour is attributed to local shear coupling mechanisms between axial and radial or hoop stresses. The following equation can be used to describe this:

$$\varepsilon(\sigma) \equiv \frac{\sigma}{e_A} + \frac{1}{2}\tan^2 \overline{\varphi}_0 \left[1 - \exp\left(-\frac{2\sigma}{g}\right)\right] \tag{3.20}$$

where e_A=180 GPa and $\overline{\varphi}_0$ is the (average) *initial misorientation angle* with respect to the fibre axis [**Allen 1981a**].

The crystalline orientation distribution changes with the applied stress as has been experimentally confirmed for aramid fibres [**Northolt 1980**]. This can be expressed in mathematical terms as follows:

$$\langle \sin^2 \varphi \rangle = \langle \sin^2 \varphi_0 \rangle \exp\left(-\frac{2\sigma}{g}\right) \tag{3.21}$$

for the aggregate structure model, or for the pleated structure model:

$$\tan^2 \overline{\varphi} = \tan^2 \overline{\varphi}_0 \exp\left(-\frac{\sigma}{2g}\right) \tag{3.22}$$

Any increase in the macroscopic applied stress will result in a decrease in the crystalline orientation distribution or crystalline misorientation angle and therefore an increase in the fibre tangent modulus $E^t(\sigma)$ is predicted. By taking the first derivative of the strain functions (equations 3.19 and 3.20) with respect to stress:

$$\frac{1}{E^t(\sigma)} = \frac{d\varepsilon(\sigma)}{d\sigma} \tag{3.23}$$

which gives:

$$\frac{1}{E^t(\sigma)} = \frac{1}{e_N} + \frac{\langle \sin^2 \varphi_0 \rangle}{2g} \exp\left(-\frac{\sigma}{g}\right) \tag{3.24a}$$

$$\frac{1}{E^t(\sigma)} = \frac{1}{e_A} + \frac{\tan^2 \overline{\varphi}_0}{g} \exp\left(-\frac{2\sigma}{g}\right) \tag{3.24b}$$

the above correlation can be verified. The first equation (3.24a) corresponds to Northolt's model and the second one (3.24b) to Allen's model.

In figures 3.14a,b (Northolt) and 3.14d,e (Allen), the stress-strain curves and the tangent Young's modulus $E^t(\sigma)$ as a function of the macroscopic applied stress σ or strain ε for all Kevlar® fibres (Kevlar® 29, Kevlar® 49, Kevlar® 149) are plotted. The crystalline orientation distributions or misorientation angles were calculated from the initial Young's moduli estimated from the stress-strain curves using the formulae:

$$\frac{1}{E^t(\sigma=0)} = \frac{1}{e_N} + \frac{\langle \sin^2 \varphi_0 \rangle}{2g} \tag{3.25a}$$

$$\frac{1}{E^t(\sigma=0)} = \frac{1}{e_A} + \frac{\tan^2 \overline{\varphi}_0}{g} \tag{3.25b}$$

A very clear observation in these graphs is that the tangent Young's modulus increases with the increase of the applied stress or strain as expected, i.e. modulus hardening is predicted for all aramid fibres. This behaviour has been experimentally observed at high strains for Kevlar® 29 and 49 and continually for Kevlar® 149 (see experimental section). However, the above models fail to predict the noticable strain softening occurring in the low strain region which is due to the expulsion of residual moisture and/or residual stresses arising during coagulation **[Allen 1981a]**, **[Roche 1987]**. These stresses can be cancelled out either by heat treatment or conditioning (for example, by simply reloading the fibre) **[Roche 1987]**, **[Allen 1989]**.

A physical interpretation of strain hardening is considered to be the decrease of the crystalline disorder (aggregate structure model) or the 'straightening' of the slightly tilted molecular sheets (pleated structure model). In fact, any change in the initial crystalline orientation distribution $\langle \sin^2 \varphi_0 \rangle$ or the initial misorientation angle $\overline{\varphi}_0$ will result in a significant change in the value of the initial tangent Young's modulus for all three Kevlar® fibres. This can be demonstrated in figure 3.14c,f. In other words, as this figure shows, a tendency to perfect crystalline orientation or zero misorientation angle would asymptotically lead to the theoretically predicted value of Young's modulus for these materials. On the contrary, a misorientation parameter corresponding to 3° for example,would reduce the theoretically predicted Young's modulus to half, as can be seen from the curves. Experimental evidence from the literature of this has been given in chapter 1, where a hyperbolic correlation between initial modulus and misorientation has been found for aramid fibres (figure 1.10).

It has already been mentioned that equations 3.19 and 3.20 take into account only the strain component $\varepsilon_{stretch}^{elastoplastic}$ associated with elastoplastic stretching as indicated in equation 3.18. In fact, the linear term in these equations represents the reversible, elastic strain of the crystallites and the exponential term the irreversible, plastic strain of the crystallites towards the fibre axis due to shear coupling.

In our first approximation the correlation between the Raman frequency shift (which is attributed only to the stretching component as has already been stated) and the macroscopic applied strain data is considered to be linear. In figure A2.1 (see Appendix 2), a number of polynomial curves are used to fit the experimental data for Kevlar® 29, starting with a linear fit (1st degree polynomial) and gradually increasing the order. Consequently, the quality of the fit (indicated by the decrease of the R^2 parameter) increases. Therefore, we can confidently conclude that a more accurate treatment of the experimental data may involve a polynomial regression of the form:

$$\Delta\nu(\varepsilon) = a_0 + a_1\varepsilon + a_2\varepsilon^2 + a_3\varepsilon^3 + \ldots \qquad (3.26a)$$

In a similar fashion, the mechanical stress versus strain data can be represented as follows:

$$\sigma(\varepsilon) = b_0 + b_1\varepsilon + b_2\varepsilon^2 + b_3\varepsilon^3 + \ldots \qquad (3.26b)$$

In a more accurate appproach, Raman frequency shift versus strain and mechanical stress versus strain data were fitted by employing cubic spline functions available from a commercial FORTRAN library (see Appendix 2).

The results of the conventional mechanical data were demonstrated in figures 3.3 and 3.4. In these figures, cubic spline functions simulate the non-linear response of the fibres. The first derivative of these functions which

represent the tangent Young's modulus E^t were also calculated and plotted as a function of strain for each fibre. In a similar fashion, the cubic spline functions associated with the spectroscopic-mechanical response of Kevlar® and PBO fibres are presented in figures 3.15a-d along with the raw experimental data. The first derivative of each of the above functions which represents the Raman Frequency Strain Dependence, $\alpha^\varepsilon(\varepsilon)$, for each fibre are also plotted as a function of strain. In mathematical terms, the above relations can be written as follows:

$$\frac{d\Delta\nu(\varepsilon)}{d\varepsilon} = \alpha^\varepsilon(\varepsilon) \tag{3.27a}$$

$$\frac{d\sigma(\varepsilon)}{d\varepsilon} = E^t(\varepsilon) \tag{3.27b}$$

In figure 3.16a the Raman Frequency Strain Dependence at zero strain i.e. $\alpha^\varepsilon(\varepsilon = 0)$ is plotted as a function of the initial tangent Young's modulus $E^t(\varepsilon = 0)$ for all Kevlar® and PBO fibres respectively. As we see, a linear fit to the data confirms that:

$$\alpha^\varepsilon(\varepsilon) = kE^t(\varepsilon) \tag{3.28}$$

where $k = \alpha^\sigma$, the *Raman Frequency Stress Dependence.*

The physical interpretation of the above equation is that all fibres belonging to the same family (i.e. derived from the same manufacturing root) should have one value **k** associated with a backbone vibrational mode regardless of their tangent Young's moduli. A direct measurement of the parameter Raman Frequency Stress Dependence, **k**, should provide further evidence for the above. Experiments in order to measure the Raman frequency shift as a function of the applied stress were carried out for Kevlar® fibres employing the Remote Laser Raman Spectroscopy set-up and the results are shown in figure 3.16b. In this

figure, the Raman frequency shift (obtained almost instantly during deformation) was plotted as a function of the applied stress (obtained directly from the mechanical tester) for a group of various Kevlar® fibres (different tenacity and strength: Kevlar® 29, Kevlar® 49, Kevlar® 119 and Kevlar® 129). Linear relationships of slopes identical to that in figure 3.16a (within the experimental error) were observed. This is in full agreement with equation 3.1 and therefore further verifies that Raman frequency shift is proportional to macroscopic mechanical stress.

3.5.2. Other spectroscopic observations during tensile deformation of LCP fibres.

Another crucial spectroscopic observation during deformation of the LCP fibres examined in this work, involves the *broadening* of the Raman bands which has already been shown in figures 3.5 for all fibres. The shape of the 1615, 1480 and 1610 cm^{-1} bands in the Raman spectrum are compared for two extreme cases: unstretched fibre and prior to fracture. The full width at half maximum (FWHM) for the Gaussian distributions (Kevlar® fibres) or Lorentzian distributions (PBO and PBZT fibres) fitted to the raw data was plotted as a function of the applied strain in figures 3.7, 3.9 and 3.11 for all fibres examined in this work. The FWHM strain dependence is strongly non-linear especially at very high strains. Similar broadenings were observed for other pronounced frequencies in the Raman spectra of these fibres. Band-broadening phenomena were monitored along with frequency shifts and have been reported in the literature for various polymeric materials [**Bretzlaff 1983**], [**Shen 1982a,b**], [**Wool 1986**], [**Day 1987**], [**Jahankhani 1990**] or carbon [**Melanitis 1991**]. In this section we will attempt to interpret these alterations based on the molecular structure and morphology of the fibres.

The mathematical routines employed for band position, intensity and width (described in the previous chapter) are very satisfactory for aramid fibres up to approximately 2.0% applied strain (see Appendix 1, where satisfactory fits

are shown for 0.0%, 1.0% and 2.0% applied strain in figure A1.2). As far as the aramid fibres are concerned, FWHM alterations of the 1615cm^{-1} band show the following trend:

- (a) gradual, smooth increase of FWHM of the above vibrational frequency in a insignificantly *asymmetric* manner up to approximately 2.0% of applied tensile strain for all fibres (exluding Kevlar® 149 where very small changes in the FWHM were observed).
- (b) rapid, abrupt increase of FWHM in a significantly *asymmetric* manner for applied tensile strain above 2.0%.

The above observations can be assigned quantitatively by superimposing the bands at the deformed state with the 'undistorted' band prior to any deformation. By subtracting the two sets of raw data, a direct comparison between the two areas left and right of the maximum value can be compared. In figure 3.17a this comparison is given for the extreme case prior to fracture. If the two areas are equal, this means that symmetric broadening has occured (which is the case for deformations less than 2.0% applied strain). If the two areas are not equal (see figures 3.5b,d,f), an asymmetric broadening has occurred. The results for four Kevlar® 49 fibre specimens are demonstrated in figure 3.17b. In this graph the area ratio A_1/A_2 is plotted as a function of the applied strain. As can be seen, the A_1/A_2 experimental values show small increase up to 2.0% applied strain and shoot up to higher values for higher applied strain, especially near fracture. It is quite obvious that in this region of applied strain, the shape of the band is composed of two separate distributions: one corresponding to the highly stretched fibrils (towards lower frequency values) and one corresponding to the weak fibrils which have failed (towards high frequency values).

The aggregate structure model for aramid fibres proposed by Northolt has been mentioned previously. According to this model, the fibre is made up of a parallel array of identical fibrils. Each fibril consists of a series of crystallites and each crystallite is composed of polymer chains. Although the molecular chain

packing does not necessarily correspond to the thermodynamic equilibrium, it is well established that under favourable experimental conditions chain ends segregate to form a paraffinic arrangement [**Kovacs 1975**] demonstrated in figure 3.12. All crystallites have identical mechanical properties and are transversely isotropic. The crystallites are slightly misoriented with respect to the fibre axis. In fact, the orientation angles of the symmetry axes of the crystallites relative to the fibre axis follow a statistical distribution which can be quantified and defined accurately by X-ray diffraction [**Northolt 1985**].

In a simplistic model, we can assume a normalised symmetric distribution $\rho(\vartheta)$ of crystallites with respect to the fibre axis. In the undeformed state, each infinitesimally small population of crystallites contributes to the overall Raman spectrum proportionally but at the same vibrational frequency, $\nu_{\sigma=0}$). If an external stress σ is applied to the crystallite bundle, the crystallites which are perfectly oriented ($\vartheta = 0^0$) will contribute to the Raman spectrum proportionally to their population at a vibrational frequency of $\nu_\sigma^{\vartheta=0} = \nu_{\sigma=0} - k\sigma$, where **k** is the Raman Frequency Stress Dependence which has been calculated experimentally. However, the crystallites which are slightly tilted ($\vartheta \neq 0^0$) will contribute to the Raman spectrum also proportionally to their population at a slightly higher frequency than $\nu_\sigma^{\vartheta=0} = \nu_{\sigma=0} - k\sigma$, equal to $\nu_\sigma^{\vartheta=0} = \nu_{\sigma=0} - k\sigma\cos\vartheta$. A comparison of the Raman frequencies for this model of crystallites between the undeformed and deformed state is schematically presented in figure 3.18 for small (figure 3.18a), medium (figure 3.18b) and large (figure 3.18c) values of **k**. As can be seen, the assymmetry is very much dependent on **k**: almost neglible in case (a) and observable in case (c). The broadening of the band in this case is due to the crystallites which 'lag behind' deformation due to their misorientation with respect to the fibre axis. In Appendix 1, the data concerning the peak position calculated by fitting symmetric distributions are compared with the actual peak position obtained from the maximum value of the distribution. Even in the extreme case (c), the error introduced by the above calculation is negligible and in the same order of the resolution of the system (spectrograph).

In the above model, the change of the initial distribution of crystallites with the increase of the applied stress has not been taken into account. As expected, the above distributions become narrower, and this has also been confirmed experimentally **[Northolt 1985]**. Nevertheless, the existence of weak bonds in the structure which fail prematurely during deformation has not been considered. In fact, the importance of these weak links is very much apparent at high stresses where more and more are expected statistically to fail. Evidence of the above is the asymmetric broadening of the band at very high deformations.

3.6 Conclusions.

A detailed analysis of the stress-induced changes in the Raman spectra of a whole range of LCP fibres was presented in this chapter. It was demonstrated that these changes scale accordingly with the changes of the macroscopic parameters. The crystallite misorientation characteristics of LCP fibres controls their stiffness and strength in an almost exclusive manner. Different grades of fibres derived from the same chemical unit (i.e. aramids) exhibit different stiffness due to their different initial crystallite misorientation.

In fact, the macroscopic stress-strain response of all LCP fibres can be accurately monitored by its mirror image of Raman frequency-strain response at microscopic level (compare figures 3.3, 3.4 and 3.15). Any procedure which will directly or indirecly affect the above parameter could result in a significant change of the mechanical properties and performance of these materials. Experimental evidence of the assumption that vibrational frequency shifts associated with backbone vibrational modes are proportional to the external applied stress was provided.

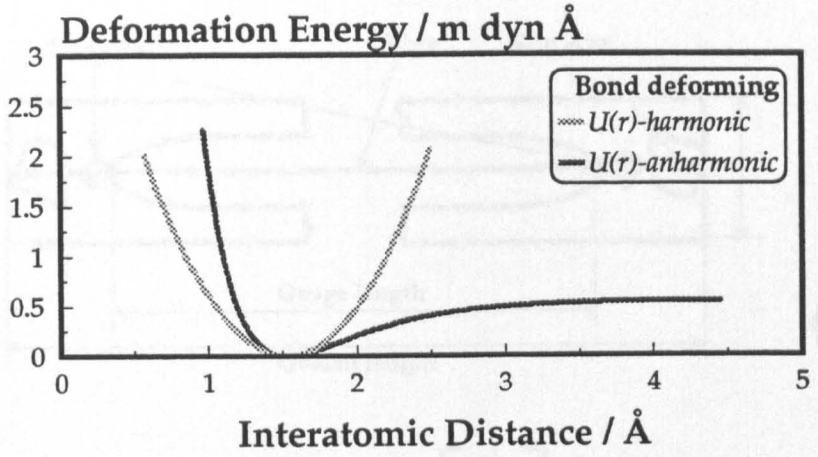

(a)

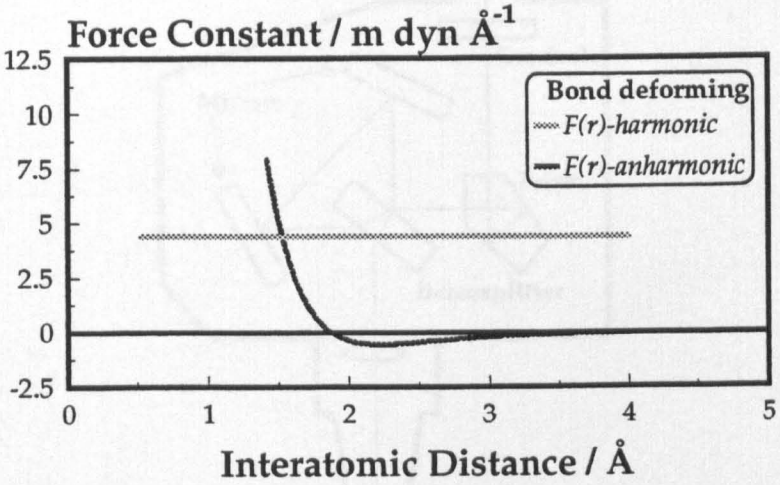

(b)

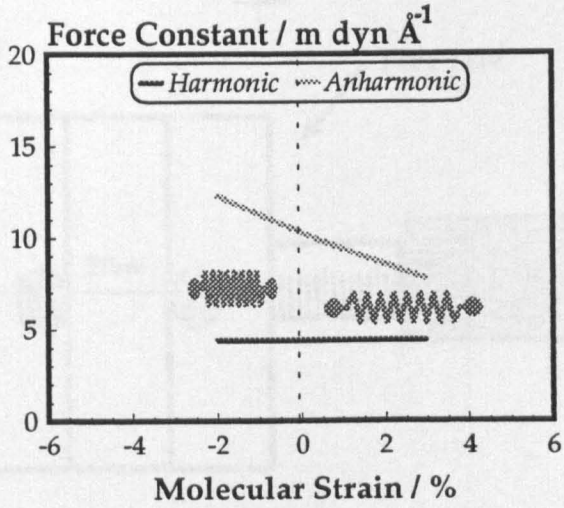

(c)

Figure 3.1. (a) Deformation (Potential) Energy as a function of the interatomic distance for a molecular dipole.
Force constant as a function of (b) the interatomic distance or (c) the molecular strain.

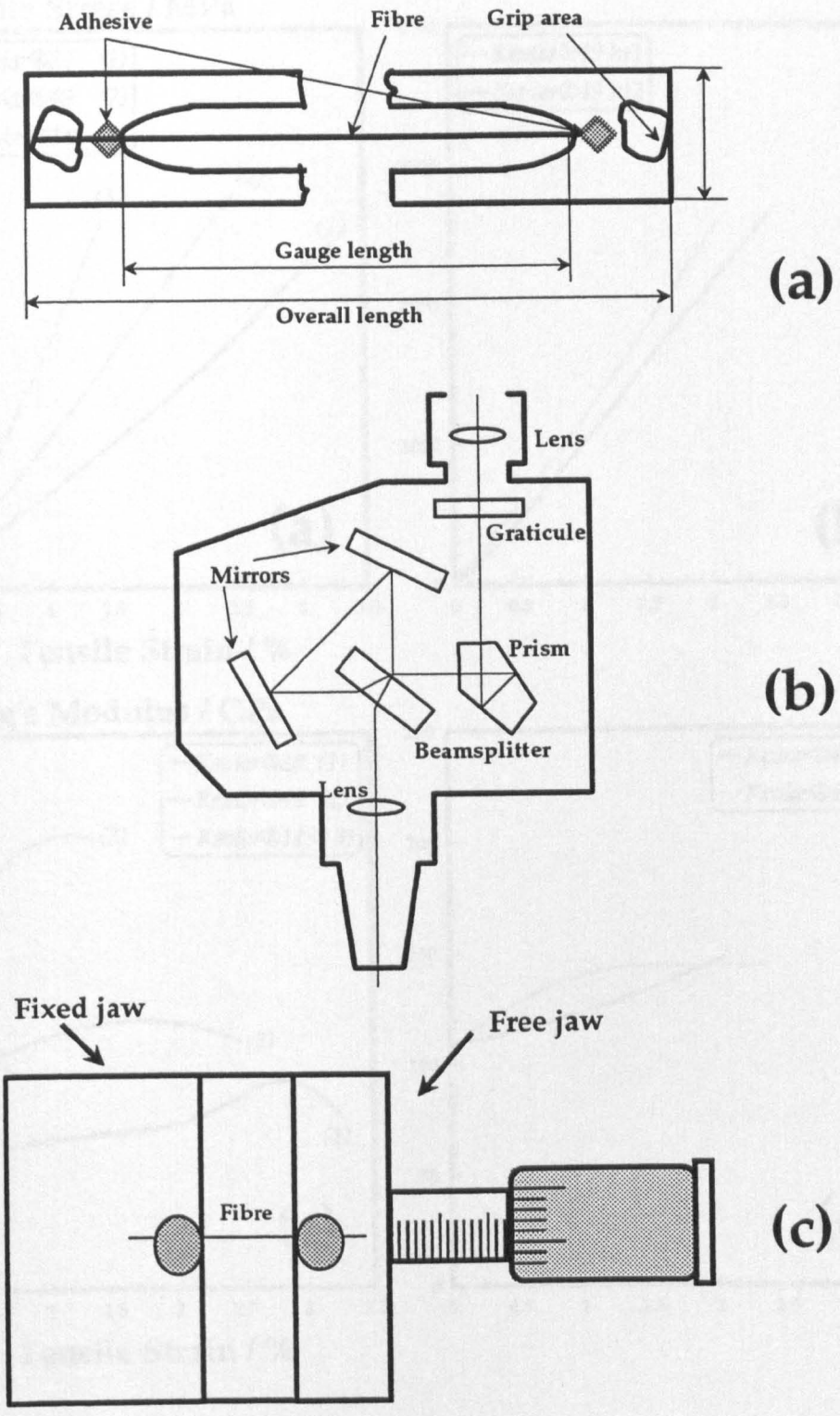

Figure 3.2. (a) ASTM D3379 specimen geometry for single fibre tensile testing.
(b) Watson Image-Shearing Eyepiece for fibre diameter measurements.
(c) Microextensometer device for fibre testing under the Raman probe.

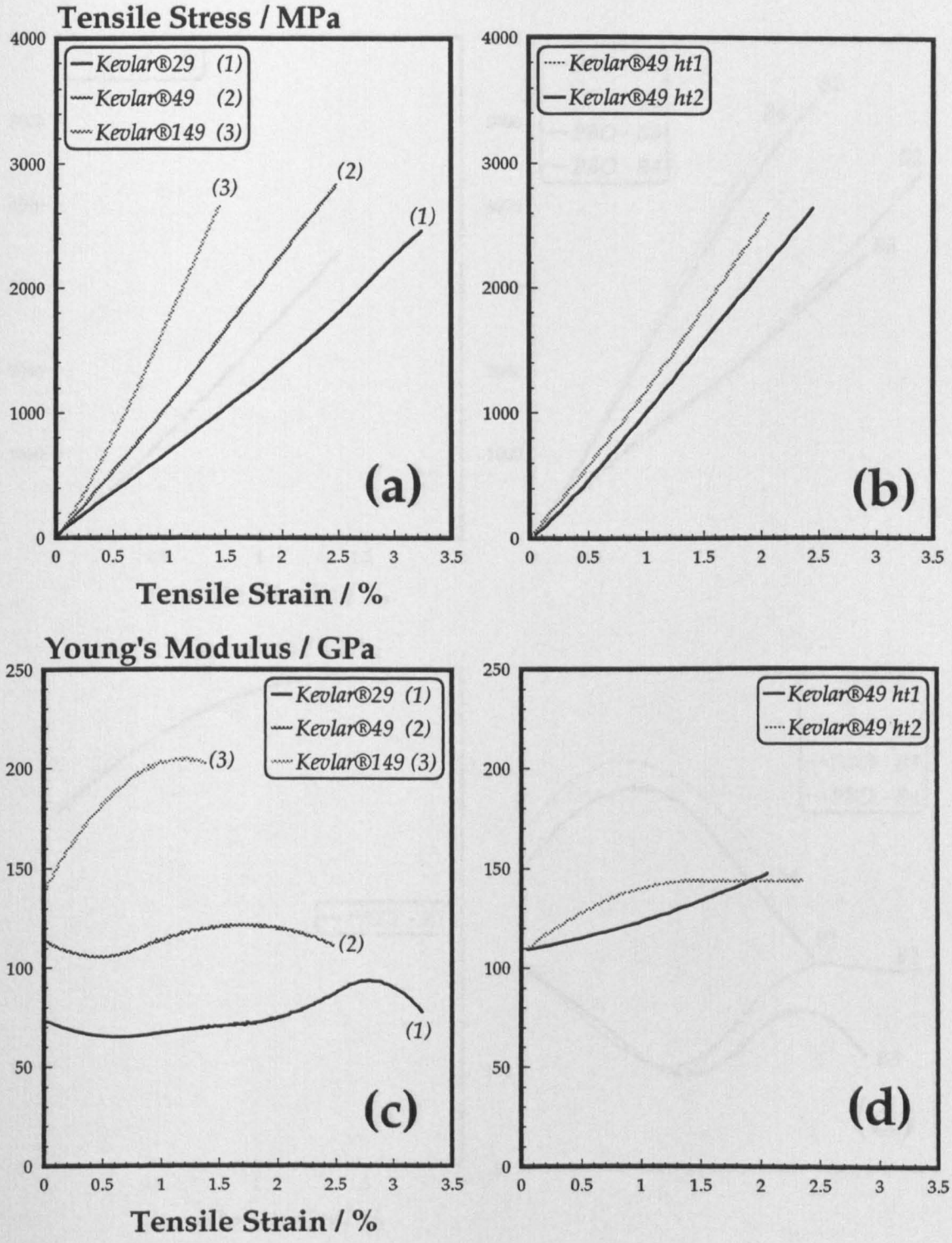

Figure 3.3. (a) Stress-strain curves for Kevlar®49, Kevlar®29 & Kevlar®149 fibres.
(b) Stress-strain curves for Kevlar®49 ht1&2 fibres.
(c) Young's modulus-strain curves for Kevlar®49, Kevlar®29 & Kevlar®149 fibres.
(d) Young's modulus-strain curves for Kevlar®49 ht1&2 fibres.

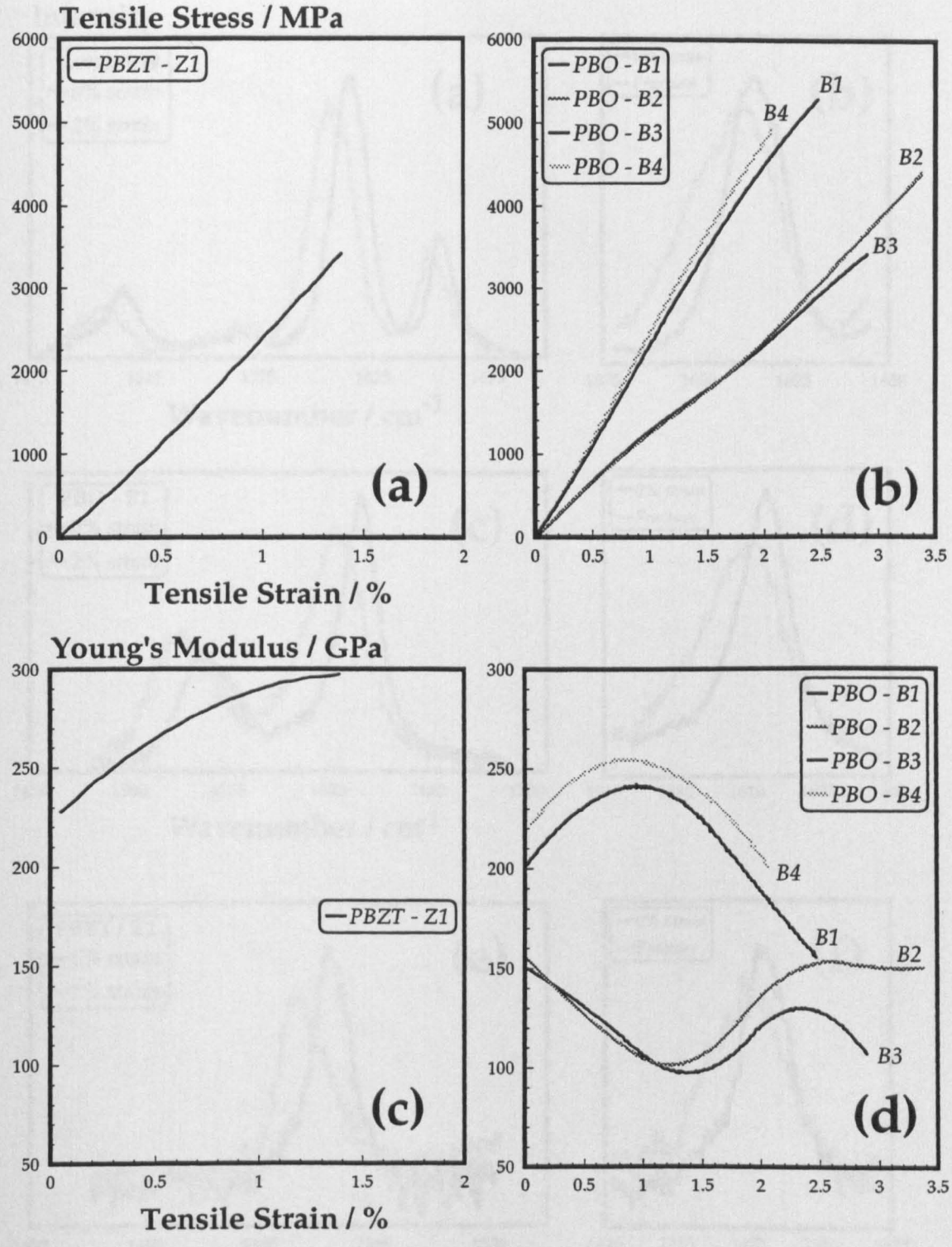

Figure 3.4. (a) Stress-strain curve for PBZT fibre.
(b) Stress-strain curves for PBO fibres.
(c) Young's modulus-strain curve for PBZT fibre.
(d) Young's modulus-strain curves for PBO fibres.

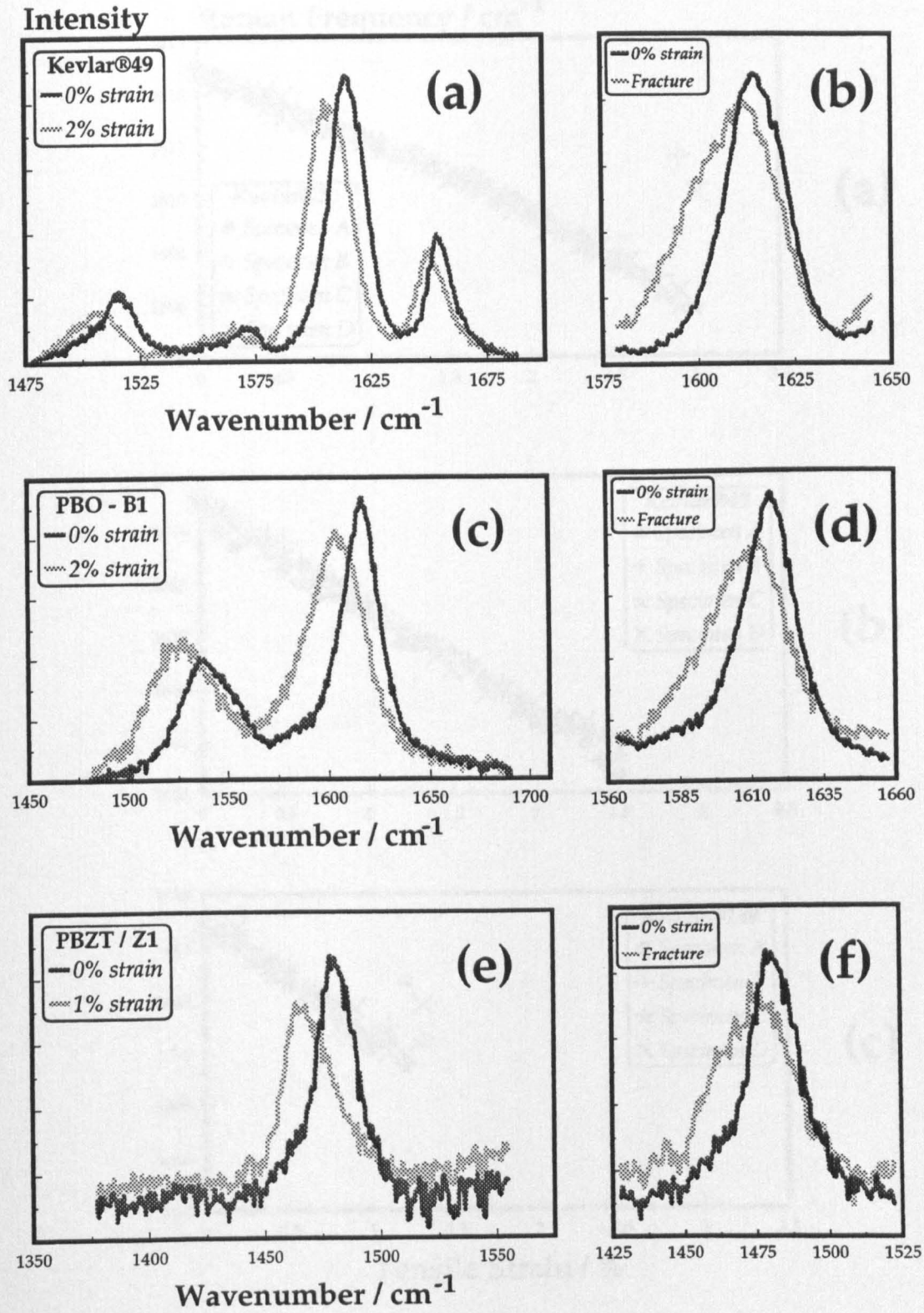

Figure 3.5. Comparison of Raman spectra for undeformed and deformed fibres in tension: (a) & (b) Kevlar®, (c) & (d) PBO and (e) & (f) PBZT fibres.

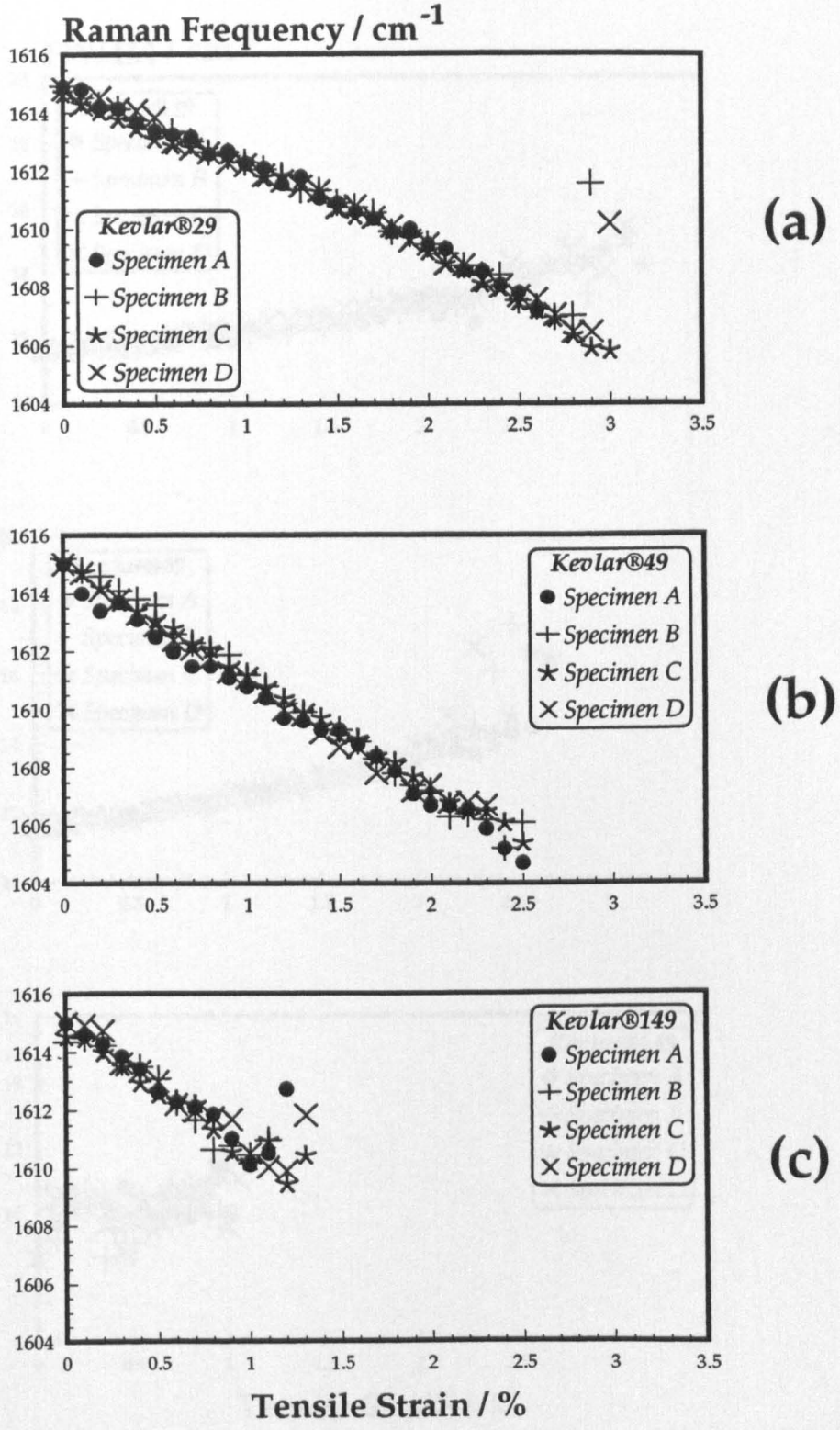

Figure 3.6. Raman frequency (1615cm^{-1})-tensile strain data for: (a) Kevlar®29, (b) Kevlar®49 and (c) Kevlar®149 fibres.

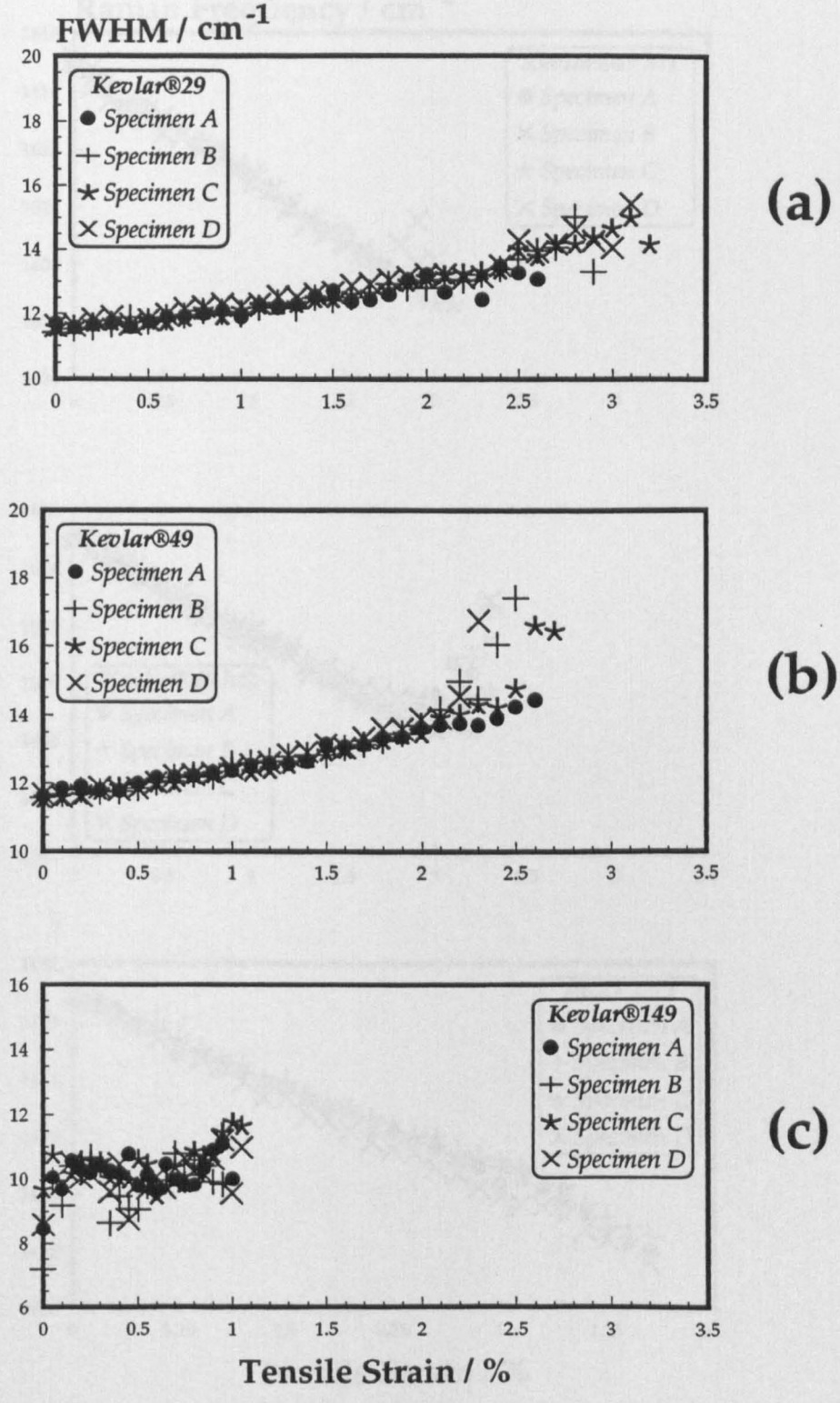

Figure 3.7. FWHM-tensile strain data for:
(a) Kevlar®29, (b) Kevlar®49 and (c) Kevlar®149 fibres.

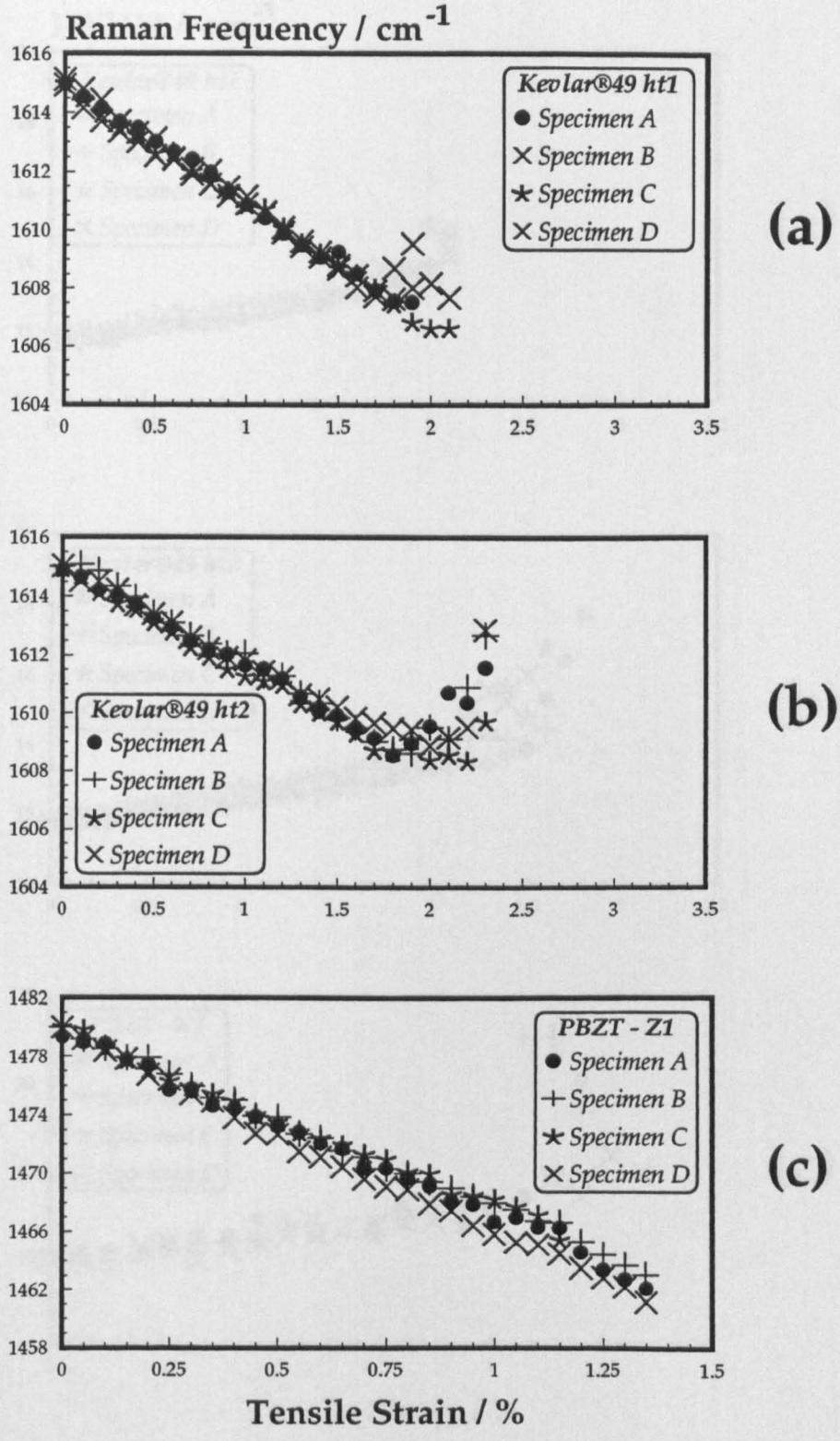

Figure 3.8. Raman frequency (1615cm^{-1} for Kevlar and 1480cm^{-1} for PBZT) -tensile strain data for (a) Kevlar®49 ht1 (b) Kevlar®49 ht2 and (c) PBZT-Z1 fibres.

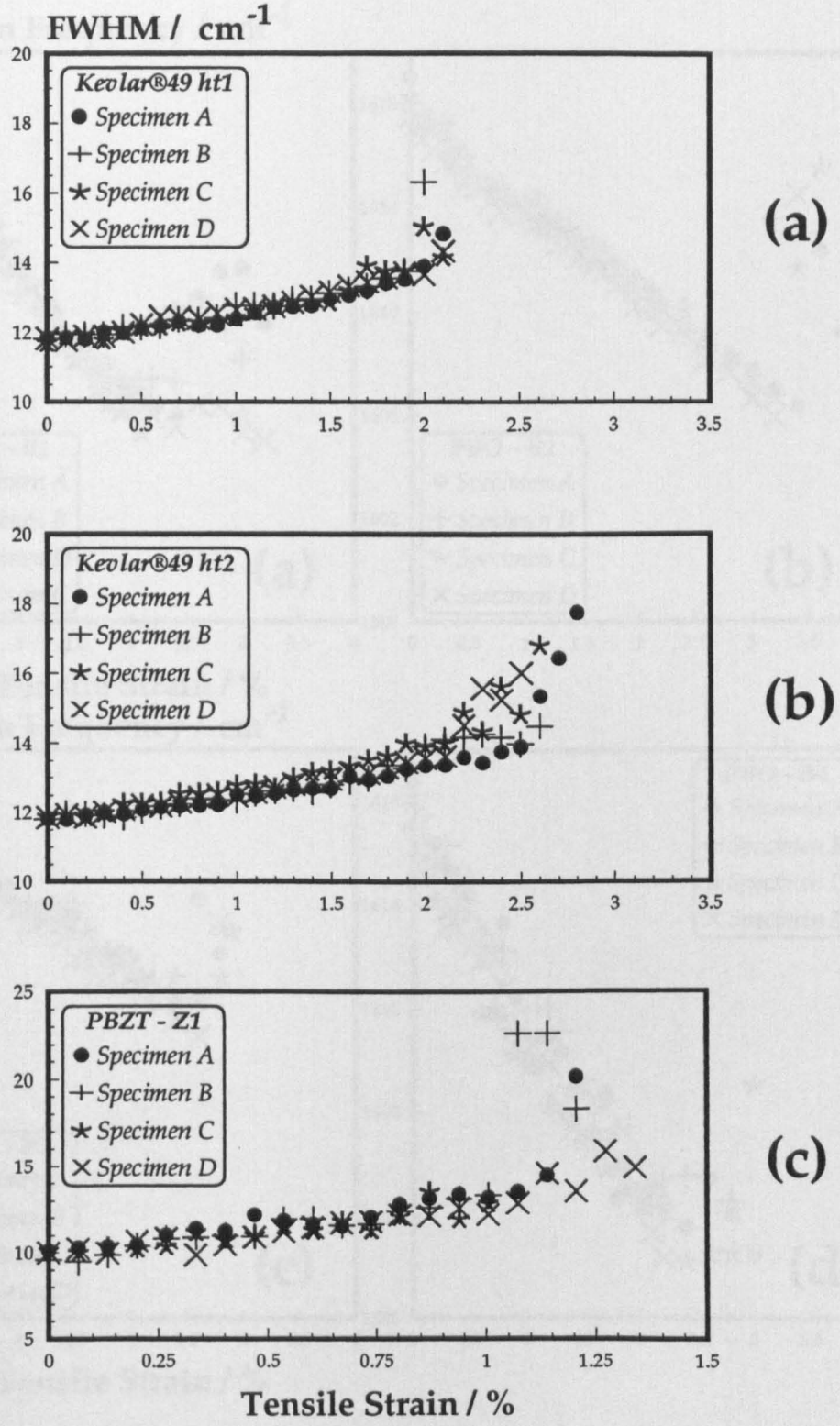

Figure 3.9. FWHM-tensile strain data for:
(a) Kevlar®49 ht1, (b) Kevlar®49 ht2 and (c) PBZT-Z1 fibres.

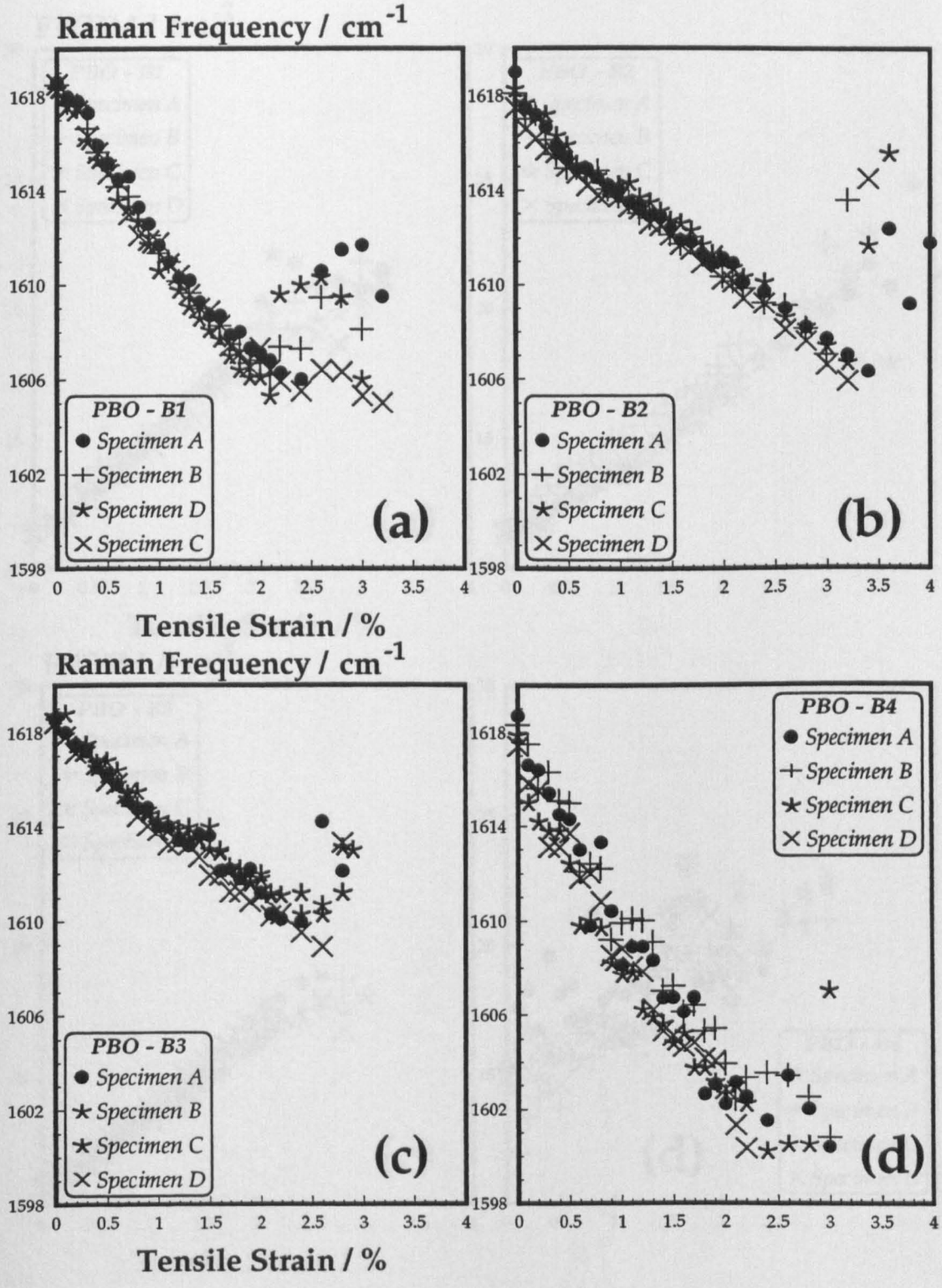

Figure 3.10. Raman frequency (1620cm^{-1})-tensile strain data for PBO fibres: (a) B1, (b) B2, (c) B3 and (d) B4 grades.

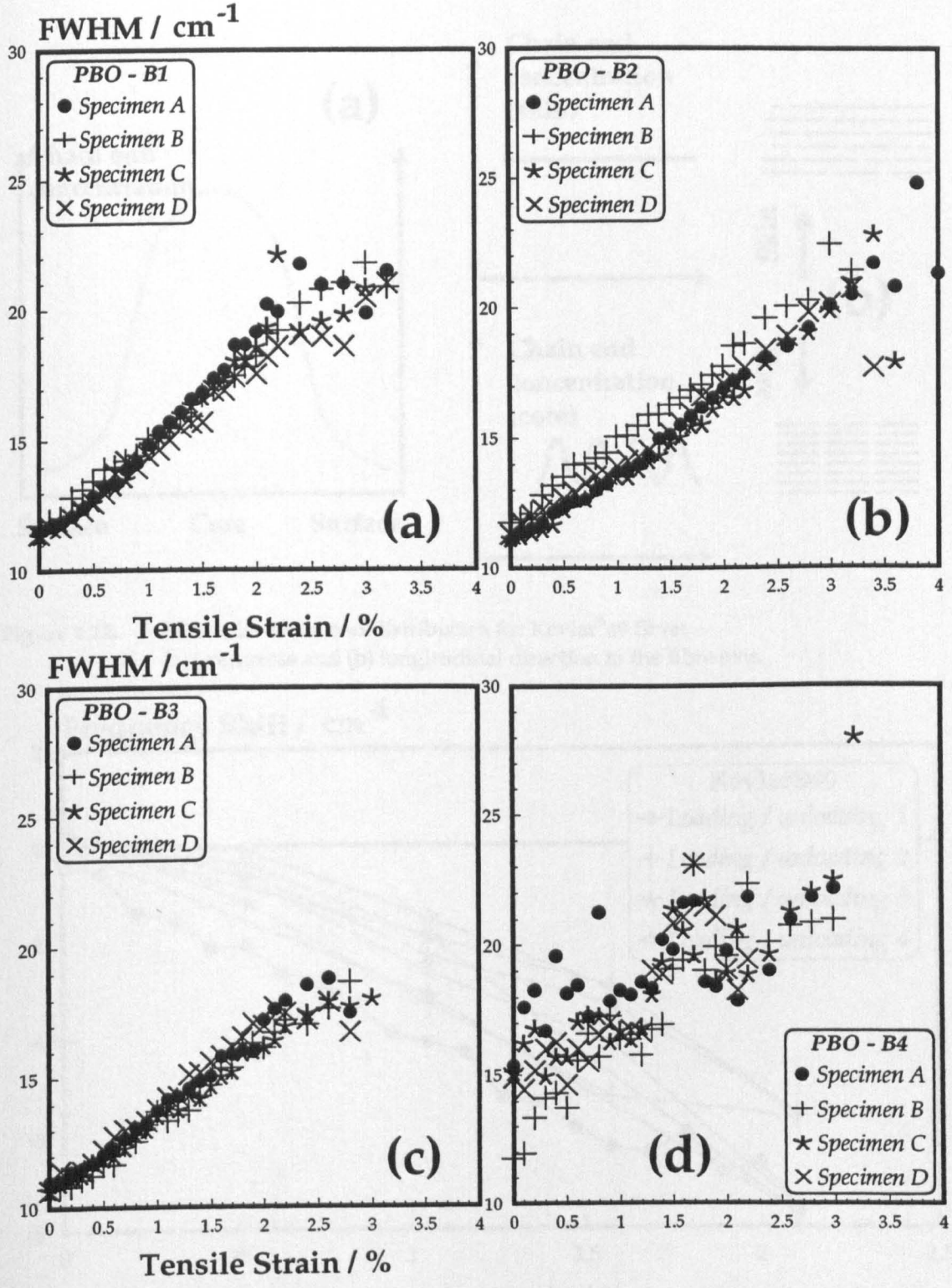

Figure 3.11. FWHM-tensile strain data for PBO fibres: (a) B1, (b) B2, (c) B3 and (d) B4 grades.

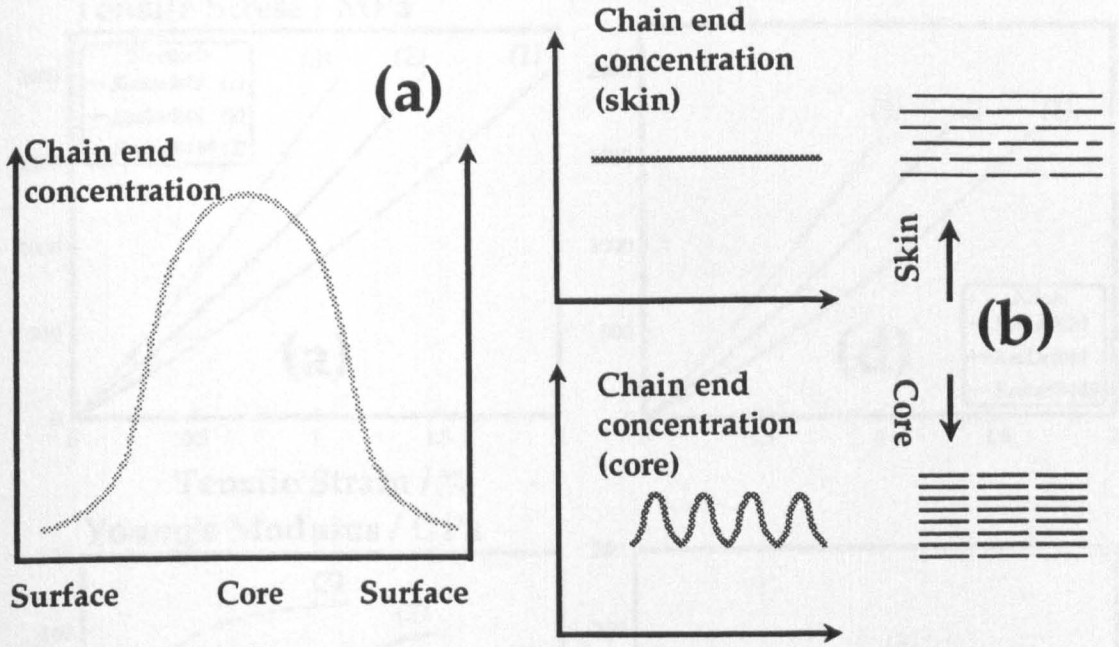

Figure 3.12. Molecular chain end distribution for Kevlar®49 fibre: (a) transverse and (b) longitudinal direction to the fibre axis.

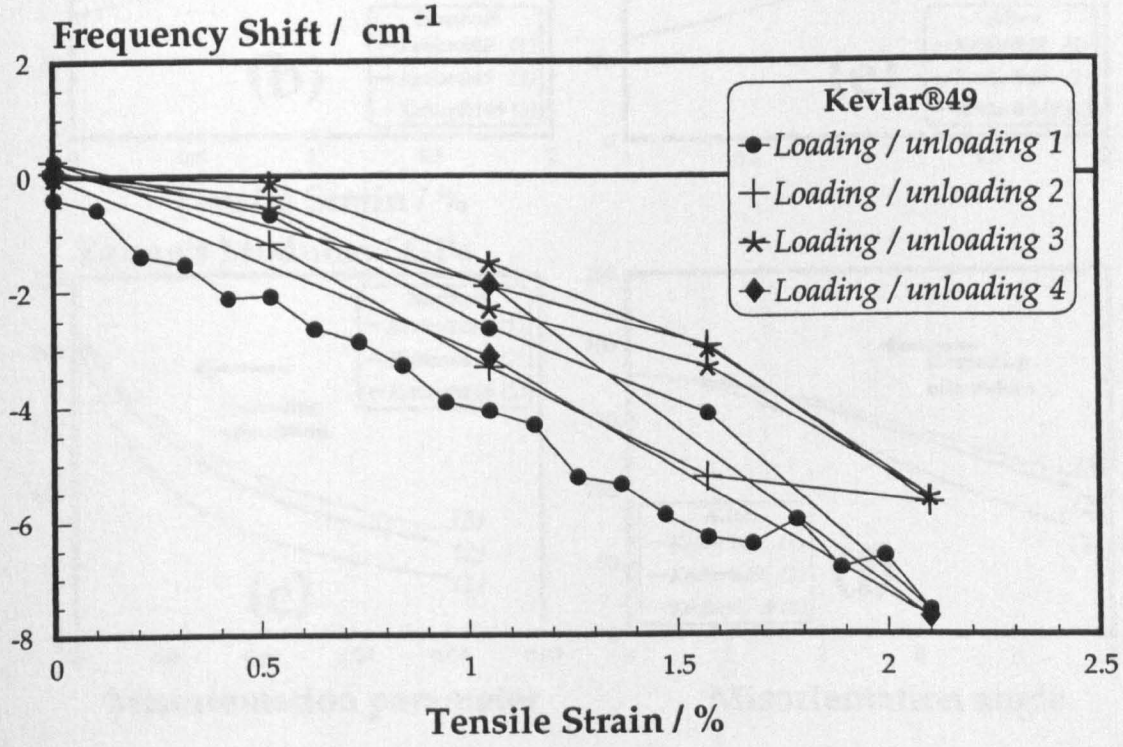

Figure 3.13. Raman frequency shift-tensile strain data for Kevlar®49 - loading and unloading cycles.

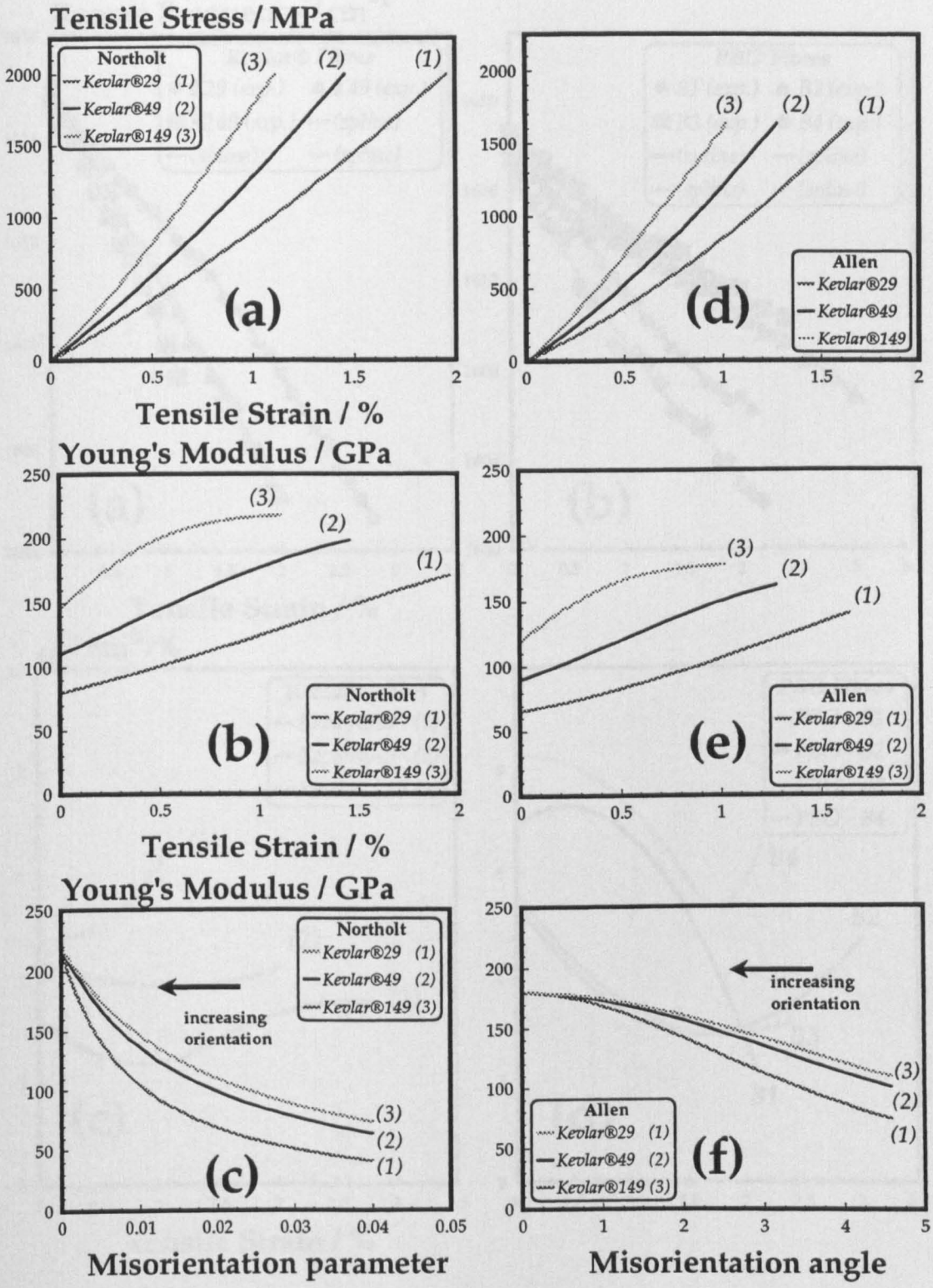

Figure 3.14. Predicted stress-strain, Young's modulus-strain and Young's modulus-misorientation curves for aramid fibres:
(a) (b) &(c) Northolt's model and (d) & (e) & (f) Allen's model.

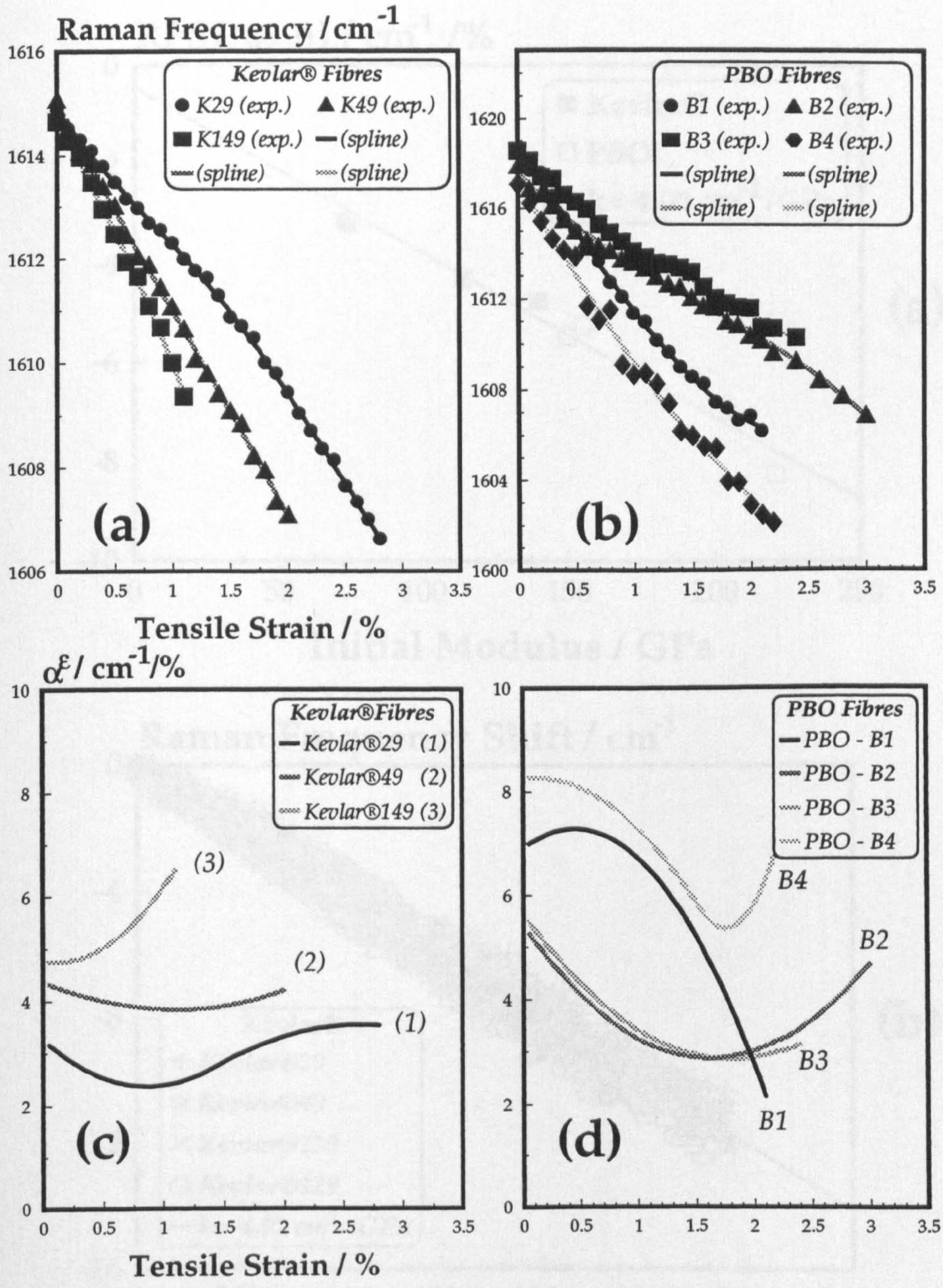

Figure 3.15. Raman frequency-tensile strain and cubic spline fits for (a) Kevlar® and (b) PBO fibres.
Raman frequency strain dependence-tensile strain for (c) Kevlar® and (d) PBO fibres.

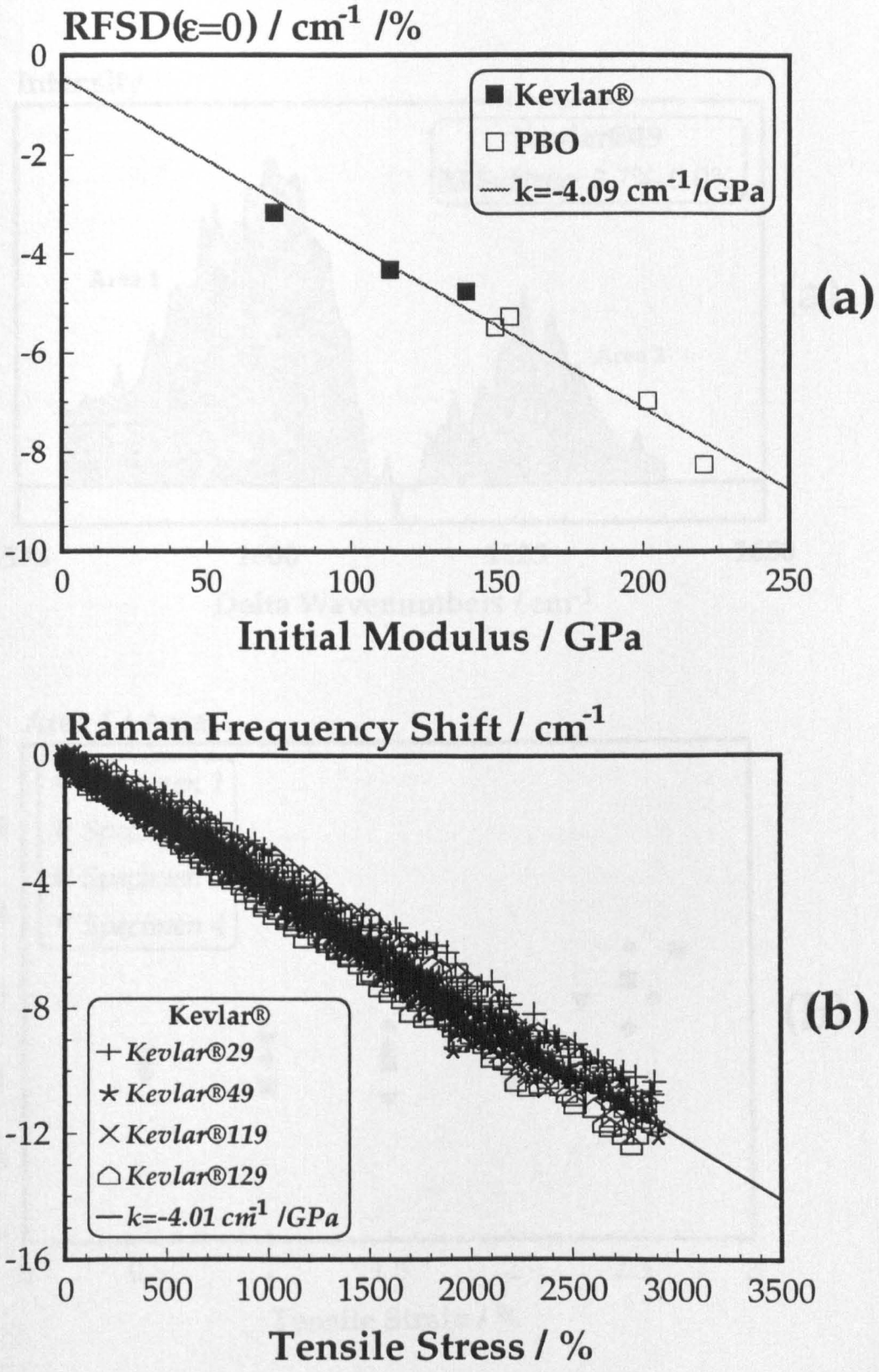

Figure 3.16. (a) Raman frequency strain dependence(ε=0) -initial Young's modulus for Kevlar and PBO fibres (1615 & 1620 cm^{-1} vibrational modes).
(b) Raman frequency shift-tensile stress for aramid fibres.

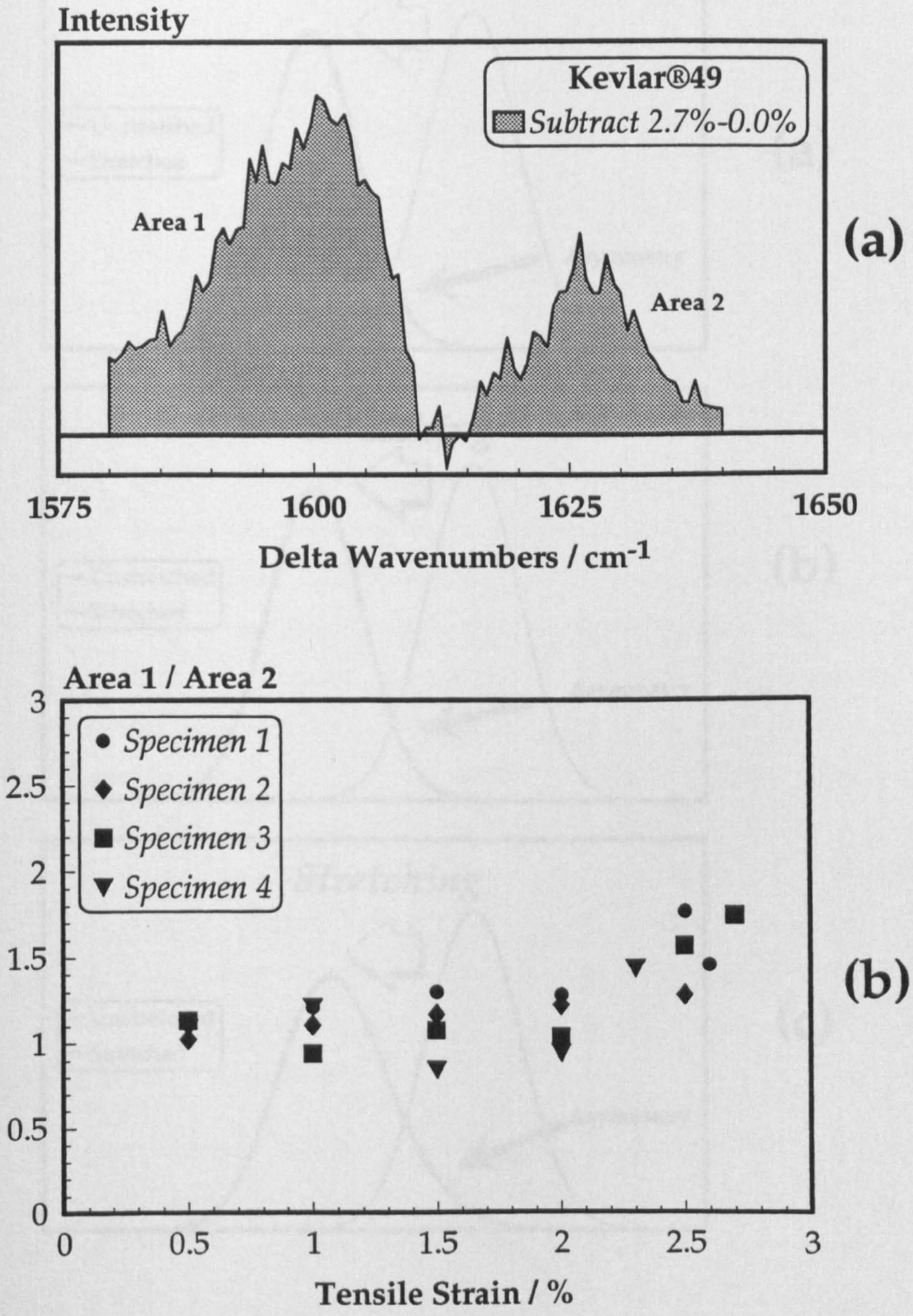

Figure 3.17. (a) Subtraction of Raman frequency (1615cm^{-1}) distributions (2.7%-0.0%). (b) Area ratio-tensile strain for Kevlar®49 fibre.

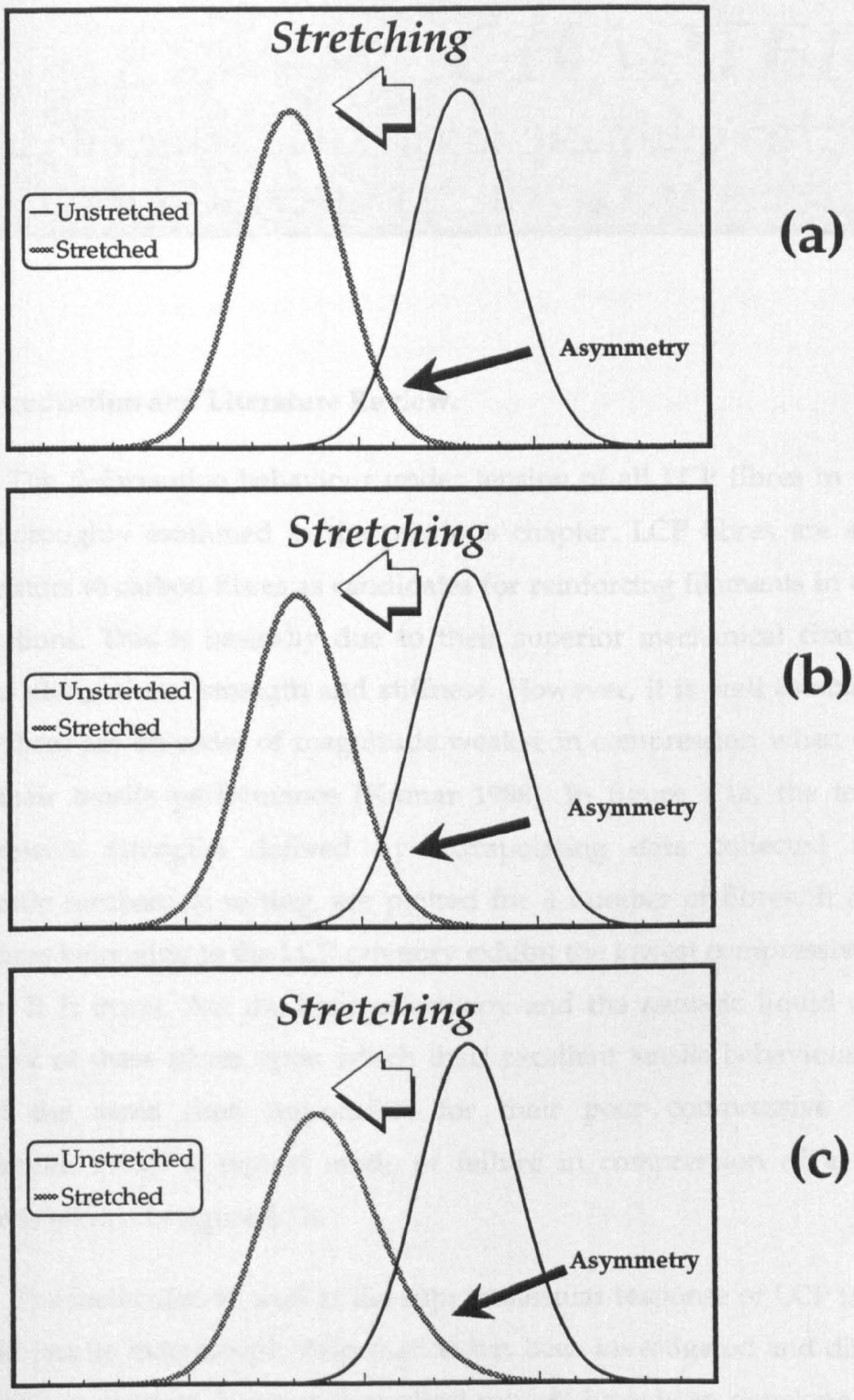

Figure 3.18. Comparison of frequency distributions (stretched and unstretched state). (a) low, (b) medium and (c) large Raman frequency stess dependence (model).

CHAPTER 4:
MECHANICAL BEHAVIOUR OF LIQUID CRYSTAL POLYMER FIBRES IN TENSION & COMPRESSION

4.1. Introduction and Literature Review.

The deformation behaviour under tension of all LCP fibres in this work was thoroughly examined in the previous chapter. LCP fibres are significant competitors to carbon fibres as candidates for reinforcing filaments in composite applications. This is basically due to their superior mechanical characteristics such as elongational strength and stiffness. However, it is well established that these fibres are an order of magnitude weaker in compression when compared with their tensile performance [**Kumar 1988**]. In figure 4.1a, the tensile and compressive strengths derived by extrapolating data collected from full composite mechanical testing, are plotted for a number of fibres. It is obvious that fibres belonging to the LCP category exhibit the lowest compressive strength values. It is ironic that the high anisotropy and the nematic liquid crystalline character of these fibres upon which their excellent tensile behaviour is based, are at the same time responsible for their poor compressive behaviour [**Wierschke 1992**]. A typical mode of failure in compression of a composite system is shown in figure 4.1b.

The molecular, as well as the supramolecular response of LCP fibres to an applied tensile macroscopic deformation has been investigated and discussed in the previous chapter. Various theoretical models have been developed in order to interpret the non-linear tensile behaviour of LCP fibres and these models are in good agreement with the experimental results. On the other hand, very little has been done towards understanding the response of these fibres to an applied compressive deformation. This is due to the lack of a method which could

unambiguously assess the relationship between macroscopic stress field and molecular structure.

In general, work already in the literature can be classified into two categories: (i) measurements of the critical compressive stress or strain to failure of these fibres and (ii) investigations into the mode of failure in compression. The tests used in category (i) are usually unable to measure the compressive strength or strain to failure directly. These parameters are estimated by using assumptions about the loading condition and deformation process. These tests include *the elastica loop test* **[Sinclair 1950]**, **[Jones 1971]**, **[Greenwood 1974]**, *the embedded fibre method* **[Hawthorne 1975]**, **[Jahankhani 1988]**, **[Van der Zwaag 1988]**, **[Young 1992]**, *the recoil test* **[Allen 1987]**, **[Dobb 1990]**, **[McGarry 1991]**, *the bending beam method* **[DeTeresa 1988]** and *the microcompression method* **[Macturk 1990]**.

In the *elastica loop test* a loop is induced in a fibre which is trapped in an oil immersion between two microscope slides. By pulling the two ends of the fibre, the loop is reduced gradually in size. In theory, the ratio of major to minor axis should stay constant and equal to 1.34 as long as the fibre behaves elastically **[Jones 1971]**. At a certain stage the loop starts to become narrower and the ratio increases. A decrease in the radius of curvature at the head of the loop occurs and therefore non-Hookean behaviour takes place. The critical strain above which plastic deformation is initiated, can be determined. The basic disadvantages of the above method are the following:

- the difficulty in pulling such thin fibres;
- the introduction of bending curvatures due to mishandling;
- the difficulty in assessing the mode of failure;
- the fact that only strain to failure measurements can be calculated.

The *embedded fibre method* is normally performed by incorporating single fibres in a polymer matrix and subsequently compressing the bulk specimens parallel to the fibre axis up to a level at which fibre failure is detected by means

of conventional optical microscopy or LRS [**Jahankhani 1988**]. Improvements to this method in particular to the measurements of the applied compressive strain in the vicinity of the fibre have been proposed [**Van der Zwaag 1988**]. The method is extremely sensitive to fibre alignment and interfacial adhesion. Also, only strain to failure measurements can be provided.

In the *recoil test* a uniaxial compressive stress is assumed to be imparted to a filament by imposing 'snap-back' forces after controlled tensile failure. This test is extremely sensitive to the experimental conditions and some experimental evidence implies that the moving stress wave may not be uniaxial and, hence may affect the mode of compressive failure[**Dobb 1990**].

The *bending beam method* involves the application of well defined and uniform compressive strains to single filaments by bonding them to the compressive side of an elastic rectangular transparent polymer beam. On subjecting the beam with bonded fibres to either three-point or cantilever bending configuration, compressive (or tensile) strain gradients are set up along the length of the beam. In this manner the compressive strain to failure can be determined from the equations of the beam theory of elasticity.

The *microcompression method* is the most recent attempt to measure directly the response of a fibre to an applied compressive stress. It is doubtful though, whether this method can produce accurate values of stresses and strains in the fibre because of limitations in experimentation and the influence of severe end-effects arising from the extremely small gauge lengths employed during testing.

The methods belonging to category (ii) yield qualitative results regarding the morphology of failed fibres in compression and usually involve optical or electron microscopy observations. The characteristic mode of compressive failure for most LCP fibres is the formation of kink bands. These kink bands can be as wide as one fibre diameter and can be extended to a maximum length of 2μm [**Takahashi 1983**], [**Martin 1991**]. It is widely considered that kink bands are regions of shear deformation occurring along slip planes which are separated

from the undeformed part of the fibre by sharp localised bending of the macromolecules. Indisputable evidence for the generation of deformation zones during compressive failure of rigid-rod fibres in which a great deal of plastic strain is 'frozen', ie. for the compressive 'yielding' of such rigid structures, has been provided **[Martin 1991]** by means of high-resolution electron microscopy (HREM). Finally, it should be mentioned that kink band formation unlike shear fracture observed in high-modulus carbon fibres, absorbs considerable amounts of energy and therefore serves as a toughening mechanism in a number of military (bullet-proof jackets, helmets etc.) or even medical (surgical gloves etc.) composite applications.

In this chapter, a modified version **[Melanitis 1991]** of the Cantilever Bending Beam (CBB) method **[De Teresa 1988]** is employed for the investigation of LCP fibres behaviour in compression combined with Laser Raman Spectroscopy measurements. The purpose is to subject all LCP fibres involved in this work to a gradient of axial compressive stress and monitor their response with the LRS microprobe. It was shown in the previous chapter that Raman vibrational frequencies shift to lower values under tension, in a well defined manner. Similarly, the Raman vibrational frequencies shift to higher values under compression. Focusing on the same frequencies in tension and compression for all fibres, well defined relationships between Raman frequency shifts ($\Delta\nu \propto \sqrt{F_c} \propto \zeta$, molecular strain, see previous chapter) and applied macroscopic strain ε can be obtained. The only physical requirement is that a smooth transition from compression to tension should be employed. Good estimates of the strain dependence of fibre modulus and of the compression strength can be calculated.

4.2. Experimental.

In the previous chapter an account of the various methods used for performing model mechanical tests on single filaments combined with Laser Raman Spectroscopy was given. The main focus was on the microextensometer (MET) method and its exploitation for tensile testing was demonstrated.

In this chapter, the modified cantilever bending beam (CBB) and four-point bending beam (FBB) methods were extensively used for axial compressive testing and axial cyclic testing respectively. The cyclic testing involves compressive loading/unloading, tensile loading/unloading, compressive/tensile loading and tensile/compressive loading model experiments.

4.2.1. Axial compressive testing.

In general, compressing single filaments especially with very small diameters is not easy. This is due to undesirable instabilities developing at small compressive loads. The modified version **[Melanitis 1991]** of the Cantilever Bending Beam (CBB) Method **[De Teresa 1988]** is applied for axial compressive testing of single filaments and simultaneous monitoring of the alterations occurring in their Raman spectra. The method enables us to subject the specimens to an axial and uniform load. Another advantage of the technique is that it is free of any 'gauge length, effects. However, 'gauge length' in the case of CBB testing, is the integral of all infinitesimaly small (dx) gauge lengths subjected to an assumed uniform loading.

(i) Mechanics of the Cantilever Bending Beam Method (CBB).

A sketch of the CBB jig is shown in figure 4.2a. The filament is bonded to the top surface of the beam and can be subjected to a gradient of applied strain by flexing the beam by means of an adjustable screw positioned at the edge of

the span of the beam. The maximum deflection of the neutral axis of the beam (elastic behaviour), is given by the following equation [**Timoshenko 1961**]:

$$\delta_{max} = \frac{PL^3}{3EI} \tag{4.1}$$

where **P** is the concentrated load applied to the end of the beam, **L** is the span of the beam, **E** is the Young's modulus of the beam material and **I** is the moment of inertia of the beam cross-section.

The deflection δ_{max} can be measured accurately using a dial gauge micrometer attached to the top surface of the beam. The mechanical strain as a function of the location (x,y) is given by:

$$\varepsilon(x,y) = \frac{M(x).y}{EI} \tag{4.2}$$

where **M(x)** is the bending moment along the beam, **x** the horizontal coordinate (distance from fixed end) and **y** the vertical coordinate (distance from neutral axis). In this case, the mechanical strain at the top surface of the beam (i.e. $y = \frac{t}{2}$) and, hence in the fibre, can be derived:

$$\varepsilon\left(x, \frac{t}{2}\right) = \frac{PLt\left(1-\frac{x}{L}\right)}{2EI} \tag{4.3}$$

By substituting equation 4.1 into 4.3, the strain in the fibre as a function of the position x ($0 \le x \le L$) along the beam span can be estimated by:

$$\varepsilon_f(x) = \frac{3t\delta_{max}}{2L^2}\left(1-\frac{x}{L}\right) \tag{4.4}$$

where L is the cantilever beam span, δ_{max} is the maximum deflection of the beam (at the free end) and t is the beam thickness.

For the above equation to be valid, the span to maximum deflection aspect ratio should be greater than 10 [**Timoshenko 1961**]. The mechanical behaviour of the beam material in tension and compression should be linear within the strain range of the experiment which is usually from -1.5% to +1.5%.

(ii) Specimen Preparation.

The main requirements for the beam are: (a) suitable mechanical behaviour for the above experimental conditions (deflections inducing maximum strain up to 1.5% were possible without yielding of the material [**Tetlow 1990**]) and (b) Raman spectrum not interfering with the Raman bands of the materials under investigation [**Melanitis 1991**]. The material which was chosen for beam preparation was a commercial PMMA product (Perspex™) supplied in rectangular sheets by ICI. The material was chosen above other flexible commercial products. Rectangular bars 80mm in length and with a cross sectional area of 10mm wide by 6 mm thick were cut from the sheets. The span of the beam was 50mm and the free length of 30mm was used to secure clamping.

The filaments separated from the yarn were carefully examined under a conventional microscope for any visible defects. The selected filaments were positioned lengthwise on the top surface of the beam (maximum two or three filaments per beam) and approximately in the centre. Extreme care was taken to align the filaments in the direction of the x-axis of the beam. Random Raman spectra were collected from all specimens before the bonding operation. These spectra were compared with spectra obtained from stress-free filaments in air to ascertain any load induced by handling. In order to secure the filaments to the top surface of the beams, they were sprayed evenly with a layer of a transparent acrylic adhesive (Krylon™). The thickness of the film was never more than two or three times the filament's diameter to avoid alterations to the geometry of the beam. The specimens were kept in an environmental chamber allowing the film

to set and dry gradually prior to the experiment. A second Raman scan was performed so samples with contained residual stresses due to film shrinkage were discarded.

(iii) Experimental Procedure.

The specimen is clamped carefully by means of a simple arrangement using four heavy duty screws. The beam is then deflected upwards by sufficient δ_{max}, to achieve the desired maximum value of applied strain ε_{max} at the fixed end, according to the formula (equation 4.4 for x=0):

$$\delta_{max} = \frac{2L^2\varepsilon_{max}}{3t} \tag{4.5}$$

The encapsulated filaments on the top surface of the beam are fixed in position after incremental loading. In fact, each infinitesimal length **dx** of the sample is under compressive strain equal to **dε**. Thus, by integrating, a gradient of macroscopic compressive strain is applied along the fibre length (zero strain at the free end and maximum strain at the fixed end) as shown in figure 4.2a. The whole device is positioned on the experimental stage of the Raman microscope. A detailed point to point examination of the fibres under load is performed by using conventional reflective illumination. Useful videographs can be obtained by means of a videoprinter connected to the microscope. The Raman monitoring can be conducted concurrently with the conventional optical examination. Acquisition of Raman spectra is obtained along the fibre length at steps of 0.25 to 1.00 mm (0.0075-0.0300 % strain steps). This procedure enables us to monitor the compressive behaviour of the fibre at molecular level with great precision.

4.2.2. Cyclic Compressive Testing.

(i) Mechanics of the Four-point Bending Beam Method (FBB).

A different loading configuration is applied for cycling loading in compression. This is the so called Four-point Bending Beam (FBB) Method, the experimental setup of which is shown in figure 4.2b. As can be seen, the beam is supported on two fixed rollers which define the outer span of the beam. A second set of rollers positioned in between are free to move up or down by means of a lever-type mechanism. These rollers define the inner span of the beam. The top surface of the beam in the inner span can be subjected to a uniform compressive or even tensile load. This is the fundamental difference between the CBB Method and the FBB Method: The fibre is subjected to a gradient of applied macroscopic strain in the fist case and a uniform applied macroscopic strain in the second case.

The specimen preparation and testing follows a similar pattern to that of the CBB Method. Single filaments are aligned along the axis of the beam in the middle of its span and sprayed with the acrylic adhesive. A strain gauge is adhered to the top surface of the beam for immediate reading of the strain field applied to the fibres. A typical calibration curve for monitoring the strain on the fibre encapsulated in the thin acrylic film is shown in figure A3.1a in Appendix 3. The indication of the strain gauge (i.e. resistance ΔR which is proportional to strain) is plotted as a function of the maximum deflection. It is important that the beam behaves elastically within a prescribed range of applied strains from 1.5% compressive to 1.5% tensile values.

Raman spectra from random points along the filaments are obtained before an increment of strain is applied to the beam. This procedure continued up to a certain strain level and then the reverse operation followed; a gradual release of the applied compressive strain is allowed gradually by strain steps equal to those during the loading procedure. The above operation can be repeated.

4.3. Results.

4.3.1. Monitoring the Raman frequency strain sensitivity of LCP fibres in compression.

The procedure employed to obtain Raman spectra during compressive deformation of LCP fibres at equal steps along the sample starting at x=L where $\varepsilon_f(x=L)=0$ and ending at x=0 where $\varepsilon_f(x=0)=\varepsilon_{max}$ was described in the previous section.

Typical graphs were produced by plotting the Raman frequency shift as a function of the applied compressive strain. The Raman frequency shift (plotted on the y-axis) was simply calculated by subtracting the average frequency value of the corresponding stress-free fibre in air from that of the embedded fibre. The compressive strain is calculated point-by-point along the fibre length as follows (N is the total number of measurements):

$$\varepsilon(x_n)=\varepsilon(x_{n-1})+\frac{\varepsilon_{max}}{N} \tag{4.6}$$

where, $x_n=x_{n-1}+\frac{L}{N}$ starting from $x_0=0$ and continuing for $n=1,2,\ldots N$.

The Raman frequency shift versus compressive strain graphs for Kevlar®,heat treated Kevlar®, PBZT and PBO fibres examined in this work are shown in figures 4.3-4.5. Examining the behaviour of all fibres it can be seen that the Raman frequency shift increases with applied compressive strain up to a critical threshold value. Conventional observations with the Raman microscope showed that this value corresponds to the critical compressive strain to failure for each type of fibre. Typical kinkband formation visible on the filaments was always seen after this value was reached (figures 4.3d and 4.4d). After the plateau, the fibre exhibits one of the following trends: either (i) a slight drop of the Raman frequency and then a fluctuation around a constant value as in

Kevlar® 29, 49 & 149 and PBO-B1 or (ii) a fluctuation around a maximum or almost maximum value, as in Kevlar® ht1&2, PBZT-Z1 and PBO-B2, B3 & B4.

In the case of the 'semi rigid-rod' aramid fibres (Kevlar®), the Raman frequency shift versus compressive strain behaviour prior to the critical compressive strain to failure, is strongly non-linear. The deviation from linearity is more prominent in the case of Kevlar® 29, less for Kevlar® 49 and even less for Kevlar® 149. On the contrary, the heat treated Kevlar® 49 fibres (1420d and 2160d) exhibit minimal non-linearity.

The 'rigid-rod' heterocyclic polymer fibres such as PBZT and PBO, on the other hand, show a more linear response to compressive deformation prior to compressive failure. In the post-failure region the formation of a plateau is typical. In fact, the higher the tangent tensile modulus the lower the critical compressive strain to failure for all LCP fibres, as can be seen in figure 4.6a. The experimental data associated with the aramid (semi-rigid rod structure) fibres and heterocyclic polymer (rigid-rod structure) fibres are summarised in this figure. No significant improvements as far as critical compressive strain to failure is concerned are observed in the case of the heat-treated Kevlar® fibres. The values are very similar to the critical compressive strain to failure observed for Kevlar® 49 fibre.

Examples of typical compressive failure modes for LCP fibres are illustrated in figures 4.3d (Kevlar® 49) and 4.4d (PBZT-Z1). In these illustrations clear kinkband formation is shown, observed locally at angles of approximately 45-50°. Extensive work described in the literature **[Martin 1991]** has dealt with the molecular mechanisms involved in this type of failure. A model for kink formation according to observations made in that work is illustrated in figure 4.6b. A comparison of findings in this work with observations reported in the literature will be given in the discussion section.

4.3.2. Monitoring the Raman frequency strain sensitivity of LCP fibres in tension and compression.

As mentioned earlier, the CBB technique for subjecting single filaments to an axial compressive gradient scan is also employed to subject single filaments to tension [**Melanitis 1991**]. This can be achieved easily by reversing the direction of deflection δ_{max} (i.e. downwards, see figure 4.2a). The monitoring of the Raman frequency as a function of the position **x** and therefore the tensile strain (the equations 4.6 and 4.7 can be used since they are still valid for tensile configuration) is done in a similar way to compression monitoring. This gives us the opportunity to compare the results obtained with those produced with the MET method in order to assess the validity of the CBB method.

Such a comparison is demonstrated for Kevlar® 49 fibre in figure A3.3 in the Appendix 3. The Raman frequency shift versus tensile strain is plotted for data obtained via MET and CBB up to 1.0% applied strain. It is apparent that within experimental error, there is no significant difference between the two sets of data. This verifies the validity of the CBB equations and also the experimental procedure used for aligning and bonding the fibres onto the surface of the beam.

Another important issue concerning CBB testing is the possibility of slippage between the fibre and the beam due to the strain gradient loading configuration. This was examined using the FBB method for a number of fibres. The advantage of the FBB method is uniform loading between inner loading points, as described in the experimental section. The results are presented in figure A3.2 also in Appendix 3. As can be seen quite clearly, both configurations yield identical data, within the experimental error, for all fibres.

By combining the experimental data obtained with the CBB technique both in tension and compression, a universal spectromechanical 'picture' of Raman frequency shift versus applied strain has been produced. Such graphs are shown in figures 4.7, 4.9 and 4.10 for all LCP fibres studied. The variation of the FWHM with macroscopic applied strain is given in figures 4.8, and 4.11. For the

first set of measurements ($\Delta\nu-\varepsilon$ data), the Raman frequency shifts to higher values with compressive strain and to lower values with tensile strain. For the second set of measurements (FWHM-ε data), the bandwidth does not change with the increase of the compressive strain and increases as the tensile strain increases. The relation between the FWHM and the tensile strain differs from fibre to fibre, e.g. slow change for Kevlar® 29 and Kevlar® 49 to rapid change for PBO-B1 and B2.

In order to derive mathematical expressions for the Raman frequency shift versus applied strain, cubic spline functions were used. Similar numerical approximations were employed for data presented in the previous chapter. The cubic spline interpolation was found more satisfactory compared to polynomial interpolations. The latter cannot describe successfully the non-linear behaviour of LCP fibres in tension and compression.

4.3.3. Monitoring the Raman frequency strain sensitivity of LCP fibres in compression by loading and unloading.

The fundamental difference between the CBB and FBB methods is the stress field along the span of the beam and consequently the induced stresses in the fibre. The uniformity of the stress field along the middle span of the beam in the FBB configuration, allows the gradual deformation of single filaments in compression (or tension) up to a certain stress level followed by a reversal of the applied load in the same manner. During the above procedure the Raman spectra of the fibre can be obtained at equal steps of loading and unloading. Therefore, the Raman frequency shift versus the macroscopic applied compressive (or tensile) strain, measured with the strain gauge were monitored for the whole cycle. Second or even third cycles of deformation were also introduced.

In our case, two types of experiments were performed: (a) The specimens were loaded up to the threshold value of the critical compressive strain to failure, without allowing failure to occur. Subsequently, the applied load was removed gradually at equal steps. The samples were loaded again up to the same level for a second time. (b) The specimens were loaded further than the threshold value of the critical compressive failure allowing kinkband formation. Similarly to the first case, the compressive load was removed gradually and a second loading was introduced. The results are shown in figures 4.12a (Kevlar® 29 for type *'a'* experiment) and 4.12b (Kevlar® 49 for type *'b'* experiment).

As can be seen by the hysteresis in loading/unloading, the deformation of aramid fibres is non-Hookean. A recovery of the fibre was observed in both cases. Kinkbands observed in the second case at the end of the first loading disappear after the total stress removal and reappear after the second loading cycle. A permanent amount of approximately 0.3% residual strain was observed in both cases of Kevlar® 49 and Kevlar® 29, which is evidence of the elastoplastic nature of the deformation of aramid (and other polymeric) fibres in compression.

4.4. Discussion.

4.4.1. Characterisation of LCP fibres in tension and compression.

In the previous chapter a thorough investigation of the behaviour of LCP fibres under tensile deformation was examined. The semi-empirical models introduced such as the aggregate structure model **[Northolt 1980]** and the pleat structure model **[Allen 1989]** were applied and the results obtained were in good agreement with the experimental data. Both models were based on the assumption that the total axial deformation ε_{total} induced by a macroscopic stress field σ is made up of the elastoplastic deformation component $\varepsilon^{elastoplastic}$ and the plastic deformation component $\varepsilon^{plastic}$. The Raman frequency shift $\Delta\nu$ for a given

backbone vibrational mode is attributed only to the deformation of covalent bonds along the chain and therefore directly related to the elastoplastic component and not affected by rotational or shearing motions associated with the pure plastic component. On the other hand, the FWHM increase with increase of the applied macroscopic strain is associated with the non-uniform stress distribution (stress gradient) as shown in the previous chapter.

In a similar fashion to equation 3.23 for tensile deformations, we can introduce the following equation for compressive deformations:

$$\varepsilon_{total} = \varepsilon^{elastoplastic}_{compression} + \varepsilon^{plastic}_{rotation} \tag{4.7}$$

The first component is responsible for frequency shift to higher values with increase of the applied compressive strain and the second component is not 'visible' by Raman spectroscopy. The fact that values of the vibrational frequencies do shift to higher values confirms that the actual compressive deformation occurs at molecular level (C-C bonds, phenyl group, heterocyclic group are compressed), induced by the macroscopic stress field. On the other hand, the observation of no changes of the band widths for all fibres in compression, provides us with an indication that rotational phenomena of the crystallites are insignificant compared to, possibly, their dramatic molecular collapse. In tension, an initial 'interlocking' of crystallites by shear is followed by synergistic crystallite rotation and strain hardening phenomena. However, in compression, failure occurs at molecular level, with the crystallites 'frozen' in position and the molecular chains buckle at the backbone C-C linkage bond, which is the more susceptible to compressive deformation **[Wiersche 1992]** and out of plane bending as molecular dynamic calculations have confirmed **[Farmer 1992]**.

For aramid (or other) fibres which can be considered as aggregates of crystallites connected in series, the validity of the argument that Raman frequency shift is proportional to the applied macroscopic stress (equation 3.1)

was proved experimentally (see chapter 3). Equations 3.1 and 3.27 can be rearranged and stress-strain along with modulus strain curves can be derived:

$$\sigma^{pr}(\varepsilon) = \frac{1}{k} f(\varepsilon) \tag{4.8}$$

$$E^{pr}(\varepsilon) = \frac{1}{k} \alpha^{\varepsilon}(\varepsilon) \tag{4.9}$$

where $f(\varepsilon) = \Delta\nu(\varepsilon)$ and $\alpha^{\varepsilon}(\varepsilon) = df(\varepsilon)/d\varepsilon$ is the Raman Frequency Strain Dependence defined in chapter 3 and can be obtained from the strain controlled spectromechanical experiments (conducted by the CBB and FBB methods). This can be achieved by numerical differentiation of the cubic spline functions fitted to the $\Delta\nu - \varepsilon$ experimental data (see Appendix 2). Thus, the above equations enable us to to derive stress and Young's modulus $E(\varepsilon)$ predictions as a function of the macroscopic applied strain ε, compressive and tensile, provided that the constant k and the function $f(\varepsilon)$ are known.

In figures 4.13 and 4.14 the predicted stress-strain and tangent Young's modulus-strain functions are plotted by means of the above method for all Kevlar® fibres, PBZT fibre and PBO fibres examined in this work. The derived stress-strain curves exhibit quite clearly all the prominent characteristics of the macroscopic deformation of LCP fibres. These are superior strength and stiffness in tension and Young's modulus softening in compression followed by abrupt 'yielding' at relatively low strain values.

The modulus softening in compression is a unique feature for all LCP fibres examined in this work. In fact, if we extrapolate again the Northolt and Allen models in compression, stress-strain and modulus-strain curves can be derived, as can be seen in figure 4.15 for aramid fibres. The models succesfully predict modulus softening in compression. In fact, these models, predict a smooth softening behaviour in compression compared with the abrupt modulus drop to zero at small compressive strains which has been found in this work (see

figures 4.13 and 4.14). This result also verifies our initial argument that crystallite rotation occurs at a very minimal level.

An examination of the stress-strain behaviour of Kevlar® fibres reveals that the Young's modulus at zero strain follows the expected sequence $E_0^{K29} < E_0^{K49} < E_0^{K149}$ which is clearly valid in tension. However, in spite of their differences in terms of initial Young's modulus in compression, all aramid fibres fail by kinking when a compressive stress of about 300 MPa is reached. The annealing process (heat treated fibres) seems to alter the strain dependence of the macroscopic modulus but affects only marginally the stress-strain behaviour in compression.

Finally, the PBZT-Z1 and PBO-B1 & PBO-B4 heat treated fibres exhibit a similar type of stress-strain behaviour to that of the aramid fibres but higher values of stiffness. The as spun PBO fibres (B2 and B3) exhibit modulus softening in tension up to a critical value of strain, in agreement with results from conventional stress-strain measurements (see chapter 3). Again, similarly to aramid fibres and despite their different behaviour in tension, PBO fibres fail at relatively low values of applied compressive strain (values similar to Kevlar® 149 and significantly lower to Kevlar® 49 and Kevlar® 29). It seems from these results that any further increase in the crystallite orientation (indicated by the increase in the initial Young's modulus, see figure 4.7a), results in no further improvement in the maximum value of compressive molecular deformation prior to yielding.

In the case of commercial aramid fibres a dramatic drop of the tangent Young's modulus is observed in compression whereas a strain hardening effect is obtained at strains higher than approximately 0.5%. With the exception of Kevlar® 149 the observed behaviour in tension looks similar to the results obtained from conventional stress-strain data presented in the previous chapter and also work by Allen [**Allen 1989**]. An initial drop of modulus at about 0.05% strain is followed by a modulus increase at higher strains. Indeed, if we consider

the fibre as a chain of crystallites slightly misoriented with respect to the fibre axis (see previous chapter), the application of a tensile load will tend to align the crystallites in the loading direction. On the other hand, the application of compressive load should align the crystallites normal to the loading direction. Simultaneously, axial compressive load induced in each individual crystallite will result in axial compression of the packed molecular chains in it with the backbone C-C linkage bond (between the heterocyclic moiety and the phenyl ring for PBZT and PBO or between phenyl rings for Kevlar®) more susceptible to length decrease [**Wiersche 1992**]. Therefore, failure in compression is predominantly controlled by the molecular morphology of these fibres which in spite of their rigid-rod structure are very flexible and out-of-plane bending motions are permitted. Compressive failure is also dependent on chain length distributions [**Farmer 1993**]. Following the supramolecular model, the strain-hardening effect in tension corresponds to the opening-up of the pleated structure in response to tensile deformation higher than 0.5% strain. By contrast, the heat treated Kevlar® fibres (figure 4.13d) do not exhibit the initial drop of tensile modulus observed in the commercial Kevlar® and, furthermore, show a lower rate of modulus increase with strain.

The heterocyclic polymer fibres PBZT-Z1 and heat treated PBO-B1 & PBO-B4 fibres also exhibit pronounced strain-hardening in tension as a result of their microfibrillar structure as shown in figures 4.14b and 4.14d, respectively. As expected, the opposite phenomenon occurs for the as spun PBO fibres (B2 and B3) with initial strain softening, up to approximately 1.2% applied tensile strain. This was attributed to the existence of internal residual stresses as discussed previously [**Allen 1981a**]. Mechanical stress-strain and modulus-strain data showed that strain hardening phenomena take over above this critical value of tensile strain. All compressive mechanical data of LCP fibres are summarised in table 4.1.

FIBRE TYPE	Young's Modulus* E_0 / GPa	Compressive strain to failure ε_c / %	Compressive Strength σ_c / MPa
Kevlar®			
Kevlar®29	70±10	0.75±0.05	304±45
Kevlar®49	110±10	0.55±0.05	362±40
Kevlar®149	140±15	0.30±0.10	281±60
Kevlar®49 ht1	110±10	0.60±0.05	373±30
Kevlar®49 ht2	110±10	0.60±0.05	469±30
PBZT			
Z1	240±20	0.35±0.05	575±40
PBO			
PBO - B1	205±10	0.28±0.04	372±40
PBO - B2	155±15	0.40±0.05	357±40
PBO - B3	150±15	0.37±0.05	360±40
PBO - B4	220±15	0.32±0.06	400±40

*Initial Young's modulus.

Table 4.1: *Compressive mechanical data of LCP fibres.*

In figure 4.16 the estimated values of compressive strength σ_c are plotted as a function of the initial (tangent) Young's modulus E_0 for all LCP fibres studied in this work. The actual corresponding values of compressive strength for each fibre are listed in table 4.1. As can be seen, all commercial aramid fibres fail within experimental error at a compressive stress of about 300 MPa. The

annealing process performed on the heat treated fibres (ht1 & ht2) seems to result in a moderate improvement in the compressive strength of the 2160d fibre and does not affect the compressive strength of the 1420d fibre. It is not clear if the improvement in the 2160d fibre is due to its size or to dramatic changes in the morphology/structure of the fibres as a result of the heat treatment. The improvement in stiffness of PBO fibres has a very small effect on the value of compressive strength. As can be seen in the above figure, only a small increase is achieved with the minimisation of misorientation (from fibre B3 to fibre B4). The high value derived for the PBZT fibre is higher than values obtained in the literature, although a wide range of fluctuation of the data reported is seen due to the different nature of the various experimental methods employed.

4.4.2. Mechanisms of compression failure in LCP fibres.

Various semi-empirical models have been employed in the past for predicting the compressive strength of composite materials. The similarities between fibre composites and oriented polymer fibres in terms of mechanisms of failure in compression make these models suitable to explain the failure mechanisms of LCP fibres. The first study examining the compressive failure of various composite materials was presented in the early 1960's **[Rosen 1964]**. This model treats the mechanism of failure as an *elastic bending/microbuckling* phenomenon. The critical stress for compression failure, σ_c is given by:

$$\sigma_c = \frac{G_m}{1 - V_f} \tag{4.10}$$

where G_m is the shear modulus of the matrix and V_f is the fibre volume fraction. The above equation can be interpreted as:

$$\sigma_c = G \tag{4.11}$$

where G is the effective longitudinal shear modulus of the composite **[Budiansky 1993]**.

A different view of the above based on a *plastic microbuckling* treatment of the compressive failure mechanism led to the following formula for the critical compressive stress **[Argon 1972]**:

$$\sigma_c = \frac{\tau_Y}{\bar{\phi}} \tag{4.12}$$

where τ_Y is the composite yield stress in longitudinal shear and $\bar{\phi}$ the initial misalignment angle. Finally, the above equation was modified even further **[Budiansky 1983]** assuming a combined behaviour such as *elastic-perfectly plastic composite* leading to the following:

$$\sigma_c = \frac{\tau_Y}{\gamma_Y + \bar{\phi}} = \frac{G}{1 + \frac{\bar{\phi}}{\gamma_Y}} \tag{4.13}$$

where $\gamma_Y = \frac{\tau_Y}{G}$ is the yield strain in longitudinal shear. It is obvious that equation 4.13 leads to equation 4.11 for $\bar{\phi} = 0$ and asymptotically to equation 4.12 for large values of $\bar{\phi}$. A schematic representation of the above three models is given in figure 4.17.

A theoretical analysis for the onset of kink band formation in rigid or semi-rigid rod fibres in terms of an *elastic buckling of the molecular chains* has been carried out **[DeTeresa 1985,1988]**. A prediction based entirely on Rosen's earlier work for composites **[Rosen 1964]**, predicts that $\sigma_c = G$, where G is now the longitudinal shear modulus of the fibre. Comparison of experimental and predicted values has shown **[DeTeresa 1985]** that this theory overestimates the compressive strength by a factor of 3-4. In fact, it is not coincidental that the

Rosen analysis overpredicts the compressive strength of composites also by a factor of about 4-5 [**Budiansky 1993**]. These findings suggest that for commercial fibres and composites microbuckling is predominantly a plastic rather than elastic event and therefore the Argon/ Budiansky model (equation 4.13) provides a more appropriate basis for analysis.

As argued above, the LCP fibres can be essentially modelled as aggregates of crystallites connected in series. The strain hardening in tension and the corresponding strain-softening in compression can be attributed to axial-shear coupling and associated orientation (or misorientation) of crystallites/pleats in Kevlar® or fibrils in PBZT and PBO. Equally, it is reasonable to assume that the shear instability induced in compression by $\bar{\phi}\rangle 0$ or as suggested elsewhere [**Martin 1991**] by an initial average orientation distribution of the macromolecules $\langle\bar{\phi}\rangle$, will be the predominant mechanism of failure in compression.

In figure 4.18 the present σ_c data for commercial Kevlar® fibres and PBZT, are plotted against G. The values of G for PBZT, Kevlar® 49 and Kevlar® 29 are taken from the literature [**DeTeresa 1985**], whereas the value for Kevlar® 149 has been supplied by Allen [**Allen 1993**]. For the PBZT fibre which exhibits a narrow distribution of orientation angles $\bar{\phi}$ along the fibre direction, a good agreement is obtained for $\bar{\phi}/\gamma_Y$ of approximately 1. For the Kevlar® 29, Kevlar® 49 and Kevlar® 149 fibres the corresponding values of $\bar{\phi}/\gamma_Y$ are approximately 6, 4 and 3, respectively. By setting γ_Y=0.02 for the Kevlar® 49 fibre (onset of non-linear behaviour [**Knoff 1987**]), a misalignment angle $\bar{\phi}$ of 4.5° is obtained which is in good agreement with previously reported values [**Ballou 1976**], [**Dobb 1977**], [**Panar 1983**], [**Allen 1989**]. If we also assume a value of γ_Y=0.02 for Kevlar® 29 and Kevlar® 149 then angles of approximately 7° and 3° are obtained, respectively, which represent quite reasonable estimates for both fibres. The above estimated values in this work, correspond to the breadth of the molecular misorientation

distribution with respect to the fibre axis. The breadth of the crystallite orientation distribution with respect to the fibre axis can be calculated from the experimentally measured misorientation parameter $\langle \sin^2 \phi \rangle$[**Young 1994**]. The results for aramid fibres are shown in the following table:

FIBRE TYPE	Predicted 'molecular' misorientation	Crystallite misorientation [Allen 1989]	Crystallite misorientation [Young 1994]
Kevlar®29	7.0°	6.0°	6.8°
Kevlar®49	4.5°	4.0-5.0°	6.3°
Kevlar®149	3.0°	2.7°	5.8°

Table 4.2: *Misorientation data for aramid fibres.*

It is concluded, therefore, that the inherent weakness of LCP fibres in compression, is a consequence of their instability in shear (low values of γ_Y and G). Hence, any improvements in $\langle \overline{\phi} \rangle$ brought about by means of hot-drawing, are bound to have very little effect upon σ_c.

One important issue which cannot be tackled by the 'macroscopic' approaches expressed by the models of equations 4.11-4.13, is the exact mode of failure at the molecular lever. In tension, failure is normally initiated by chain scission at a local stress concentration site and then propagates in the longitudinal direction. In compression, recent molecular dynamics calculations of 'rigid-rod' macromolecules such as PBZT [**Farmer 1993**], have shown that these molecules have an inherently 'soft' out-of-plane deformation mode even at room-temperature and therefore viewed individually exhibit an almost sinusoidal trajectory. Furthermore, molecular orbital calculations [**Wierschke 1992**] have shown that if a compressive load is imparted to a rigid-rod

macromolecule like PBZT, the C-C bond, phenyl group and heterocyclic moiety are compressed initially, whereas the torsion angle increases twisting the two groups out of planarity. It is worth adding here that the actual compression of the heterocyclic moiety has been experimentally confirmed by the shift of the corresponding Raman vibrational frequency to higher values with increasing compressive strain. When the input compressive energy reaches a threshold value, the molecule begins to bend out-of-plane **[Wierschke 1992]** and the bond lengths cannot be further decreased as confirmed by LRS. Such a molecular 'kinking' occurring locally at low stresses may well trigger the corresponding microscopic kinking of the fibre. The fact that the typical dimensions of a kink in the direction of the fibre axis is smaller than the average length of a rigid-rod molecule **[Martin 1991]** provides further evidence for the existence of a shear-instability phenomenon at a much smaller scale than ever envisaged before.

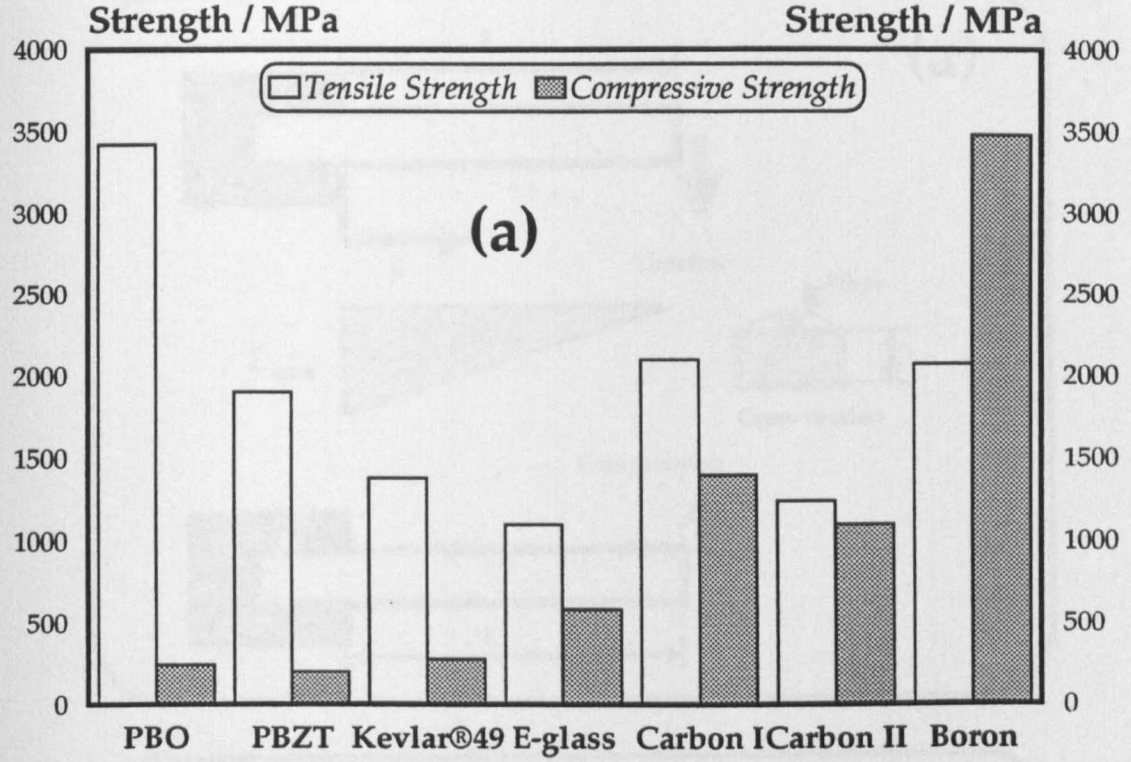

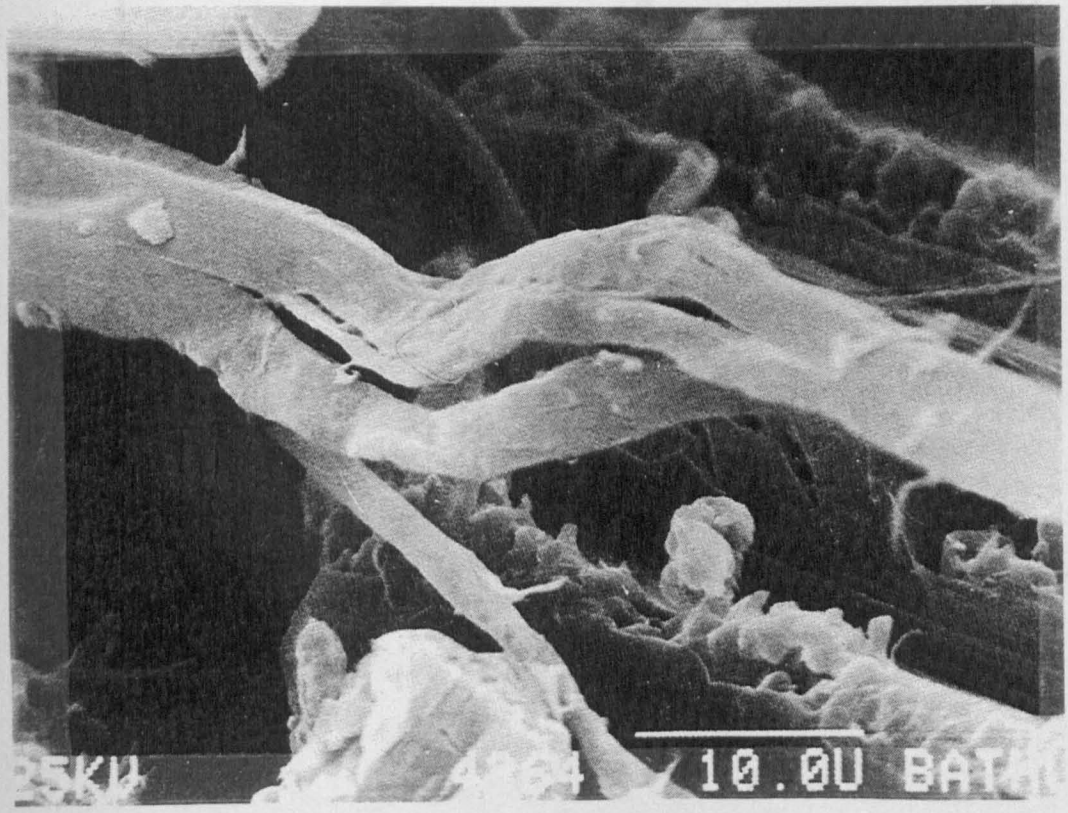

(b)

Figure 4.1. (a) Strength data for various fibres reported in the literature **[Kumar 1988]**.
(b) Compressive failure of Kevlar®49/Epoxy composite **[Harris 1994]**.

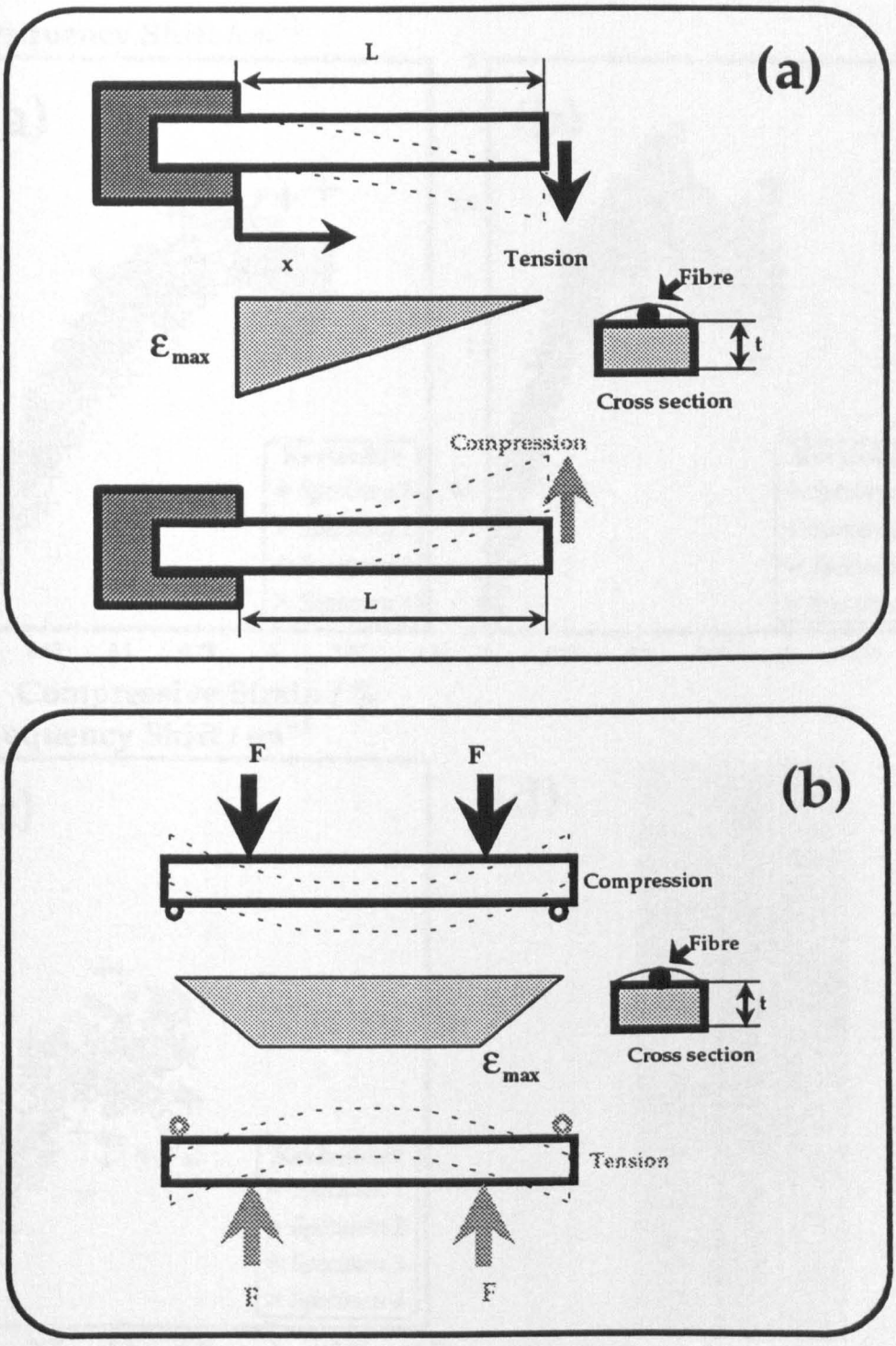

Figure 4.2. (a) Cantilever Bending Beam (CBB) method configuration.
(b) Four-point Bending Beam (FBB) method configuration.

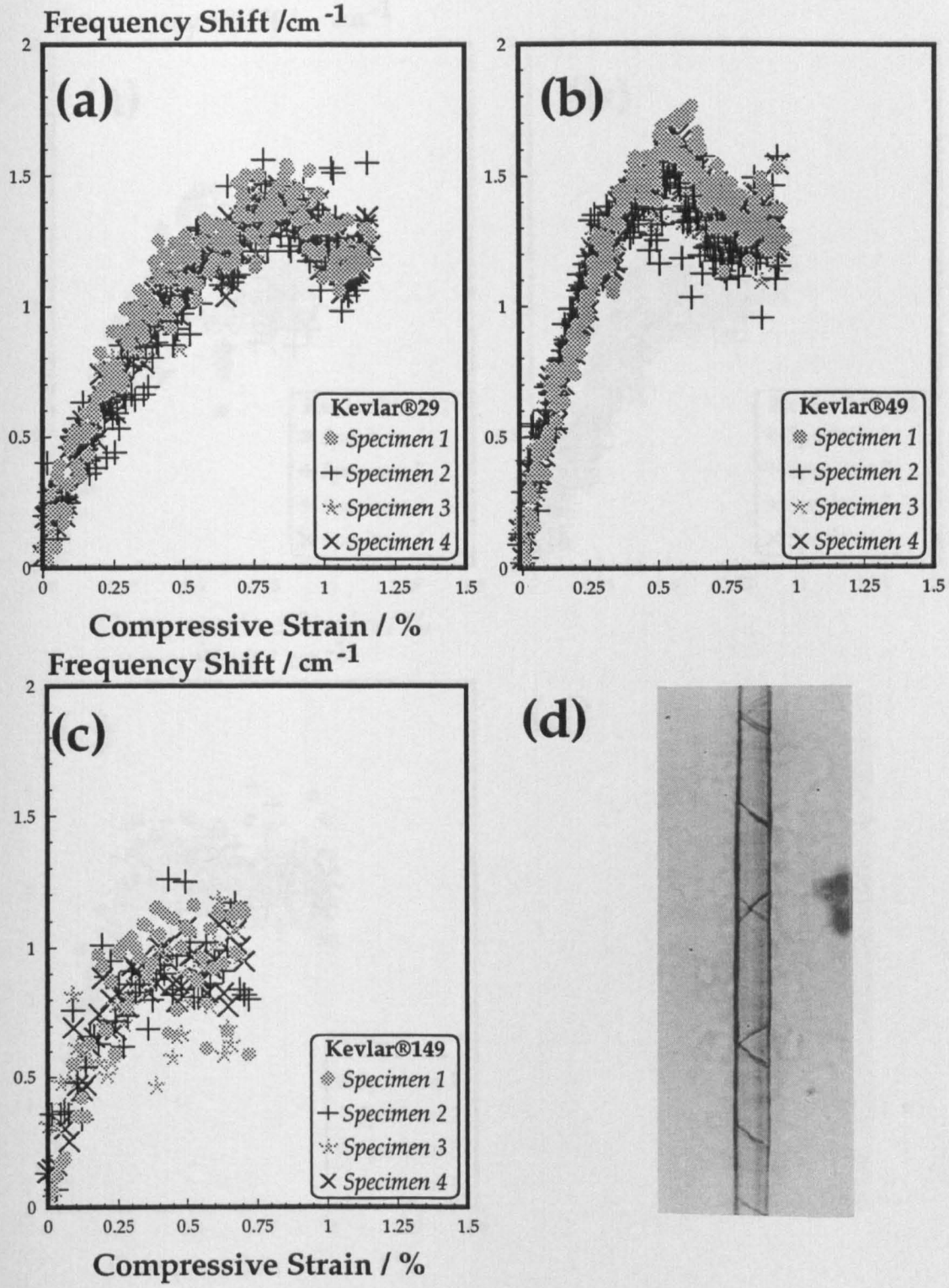

Figure 4.3. Raman frequency shift-compressive strain for:
(a) Kevlar®29, (b) Kevlar®49 and (c) Kevlar®149 fibres.
(d) Failure mode of Kevlar®49 fibre in compression.

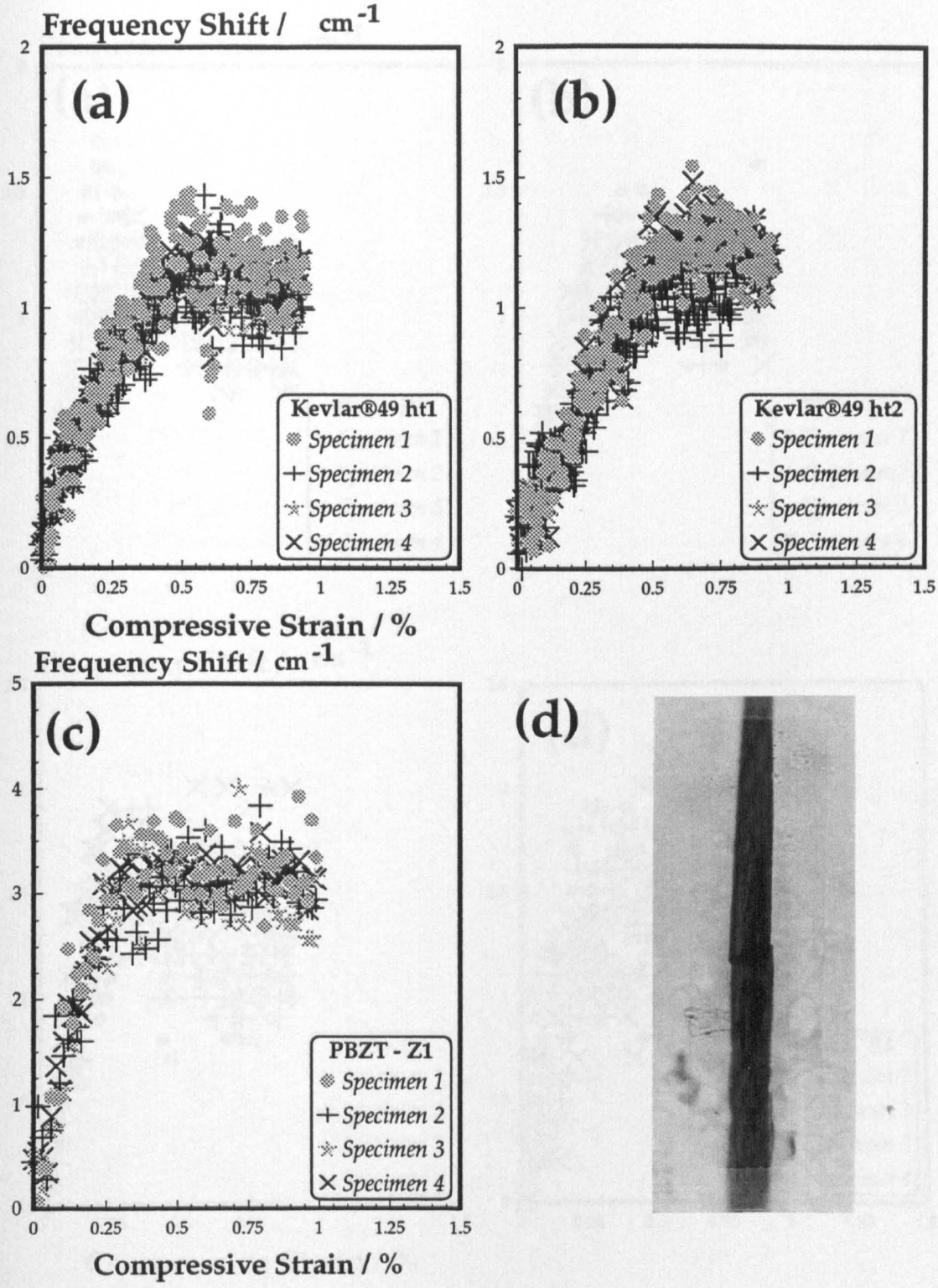

Figure 4.4. Raman frequency shift-compressive strain for:
(a) Kevlar®49 ht1, (b) Kevlar®49 ht2 and (c) PBZT-Z1 fibres.
(d) Failure mode of PBZT-Z1 in compression.

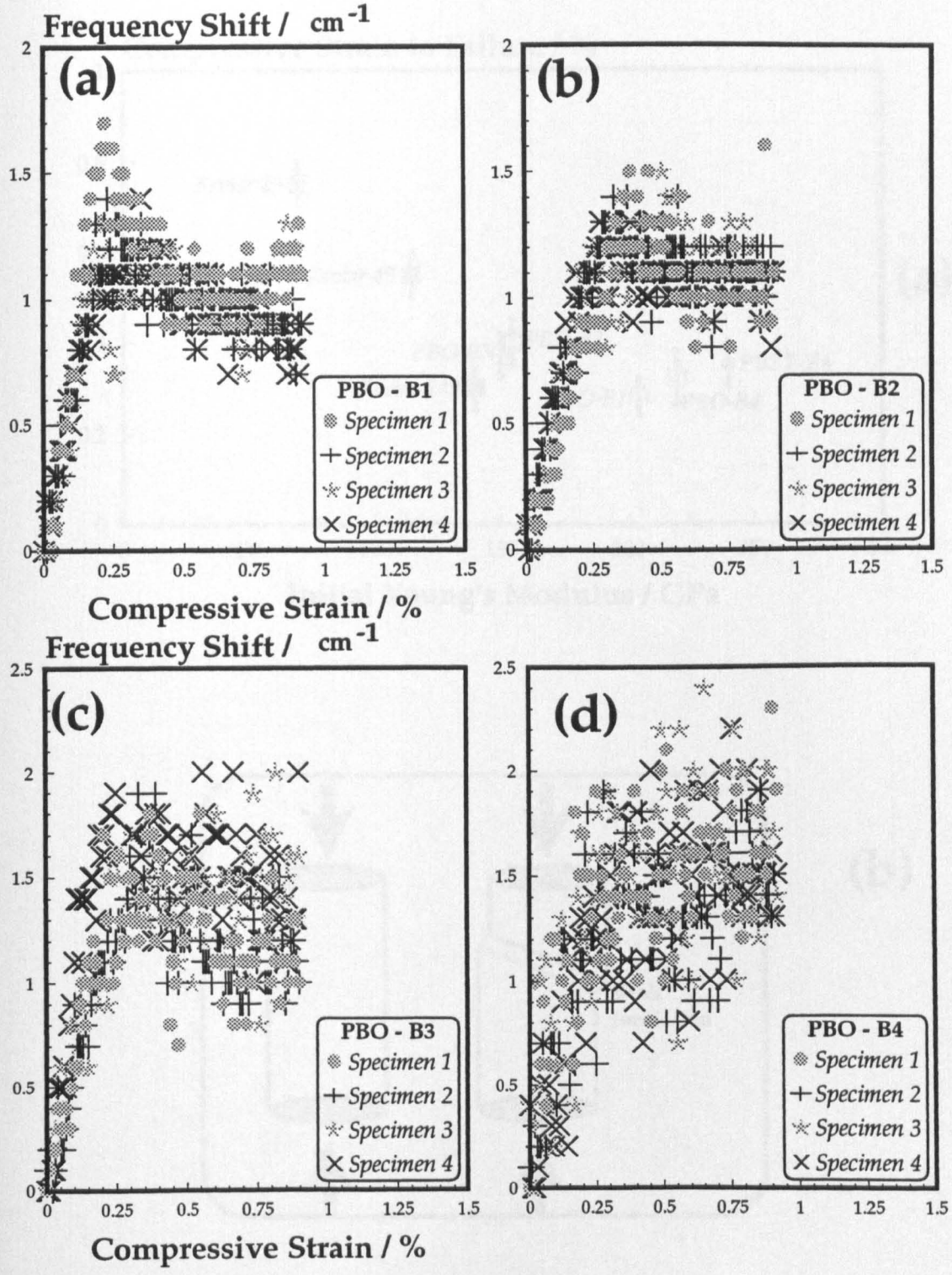

Figure 4.5. Raman frequency shift-compressive strain for:
(a) PBO-B1, (b) PBO-B2, (c) PBO-B3 and (d) PBO-B4 fibres.

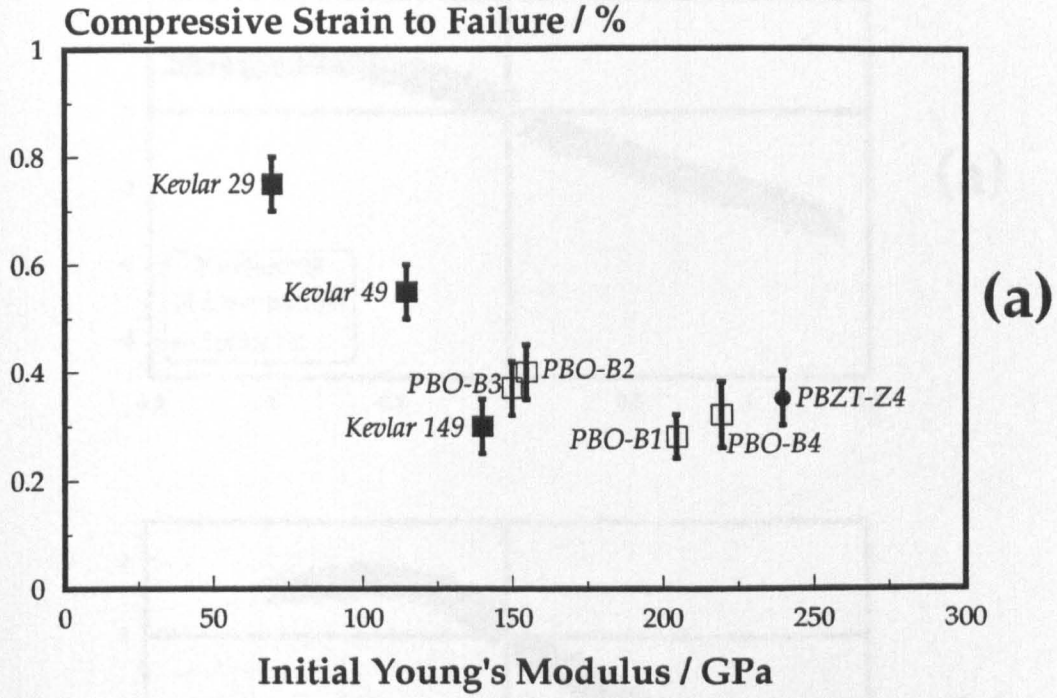

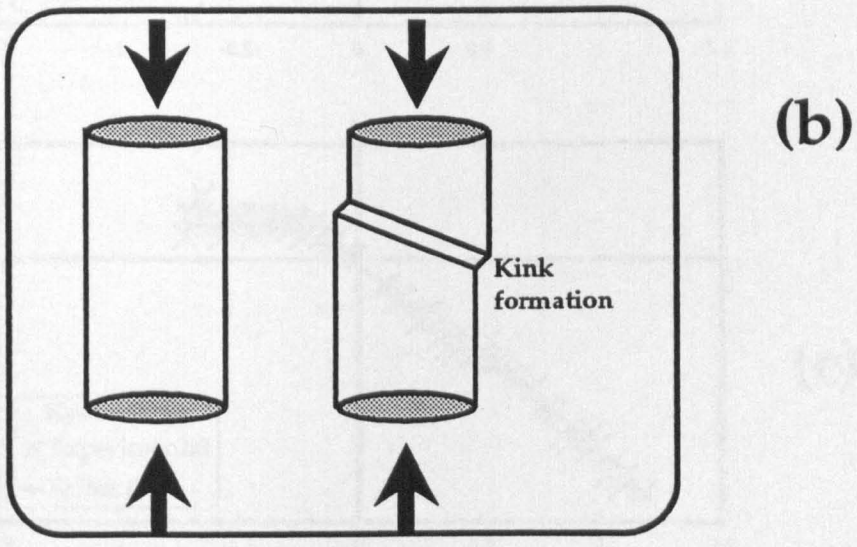

Figure 4.6. (a) Compressive strain to failure-initial Young's modulus data for all fibres. (b) Schematic representation of kink band formation.

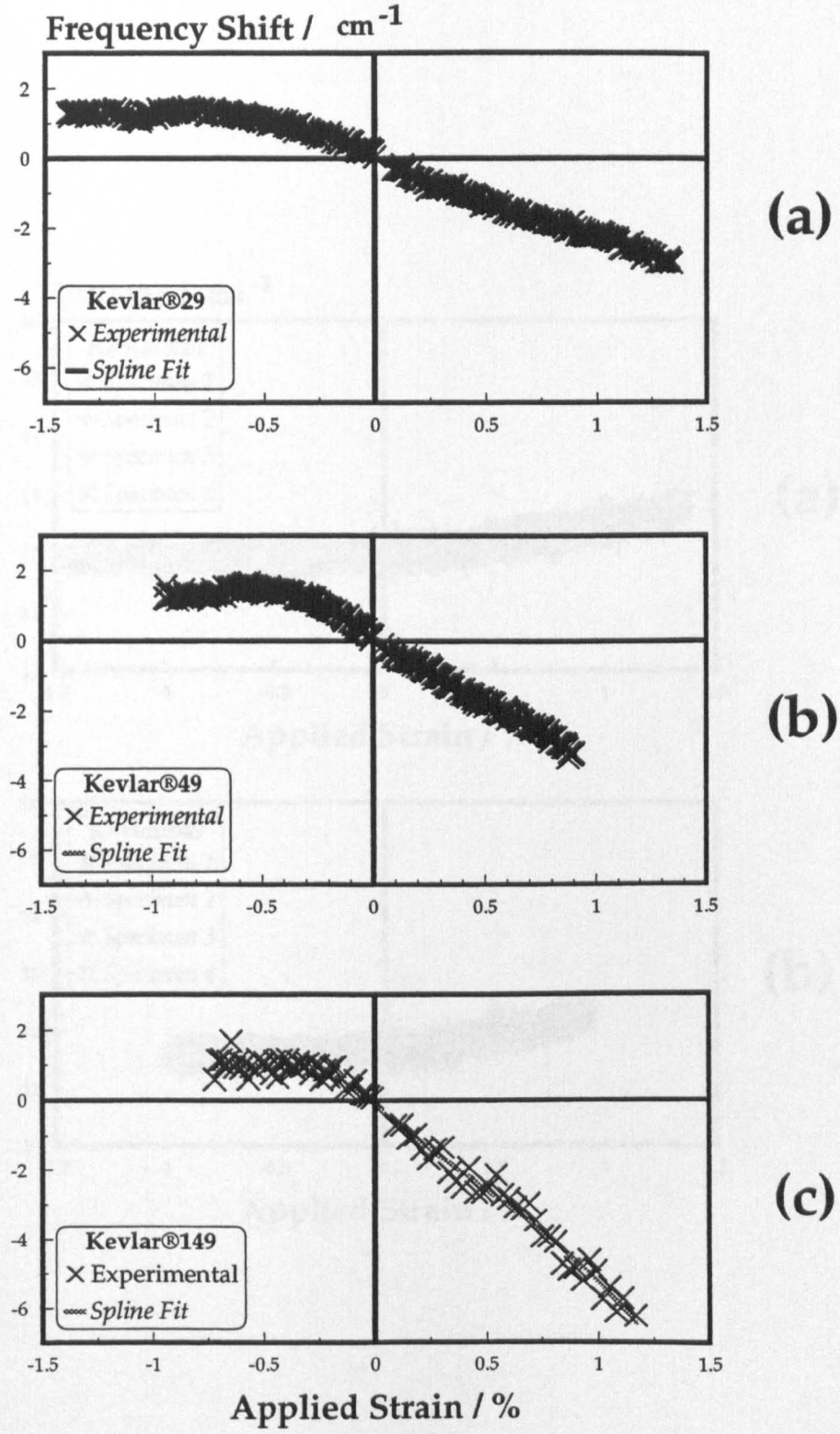

Figure 4.7. Raman frequency shift-applied strain for:
(a) Kevlar®29, (b) Kevlar®49 and (c) Kevlar®149 fibres.

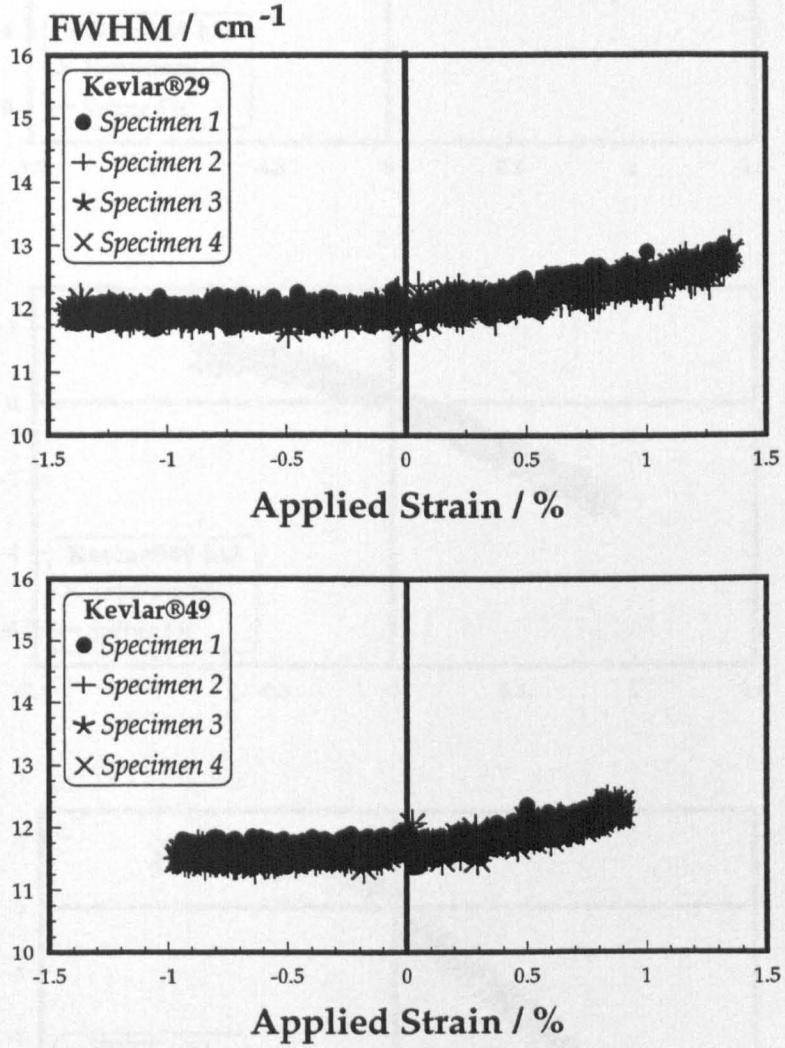

Figure 4.8. FWHM-applied strain for:
(a) Kevlar®29 and (b) Kevlar®49 fibres.

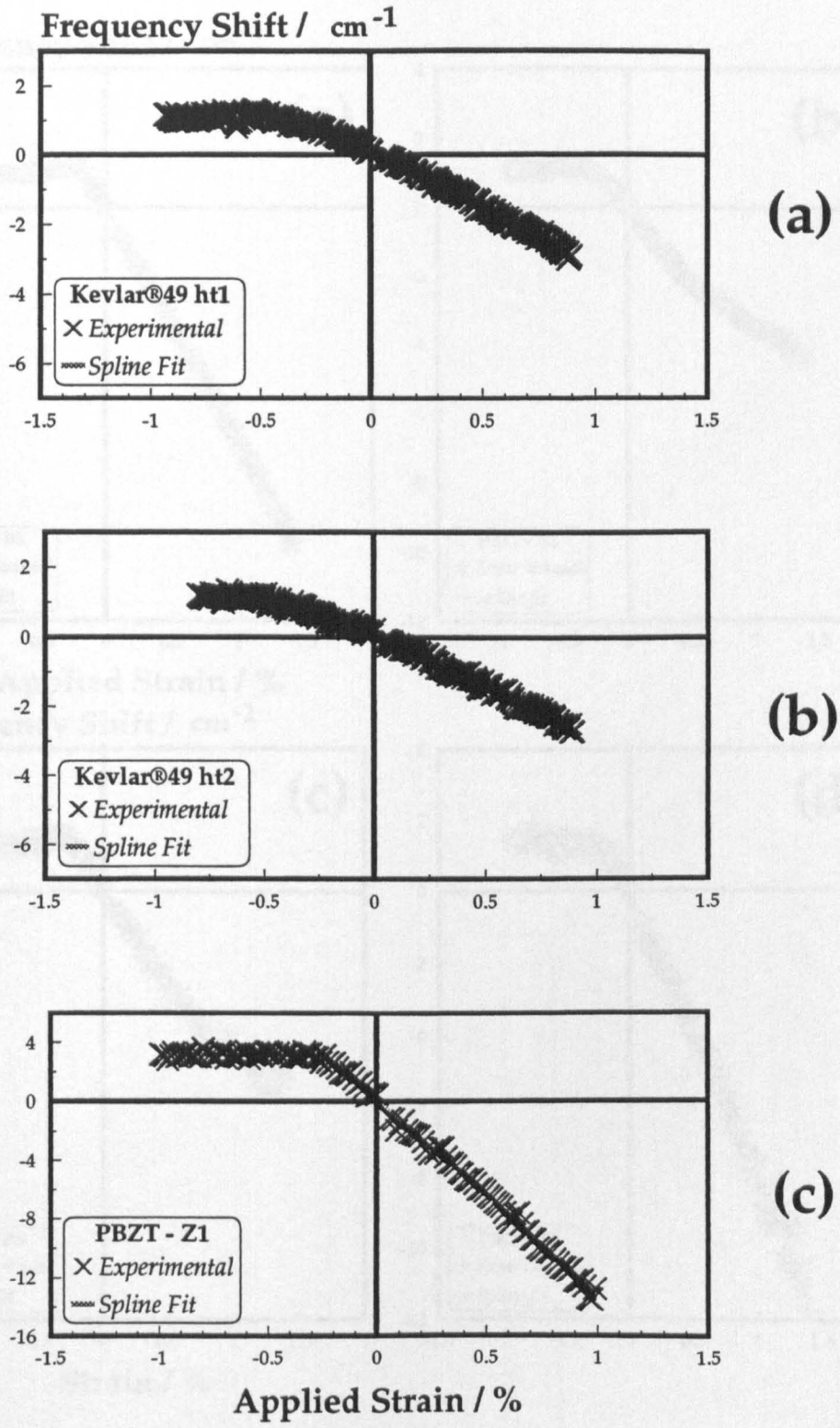

Figure 4.9. Raman frequency shift-applied strain for:
(a) Kevlar®49 ht1, (b) Kevlar®49 ht2 and (c) PBZT-Z1 fibres.

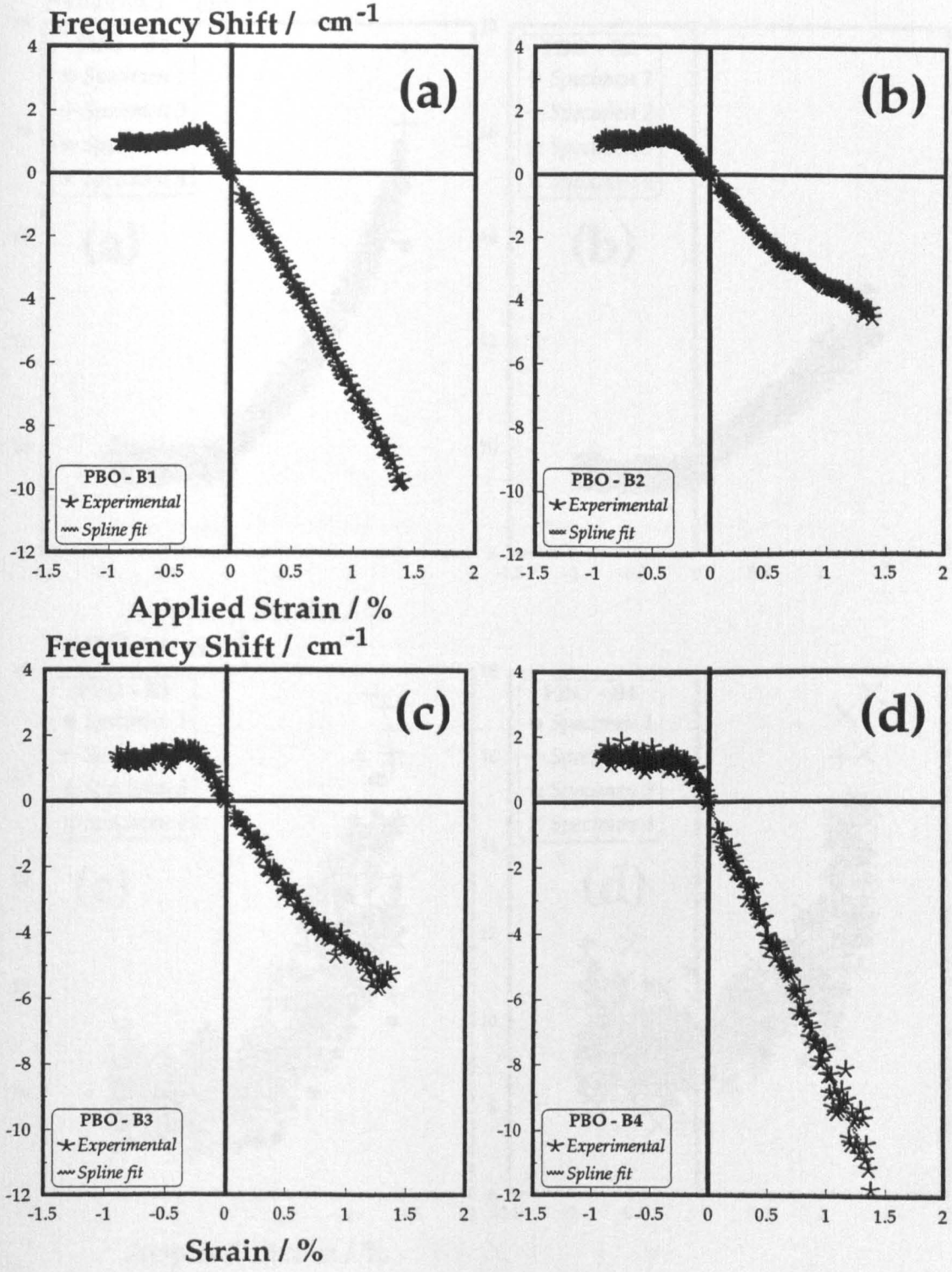

Figure 4.10. Raman frequency shift-applied strain for:
(a) PBO-B1, (b) PBO-B2, (c) PBO-B3 and (d) PBO-B4 fibres.

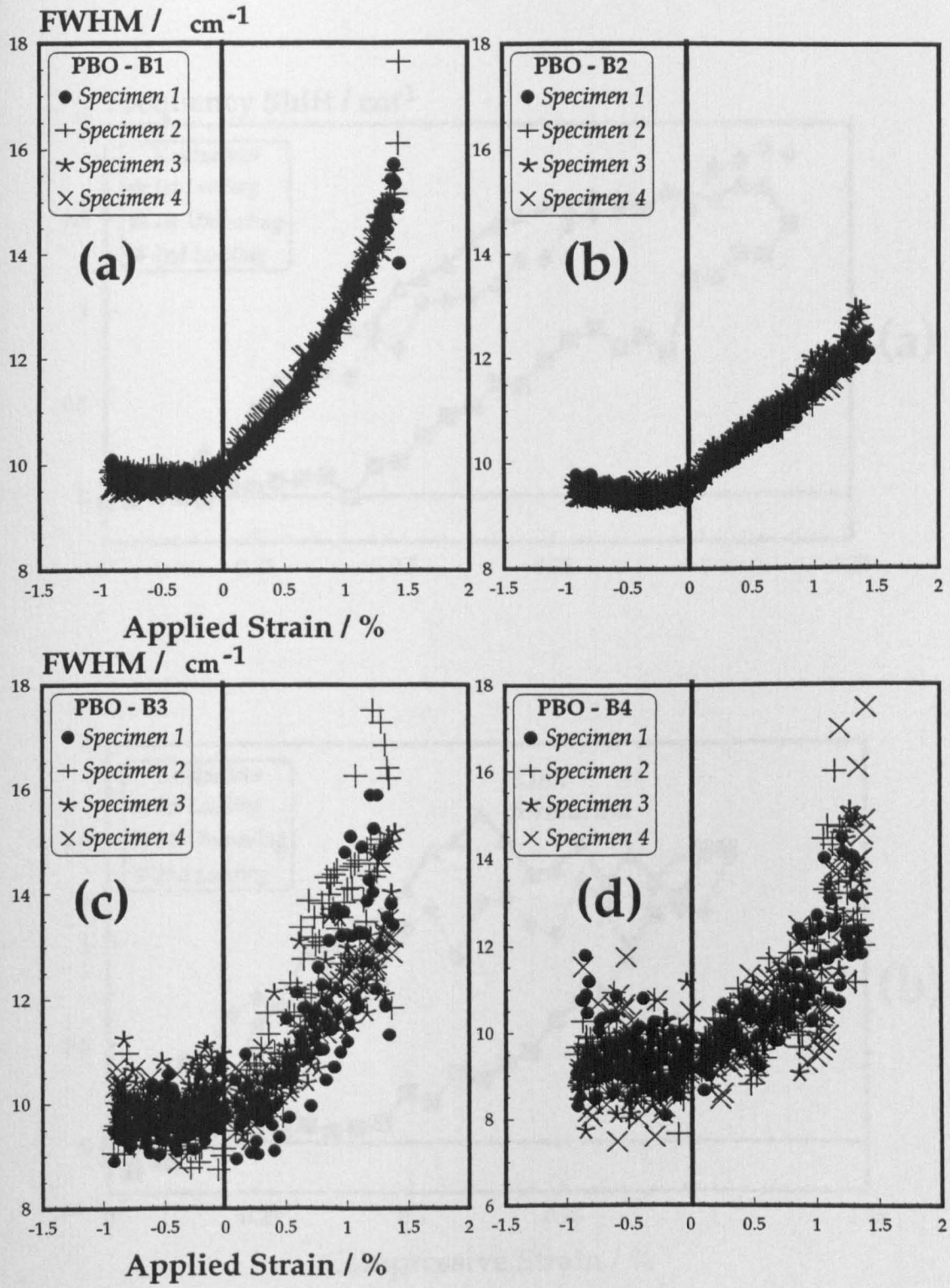

Figure 4.11. FWHM-applied strain for:
(a) PBO-B1, (b) PBO-B2, (c) PBO-B3 and (d) PBO-B4 fibres.

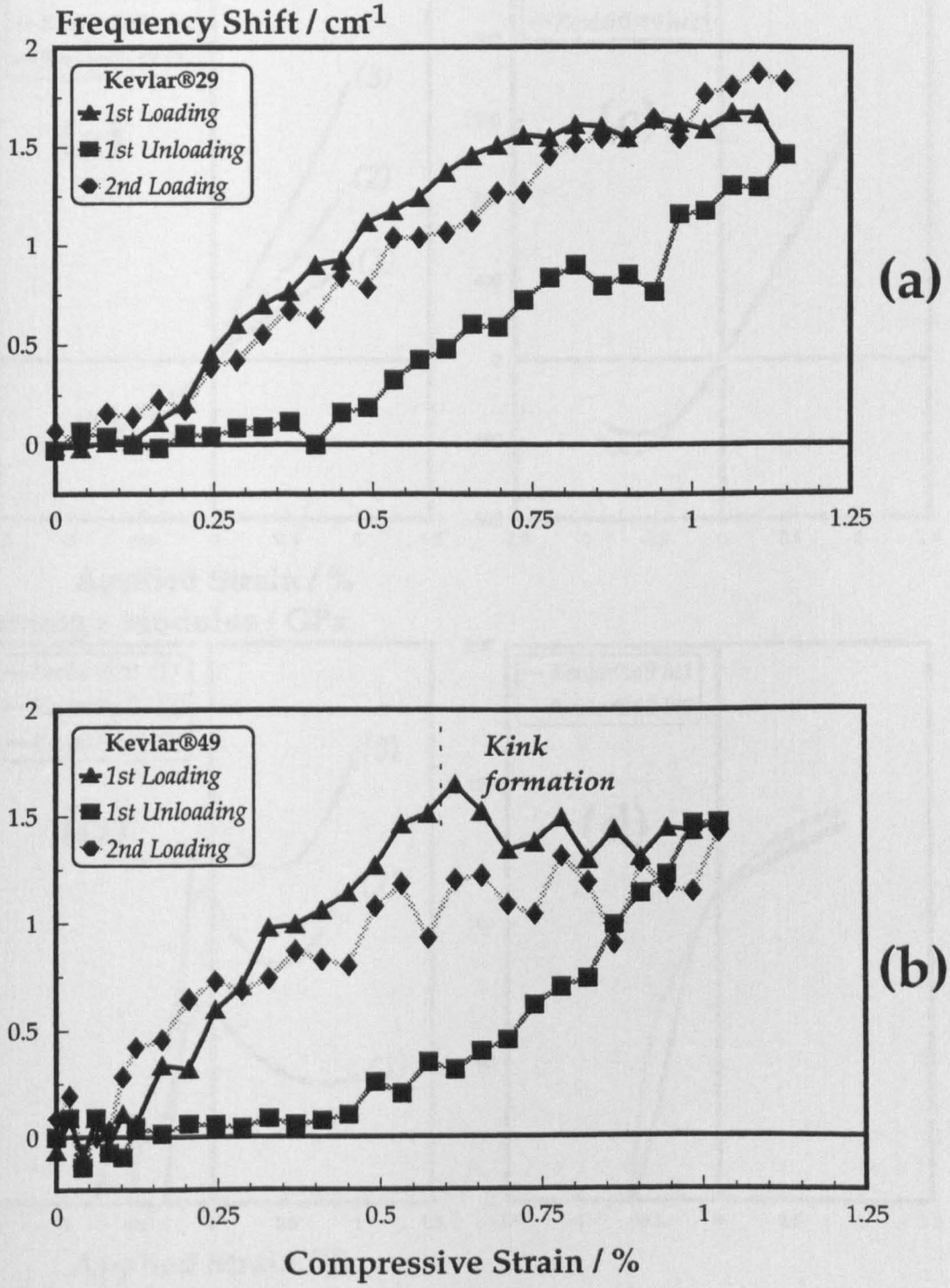

Figure 4.12. Raman frequency shift-compressive strain, loading & unloading for: (a) Kevlar®29 and (b) Kevlar®49 fibres.

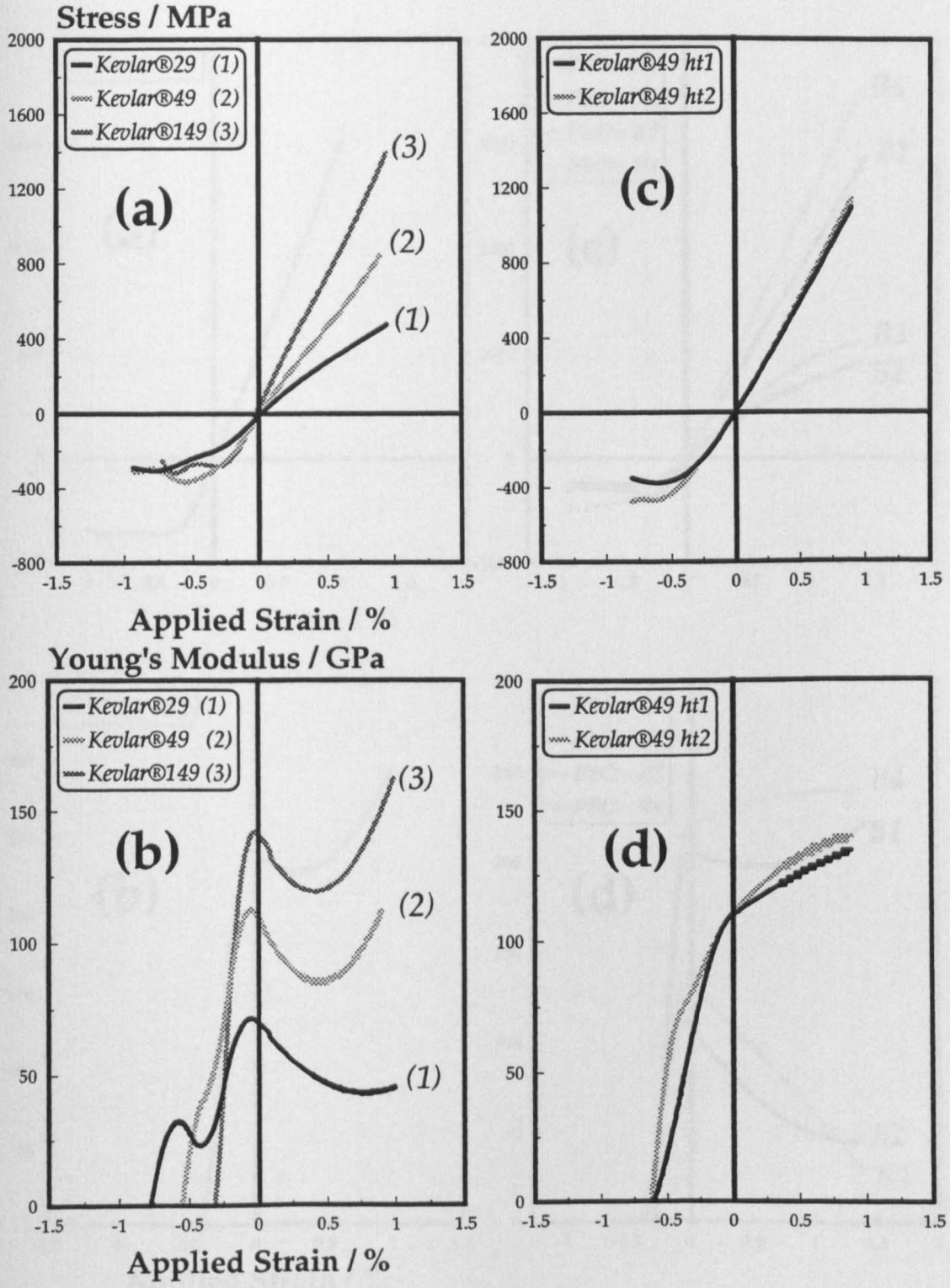

Figure 4.13. Predicted stress-strain and Young's modulus-strain curves for: (a),(b) Kevlar®29, Kevlar®49 & Kevlar®149 and (c),(d) Kevlar®49 ht1 & ht2 fibres.

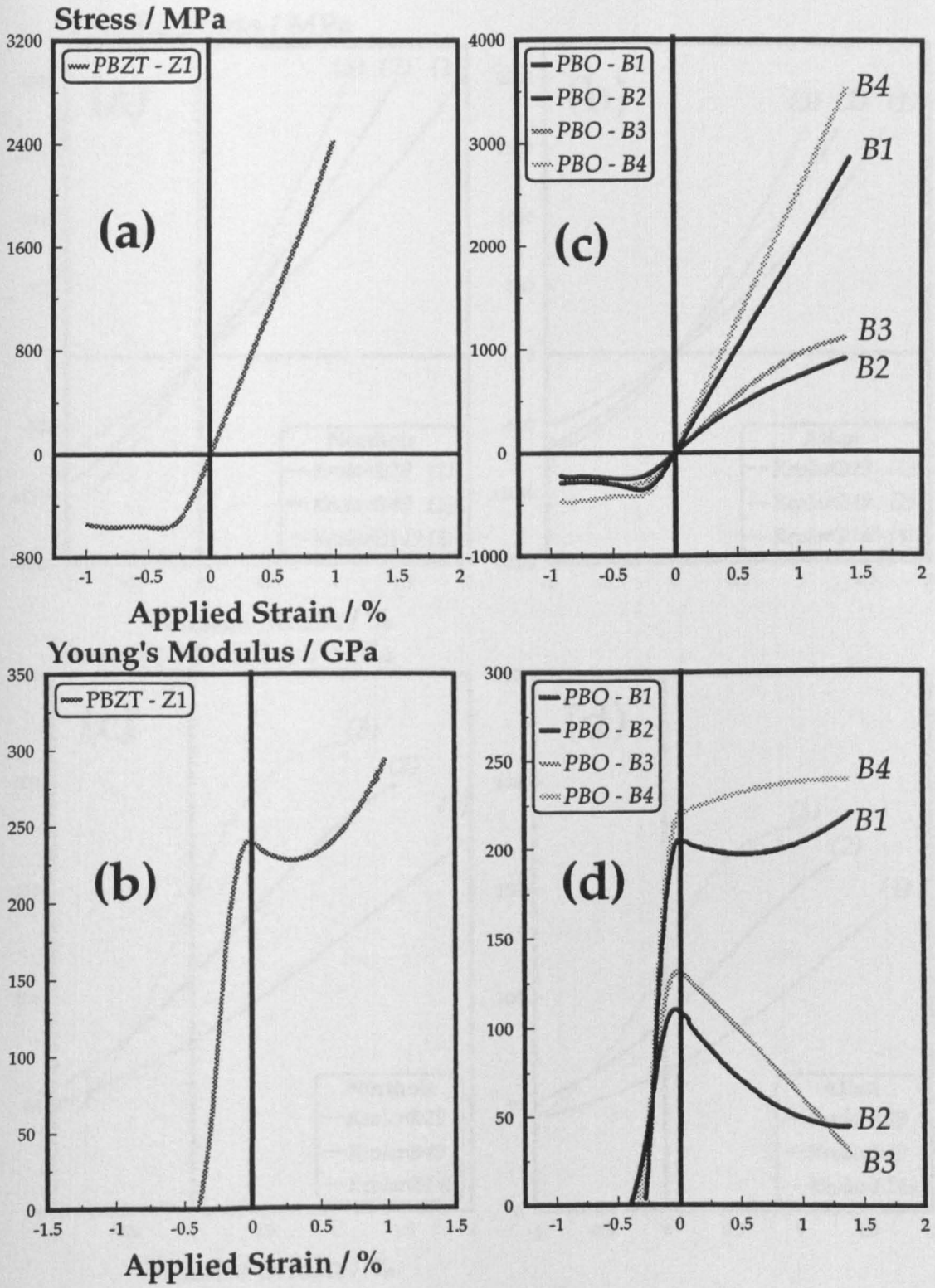

Figure 4.14. Predicted stress-strain and Young's modulus-strain curves for: (a),(b) PBZT-Z1 and (c),(d) PBO-B1, B2, B3 & B4 fibres.

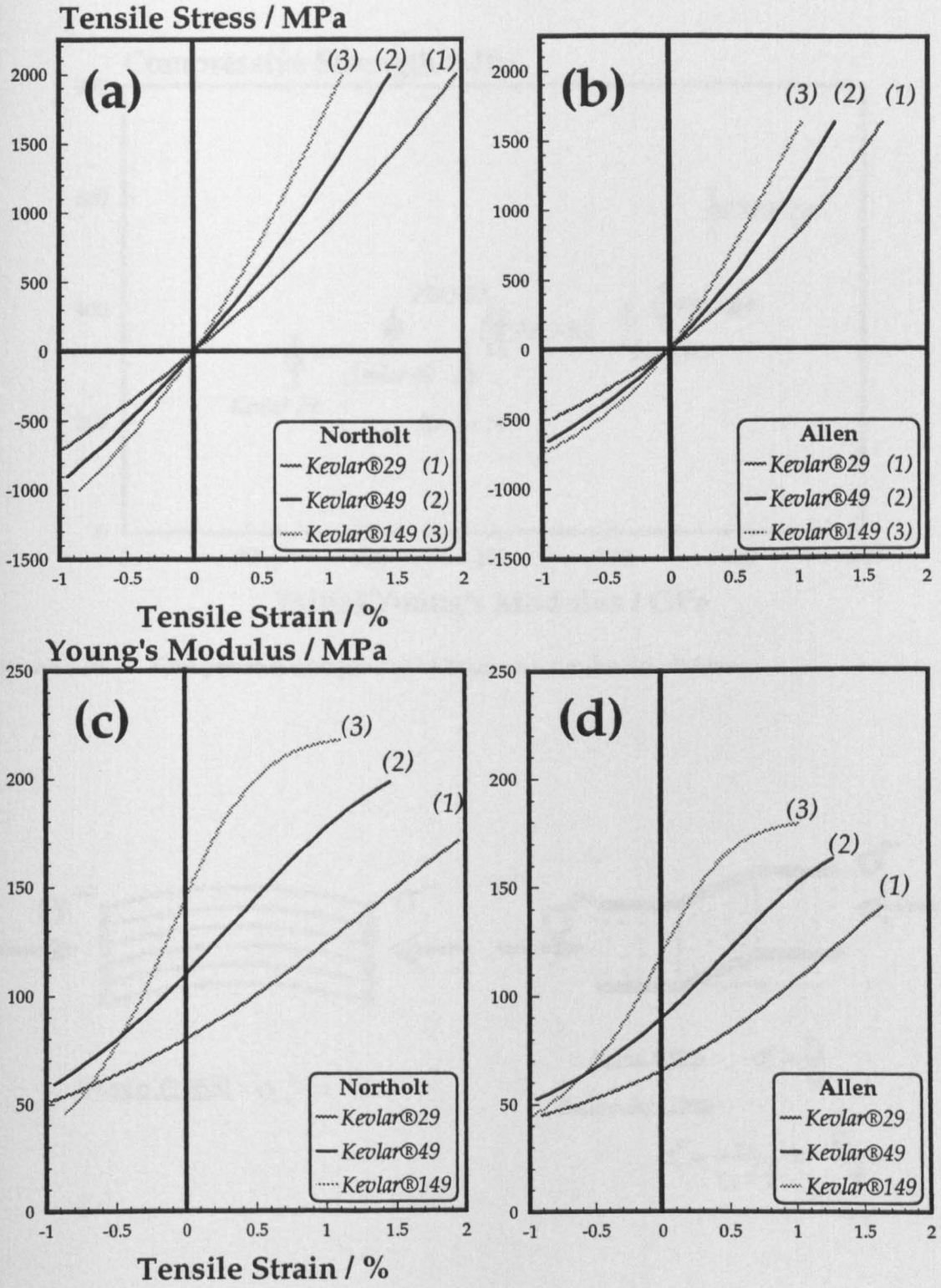

Figure 4.15. Predicted stress-strain and Young's modulus-strain curves derived from: (a), (c) Northolt's and (b),(d) Allen's models extrapolated to compression for Kevlar®29, Kevlar®49 & Kevlar®149.

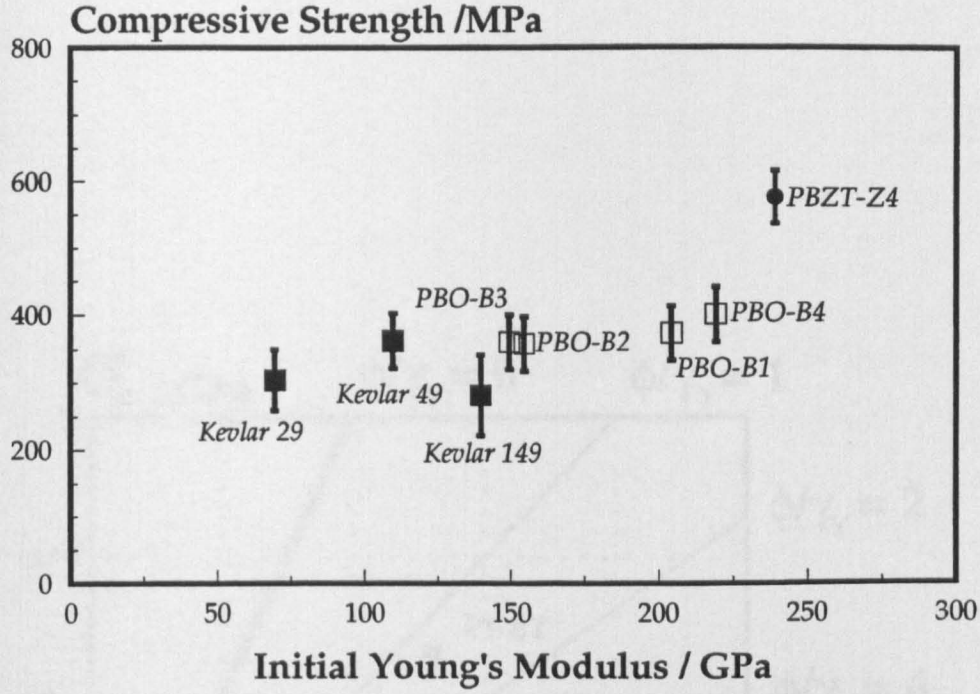

Figure 4.16. Compressive strength-initial Young's modulus for all fibres.

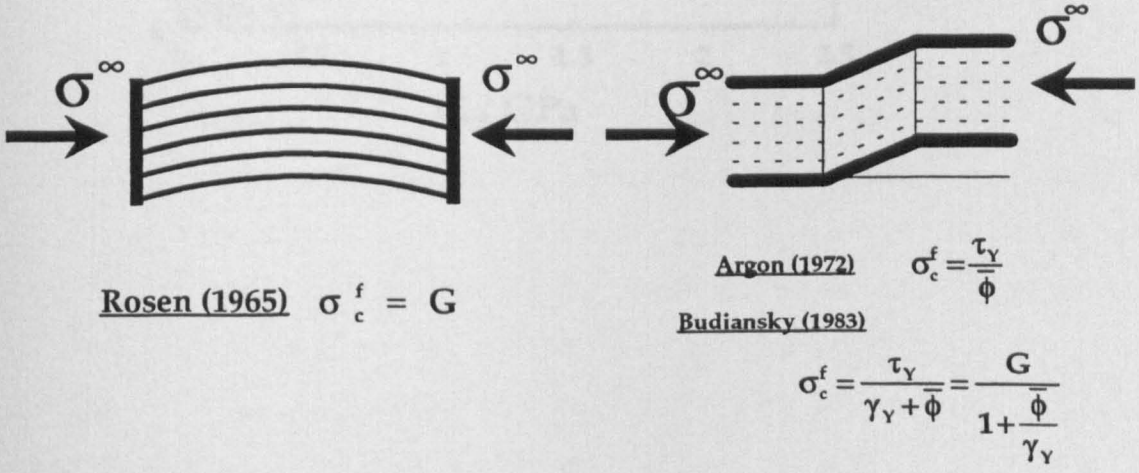

Figure 4.17. Models for compressive failure in LCP fibres.

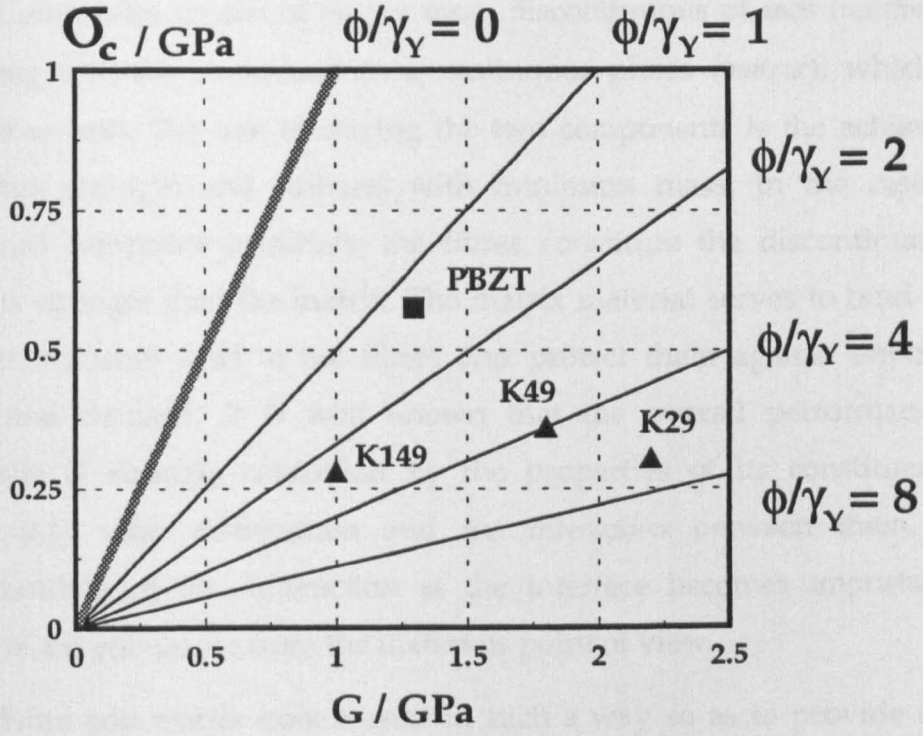

Figure 4.18. Compressive strength-shear modulus for LCP fibres.

CHAPTER 5:
INTERFACIAL MICROMECHANICS IN SINGLE FIBRE MODEL COMPOSITES

5.1. Introduction.

Composites consist of one or more discontinuous phases (*reinforcement* or *reinforcing material*) embedded in a continuous phase (*matrix*), which make a contiguous unit. The aim of mixing the two components is the achievement of maximum strength and stiffness with minimum mass. In the case of fibre reinforced composite materials, the fibres constitute the discontinuous phase which is stronger than the matrix. The matrix material serves to bind the fibres together, transmit load to the fibres and protect them against environmental attack and damage. It is well known that the overall performance of the composite is strongly controlled by the properties of its constituent phases (figure 5.1), their distribution and the *interaction* between them. A good understanding of this interaction at the interface becomes important in the design of the composite from the materials point of view.

Fibre and matrix may *interact* in such a way so as to provide composite properties that are not represented by a simple volume-fraction summation of the properties of the constituents. Thus, in describing a composite material as a system, the following important parameters should also be taken into account: (a) the geometry of the reinforcement described by its shape, size and size distribution and (b) the nature and characteristics of the *interfacial area* which plays a crucial role in determining the extent of the interaction between the reinforcement and the matrix.

The interfacial bonding between the fibres and the matrix is a very important factor influencing the mechanical properties and the general performance of fibrous composites. The mechanism of load transfer from the

matrix to the fibres through the interface is of great importance in the case of discontinuous fibre reinforced composites. In the case of continuous fibre reinforced composites, when individual fibres fracture prior to ultimate failure of the composite, the interface controls the mode of propagation of microcracks at the fibre ends.

If the adhesion between the fibre and the matrix is 'poor', the load is transmitted to the fibre and eventually will exceed its strength. As a result, fibre fracture occurs which consequently reduces the efficiency of the fibre in bearing the applied load. Simultaneously, the weak interfacial bond ruptures and a crack propagates parallel to the fibre axis (i.e. parallel to the direction of the applied load). This is a 'mode II' type of interfacial failure (figure 5.2a).

When strong adhesion exists between the fibre and the matrix, release of mechanical energy occurs in a tranverse direction and the crack propagates perpendicular to the fibre axis in the bulk matrix (i.e.vertical to the direction of the applied load). This is a 'mode I' type of failure at the interface (figure 5.2b).

In the case of an intermediate level of adhesion, rupture occurs in the vicinity of the interface in a 'mixed mode' fashion with fibre debonding and transverse matrix cracking occurring simultaneously. (figure 5.2c).

In the case of 'strong adhesion', the composite still serves its purpose even after the fibres fracture at several points along their length **[Hull 1981]**, **[Agarwal 1990]**. Strong adhesion is also essential for higher transverse strengths and for good environmental performance of composites. Improved adhesion usually enhances the water resistance of polymer matrix composites. The harmful effect of an adverse environment becomes more severe if the adhesion is poor especially when the composite is under load **[Agarwal 1990]**. For all these reasons, maximum utilisation of fibre properties requires optimum bonding across the interface. However, too strong adhesion leads to embrittlement and, hence, reduced toughness. In contrast, composite materials with weak interfaces have relatively low strength and stiffness but enhanced toughness.

5.1.1. Interface/Interphase: the macro, meso and micro approach.

Interface is the common surface between the two (or more) constituents brought together to make an integral unit, the composite material. In the case of fibre reinforced composite materials, the interface is the entire 'shared' surface between the fibre and the matrix. There have been a number of basic approaches to studying the nature and the role of the interface: The (global) *macroscopic approach,* and the *microscopic approaches,* which in turn, may differ in scale (i.e. microscopic versus atomic). The former is based on classical mechanics and theory of elasticity. The latter takes into account not only the mechanical but also the chemical and physical nature of the interface.

A schematic illustration of the model upon which all various macroscopic approach studies are based is shown in figure 5.3a. According to this model, there is no difference between the material properties in the vicinity of the interface and those of the bulk material away from the interface. Bonding is assumed to be perfect [**Hull 1981**].

If, on the other hand, we take into account crucial physico-chemical phenomena occurring between the fibre and the matrix in the vicinity of the interface, a more realistic model representing the interface is given (figure 5.3b). These parameters such as *wetting, material absorption* and *interdiffusion* arise during the composite fabrication and are completely neglected from a macroscopic point of view. Wetting and absorption represents the compatibility between the (solid) fibre and the (liquid) matrix in terms of the thermodynamic work of adhesion when the surfaces are brought close to each other. Interdiffusion is the formation of bonding between two polymer surfaces by the entanglement of the polymer molecules on one surface with the molecular network of the other surface.

If we focus even further on the area between fibre and matrix (figure 5.3c), at the atomic scale level, we may consider the *electrostatic attractions* and *chemical bonding*. Electrostatic attractions occur between two surfaces due to opposite

charges (acid-base interactions for aramid/epoxy systems). The strength of the interface will depend on the charge density. A chemical bond is formed between a chemical grouping of the fibre surface and a compatible chemical group in the matrix. The strength of the bond depends on the number and type of bonds. Bond rupture occurs during interfacial failure.

As has been mentioned, it is not unusual to introduce a third phase in between the fibre and the matrix with unknown properties, termed as *interphase* or *mesophase*. Therefore, the strengthening mechanism proposed by the last two advanced approaches is a combination of diffusion across the multilayer interfaces and chemical bonding of the various species.

At this point, it is important to note that fibre surface energetics play a major role in wetting with epoxy resins for aramid/epoxy composite systems. In general, for effective wetting of a fibre surface, the liquid epoxy resin must cover most of the fibre area and displace all the air. It has been found that aramid fibres and epoxy resins exhibit compatible surface energetics, associated primarily with dispersion and acid-base interactions **[Penn 1980,1984]**, **[Wesson 1984]**. Therefore, a very close matching of surface energy components between aramid filaments and epoxy resins exists.

A number of investigations exist in the literature concerned with the improvement of the fibre/matrix adhesion for aramid reinforced composites. These approaches include (a) filament surface oxidation or etching **[Wertheimer 1981]**, **[Allred 1984]** (b) matrix chemical modification **[Chiao 1977]**, **[Allred 1979]** (c) addition of coupling agents **[Penn 1983]** and (d) formation of reactive surface groups on the filaments **[Hoffman 1983]**, **[Allred 1985]**. These methods resulted in moderate to small improvements of off-axis properties of aramid reinforced composites.

In the case of aramid/epoxy systems, full composite experimental data (from transverse tensile strength evaluation tests) have shown that fracture surfaces of these composites are characterised by bare, visually unaltered

filaments with little epoxy adhering to them [**Morgan 1980**], [**Allred 1983,1984**]. Therefore, for aramid/epoxy systems the interphasial strength rather than the fibre or matrix strength limits(to a certain extent) the off-axis strength of these composites.

5.2. Theories of Stress Transfer Mechanisms.

In the case of continuous fibre reinforced composites the effect of fibre ends is generally considered insignificant. The stress field in the vicinity of the fibres is assumed to be constant over the whole length of the fibres. However, individual fibres fail prior to the entire composite fracture. In this case, the stress transfer to the broken fibres by the matrix via the interface will influence the composite fracture, especially as the number of broken fibres increases with the increase of the macroscopically applied stress in the composite. In a discontinuous fibre reinforced composite, the attainment of high strength in the composite will depend upon efficient stress transfer from the matrix to the fibres. Therefore, a good understanding of the stress field at the fibre/matrix interphase is required for the strength evaluation of the entire interphase. A complicated stress field (including *normal* σ_{xx}, *radial* σ_{rr} and *hoop stresses* $\sigma_{\theta\theta}$ along with *shear stresses* τ_{rx}, $\tau_{x\theta}$ and $\tau_{r\theta}$) exists in an infinitesimal volume element. A number of studies deriving analytical solutions to the above problem have been carried out over the last 40 years. All these treatments were based on various assumptions necessary to simplify the complexity of the problem.

In the first part of this section, all analytical studies supported by a simple 'shear-lag' type of deformation concerning the fibre and matrix material, are reviewed. The equations characterising the stress field which is minimized to a set of axial fibre stresses $\sigma_{xx}(x)$ and shear stresses $\tau_{rx}(x)$ in the vicinity of the interface, are predicted as a function of one independent variable x. These stresses will be denoted as $\sigma_f(x)$ (axial fibre stress) and $\tau(x)$ (interfacial shear

stress, abbreviated as ISS) accordingly. The limitations of these approaches are investigated and discussed.

5.2.1. Shear-lag analysis approaches.

(i)'Shear-lag' analysis I [Cox 1952],[Outwater 1956].

The fundamental assumptions of this analysis are the following:

- a round fibre is surrounded by a cylindrical matrix,
- perfect adhesion exists between fibre and matrix,
- both fibre and matrix behave elastically,
- there is no load transfer through the fibre ends.

According to this study, only the axial forces at the fibre and the shear forces at the interface have been taken into account (figure 5.4a). If the whole matrix is subjected to a macroscopic strain ε, the rate of transfer of load from matrix to the fibre will depend on the relationship between the displacement in the direction of the length of the fibre at distance x from one end and the displacement of the matrix at the same point if the fibre were absent. The above argument leads to a closed-form solution for the axial fibre stress:

$$\sigma_f(x) = E_f \varepsilon_\infty \left[1 - \frac{\cosh\beta\left(\frac{L}{2} - x\right)}{\cosh\beta\frac{L}{2}} \right] \tag{5.1}$$

where $\beta = \frac{1}{R}\sqrt{2\left(\frac{G_m}{E_f}\right)\frac{1}{\ln\left(\frac{R_\infty}{R}\right)}}$, E_f is the Young's modulus of the fibre, G_m is the shear modulus of the matrix, R is the radius of the fibre and R_∞ is the radius of the matrix cylinder.

Considering the force equilibrium between axial and shear stresses of the infinitesimal fibre length **dx**:

$$(\pi R^2)\sigma_f(x) + 2\pi R dx \tau(x) = (\pi R^2)[\sigma_f(x) + d\sigma_f(x)] \qquad (5.2)$$

an estimation of the interfacial shear stress $\tau(x)$ along the fibre based on the following equation can be derived:

$$\tau(x) = E_f \varepsilon_\infty \sqrt{\frac{G_m}{2E_f \ln\left(\frac{R_\infty}{R}\right)}} \frac{\sinh\beta\left(\frac{L}{2} - x\right)}{\cosh\beta\frac{L}{2}} \qquad (5.3)$$

(ii) 'Shear lag' analysis II [Dow 1963].

Another analysis analogous to that presented above was proposed by Dow for a similar fibre reinforced composite system. According to this model, a single filament ('fibre') is embedded in a matrix material ('binder'). The load is assumed to be applied at one end either to the binder alone (as if the fibre were broken within the binder), or the fibre alone (as if the binder were cracked perpendicular to the fibre). Both fibre and binder at the other end are supposed to be fixed at equal strain (figure 5.4b). The most important condition introduced as compared to Cox's analysis, is a consideration of *plastic yielding* of the binder material. Closed form equations were also derived from this model concerning the interfacial shear stress distribution in the case of elastic behaviour for the binder and the fibre. Similar equations were derived in the case of plastic yielding of the binder material. In all cases the ratio of shear modulus to Young's modulus for the binder material was assumed constant.

Both 'shear-lag' interpretations described above compute analytical formulae for the shear stress $\tau(x)$ distribution at the interface between fibre and matrix as a function of the applied load, the geometry of the components, their elastoplastic moduli and their 'effective stiffness'.

A qualitative plot of the axial and shear stresses based on these two studies is given in figure 5.4. The maximum ISS is located at the discontinuity (fibre end) and declines to zero towards the middle of the fibre. These maxima are very high and local. Yielding in shear occurs to relieve these stresses. This effectively would reduce the stiffness of the composite and increase the fibre length neccessary for complete load transfer.

(iii) Plastic stress transfer [Kelly 1965].

Another study by Kelly [**Kelly 1965**] introduced a simple model for stress transfer in whisker reinforced metals taking into account the elastic - perfectly plastic behaviour of the metal matrix material. In fact, two distinct stages prior to reaching the ultimate stress of the composite were considered:

- (i) elastic deformation of both constituents, and
- (ii) the matrix deforms plastically whereas the fibres deform elastically.

The applied load is transferred to the fibre by means of shear forces at the fibre matrix interphase. If these shear forces/stresses exceed the yield stress of the matrix, *plastic flow* will occur at the vicinity of the fibre ends. The tensile strain in the matrix at the fibre ends is plastic and larger than the macroscopic strain of the composite. The axial tensile stress in the fibre builds up linearly from the fibre ends towards the middle of the fibre described by the following equation:

$$\sigma_f(x) = 2\tau_i \frac{x}{r} \qquad (5.4)$$

where τ_i is the shear stress at the fibre-matrix interphase, assumed to be constant and equal to the matrix yield stress τ_{my} in shear (i.e. $\tau(x) = \tau_i = \tau_{my} = \text{const.}$). The applied macroscopic stress is transfered to the fibre and when its fracture strength σ_{fu} is exceeded the fibre breaks. This will occur if the fibre is longer than a *critical length* L_c and the correlation between L_c and the (constant) shear stress τ_i at the interface region is the following:

$$\frac{L_c}{d} = \frac{\sigma_{fu}}{2\tau_i} \tag{5.5}$$

where **d** is the diameter of the fibre. The L_c is often referred in the literature as the *critical length* and L_c / d the *critical aspect ratio.* The critical aspect ratio is a very important parameter which controls the behaviour of composites. During mechanical deformation and consequently fracture, short fibres will tend to be pulled out of the composite while long fibres will be broken. A representation of this model based on the above assumptions is given in figure 5.5a.

(iv) Other analyses [Piggot 1966], [Piggot 1980].

Another theory of stress transfer [**Piggot 1966**] was introduced and modified [**Piggot 1980**] for a range of different composite materials (reinforced metals, polymers, ceramics and cements). The nature of the constituents for each combination of matrix and reinforcing filament was taken into account.

A. In the case of reinforced metals (where elastic behaviour for the fibre and elastic-plastic behaviour for the matrix are considered) the interfacial shear stress will be constant up to a certain distance from the fibre ends and equal to the shear yield stress of the matrix:

$$\tau_i(x) = \tau_{my} \qquad 0 \le x \le \ell \tag{5.6}$$

where the length ℓ depends on the applied stress.

Near the fibre mid-section the interfacial shear stresses are generated by elastic, Cox-type interaction. A model example for this kind of stress transfer is given in figure 5.5b for a well-bonded reinforced metal.

B. In the case of reinforced polymers, the stress transfer is controlled by Coulomb's friction taking place at the interface, between the fibre and the matrix. The frictional stresses are the result of the compressive stresses normal to the

fibre-matrix interface, i.e. the radial stresses σ_r introduced by (a) fibre and matrix contractions during manufacturing (different thermal expansion coefficients) and (b) Poisson's contractions of the matrix when a stress is applied to the composite. In this case, the interfacial shear stress near the fibre ends is described by the following equation:

$$\tau_i(x) = \mu\sigma_r \qquad 0 \le x < \ell \tag{5.7}$$

In figure 5.5c a model example for an imperfectly bonded reinforced polymer is shown. The discontinuity at the interfacial shear stress profile is due to the fact that the adhesion strength is different from the frictional stress.

C. With reinforced cements and similar materials the stress transfer regime is very similar to that of reinforced polymers described above. Since the ultimate tensile strain of the cement is very small, the matrix Poisson's shrinkage can be neglected. In the case of reinforced ceramics, the matrix Poisson's shrinkage cannot be neglected. Also, the moduli of fibres and matrix are not very different and therefore fibre Poisson's shrinkage must also be included. The interfacial shear stress near the fibre ends is not constant. In fact, it increases towards the fibre ends. A schematic representation of this model is shown in figure 5.5d.

It is quite clear from the above models for stress transfer that the maximum interfacial shear stress is not necessarily located at the fibre end as was predicted by the previous approaches ([**Cox 1952**], [**Dow 1966**]).

In a similar analysis [**Piggot 1987**], the existence of a thin distinctive layer of interphase around the fibre was introduced. The shear modulus of this layer was assumed to be less than that of the matrix. Analytical solutions were derived, based on the above assumption. The axial and shear stresses were found to be dependent on the Young's moduli of fibre and matrix, the shear moduli of the matrix and the elastic properties of the interphase layer. These were the volume fraction of the fibre and the interphase, the Poisson's ratio of the matrix

and the fibre packing. Nevertheless, a disagreement with experimental results indicated that a more realistic approach should be taken. The interphase may be modelled as a phase with a gradient of mechanical properties in the axial and radial direction rather than uniform properties throughout [**Theocharis 1987**].

5.2.2. Other analytical approaches.

The three analytical studies based on the 'shear lag' type of assumption do not take into consideration the transverse stiffness of the fibre and the matrix. In fact, the transverse properties of the fibre and the matrix are assumed to be equal which results in a two dimensional problem so only axial stresses, σ_{xx} and shear stresses, τ_{rx} are considered. More recent investigations include derivations of other stress components equally important. Closed-form, three dimensional axisymmetric solutions can be derived by satisfying the equilibrium equations, and boundary conditions. These approaches are closer to reality, offering a better understanding of the stress transfer mechanisms and the complicated stress fields involved. These studies, which, of course, are very sensitive to the equilibrium and boundary conditions mentioned above will be reviewed in the following paragraphs and compared with other models.

(i) Isolated fragment analysis [Whitney 1987].

The model is based on a single fibre with a single isolated fracture surrounded by an unlimited matrix. Axisymmetric behaviour is considered and the fibre is assumed to be orthotropic (transversely isotropic). Therefore, the stress components σ_{rr}, $\sigma_{\theta\theta}$, σ_{xx} and τ_{rx} are all independent of the variable θ and all the other stress components are zero. Consequently, there are two independent variables, **r** and **x** where **r=R** corresponds to the fibre surface and **x=0** to the locus of the fibre fracture. The effect of expansional strains as a result of moisture and temperature is also included. The solution is derived by the superposition of the solutions to two axisymmetric problems, an exact 'far field'

solution and an approximate 'transient' solution. The model is also suitable to account for nonlinear stress-strain behaviour of the matrix.

In contrast to all previous models, the interfacial shear stress at the fibre end is zero which *a priori* is a boundary condition. Calculations concerning the radial stresses revealed their importance as a supportive mechanism to the fibre. The application of the above equations to two different systems (AS4 carbon fibre/Epon® 828 resin and Kevlar® 49 fibre/Epon® 828 resin) revealed that this mechanism is not very significant for the second system as a result of small difference of the Poisson's ratio and thermal expansion coefficient between fibre and matrix.

(ii) Single discontinuity analysis [McCartney 1989].

Another analytical method predicting stress transfer between fibre and matrix in a fibre reinforced composite was developed by introducing a single dicontinuity into the composite. In a similar manner to the previous analysis [**Whitney 1987**], the mode of deformation is axisymmetric with axial and shear stress vanishing to zero at the locus of the discontinuity. This discontinuity is of a matrix crack form. Two different regimes were introduced:

- perfect bonding at the interface;
- perfect bonding (*no-slip* region I) and imperfect bonding (*frictional slip* region II) at the interface.

In the second case, the 'frictional type' of fibre-matrix interface is governed by the *Coulomb friction law* which offers a more accurate description than the assumption that the interfacial shear stress takes a constant value at region II ([**Piggot 1966**] [**Piggot 1980**], [**Favre 1991**]). The friction coefficient μ, however, is considered to be constant. In fact, the Coulomb friction law for the two distinct regions can be expressed as follows:

$$\tau_{rx}(R,x) < \mu\sigma_{r}(R,x), \qquad \ell \le x < \infty \qquad \text{(region I)} \tag{5.8a}$$

$$\tau_{rx}(R,x) = \mu\sigma_{r}(R,x), \qquad 0 \le x < \ell \qquad \text{(region II)} \tag{5.8b}$$

These equations are valid only for compressive radial stresses.

An interesting observation concerning the two different regions is that if matrix yielding occurs before relative frictional slip between fibre and matrix, region I and II represent the 'plastic stress transfer' and 'elastic stress transfer' regions described in the shear-lag analyses of Piggot [**Piggot 1966, 1980**]. This treatment provides closed-form solutions for all stress components which fulfill the equilibrium equations and the boundary conditions. When a matrix crack is present (perfect bonding case), the shear stress distribution at the interface exhibits zero value at the locus of the matrix crack. It rises to a maximum value away from the crack and then decays gradually to zero. On the other hand, normal stresses at the interface are compressive away from the matrix crack and change sign (they become tensile) as the matrix crack is approached. In the case of frictional slip, the maximum shear stress is located further away from the matrix crack and is nevertheless non-uniform along the slip length which is large compared to the fibre radius.

The model presented here assumes that the fibre-matrix interface is a region of two extremes: perfectly bonded and/or totally unbonded areas but it could be modified in a form which would include a partially bonded area in between.

(iii) Multi-fragment analysis [Nairn 1992].

One of the most recent approaches concerning stress transfer mechanisms in composites has been proposed by Nairn [**Nairn 1992**]. Equilibrium equations and boundary conditions are obeyed, residual stresses and fibre fracture interactions have been taken into account. The attempt accounts for an accurate prediction for an 'ideal' single fibre fragmentation test and can be adapted for other experimental methods used in the literature for interphase strength evaluation.

The fundamental advantages of this study compared with the two previous approaches [**Whitney 1987**], [**McCartney 1989**] are the following:

- the choice of stress functions which minimize the complementary energy of the system and,
- the introduction of multiple discontinuities which interact with each other.

On the other hand, the model is limited by assuming perfect adhesion between fibre and matrix. The solution in a matrix form is as follows:

$$\begin{bmatrix} \sigma_{rr}(r,x) \\ \sigma_{\theta\theta}(r,x) \\ \sigma_{xx}(r,x) \\ \tau_{rx}(r,x) \end{bmatrix} = \begin{bmatrix} -\frac{1}{2V_f} & \frac{V_m}{V_f} & \frac{1}{2} & 0 & \frac{1}{4}\left(\frac{r^2}{R^2}+\frac{\ln V_f}{V_m}\right) & V_f \\ -\frac{1}{2V_f} & \frac{V_m}{V_f} & \frac{1}{2} & 0 & \frac{1}{4}\left(\frac{r^2}{R^2}+\frac{\ln V_f}{V_m}\right) & V_f \\ 0 & 0 & 1 & 0 & 0 & 0 \\ 0 & 0 & 0 & -\frac{r}{2R} & 0 & 0 \end{bmatrix} \begin{bmatrix} \sigma_0 \\ \eta \\ \psi(x) \\ \psi'(x) \\ \psi''(x) \\ \sigma_- \end{bmatrix} \tag{5.9}$$

where $\psi(x)$ is the calculated stress function, η is an integration constant, σ_0 is the total applied stress, σ_- is the radial stress at $r = R$, V_f and V_m are the volume fractions for the fibre and the matrix respectively. The adhesion between fibre and matrix is considered to be perfect. By introducing regions of *imperfect* or *failed* interface, a better simulation is achieved. A suggestion regarding the governing regime as far as stresses are concerned could be the following condition (similar to the single discontinuity analysis [**McCartney 1989**]):

$$\tau_{rx}(R,x) = \mu\sigma_{rr}(R,x) + \tau_y \qquad (5.10)$$

where μ is the coefficient of friction τ_y is is *interfacial shear yield stress*. An application of this approach could be useful in an interpretation regarding interfacial failure. A prediction of the onset and propagation of the interfacial damage is possible by calculating the total energy release rate associated with it. Various changes in the equilibrium and boundary conditions make the model a flexible tool for other types of single fibre composite tests.

5.2.3. Numerical Approaches.

In complicated (mostly three dimensional) engineering systems where stress functions are difficult to obtain theoretically, simulations based on various numerical methods are widely employed. These methods, such as *Finite Element Analysis* (FEA) or *Finite Differences Analysis* (FDA) have been used succesfully in the field of composite materials. By satisfying the *boundary* and *equilibrium conditions*, numerical values of the stress functions at each individual element or array can be determined. These techniques are interesting and very useful, due to their major advantages over the elaborate theoretical approaches: (a) suitable for almost any type of problem regardless its complexity (b) controlled approximation with mimimum calculations, (c) easy alteration by simple input modification and (d) fast data aquisition.

An early attempt at studying the stress transfer mechanism in a single fibre model composite focussed on the influence of the shear stress concentration upon the fibre tip geometry [**Carrara 1968**]. Three different geometries were studied: (i) blunt end, (ii) tapered end and (iii) ellipsoidal end. It was found that over all geometries, the gradually tapered end showed the lowest shear end concentration.

The extremely difficult task of studying the existence of the interphase by introducing a thin layer of a third phase in between fibre and matrix can be

handled more effectively with FEA techniques. A model based on interphase simulation was proposed [**Broutman 1974**]. A thin layer of a 'third' material was introduced between the fibre and the matrix. The mechanical properties of this finite interphase layer were variable. It was found that the the shear stress concentration factor and the axial fibre stress attenuation to a maximum value (i.e. the 'transfer length'), increase with the increase of the interphase Young's modulus. In fact, one could say that a 'soft' interphase would accomodate a shear stress concentration by local matrix yielding in contrast to a 'stiff' interphase which would relieve shear stress concentration by matrix cracking.

In another analysis, the FDA analysis was applied for simulating the 'bonding efficiency' between fibre and matrix in a single fibre model composite [**Termonia 1987**]. This was achieved mathematically by varying the interphase thickness and introducing breaking bonds at the fibre-matrix with probability. It was found that the stress transfer efficiency decreases with the increase of the fibre's modulus and the *adhesion factor*. In fact, the transfer length is doubled if the number of breaking bonds is 30%. A reduction of the matrix diameter also led to a slow build-up of axial strain on the fibre.

Considerable efforts towards the understanding of stress transfer mechanisms have been applied over the last four decades using theoretical approaches or numerical techniques. The ultimate aim of these efforts is the derivation of all stress components arising in the interface/interphase, either in a closed-form function or in a local-type individual estimation. Consequently, the design of *better* interphases can be achieved. This can only be succesful if complicated interfacial phenomena are mimicked in a more realistic way. This is possible if the interphase is regarded as a phase with finite thickness of random mechanical properties along the fibre axis (x-direction) and a gradient of properties across the fibre axis (r-direction) rather than a geometrical surface shared between the fibre and the matrix.

5.3. Experimental techniques for interphase strength evaluation.

5.3.1. Indirect methods: full composite (FUC) tests.

An extensive survey of all major theoretical approaches concerning interfacial mechanisms in model composites was presented in the previous section. In this section, various experimental techniques employed for interfacial shear strength (IFSS) evaluation are reviewed and discussed. These techniques can be subdivided into two general categories: (i) techniques employing full composite tests (FUC), also termed as *indirect methods* and (ii) techniques employing single fibre composite tests (SFC), also termed as *direct methods*.

Techniques classified in the first group (**[Chamis 1974]**, **[Jones 1975]**, **[Whitney 1984]**) involve standard composite tests such as the following:

- short beam shear test (three-point bending test),
- four-point bending beam test,
- Ioscipescu shear test and,
- transverse loading test.

Generally the stress field during testing of the above tests is rarely pure in-plane shear so the results obtained from those tests are rather qualitative. Macroscopic properties such as interlaminar shear strength, flexural strength or transverse strength are measured and assumed to be related to the interface strength. A schematic representation of the most commonly used direct tests is shown in figure 5.6a,b. A special category of tests by means of photoelastic analysis which are usally applied to SFC rather than FUC samples, will briefly discussed in the following section.

5.3.2. Photoelastic techniques.

Standard photoelastic methods have been succesfully applied to yield the nature of the matrix stress field in specially fabricated model composites. The underlying principle of these techniques is based on the 'optical anisotropic' (birefringent) behaviour of the matrix material induced by internal stresses arising due to shrinkage or a macroscopic stress applied to the composite. If ϕ is the angle between the y-axis (parallel to the direction of loading) and the principle axis of σ_1, the interfacial shear stress can be determined by means of the following formula:

$$\tau_{xy} = \frac{1}{2}(\sigma_1 - \sigma_2)\sin 2\phi = \frac{C_\sigma}{2t} N \sin 2\phi \qquad (5.11)$$

Stress transfer characteriation involving different combinations of fibre/matrix adhesions in model composites were carried out by many researchers and summarized in the following table:

Reference	System
[Schuster 1964]	Sapphire whisker / Photoelastic resin
[Tyson 1965]	Dural strip* / Araldite
[McLaughlin 1966,1968]	Strips PLM-4B** / Epoxy resin
[Allison 1967]	Dural strip* / Araldite
[McGarry 1968]	Glass fibre / Epoxy resin
[Hunter 1973]	Glass fibre / Epoxy resin
[Starikovskii 1984]	Laminated carbon-reinforced plastic
[Ashbee 1988]	Carbon fibre / Epoxy resin

Table 5.1: *Photoelastic investigations in model composites.*

* Aluminium whisker
** Brittle epoxy strips as "fibres"

In one of the first investigations **[Schuster 1964]** photoelastic techniques were employed in order to calculate stress concentration factors in a model SFC specimens (sapphire whiskers embedded in a birefringent resin). Three different whisker end conditions were examined: (i) blunt end, (ii) irregular end and (iii) fine tapered end. The last condition caused the smallest stress concentration and the first condition the largest. The shear stresses reached their maximum values half diameter away from the whisker tip. The radial stresses were extended radially into the matrix by approximately 4 to 5 whisker diameters.

5.3.3. Direct methods: single fibre composite (SFC) tests.

SFC tests are favoured by many researchers mainly because they provide a consistent tool for *in situ* assessment of the adhesion strength of various fibre/matrix systems. Furthermore, the evaluation of fibre/matrix adhesion without the influence of neighbouring fibres and/or fibre ends is a prerequisite for gaining information about fibre/matrix interactions at a fundamental level **[Jahankhani 1991]**. Although no official protocol exists for most of these tests by either American or British Standards, the tests are classified in the literature by the following names:

Reference	Test
[Broutman 1966], [Chamis 1974], [Miller 1987]	fibre pull-out test micro-bond test
[Mandell 1980,1986], [Tse 1985]	microindentation test
[Broutman 1970]	shear debond test
[Hawthorne 1974]	tensile debond test
[Kelly 1966],[Frazer 1975], [Drzal 1982]	fragmentation test

Table 5.2: *Various single fibre composite (SFC) tests available in the literature.*

A brief review of the above tests is presented in this section with emphasis on the fragmentation test. A modified version is employed for IFSS estimation of LCP fibre/epoxy resin SFC model tests with LRS. All the above configurations are summarised schematically in figure 5.6c-h.

Single fibre composite (SFC) techniques can be devided in two major categories, according to the specimen's geometry. In the first category, the fibre is partially embedded in the matrix (pull-out, micro-bond type of geometries) or it can be isolated from neighbour fibres for testing (push-in, microindentation type of geometries). The latter, are not trully SFC tests. In the second category, the fibre is totally embedded in the matrix and the tests associated with this geometry are termed as 'coupon tests'. These tests are the fragmentation test, shear/tensile debond tests and the short fibre coupon test (SSFC) [**Galiotis 1984**], [**Robinson 1987**], [**Jahankhani 1991**]. More details of the above will be given in the following paragraphs:

A. Pull-out test. The original idea of measuring adhesion of polymeric binders to glass fibres by the so called 'pull-out test' was developed in the early 1960's [**Shiryaeva 1962**]. The adhesion strength can be calculated from the following relationship:

$$\tau_{au} = \frac{P_{max}}{\pi d \ell} \tag{5.12}$$

where P_{max} is the maximum load applied to the fibre, **d** is the diameter of the fibre and ℓ is the embedded length of the fibre.

If the value of the maximum axial stress applied to the fibre, σ_{max} ($\sigma_{max} = \frac{P_{max}}{\pi d^2/4}$), exceeds the fibre strength, σ_{fu}, the fibre will fail in tension before pull-out occurs [**Broutman 1969,1970**]. Therefore, the embedded length of the fibre during the test is limited by a threshold value.

The pull-out process is extremely complex and is not controlled by the embedded length of the fibre only **[Chua 1985]**, **[Marotzke 1993]**. Parameters such as hydrostatic pressure at the interface, interfacial friction coefficient, fracture energy of the interface adhesion and fibre free length are equally important. The dependence of the interfacial strength upon these parameters has been studied theoretically in the literature. Initial work was based on a shear-lag type of analysis **[Greszczuk 1969]** which was modified to account for the debonding of the fibre from the matrix **[Lawrence 1972]** or the variation of hydrostatic pressure **[Takaku 1973]**. Up to date, there are two different geometries of fibre pull-test, presented in figure 5.6c,d.

It was, however, found that the pull-out test is not suitable for LCP systems such as Kevlar®49/thermoplastic materials **[Eagles 1976]**. Observations after testing revealed the complexity of the failure mode at the fibre-matrix interface. The predominant failure mode was fibre debonding at the interface with, in some cases, cohesive failure of the fibre surface resulting in strips of fibre skin torn and separated from the fibre surface.

B. Micro-bond test. This method is a modified version of the fibre pull-out test where the matrix in a 'droplet' form is pushed away from the fibre instead of fibre pull-out, shown in figure 5.6e **[Mandell 1980]**, **[Miller 1987]**. The method has distinct advantages over the classical pull-out test (easy to fabricate, maintenance of droplet shape after curing). The data interpretation depends on whether interfacial stress distributions are uniform (interfacial failure occurs by yielding) or non-unform (interfacial failure occurs by crack propagation). In the latter case, fracture mechanics analysis is employed to interpret the results **[Chua 1985b]**, **[Penn 1990]**. On the other hand, high stress concentration factors at the locus of the fibre edge, affect interfacial shear strength measurements **[Gu 1995]**.

C. Microidentation test. Another type of test which is considered as SFC type of test although it is usually performed in full composites is the 'microindentation test', schematically presented in figure 5.6f **[Mandel**

1980,1986], [Tse 1985]. The fundamental equipment for this type of test includes a microdebonder which is attached to a powerful optical microscope. The microdebonder consists of a rod with a tapered fine, usually diamond tip. A single fibre from the well polished cross-section of the specimen is isolated, focused and aligned at the centre of the objective lens. The microdebonder takes over and the debonding force is recorded electronically. The compression stress is calculated (by measuring fibre diameter and interfibre distance at the onset of the interfacial debonding). This is converted to interfacial shear stress by means of stress analysis and FEA [**Mandell 1986**]. The method has not gained much popularity among interface researchers because expensive equipment is required and also it does not derive a straight forward measurement. Also, the test is more suitable for carbon fibres because LCP fibres tend to deform or be penetrated by the microidentor rather than pushed out.

<u>D. Shear/Tensile Debond test.</u> Another alternative method of measuring interfacial strength of composites is the 'shear/tensile debond' test which has been developed in two different geometry configurations [**Broutman 1970**]: (i) the 'shear debond' and (ii) the 'tensile debond' arrangements. The methods can be classified into the coupon type because the fibre is fully embedded into the resin.

The technique involves an axial compressive loading of either a trapezoidal shape specimen (first case) or a curved neck shape specimen with a single embedded fibre. The trapezoidal specimen is designed to fail the interface by shear and the curved neck specimen is designed to fail at the interface by tensile debonding. The method is suitable for interfaces of glass fibres but is not appropriate for interfaces involving LCP fibres because in general LCP fibres have very low compressive properties and therefore the fibres will fail in compression before any interfacial failure occurs. Also, the special geometric requirements of the specimen make their fabrication very difficult. In figure 5.6g,h the geometries of the shear debond and tensile debond tests are demonstrated.

E. Classical Fragmentation test. The most common method for interfacial strength evaluation is the 'classical fragmentation' test, originally designed and developed in brittle fibre/metallic matrix composites **[Kelly 1966]** by taking into account the plastic behaviour of the metallic matrix and the fibre stress to failure (see previous section). A continuous single filament is embedded in the matrix, as seen in figure 5.7. One important requirement is that the failure strain of the embedded fibre is much lower than the failure strain of the matrix. The specimen is gradually loaded in tension parallel to the fibre at well defined increments of strain. Stress is induced in the fibre by shear mechanisms along the fibre surface. When the fibre stress reaches the tensile strength of the fibre, the fibre will begin to fracture. By increasing the macroscopic applied strain in the specimen, the stress in the fibre will build up from the broken ends of the fibre until fibre fragments fracture again and the process repeats itself. As the stress in the fibre is induced by shear stresses along the interface, the maximum attainable fibre stress is limited by the fibre length and the maximum achievable shear stress at this interface.

Successive fibre fractures will continue to occur with the increase of the applied strain until the fibre fragments reach a critical fibre length L_c; further application of loads will not induce further fibre fractures. Thus, an equilibrium is reached between interfacial shear stress forces and tensile strength of the fibre, at a particular fibre fragment length. By balancing the forces acting at the interface, the following equation for the interfacial shear stress $\tau_i(x)$ can be derived:

$$\tau_i(x) = \frac{d}{4}\frac{d\sigma_f(x)}{dx} \qquad (5.13)$$

where $\sigma_f(x)$ is the fibre stress at each point x along the fibre length and **d=2R**, of course, is the fibre diameter.

Kelly assumed that the shear stresses between fibre and metal matrix along the fibre fragment are constant, a fair assumption for metal matrices [**Kelly 1966**]. At the saturation level, the maximum fibre stress equals the fibre strength and the fibre fragment length equals the critical fibre length. Integration of the equation 5.13 over the fibre fragment length L, yields:

$$\tau_i = \frac{\sigma_{fu(L_c)} d}{2L_c} \tag{5.14}$$

where $\sigma_{fu(L_c)}$ is the strength of the filament of length L_c.

The above value of the fibre strength at the critical length is difficult to measure. The mean fibre strength is a function of the fibre length. As the fibre fragment lengths range from several hundred microns to a few millimiters, experimental data are not easy to obtain. Therefore, extrapolation from tests on longer gauge lengths are carried out. This involves direct measurement of the strength statistics of a large number of fibres of various lengths [**Drzal 1982,1983**], [**Bascom 1986**] or, alternatively, of a fixed length and the application of Weibull statistical methods for the calculation of the fibre strength at the critical length, [**Ohsawa 1978**], [**Jacques 1989**], [**Netravali 1989**] [**Baillie 1993,1994**]. Methods have recently been suggested to derive the fibre strength indirectly from the fibre fragment length distribution [**Wagner 1990**] [**Baillie 1993,1994**].

In most fibre/matrix systems, the fragment length will reach saturation when the applied strain is approximately equal to three times the mean fibre fracture strain. Consequently, the failure strain of the matrix should be at least three times that of the fibre. In the case of LCP fibres, the classical fragmentation test is not applicable because the fibre fracture strain (aramids and PBO) is very high (2.0-3.5%). Also, LCP fibres fail in tension by transverse cracking followed by longitudinal splitting and therefore a clear fibre fracture in the epoxy cannot

be detected. A coupon geometry based on short single fibre composite is used instead for IFSS evaluation which is described in the following section.

To summarise, the assumption of constant interfacial shear stress is not correct, even at high macroscopic applied strains. In fact, when the stress transfer mechanisms between the fibre and the matrix are 'elastic' (low macroscopic applied strains), the shear stresses developed in the interface are not constant. The 'interfacial shear strength' obtained in this case is an average value of the real situation.

5.3.4. The single short fibre composite (SSFC) test.

The major disadvantage of the continuous single fibre composite (CSFC) test (i.e. classical fragmentation test) is the fact that it can only provide an average, general estimation of the stress field developed in the interface region at macroscopic applied strains higher than the fracture strain of the fibre. In fact, the fragmentation procedure has to be completed and the critical length L_c to be obtained, in order to evaluate qualitatively the interfacial shear strength (IFSS) for the given system. Also, it is only possible to provide very little or no information about many complicated interfacial phenomena arising during the gradual deformation of the specimen from the first fracture appearance to saturation of the fragmentation process. These phenomena, associated with mechanisms which trigger failure/damage of the interfacial bond in the vicinity of a fibre fracture, which could be partial or total scission between fibre and matrix are termed as 'debonding' or even local plastic 'yielding' of the bulk matrix.

Generally speaking, discontinuities such as fibre fractures occur during manufacture of composite laminates or exist due to the nature of the composite (see short fibre composites). Also, the engineering design of composites is based on very low strain to failure (less than 1%) calculations. From that point of view,

CSFC coupon tests derive very limited information with respect to stress transfer mechanisms and, even, interfacial shear strength.

The above limitations led to the development of a second type of single fibre composite (SFC) coupon geometry involving a short fibre embedded in the matrix (SSFC). The application of this geometry for the first time involved needle-like polydiacetylene (PDA) crystals embedded in a two-part, solvent free cold-setting epoxy resin from Ciba-Geigy **[Galiotis 1984]**. Stress transfer mechanisms of other type of PDA/Epoxy **[Robinson 1987]** or aramid/epoxy **[Jahankhani 1991]** composites were examined by means of this coupon geometry using laser Raman Spectroscopy.

The advantage that the SSFC test offers over the classical fragmentation test geometry is that strain and/or stress transfer profiles and transfer lengths for reinforcement at various levels of applied macroscopic strain are obtained at the very onset of the loading process and prior to fibre fracture. Also, residual stresses induced during curing can be detected. It is also possible to monitor yield/failure mechanisms in the vicinity of the interface along with stress concentration measurements in model composites with blunt cracks. Thus, *in situ*, point-to-point strain and/or stress measurements in the reinforcing filament can be determined accurately. Finally, the interfacial shear stress distributions can be derived along the fibre length and at various levels of applied macroscopic strains. In this work, the SSFC coupon geometry was employed to monitor interfacial phenomena for model LCP fibre/epoxy systems. The relevance to the adhesion strength of the following parameters was examined:

- *the effect of the fibre modulus,*

  (Kevlar®49/Epoxy vs Kevlar®29/Epoxy)
- *the effect of the fibre diameter,*

  (Kevlar®49 ht1/Epoxy vs Kevlar®49 ht2/Epoxy)
- *the effect of the LCP fibre structure,*

  (PBZT-Z1/Epoxy).

5.4. Experimental.

5.4.1. Short Single Fibre Composite (SSFC) Specimen Preparation.

Detailed descriptions of specimen fabrication and other experimental procedures are given in the following paragraphs. The simple model which was employed for interfacial shear stress measurements is also applied here.

The specimen preparation procedure is as follows: Short individual filaments of approximately 1-3mm in length were carefully chopped from the continous yarn by means of ceramic scissors. Special care was taken that all selected short fibres for SSFC specimen fabrication were from separate filaments of the yarn. Rubber moulds designed according to the above specifications were half-filled with a two-part, solvent free epoxy resin supplied by Ciba-Geigy. The resin was prepared following the manufacturer's specifications by mixing 100 parts of resin (*Araldite LY 1927 GB*, modified epoxy novolac resin) to 36 parts of hardener (*Hardener HY 1927 GB*, amine curing agent) by weight. The resin was allowed to set partially for about half hour. A single short filament was very carefully lifted by means of a very fine pair of tweezers and positioned at the surface of the epoxy layer. Extreme care was taken to align the filament parallel to the specimen's symmetry axis. A second batch of epoxy resin was prepared and poured into the mould. The whole procedure was completed by transferring the mould into an enviromental chamber and allowing the specimens to cure for seven days at room temperarure with temperature fluctuation at a minimum of $\pm 1^{\circ}C$.

Specimens which contained misaligned fibres or other defects, such as air bubbles, were discarded. The selected specimens were ground uniformly in order to bring the embedded fibre to about 400-500μm from the resin surface. At the final stage, they were extensively polished to a high level in order to prepare a perfectly smooth surface. The final geometry and specifications of LCP fibre/ epoxy resin SSFC coupon is schematically shown in figure 5.8.

5.4.2. Mechanical Characterisation of the Matrix.

The mechanical characterisation of this epoxy involved tensile testing of specimens with geometry given in figure 5.8. The specimen preparation was based on the manufacturer's specifications (see previous section). The stress-strain relationship of this epoxy system was monitored by using a mechanical tester supplied by Hounsfield Tensile Testing Equipment. A 1000N load-cell at full-scale was employed for load measurements. The cross-head speed was 1mm/min, corresponding to $0.025min^{-1}$ for the above specific geometry.

5.4.3. Optomechanical measurements in SSFCs.

Various different specimens fabricated according to the description above were checked randomly with the Laser Raman microscope for good quality spectrum repeatability. White light was also used for conventional examination under the microscope. One specimen at a time was finally selected for IFSS measurements. Four sensitive strain-gauges (nominal resistance 350.0±0.5Ω and *gauge factor* 2.09 from the manufacturers) were attached to the top and bottom surface of the specimen by means of a strong CN adhesive. The specimen was ground locally at the future strain-gauge locations for satisfactory strain-gauge attachment and reliable strain monitoring. Instant reading of the strain-gauges resistance was obtained by means of a digital multimeter. The strain-gauge resistance was converted to strain ε_{∞} (macroscopic applied strain) by applying the following equation:

$$\varepsilon_{\infty} = \frac{1}{k_s}(R_s - R_0) \tag{5.15}$$

where k_s is the gauge factor, R_0 is the resistance of the strain-free strain-gauge and R_s is the resistance indicated at the multimeter during the experimental procedure. It must be mentioned that above 3.0% applied strain the strain-gauge

reading is only an indicative measurement. This is due to the fact that the correlation between strain-gauge resistance and strain deviates from linearity at those levels and a correction factor may be needed.

The microtensometer employed for specimen stretching is shown in figure 5.9. It was designed and manufactured for tensile testing of this particular coupon geometry and can be accomodated under the Raman microscope. The candidate specimen was carefully mounted on it by clamping its ends between its jaws and secured by tightening the screws. The local strains were continually monitored during tightening to avoid imparting undesirable bending tensile or compressive stresses to the specimen. Finally, the microtensometer was positioned on the experimental stage under the Raman microscope. The stage is translated in xy-direction (specimen's plane) and z-direction (laser beam direction) by means of three heavy duty micrometers with a resolution of 10 μm.

A typical microphotograph of a short single aramid filament embedded in epoxy resin is given in figure 5.10 (fibre diameter 12μm). A higher magnification of the fibre tips is also shown. It is quite clear that blunt tips are impossible to achieve. In fact, the less deformed ends were obtained by cutting with the ceramic scissors. Other attempts at cutting with sharp blades or even by snapping the fibre after freezing it with liquid nitrogen were not successful.

A typical experimental procedure for monitoring stress transfer along the fibre length is as follows: The specimen is stretched gradually by pulling apart the moving jaw of the microtensometer. This can be achieved by rotating a small lever connected to a set of gears and a long screw attached to the moving jaw of the microtensometer. Slow travelling of the moving jaw results in accurate incremental steps of applied strains to the specimen. In fact, it has been calculated that one full turn of the lever corresponds to approximate elongation of 1.75mm which is converted to approximately 0.20% of applied strain. This is an alternative method of monitoring the strain on the specimen, although one should expect some 'slippage' at high strains and therefore the strain-gauge measurement would be more reliable.

At every level of applied strain, Raman spectra are obtained along the embedded fibre starting approximately 10μm away from either fibre end. Spectrum acquisition occurs at increments of 10μm close to the fibre ends and 20μm in the middle of the fibre. As a result, a detailed 'Raman frequency profile' can be obtained for each macroscopic applied strain level. Raman spectra from stress free (in air) individual filaments were also collected prior to each 'Raman mapping'. Therefore, the Raman frequency ν_0 which is used for stress monitoring (see chapter 3) was accurately calculated by averaging the values for all strain-free filaments data. Thus, the experimental strain value was calculated by employing the following calculation:

$$\sigma_f(x) = \frac{\nu^f(x) - \nu_0}{k} \tag{5.16}$$

where $\nu^f(x)$ corresponds to the Raman frequency measurement at each individual point along the embedded fibre axis and **k** is the Raman frequency stress dependence which as mentioned in the previous chapter, is a unique parameter for different families of LCP fibres.

Prior to any application of macroscopic load to the model composite, Raman spectra were also obtained along the fibre axis in order to investigate the amount of residual strain in the fibre due to the matrix shrinkage. It was found that a small amount of compressive strain was always deposited on the fibre.

Following the above conversion, 'Raman frequency profiles' were transformed to 'axial fibre stress profiles' along the embedded fibre. A full set of these profiles were produced for each system and its tensile loading history. Three different set of data were obtained for each individual interface system for a good statistical examination. In general, the behaviour of each system was unique within the experimental error.

5.4.4. Estimation of the Interfacial Shear Stress Distribution in SSFCs.

In our short fibre model composite configuration there is no influence of neighbouring fibres and/or fibre discontinuities. It is, therefore, assumed that the stress is transferred to the fibre by a shear mechanism between the fibre and the matrix. This is in full accordance with the shear-lag analyses presented earlier. This correlation is a result of the assumed balance of stresses at the interface for an infinitely small fibre element described by the equation 5.2. This leads to **[Jahankhani 1990], [Melanitis 1991]**:

$$\tau(x) = \frac{R}{2}\frac{d\sigma_f(x)}{dx} \tag{5.17}$$

where **R** is the fibre diameter and $\sigma_f(x)$ is the experimental data for fibre tensile stress versus position along the fibre. The experimental data are fitted with cubic spline routines (identical to those used in the previous chapter) and the derivatives are estimated by means of the cubic spline coefficients of the cubic spline interpolations. A full account of the procedure is given in the Appendix 2.

The advantage of the method lies in the fact that an *in situ* measurement of the axial tensile stresses acting along the fibre length and the interfacial shear stresses acting at the interface along the fibre length can be derived experimentally for different far-field applied strain levels.

In the previous sections the micromechanics of stress transfer for various SSFC systems concerning LCP fibres and a room temperature, two-part epoxy resin was monitored in detail. Axial fibre stress profiles were produced and interfacial stress profiles were derived by means of a balance of forces argument. The interfacial strength for a number of systems with different characteristics was estimated.

5.4.5. Modelling Stress Transfer in SSFCs with Finite Element Analysis (FEA).

In this section, an investigation of stress transfer characteristics using Finite Element Analysis (FEA) will be presented for one of the systems. This investigation provided us with some more in depth knowledge of the complicated stress field and interfacial characteristics of these model composites. An advantage of the FEA method is that simulations for stresses and strains in three dimensions can be obtained both for the fibre and the matrix. Therefore, a more detailed picture of the mechanisms associated with any deformation and/or damage of the interfacial adhesion can be produced.

The Finite Element Analysis model.

The work was carried out in collaboration with a co-worker **[Guild 1994]**. The FEA package used was LUSAS™ running on a Convex C240 or C3840 computer. The results from the simulation were directly compared with the experimental results. This comparison between FEA results and LRS data is very important because it enables (a) refinement of FEA modelling applied to single fibre model composites, (b) evaluation of the model and the location of the interfacial failure and (c) an assessment of the accuracy and the validity of the balance of forces argument for converting spectroscopic data to stress profiles (axial fibre tensial and interfacial shear).

The existing symmetry for a system such as single fibre in a block of epoxy resin was fully exploited to reduce the size of the model and therefore the computing time. The FEA model required was a single fibre surrounded by sufficient bulk resin that the stress transfer is unaffected by the edges of the simulating grid. In figure 5.11 the chosen model, which comprises a cylindrical fibre centered in a cylinder of matrix material, is shown. The FEA model was drawn by using axisymmetric elements for the rectangle ABCD. A one radian segment of the cylinder represented by the rectangle is analysed. The grid was drawn using eight-noded axisymmetric elements. Typically the grid was drawn using 1944 elements. Such refinement was found necessary to obtain radial stress continuity across the interface, except around singularities, i.e. regions where

discontinuities occur for the stress functions and are difficult to be modelled numerically. The tensile deformation is simulated by applying prescribed displacements to the nodes along the top, CD. The sides AB and AD are restrained, in order to remain stationary arising from the symmetry status of the whole cylinder. The shape of the deformed grid is also indicated in figure 5.11a.

The grid shown in figure 5.11a indicates a cylindrical fibre with a square end. A magnification of the FEA grid around this square-end fibre is shown in figure 5.10a. The corner node of the last fibre element is a singularity. In other words, mathematical continuity of the stress functions cannot be achieved at this point. This could be physically understood by the hypothetical occurrence of infinite stress value at the point of singularity. The effects of the singularity on measured stress values may extend across several nodes beside and below the singularity point. The shape of the end of the Kevlar®49 fibre chopped from the fibre yarn indicates the existence of stress concentrations. This 'mushroom' type of shape could be most closely represented with the square-end model. However, by rounding the fibre corner, the mathematical instability is smoothed out. An alternative grid, with the end of the fibre rounded was developed and it is shown in figure 5.11c.

The accuracy of the FEA modelling is crucially dependent on the accurate description of the material properties of the constituent materials. Earlier attempts to model single fibre composites with FEA were based on models assuming elastic behaviour of the reinforcing fibre and matrix [**Robinson 1989**]. In this analysis, the model is based on an axisymmetric analysis, including stress calculations in three dimensions. The fibre is modelled as linear elastic, with orthotropic material properties. A more accurate model would require elasto-plastic behaviour for the fibre, taking into account stress hardening effects in the mechanical behaviour of aramid fibres, already discussed in the previous chapter. Nevertheless, to a first approximation and for the purposes of the model, a linear behaviour is satisfactory for Kevlar®49 ht1. The Young's modulus parallalel to the fibre axis was obtained from the least-square fit to experimental

data. The Young's modulus normal to the fibre axis along with the two Poison's ratios were obtained from the literature [**DeTeresa 1984**]. The epoxy resin is modelled as isotropic but with elasto-plastic material properties defined by the von-Mises yield criterion. This fundamental introduction of material non-linearity in the model is very important for a better understanding of the interfacial behaviour of systems such as aramid fibre / epoxy resin.

5.5. Results.

5.5.1. Mechanical Properties of the matrix.

A typical tensile stress-strain curve of the bulk epoxy resin is shown in figure 5.12a. The curve represents a cubic-spline fit to a set of experimental data from eight different tests. As can be seen, the correlation is significantly non-linear. In figure 5.12b, the Young's modulus is plotted as a function of the applied strain. As expected, the initial Young's modulus of the matrix E_{m0} of 2.60±0.30GPa, drops to lower values with the increase of applied strain. The tensile yield stress of the matrix σ_{my} is evaluated to be 70±4 MPa. By applying the von Mises failure criterion, the matrix yield stress in shear, τ_{my}, is estimated to be of the order of 40±2 MPa.

For numerical modelling purposes of the non-linear behaviour of the matrix material, its stress-strain curve was sectioned into a series of linear steps. There is no limit to the number of straight line portions defined. The initial portion represents the perfectly elastic region, the second portion represents the elasto-plastic region and the third portion represents the perfect plastic region. This last portion is extended to infinite strain in this numerical approximation.

5.5.2. Interfacial measurements in Kevlar®49/Epoxy System.

The examination of the interfacial properties was performed for a number of aramid fibre/epoxy systems. Firstly, a medium Young's modulus aramid fibre with 'no finish', Kevlar®49, was investigated. In the following section, the results obtained from an also 'un-finished', low Young's modulus, Kevlar®29, will be shown. A direct comparison between the Kevlar®49 system with no finish and a commercial Kevlar®49 system with 'finish' [**Jahankhani 1989**] can now be made. It has already been reported in the literature that Kevlar® fibres with 'finish' had greater interfacial bond strength to various matrix materials compared to fibres with no 'finish' [**Eagles 1976**].

Prior to any application of strain to the SSFC specimen, two scans along the fibre were performed with the Laser Raman probe. In the first scan, an estimation of the residual stresses along the fibre due to matrix shrinkage could be identified, as seen in figure 5.13a. It is shown quite clearly that axial compressive stresses reaching an absolute maximum of 200 MPa in magnitude in the middle were induced in the fibre. These stresses, form a plateau in the middle of the fibre and drop to zero at the fibre tips, within of course, the experimental error. After mounting the specimen onto the microtensometer, a second scan was performed. As can be clearly seen in figure 5.13b, a combination of small tensile stresses acting in the fibre due to gripping have been induced in the fibre. Although the filament is still in compression, only an (average) of 80-100MPa compressing stresses are now acting in it. The application of a small applied macroscopic strain (0.20%) brings the filament in tension (fgure 5.13c).

The variation of the axial fibre stresses along the fibre length and the interfacial shear stresses derived from the conversion of the cubic spline fit to the direct experimental data are shown for a number of applied strain levels ε_m (0.85%, 1.25%, 1.85% and 2.50%) in figures 5.13d-g and 5.14a-d respectively. The stress transfer from the matrix to the fibre up to 1.00-1.20% applied macroscopic strain ε_m is similar to the elastic stress transfer model [**Cox 1952**]. Both fibre and

matrix to a very close approximation are deforming in the elastic region. The axial fibre stress builds up from a low non-zero value very close to the fibre tip to a plateau in the middle of the fibre. Measurements at the exact locus of the fibre tip cannot be made due to the distortion introduced by the cutting procedure (see figure 5.10). The plateau stress fluctuates around the elastically predicted value of $E_f\varepsilon_m$. The interfacial shear stress (ISS) profiles derived from the experimental data show that the maximum ISS values are located near fibre tips. Again, the lack of experimental data in the region of one diameter away from the fibre tip prevents any experimental evidence of the stress field very near the fibre tip discontinuity. Nevertheless, the ISS decays from a maximum value to zero towards the middle of the fibre, where matrix and fibre strains are the same.

The above distribution of axial tensile stresses and interfacial shear stresses along the fibre length indicate good adhesion between the fibre and the matrix. In fact, the maximum values of shear stresses at the fibre tips increase with the increase of the applied macroscopic strain up to a value of ~40 MPa. This value is close to the matrix yield stress in shear of the bulk matrix as calculated using the von Mises criterion.

By increasing the macroscopic applied strain in the composite above 1.20%, the axial tensile stress profiles on the fibre show a transition from a 'hyperbolic' behaviour to a less curved, near 'trapezoid' shape. This transition does not occur suddenly but in a rather gradual manner, by increasing the applied macroscopic strain from 1.20% to 1.85%. At this strain level, the phenomenon is clear. The ISS profiles change accordingly, with the maximum ISS value shifting away from the fibre tip. The locus of this maximum moves further away from the fibre tip with increasing applied macroscopic strain.

It is interesting to note that the maximum value of ISS fluctuates around the value of 40 MPa with any further increase of the applied macroscopic strain. At applied macroscopic strains higher than 1.80%, the maximum interfacial shear stress has been significantly shifted away from the fibre tip. The above

observation indicates that the shear stresses cannot exceed a critical threshold value, characteristic for the system under consideration. The results are summarised in table 5.3.

5.5.3. Interfacial measurements in Kevlar®29/ Epoxy System.

In order to examine the influence of the fibre modulus upon the stress transfer characteristics of aramid/epoxy systems, SSFCs of Kevlar®29/ epoxy were made and tested in a similar fashion. The axial tensile stresses along the fibre were monitored and converted to ISS profiles. The behaviour of such a system is somehow different. Kevlar®29 fibre has very high strain to failure and the matrix deformation was not sufficient to develop stresses of the same level as those in the Kevlar®49/ epoxy system. The same amount of applied macroscopic strain would develop almost half the amount of (plateau) axial tensile stress in the fibre compared to the equivalent value in a Kevlar®49 fibre.

For this sytem, the maximum ISS value increases with the increase of the macroscopic applied strain, up to a value of 40 MPa. This behaviour is observed up to 1.50%-1.80% strain. Beyond this level of applied strain, any further increase in the macroscopic applied strain does not lead to an increase of the maximum ISS value. This indicates that the maximum value of shear stress that the system can accomodate has been reached. Characteristic stress profiles and ISS profiles converted from the stress distribution data are shown in figures 5.15 and 5.16 (applied strain ε_{∞} of 0.65%, 1.00%, 1.50% and 2.75%) respectively. All the results are summarised in table 5.4.

5.5.4. Interfacial measurements in Kevlar®49 ht1/ Epoxy System.

In the previous two sections, two different aramid systems were examined: A medium Young's modulus fibre with no surface 'finish' (Kevlar®49/ epoxy SSFC system) and a low Young's modulus fibre also with no 'finish' (Kevlar®29/ epoxy system). Results from two heat treated fibres whose mechanical properties have already been discussed in the previous chapters will be presented here. The focus of this examination is on the effect of fibre diameter: One fibre (Kevlar®49 ht1), has a diameter of 11.9μm and the other fibre (Kevlar®49 ht2), has a diameter of 14.6μm. Their (nominal) Young's moduli are similar (120GPa). However, the tensile strain to failure of the 'thicker' fibre is slightly higher than that of the 'thinner' one.

The stress transfer characteristic of this system can be mainly understood by looking at the stress profiles at small applied macroscopic strains, intermediate applied macroscopic strains and high applied strains (figure 5.17). In the first part, stress transfer is elastic, according to Cox's model. Maximum ISS increases at low applied macroscopic strains up to a value which could be considered the strength of the interfacial adhesion, approximately of the magnitude of 40 MPa. At higher levels of applied strains, the maximum ISS value shifts towards the middle of the fibre. Tensile stress profiles and ISS profiles are given in figures 5.17 and 5.18 (for applied strains of 0.60%, 1.20%, 1.90% and 2.50%) respectively. A summary of the ISS results is given in table 5.5.

5.5.5. Interfacial measurements in Kevlar®49 ht2/Epoxy System.

Another very interesting system for examination is the Kevlar®49 ht2/ epoxy. The effect of fibre size is examined here by embedding a fibre with diameter of 14.6 μm in the same epoxy resin.

The stress transfer is again 'elastic' for applied macroscopic strains less than 1.2%. For strains higher than this value but less than 1.70-1.80%, although

the axial tensile stress profiles are of 'Cox's' type, the maximum shear stresses developed at the interface do not increase any further (figure 5.19). For very high macroscopic strains (beyond 1.80%) the transition from one stress transfer mechanism to another is very obvious. Stress and ISS profiles along the fibre length are given in figures 5.19 and 5.20 (for the applied strain levels 0.60%, 0.90%, 1.50%, 2.00% and 3.00%) respectively. Quite surprisingly, even at the extreme level of 3.00% applied strain, an amount of 3500 MPa axial tensile stress is carried by the fibre, well above its strength. In table 5.6, the data are summarised for experiments concerning the system Kevlar®49 ht2/ epoxy for all strain levels.

5.5.6. Interfacial measurements in PBZT-Z1/ Epoxy SSFC System.

In the previous paragraphs results concerning aramid fibres systems were presented and parameters such as fibre diameter and Young's modulus were examined by using the same matrix as reference for SSFC preparation. A different fibre, PBZT-Z1, was also employed for interfacial examination. The only information available about the fibre as far as its surface condition is concerned is that it is heat-treated with no sizing or finish.

The axial tensile fibre stress profiles along with interfacial shear stress distributions derived from the well known conversion from the balance of forces argument are given in figures 5.21 and 5.22 for four distinct applied strain levels. As can be seen, the stress transfer characteristics indicate a near Cox type stress transfer mechanism which changes gradually to a rather more parabolic type especially at the intermediate to high applied strains levels. The interfacial shear strength of the system is estimated to be 45MPa. Summarised results for all strain levels are given in table 5.7.

	LHS		*RHS*	
ε_m / %	τ_{tip} / MPa	τ_{max} / MPa	τ_{tip} / MPa	τ_{max} / MPa
0.20	4.3	4.3	13.6	13.6
0.50	15.3	15.3	18.3	18.3
0.70	24.8	24.8	28.1	28.1
0.85	33.4	33.4	33.7	33.7
0.95	29.4	29.4	36.6	36.6
1.05	35.4	35.4	44.2	44.2
1.15	29.3	29.3	44.7	44.7
1.25	40.4	40.4	38.6	38.6
1.35	30.2	30.2	32.9	32.9
1.45	6.2	30.1	30.7	30.7
1.60	33.3	33.3	35.7	35.7
1.75	16.8	30.9	36.8	36.8
1.85	12.8	35.1	26.7	29.9
2.10	23.9	28.7	38.9	38.91
2.50	15.5	26.6	39.8	39.8
3.00	27.3	30.9	34.5	34.5
3.50	0.0	15.2	11.9	22.7

LHS : Left hand side fibre tip RHS : Right hand side fibre tip

Table 5.3.: *ISS data for Kevlar® 49/ epoxy SSFC system.*

	LHS		*RHS*	
ε_{∞} / %	τ_{tip} / MPa	τ_{max} / MPa	τ_{tip} / MPa	τ_{max} / MPa
0.25	0.0	4.6	6.2	6.2
0.45	15.0	15.0	11.5	11.5
0.65	21.5	21.5	17.9	17.9
0.75	33.8	33.8	18.6	18.6
0.80	22.8	22.8	22.7	22.7
0.85	26.3	26.3	29.7	29.7
1.00	40.2	40.2	35.2	35.2
1.10	49.1	49.1	34.1	34.1
1.20	28.7	28.7	38.2	38.2
1.30	32.1	32.1	26.6	26.6
1.50	46.6	46.6	50.0	50.0
1.80	33.7	33.7	36.9	36.9
2.25	33.7	33.7	52.6	52.6
	29.5	29.5	41.9	41.9

LHS : Left hand side fibre tip RHS : Right hand side fibre tip

Table 5.4.: *ISS data for Kevlar®29/ epoxy SSFC system.*

	LHS		*RHS*	
ε_m / %	τ_{ip} / MPa	τ_{max} / MPa	τ_{ip} / MPa	τ_{max} / MPa
0.30	14.2	14.2	10.7	10.7
0.60	24.8	24.8	22.8	22.8
0.90	33.6	33.6	44.1	44.1
1.20	43.7	43.7	34.8	34.8
1.35	50.2	50.2	45.3	45.3
1.50	30.1	35.8	41.2	41.2
1.70	44.5	44.5	38.4	38.4
1.90	32.3	40.6	37.7	39.1
2.20	30.8	35.5	43.0	43.0
2.50	31.4	39.1	48.8	48.8
2.75	28.8	33.4	31.7	31.7
3.00	25.8	42.5	33.9	33.9

LHS : Left hand side fibre tip RHS : Right hand side fibre tip

Table 5.5.: *ISS data for Kevlar®49 ht1/ epoxy SSFC system.*

	LHS		*RHS*	
ε_{∞} / %	τ_{tip} / MPa	τ_{max} / MPa	τ_{tip} / MPa	τ_{max} / MPa
0.25	17.6	17.6	6.1	6.1
0.60	36.6	36.6	25.7	25.7
0.90	46.8	46.8	39.9	39.9
1.25	51.8	51.8	52.4	52.4
1.50	49.8	49.8	49.4	49.4
1.70	76.9	76.9	51.2	51.2
1.80	59.2	59.2	32.8	42.0
2.00	41.8	49.7	34.2	45.6
2.20	41.5	49.1	29.1	45.2
2.50	32.1	43.4	36.2	43.8
3.00	37.4	47.5	30.9	45.4

LHS : Left hand side fibre tip RHS : Right hand side fibre tip

Table 5.6.: *ISS data for Kevlar® 49 ht2/ epoxy SSFC system.*

	LHS		*RHS*	
ε_m / %	τ_{tip} / MPa	τ_{max} / MPa	τ_{tip} / MPa	τ_{max} / MPa
0.20	16.1	16.1	7.9	7.9
0.30	19.5	19.5	20.2	20.2
0.40	22.3	22.3	33.4	33.4
0.50	33.6	33.6	41.3	41.3
0.60	44.1	44.1	34.2	34.2
0.70	38.7	38.7	56.8	56.8
0.80	20.5	33.1	47.0	47.0
0.85	35.9	35.9	31.9	34.5
0.90	37.7	40.5	57.3	57.3
1.00	59.7	59.7	54.5	54.5
1.05	46.2	46.2	41.8	41.8
1.15	38.9	38.9	45.0	45.0
1.25	45.6	45.6	54.7	54.7
1.50	44.4	44.4	39.5	40.0

LHS : Left hand side fibre tip RHS : Right hand side fibre tip

Table 5.7.: *ISS data for PBZT-Z1/ epoxy SSFC system.*

5.5.7. FEA predictions for Kevlar®49 ht1/ epoxy resin system.

Comparison between experimental results and FEA predictions were made using simulations from both FEA models (square fibre end with mathematical singularity and round fibre end without mathematical singularity). More satisfactory agreement between the FEA and experimental results around the fibre tip is obtained if the we assume that the spectrum acquisition comes from a nominal depth of about 2μm. Since the amount of backscattered (Raman light) is inversely related to the fibre depth, the FEA results may indicate that the optical skin depth of Kevlar®49 fibre is of the order of about half a fibre diameter, allowing the scattering to 'peak' at 2μm. Therefore, the Raman measurements of fibre stress may be 'average' values assumed to be taken at a depth of about 2μm inside the fibre. In other words, the stress has reached its 'average' value at a depth of 2μm from the fibre surface. The FEA predictions of axial fibre stress were recorded and compared with the experimental results for the nodes at the fibre surface and for the nodes at 1.9 μm depth.

In figures 5.23 and 5.24 the experimental results for three applied strain levels (0.60%, 1.50% and 2.10% far-field applied strain) are compared with the predictions from the square end and round end models, respectively. It is quite clear that the existence of the singularity is responsible for the erroneous stress values at the fibre surface nodes near the fibre end for the higher strain level. In fact, the stress function is decreasing for about 15μm of length to a local minimum value and then increases towards the middle of the fibre, reaching an expected plateau value. On the other hand, the stress function at 1.9μm below is monotonic, starting, however, from negative values at the fibre end (for the higher strain levels). Overall, a more satisfactory prediction is derived from the round-end predictions. The FEA data are closer to the experimental measurements near the fibre end than those generated using the square end model.

It was shown in a previous section how experimental axial fibre stress profiles can be converted to interfacial shear stress (ISS) profiles by a simple balance of forces argument. In contrast, FEA modelling allows direct determination of the ISS profiles along the interface. Values of ISS for all applied strain levels discussed above were obtained for both square end and round end models. The predicted values are compared with the experimental values for all three applied strain levels mentioned above (0.60%, 1.50% and 2.10%) in figure 5.25.

The predicted values from the two different fibre end geometries are found to be in close agreement with the experimental results except around the end for the square end model. At low levels of applied macroscopic applied strains, the FEA predictions for the ISS distributions have a Cox model shape: maximum values at the fibre end which decay to zero towards the middle of the fibre, indicating elastic stress transfer. At higher levels of applied macroscopic strains, the FEA model predictions show interfacial shear stresses which reach a constant plateau value near the fibre end and then decay to zero towards the middle of the fibre. The length of this plateau increases with increasing applied strain.

The experimental results are direct measurements of the fibre stresses and show excellent agreement with the predicted stresses from the FEA model. However, due to the nature of the matrix material (amorphous solid), it is not possible to directly monitor the strain and stress distributions in the matrix experimentally. On the other hand, FEA can provide us with such estimations.

The yield behaviour of the resin material has been defined by the von Mises yield criterion. The contour diagrams of the von Mises strain were examined for all six strain levels. In figure 5.26, the von Mises contour diagrams are shown for the applied level 0.9%. Only the part of the grid which magnifies the tip of the fibre is shown. As can be seen, there are very high concentrations of von Mises strain. In fact, the highest value is 16.3% and its locus is at the interface, very close to the fibre length (see arrows in figure 5.26). However,

there is another position of high concentration of von Mises strain which is located in the bulk resin above the fibre tip. Similar features are observed for the contour diagrams of von Mises strain for all strain levels. The positions of maximum von Mises strain are all similar (at the interface near the fibre tip and in the matrix above the fibre tip). The correlation of the maximum values for the von Mises strain at the two loci described above with the macroscopic applied strain is demonstrated in figure 5.27a. At lower strain levels the two maxima are almost equal, but at higher strain levels the interface maximum rises to very high values.

The matrix material has been modelled as perfectly plastic for strains higher than 3.5%. In fact, for a strain level as low as 0.9%, this von Mises strain is reached at 3.7μm from the fibre tip. In general, the region of matrix subjected to von Mises strains higher than 3.5% (i.e. matrix material perfectly plastic) extends further towards the middle of the fibre with increasing the macroscopic applied strain. The extent of the perfectly plastic matrix for different strain levels is shown in figure 5.27b.

The presence of the fibre influences the level of von Mises strain close to the fibre. The extent of this influence may be described as the region around the fibre where the von Mises strain exceeds the strain that would exist without the presence of the fibre. Following that definition, the 'zone of influence' would extend to infinity. Therefore, a more realistic approach would be defining the 'zone of influence' as the region of matrix around the fibre where the von Mises strain exceeds the value expected with the fibre absent by more than a finite value of 10%, for the same applied strain. This 'zone of influence' contour was estimated for two different approximations: (a) perfectly elastic matrix and (b) elastoplastic matrix. These contours represent the extent of fibre influence upon the bulk matrix material. The results of the FEA approximation show that this shape is ellipsoid rather than a cylinder. The magnitude of the half minor axis of the ellipsoid was found in the order of 5-7 fibre radii for elastic response and increases to 7-9 fibre radii for elasto-plastic response of the matrix.

The FEA simulation assumes perfect bonding around the whole fibre and the matrix at the interface. Therefore, direct stress can be transferred across the fibre tip. The stress and strain profiles of the applied direct stress and strain through the middle of the fibre were examined. Two profiles, for 0.90% and 2.10% macroscopic applied strain are shown in figure 5.28. The stress continuity accross the interface is almost perfect. The direct stress transferred across the interface is approximately the same for the two strain levels at about 100 MPa. This must be due to the plastisication of the resin. The stress and strain concentrations only extend about 20 μm above the fibre tip. The stress in the matrix is at its maximum at the interface. However, the maximum strain in the matrix is about 6μm from the fibre tip. This is similar position to the maximum von Mises strain shown in the contour diagrams. The maximum strain in the matrix increases with increasing applied strain.

The stress transfer along the fibre length is mostly achieved via the interfacial shear stess. However, small direct compressive stresses also exist along the interface. These stresses are perpendicular to the applied strain, in the radial direction with respect to the interface. The compressive stress reaches its maximum at the end of the fibre. For 0.90% applied strain, the maximum transverse radia stress at the end of the fibre is about -5 MPa.

5.6. Discussion.

It has already been mentioned earlier in this chapter how the adhesion between fibre and matrix can affect the general behaviour of fibre reinforced composites. Usually, individual fibre fractures in a composite structure under service, initiate the complete, catastrophic failure of the structure. Since the stress transfer mechanisms in composites at fibre fractures/ends depend strongly upon the interfacial adhesion, these mechanisms influence strongly the fracture characteristics of these materials. Data concerning interfacial strength are very important for the design process of composite structures.

The methods for evaluating interfacial shear strength (IFSS) were reviewed in a previous section. FUC techniques generate IFSS results derived from loading configurations which do not induce in-plane shear stresses. Therefore the results are usually irrelevant to true IFSS between fibre and matrix. On the other hand, conventional SFC tests involve assumptions about the stress field in the interface which are not always close to the reality.

In contrast to the above, LRS has been proven to be a very accurate tool for measuring interfacial shear stresses in model SSFC coupons at microscopic level with high spatial resolution. The most important development in the results presented in the previous sections compared to results derived in a similar fashion in the past ([**Jahankhani 1990**], [**Melanitis 1991**]) is the ability to measure axial fibre stress instead of fibre strain. This is due to the fact that the Raman frequency shift vs fibre stress relation is used here as a calibration curve. This new approach is extremely valuable in the case of aramid fibre / epoxy systems because a distinct non-linear mechanical behaviour has been observed. Therefore, any linear correlation between Raman frequency shift and applied strain deviates from the linearity, especially at high strains where strain hardening effects are observed. Consequently, strain measurements in SFCs are underestimated. An important advantage of the above is the fact that in order to estimate interfacial shear stress distributions, stress profiles instead of strain profiles are fitted with cubic spline polynomials and the use of a 'nominal fibre modulus' is avoided (see Appendix 2).

In order to assess the mechanics of stress transfer in LCP fibre/epoxy model composites, two extreme situations are presented here in parallel and compared directly with the experimental data available:

- **elastic stress transfer** (analysis proposed by Cox)
- **plastic stress transfer** (analysis proposed by Kelly for metal matrices).

In the first case, both fibre and matrix respond elastically to tensile and shear strains respectively (figure 5.29a). The axial tensile and interfacial shear stress

distributions according to this model are plotted as a function of the distance along the fibre length (figure 5.29b, see also section 5.2.1). The aspect ratio **a**, is defined as $a = L/2R$ (where **L** is the length of the fibre and **R** the fibre radius) and the volume fraction is associated with the R_{-}/R parameter (see previous section).

In the second case, the tensile stress-strain response of the fibre is also assumed to be elastic but the shear stress-strain response of the matrix is assumed to be perfectly elastic-perfectly plastic (figure 5.29b). The stress transfer mechanism at the interface is controlled by the plastic behaviour of the matrix and consequently the matrix shear strength τ_{my} (see equation 5.5 where $\tau_i = \tau_{my}$). Tensile fibre stress and ISS distributions are also plotted as function of the distance along the fibre length.

In order to derive a quantitative estimation of the interfacial adhesion, the fibre reinforcing efficiency factor (FREF) is defined as the ratio of the area under the stress vs distance along the fibre curve and the enclosing imaginary 'rectangle' [**Bader 1994**]. The imaginary rectangle represents stress transfer equal to infinity (i.e. $\tau|_{x=0} = \tau_{max} = \infty$). The above parameter can be expressed mathematically as follows:

$$\eta = \frac{\int_0^L \sigma_f(x)dx}{\sigma_f^{max} L} \tag{5.18}$$

where $\sigma_f(x)$ is the axial tensile fibre stress along the fibre length, σ_f^{max} is the maximum stress induced in the fibre and **L** is the fibre length. In a long, continuous fibre where the transfer length L_t is much smaller compared to the actual length **L** of the fibre, i.e. $L_t << L$, the reinforcing efficiency is approaching its maximum possible value, i.e. 1 [**Bader 1994**] and its estimation is meaningless. However, in a short fibre embedded in a matrix where the aspect ratio is much smaller compared to a continuous fibre, the adhesion efficiency can be evaluated

and compared to its maximum possible value (in this case L_t is tending to zero). This parameter, therefore, is very important in order to evaluate the stress transfer quantitatively.

The calculation of the integral in equation 5.18 (area under the fibre stress transfer curve, figure 5.29a) by simply integrating equation 5.1 from 0 to L, yields to the following equation for the parameter η associated with the elastic model:

$$\eta^{elastic} = 1 - \frac{1}{\beta Ra} \tanh \beta Ra \tag{5.19}$$

where **a** is the aspect ratio, **R** the fibre radius and β a material property and geometry parameter, defined in equation 5.1.

In the case of the plastic stress transfer model, the transfer length L_t (see section 5.2.1ii) is calculated as follows:

$$L_t = \frac{\sigma_{fu} R}{2\tau_{my}} \tag{5.20}$$

where σ_{fu} is the tensile strengh of the fibre and τ_{my} is the matrix shear strength. By calculating again the integral in equation 5.18 (area under the fibre stress transfer curve, figure 5.29b) we derive the following equation for the FREF parameter η associated with the plastic model:

$$\eta^{plastic} = 1 - \frac{\sigma_{fu}}{4a\tau_{my}} \tag{5.21}$$

The calculated values for the parameter η for the systems examined in the previous section for different R_∞ / R ratios are given in table 5.8 (elastic model)

and 5.9 (plastic model), assuming, to a first approximation, a constant nominal Young's modulus E_f of the fibre and a constant shear modulus G_m of the matrix, calculated from the measured initial (i.e. 0% strain) Young's modulus of the matrix E_m:

System	a	η (R_/R=5)	η (R_/R=10)	η (R_/R=50)
Kevlar®49	130	0.924	0.909	0.871
Kevlar®29	150	0.949	0.939	0.913
Kevlar®49 ht1	90	0.886	0.866	0.807
Kevlar®49 ht2	100	0.903	0.884	0.835
PBZT-Z1	80	0.820	0.785	0.697

Table 5.8.: *Fibre Reinforcing Efficiency Factor data (elastic model).*

System	a	σ_m / MPa	η^*
Kevlar®49	130	2800	0.845
Kevlar®29	150	2500	0.878
Kevlar®49 ht1	90	2600	0.790
Kevlar®49 ht2	100	2650	0.816
PBZT-Z1	80	3500	0.683

Table 5.9.: *Fibre Reinforcing Efficiency Factor data (plastic model).*

The above data are derived from two different theoretical predictions of stress transfer using the mechanical and geometrical properties of fibre and matrix examined in the previous section. As can be seen from equations 5.19 and

5.21, the FREF η is not dependent on the macroscopic applied strain ε_{-}. Also the FREF predicted for the elastic model is always higher compared with the FREF predicted for the plastic model, as expected.

Similar calculations can be performed on the experimental data obtained in the previous section for a direct estimation of the parameter η at all strain levels. The integral in equation 5.18 is calculated graphically point-by-point along the cubic spline interpolation of the data. The results are demonstrated in figure 5.3oa-5.34a for all systems examined. The continuous lines represent stress transfer efficiency curves as predicted from the above models, taking into account the change in Young's modulus of the fibre and the shear modulus of the matrix, for different $\mathbf{R_{-}/R}$ ratios. The dependence of the above elastic parameters on the applied strain is given in the table 5.10. The Young's modulus E_f of the fibre is derived directly from the stress-strain data (see figures 3.3 and 3.4 in chapter 3). The shear modulus of the matrix is calculated from the equation $G_m = \frac{E_m}{2(1+\nu)}$, where the Young's modulus of the matrix E_m is obtained from the epoxy stress-strain data (see figure 5.12) and ν is the measured (=0.36) Poisson's ratio [**Jahankhani 1990**] for the isotropic matrix. The upper limit defined by the top curves corresponds to elastic stress transfer and the lower limit (table 5.9) corresponds to plastic stress transfer.

As can be seen in the above figures, the reinforcing efficiency η for all systems is fluctuating around a plateau value up to a critical applied strain level. For applied macroscopic strains ε_{-} higher than this critical value, the reinforcing efficiency η is reduced quite rapidly, especially in the case of the heat treated fibres (aramids ht1&2 and PBZT-Z1). From the data illustrated in these figures, it is quite clear that the load transfer mechanism is characterised by three fundamental regimes with smooth transition from one to the other (a schematic representation is shown in figure 5.35):

- elastic stress transfer prior to the critical applied strain $\varepsilon_{m,y}$ (*Regime A*)
- elastic - partially plastic stress transfer for macroscopic applied strain values around the critical applied strain $\varepsilon_{m,y}$ (*Regime B*).
- elastic - plastic stress transfer for macroscopic applied strain much higher than the critical applied strain $\varepsilon_{m,y}$ (*Regime C*).

It must be mentioned here that the term critical applied strain $\varepsilon_{m,y}$ represents a threshold value of transition from Regime A to Regime C and is only indicative of this transition. Alternatively, information about the deformation of the interfacial bonding between the fibre and the matrix can be drawn by simply observing the interfacial shear stress profiles at various applied strains. In all systems except in the case of Kevlar®29, at applied strains $\varepsilon < \varepsilon_{m,y}$, the maximum ISS is located at the fibre tips. In contrast, the maximum ISS moves away from the fibre end for $\varepsilon > \varepsilon_{m,y}$. This behaviour is established in a quite prominent way at high values of applied strain. In fact, the higher the applied strain, the further away is the maximum ISS located from the fibre end. This behaviour is very different when compared to carbon fibre / epoxy systems where the ISS distribution at high applied macroscopic strains denotes fibre/matrix debonding close to the discontinuity (fibre fracture), followed by partial bonding for a certain length and, finally, full bonding towards the middle of the fragment [**Melanitis 1991**].

The maximum ISS obtained from the fibre stress profile conversion using the balance of forces argument is plotted as a function of the macroscopic applied strain in figures 5.30b-5.34b for all systems. According to the elastic stress transfer model, the maximum ISS occurs at the fibre tip and from equation 5.13 for x=0 we derive the following expression for the maximum ISS as a function of the macroscopic applied strain :

$$\tau^{max}(\varepsilon_m) = \frac{1}{2} E_f \beta R [\tanh(2\beta Ra)] \varepsilon_m \qquad (5.22)$$

where E_f is the Young's modulus of the fibre, **R** is the fibre radius, **a** is the aspect ratio and β is already defined. We can introduce material properties changes in the above equation by simply taking into account the dependence of the elastic parameters with respect to the applied strain. This is given in table 5.10.

ε_m / %	E_m / GPa	G_m / GPa	E_f-K29 / GPa	E_f-K49 / GPa	E_f-K49* / GPa	E_f-K49** / GPa	E_f-PBZT / GPa
0.00	2.68	0.99	73.6	113.7	110.0	110.0	230.0
0.25	2.59	0.95	68.4	107.5	111.6	118.1	243.0
0.50	2.47	0.91	65.6	105.5	115.3	126.2	264.5
0.75	2.36	0.87	65.3	108.4	118.6	134.8	279.1
1.00	2.25	0.83	67.1	114.1	123.5	139.5	289.0
1.25	2.13	0.78	69	117.8	128.0	142.3	289.0
1.50	2.02	0.74	70.4	120.5	133.1	143.6	289.0
1.75	1.91	0.70	72.7	121.4	138.8	143.8	289.0
2.00	1.80	0.66	75	120.5	145.4	143.2	289.0
2.50	1.58	0.58	87.1	111.0	145.5	143.6	289.0

*Kevlar®49 ht1 ** Kevlar®49 ht2.

Table 5.10.: *Elastic parameters for fibres and matrix.*

The continuous curves represent the predicted relationship between maximum ISS and applied strain based on the above equation for various R_m/R ratios, taking into account the change of fibre's Young's modulus and matrix's shear modulus with applied macroscopic strain. The horizontal line represents the ISS versus applied strain dependence based on the plastic stress transfer approximation (constant ISS). Quite clearly, for applied strains above the critical applied strain ε_{my} the maximum ISS fluctuates around a plateau value for all systems. This value should be considered the shear strength of the *interphase* (IFSS) the interfacial shear strength of each system and clearly represents the yield stress of the interfacial bond. All the results concerning the critical macroscopic applied strain ε_{my} and IFSS data for all systems are given in the following table:

System	ε_{my} / %	τ_y / MPa
Kevlar®49	1.00±0.10	40±6
Kevlar®29	1.50±0.15	40±6
Kevlar®49 ht1	1.20±0.10	45±7
Kevlar®49 ht2	1.40±0.10	45±7
PBZT-Z1	1.10±0.15	50±8

Table 5.11.: *Interfacial strength data for all systems.*

However, in the case of Kevlar®49/ epoxy system, there is an indication that the maximum value of ISS (equal to 45MPa) reached at approximately 1.0% of applied strain, drops slightly to 30MPa. This behaviour may be attributed to initiation of 'rupture' of the interfacial bond and consequently, debonding between fibre and matrix at the locus of the fibre tip. An indication of the above

can be obtained by monitoring the transfer length change with the applied macroscopic strain at high levels as discussed below.

The variation of the transfer length L_t (defined as the fibre length required to build-up the 0.90% of the maximum stress from the end of the fibre) with the macroscopic applied strain or stress offers another way of examining the quality of the interfacial adhesion. The elastic stress transfer model can provide us with a prediction of the transfer length based upon the above definition. This can be achieved by simply solving the following equation over **x**:

$$\frac{\sigma_f^{max}(x = L/2)}{\sigma_f(x = L_t)} = 0.9 \tag{5.23}$$

where $\sigma_f(x)$ is defined by equation 5.1.

The solution of the above equations yields the following closed form prediction for the transfer length derived from the elastic stress transfer model:

$$L_t = \frac{C}{\beta} \tag{5.24}$$

where C is a constant.

Measuring transfer length from the experimental data is achieved graphically by using the cubic spline fits to the experimental stress profiles along the fibre length. Predicted transfer length data using equation 5.20 associated with the plastic model are given in the following table:

System	R / μm	σ_{fu} / MPa	$L_t^{plastic}$ / μm
Kevlar®49	6.0	2800±150	210±25
Kevlar®29	6.0	2500±150	187±20
Kevlar®49 ht1	5.9	2600±150	194±25
Kevlar®49 ht2	7.3	2650±150	242±25
PBZT-Z1	8.2	3500±100	360±20

Table 5.12: *Transfer length data for all systems (plastic model).*

The experimental data concerning transfer lengths for all systems examined are shown in figures 5.30c-5.34c plotted as a function of the macroscopic applied strain and stress respectively. Predicted curves of L_t variation with applied strain (derived from equation 5.24 for various R_m/R ratios) using the data for elastic parameters from table 5.10, are shown. As can be seen, data for Kevlar®49 system show that the transfer length increases with applied strain for low macroscopic applied strains/stresses and then takes up quite rapidly. In fact, at strain levels between 1.0-1.3%, the transfer length equals the value predicted from the plastic stress transfer model and continues to increase to very high values (almost twice as $L_t^{plastic}$). This observation provides some more indication of the fibre/matrix debonding which may occur at high applied strain levels. On the other hand, in the case of Kevlar®29 system, L_t increases initially up to 1.0% applied strain and then stabilises around the $L_t^{plastic}$ value (see table 5.12). Continuous increase of L_t at small strain levels is observed for the heat treated Kevlar®49 fibres with the rate of increase dropping significantly around the $L_t^{plastic}$ prediction. Similar observations are made for the (heat treated) PBZT-Z1 system where the rate of increase of L_t with applied strain drops significantly at intermediate levels of applied strain. In fact, if we

reverse the equation 5.24 by rearranging and solving over the 'G_m' parameter (material property for the bulk matrix), a prediction for the shear modulus of the interphase G_i can be made. Its dependence on the macroscopic applied strain can be derived indirectly from the experimentally measured L_t values:

$$G_i = \frac{1}{2} C^2 R^2 \frac{E_f}{L_t^2} \ln(R_\infty / R) \qquad (5.25)$$

where the R_∞ / R value is taken as the one which corresponds to the best fit of L_t curve to the experimental data (see figures 5.30c-5.34c). The results for all LCP/ epoxy systems are demonstrated in figure 5.36. As can be seen, a rapid exponential decay for the G_i parameter is observed, associated with the viscoelastic behaviour of the matrix itself and consequently the fibre/matrix interphase. This prediction confirms the interphase existence with shear properties decaying rapidly with the increase of the macroscopic applied strain.

The values of the macroscopic applied strain at which this transition occurs coincide with the values obtained by monitoring the reinforcing efficiency deterioration, approximately 1.10% for Kevlar®49. In the case of Kevlar®29 system, this transition is not clear. In general, the increase of transfer length with applied strain is due to the yielding/softening of the matrix material near the fibre ends. It can be said that the interphase in this case is yielding in shear and the volume of this plastically deformed interphase extends further towards the middle of the fibre with increasing the macroscopic applied strain. The transfer length increase with applied strain quite early indicates the formation of plastic zones around the fibre tips even at small strain levels. This type of interphase yielding is predicted by the FEA model described earlier.

From our research, it is demonstrated that the interfacial behaviour for Kevlar®/ epoxy systems is elastic up to a critical applied strain. The interphase

cannot support any shear stress higher than a critical value of ISS, which is considered to be the interfacial yield strength (IFSS). Any increment of the applied macroscopic strain, leads to yielding of the interphase locally (fibre discontinuity) which expands towards the middle of the fibre.

The interfacial behaviour of the systems examined in this work is different compared to other model composites examined in the past **[Jahankhani 1990]**, **[Melanitis 1991]**. As far as carbon systems are concerned, an initial drop of the ISS at the fibre end is followed by a drop of the ISS to zero value at the fibre tip and the consequent development of an area of constant shear stress at higher strains (figure 5.37a). The above behaviour indicates initial elastic stress transfer followed by ductile behaviour, finishing with rupture of the interfacial bond **[Galiotis 1992]**. A proposed model of this interfacial behaviour is given also in figure 5.37a.

On the other hand, aramid fibre systems with 'finish', exhibit the interfacial behaviour which is shown in figure 5.37b. Maximum values of the level of 60-80 MPa were reported for as-received, conditioned and surface-treated Kevlar®49 SSFCs **[Jahankhani 1990]**. The high values of shear stresses at the interface eventually cause rupture of the interfacial bond. A schematic model of this type of interfacial behaviour is demonstrated in figure 5.37b. A direct comparison, though, would not be appropriate, due to the fact that the experimental data in that work were curve-fitted using fifth degree polynomials, a method which has since been proven somewhat limited.

In our case concerning aramid systems with no sizing (finish) a situation such as that shown in figure 5.37c is observed. The stress transfer mechanism is elastic up to a critical level of applied strain and then yielding of the interface occurs, propagating towards the middle of the fibre: behaviour similar to shear slip in reinforced cements or metals **[Piggot 1980]**, see section 5.2.1(iii). We can classify in this category all aramid systems examined in this work apart from the

Kevlar®49 system where indications of debonding may place it in the previous category.

As far as the PBZT/ epoxy system is concerned, slightly higher shear stresses are developed in the interface. This observation enhances our belief that the properties of the interphase are a gradient of values from fibre to bulk matrix properties with unknown distribution. Obviously, the combination of a stiffer fibre than aramids together with the same matrix will create a stiffer interphase. The mechanisms of stress transfer, though, are very similar to aramid systems with yielding phenomena at applied strains higher than a critical value.

The stress transfer mechanism in the vicinity of a discontinuity, such as a fibre fracture is very much dependent on the properties of the interphase. The most common approach to the interphase and its properties, is to assume similar behaviour to the bulk matrix. This approximation, in fact, is not correct but a more appropriate estimation is difficult to make because there is no possible way to measure (a) how far the interphase extends for each give system (b) the gradient of its mechanical properties (values close to the fibre properties near the fibre and values close to the bulk resin properties away from the fibre surface and continuity in between). Other parameters which control the stress field are the resin curing procedure, the thermal expansion coefficients of the two constituents and the geometry of the discontinuity.

5.6.1. Comparison of experimental results and FEA modelling data.

The experimental profiles of the axial tensile stress along the fibre length for the system Kevlar®49 ht1/ epoxy resin are directly compared to the predicted stress profiles from the FEA simulation. The agreement is quite satisfactory. It has already been mentioned that the predictions around the fibre tip are controlled by the existence of a mathematical singularity for the square-end fibre tip model. In this case, stress continuity is impossible to achieve. The

irregularity. However, only an extremely fine grid would allow a complete stress continuity. The experimental results close to the fibre end fit better to the predictions from the round-end fibre tip model, although the FEA grid may be insufficiently fine to remove fully the apparent singularity. The closer agreement for the round-end grid suggests that no singularity exists at the end of the 'real' fibre. This is not surprising, since, on a molecular scale, all 'corners' are rounded. Thus, modelling makes sense only if grids which avoid singularities are employed.

A useful observation regarding the agreement between experimental and FEA data is the fact that, the matching is more satisfactory at lower applied strain levels compared with high applied strain levels. This is attributed to the imprecise description of the elasto-plastic behaviour of the resin material which becomes more evident at high applied strains. Nevertheless, the change of the stress transfer curve shape from curved, Cox type to almost linear at high applied strain levels is due to interphasial yielding, i.e. the local plastisization of the resin, a phenomenon which is predicted by the FEA modelling.

The axial tensile stress profiles are converted to ISS profiles with the balance of forces argument described before. The FEA predictions lead to direct generation of the ISS distribution along the interface. The validity of the balance of forces model is therefore, verified. This has been investigated by employing the same principle for converting FEA stress predictions to ISS profiles and comparing independently to the FEA results for the ISS distributions. In figure 5.37, this comparison takes place for three applied strain levels. The conversion has been carried out using the data sets from 1.9mm depth from the fibre surface. It is quite clear that the two sets of data match quite closely not only for low macroscopic applied strains (elastic stress transfer) but also at intermediate and high strains where the resin starts yielding near the fibre tip with propagation of this yielding to a bigger volume around the fibre and towards the middle of the fibre.

The 'plateau' region close to the fibre end observed at high applied strains represents the perfectly plastic interphase and bulk resin. The ISS value in this region is of the order of 40MPa. This value corresponds to the von Mises yield stress for the perfectly plastic zone, assuming all other stresses are zero. This condition is satisfied for the perfectly plastic resin.

5.7. Conclusions.

The main conclusions which can be drawn from the above results concerning the interfacial behaviour and failure of LCP fibre/epoxy resin model composites are the following:

- The existence of the interphase in LCP fibre/epoxy systems is more evident compared with similar carbon fibre/epoxy resin systems. This is mainly due to the chemical relation between polymeric fibres and epoxy resin matrices.

- The interfacial behaviour of LCP fibre/epoxy systems is based on a mainly elastic stress transfer mechanism up to a critical applied macroscopic strain. For applied strains higher than this critical value, the interfacial behaviour is elastoplastic. The predominant mechanism of interfacial failure is yielding in shear, indicating a ductile behaviour, associated with a tough interphase. The nature of this interfacial behaviour is different compared with sized carbon/epoxy or other sized polymer fibre/epoxy sytems, which show interfacial behaviour of brittle nature. A graphical representation was given in figure 5.37. In case (a), high interfacial shear stresses developed at the interface are responsible for fibre-matrix debonding in the vicinity of the fibre fracture and fibre recoil (classical fragmentation results[**Melanitis 1991**]). A significant drop of the maximum ISS obtained for high applied strains is observed thereafter. In case (b), interfacial damage is in the form of yielding in shear combined with fibre debonding [**Jahankhani 1990**]. A drop of the maximum ISS is also observed.

- The yield shear strength of all aramid systems examined in this work is of the same magnitude, approximately 40-45 MPa. The predominant mechanism of interfacial failure is yielding of the interphase in shear. No significant drop of the maximum ISS measured at high applied strains is observed with an exception of the Kevlar®49/ epoxy system. However, a stiffer fibre of different chemical nature, derives a slightly stronger interfacial bond with the same epoxy matrix with strength approximately equal to 50 MPa. A schematic representation of this behaviour was shown in sequencial form for the three different regimes discussed in the previous section in figure 5.35. The formation and propagation of the plasticity zone around the fibre tip is shown. This behaviour was confirmed by the FEA analysis.

The critical macroscopic strain above which interfacial yielding occurs is different for each system. It seems that a low modulus fibre (Kevlar®29) develops an interphase which yields at slightly higher values of applied macroscopic strain compared with a medium modulus fibre (Kevlar®49).

The material properties change during deformation is very critical for the interfacial behaviour of all LCP/ epoxy systems. In fact, it was shown that by reversing the calculations concerning derivations of L_t vs applied strain curves and employing the experimentally measured L_t values, predictions for the shear properties of the interphase can be made. According to these predictions, the shear parameter G_i of the interphase estimated initially to the value of the bulk matrix, decays rapidly to lower values with increasing applied macroscopic strain for all systems.

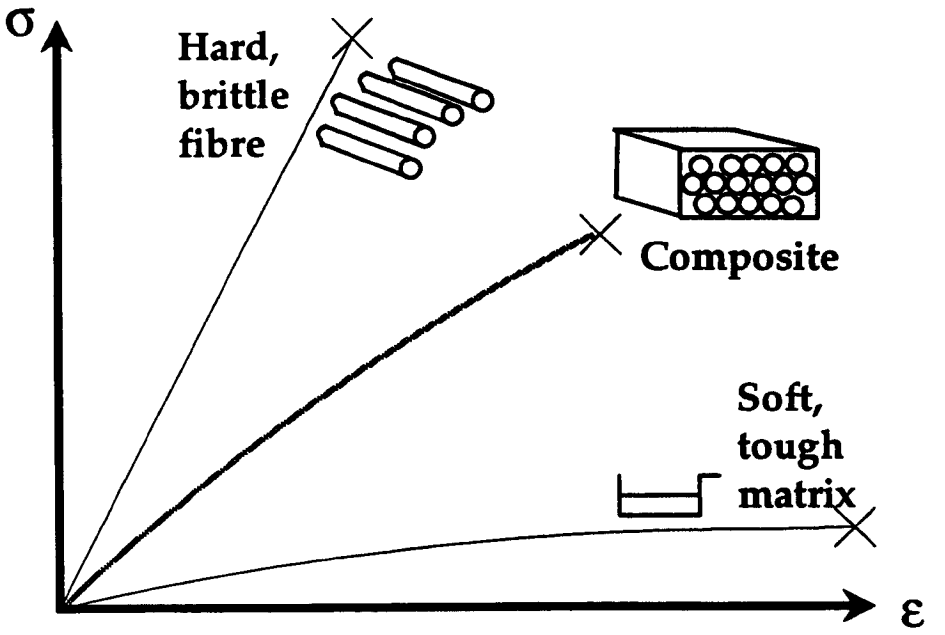

Figure 5.1. Stress-strain curves for fibre, matrix and resulting composite.

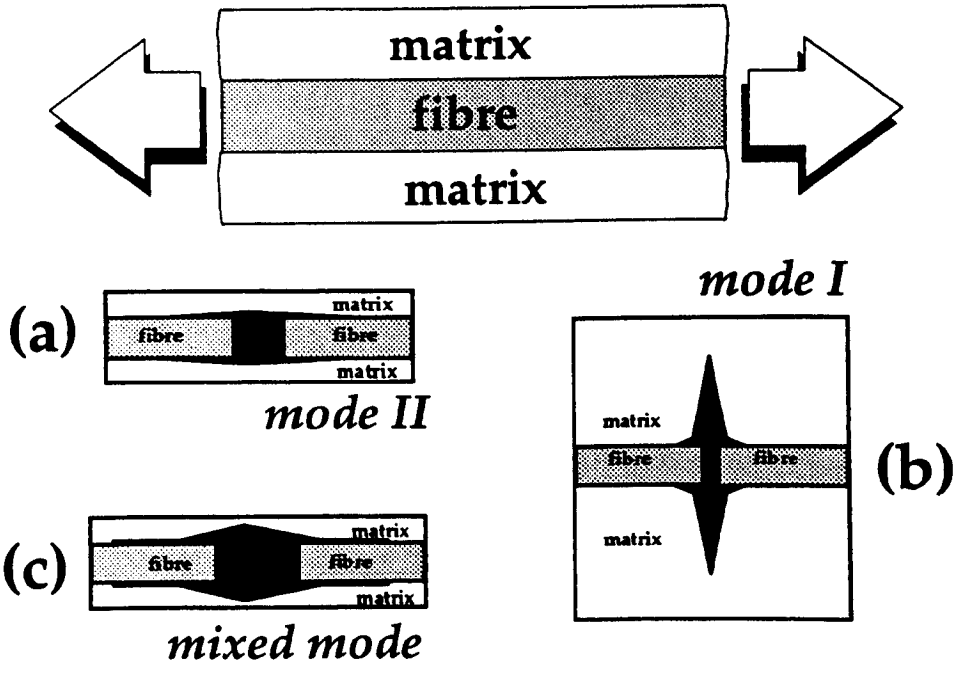

Figure 5.2. Interfacial failure modes for various levels of adhesive strength.

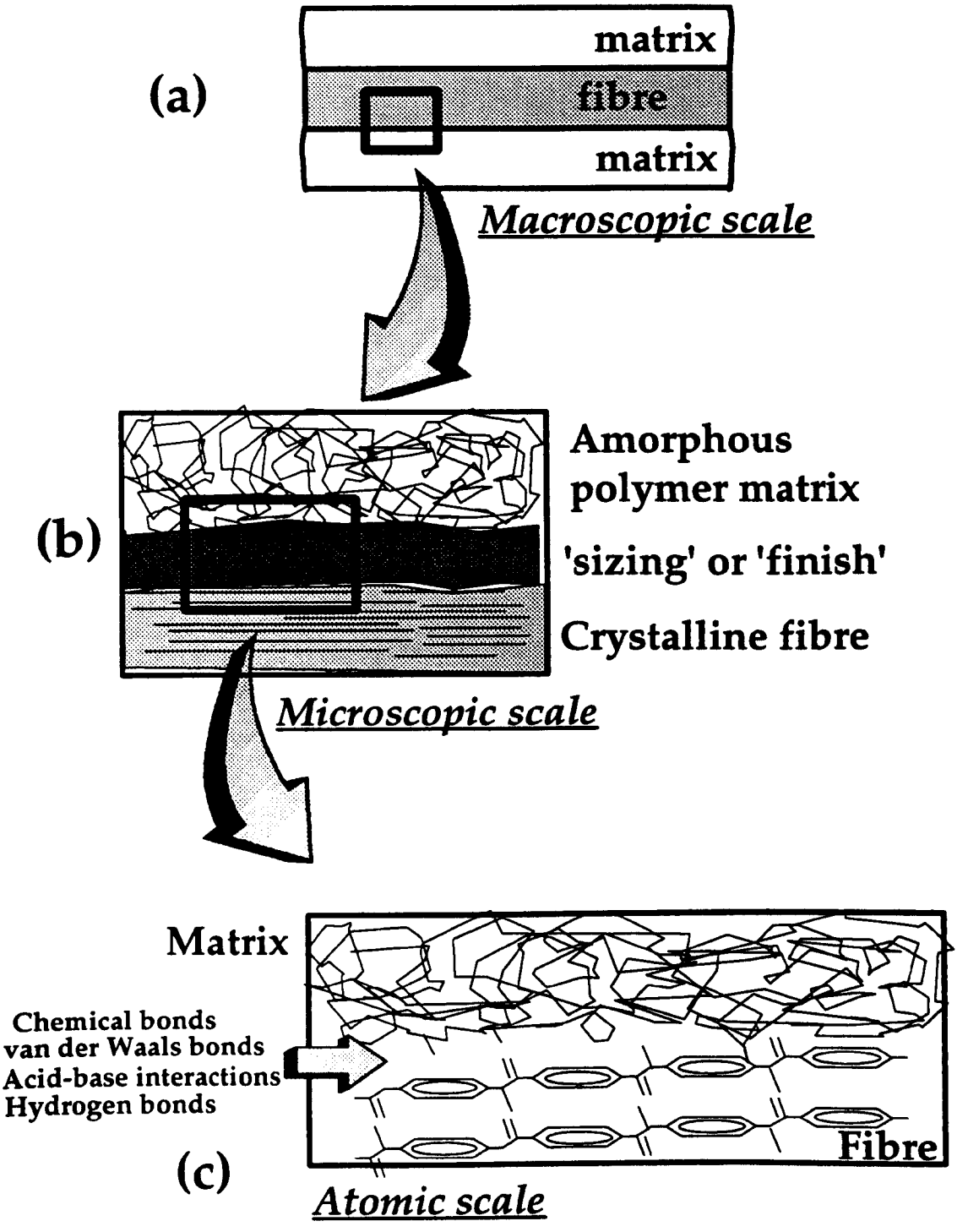

Figure 5.3. Macroscopic, microscopic and atomic approaches for the interface/interphase in composite materials.

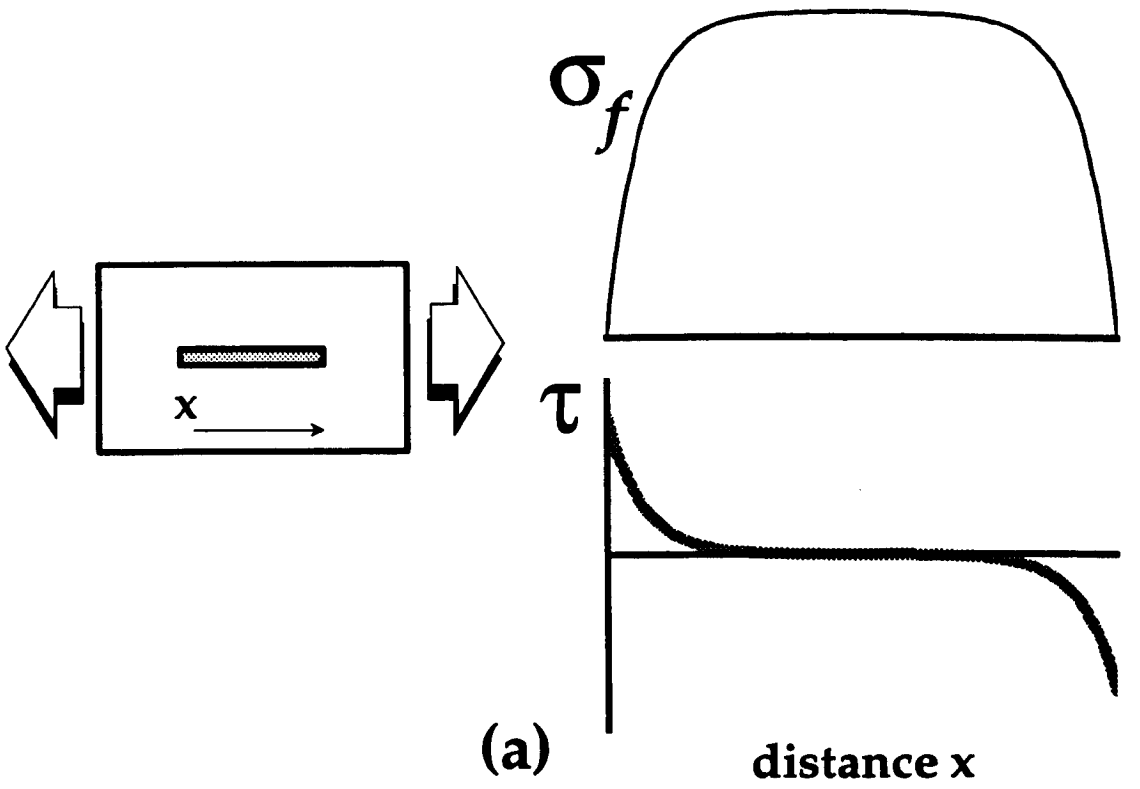

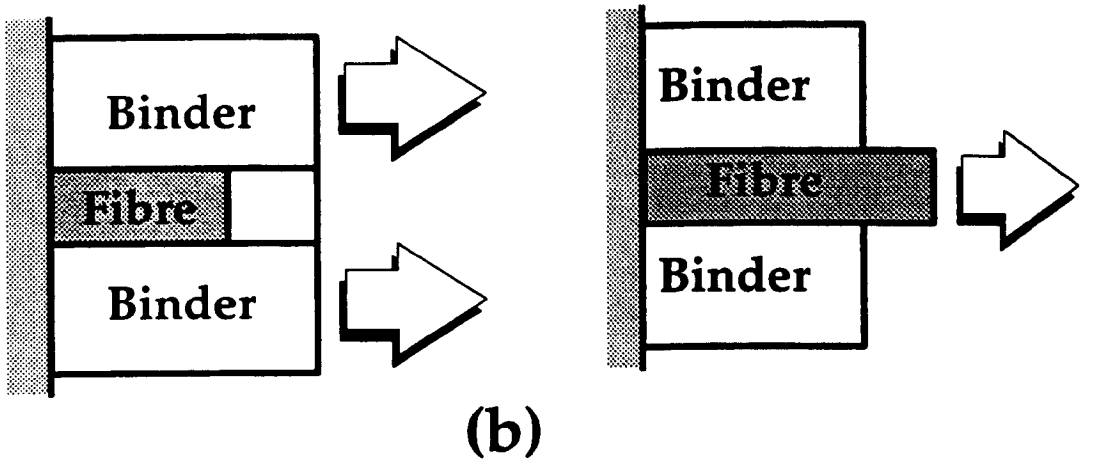

Figure 5.4. Schematic representation of shear lag analyses (a) analysis I [Cox 1952] and (b) analysis II [Dow 1963].

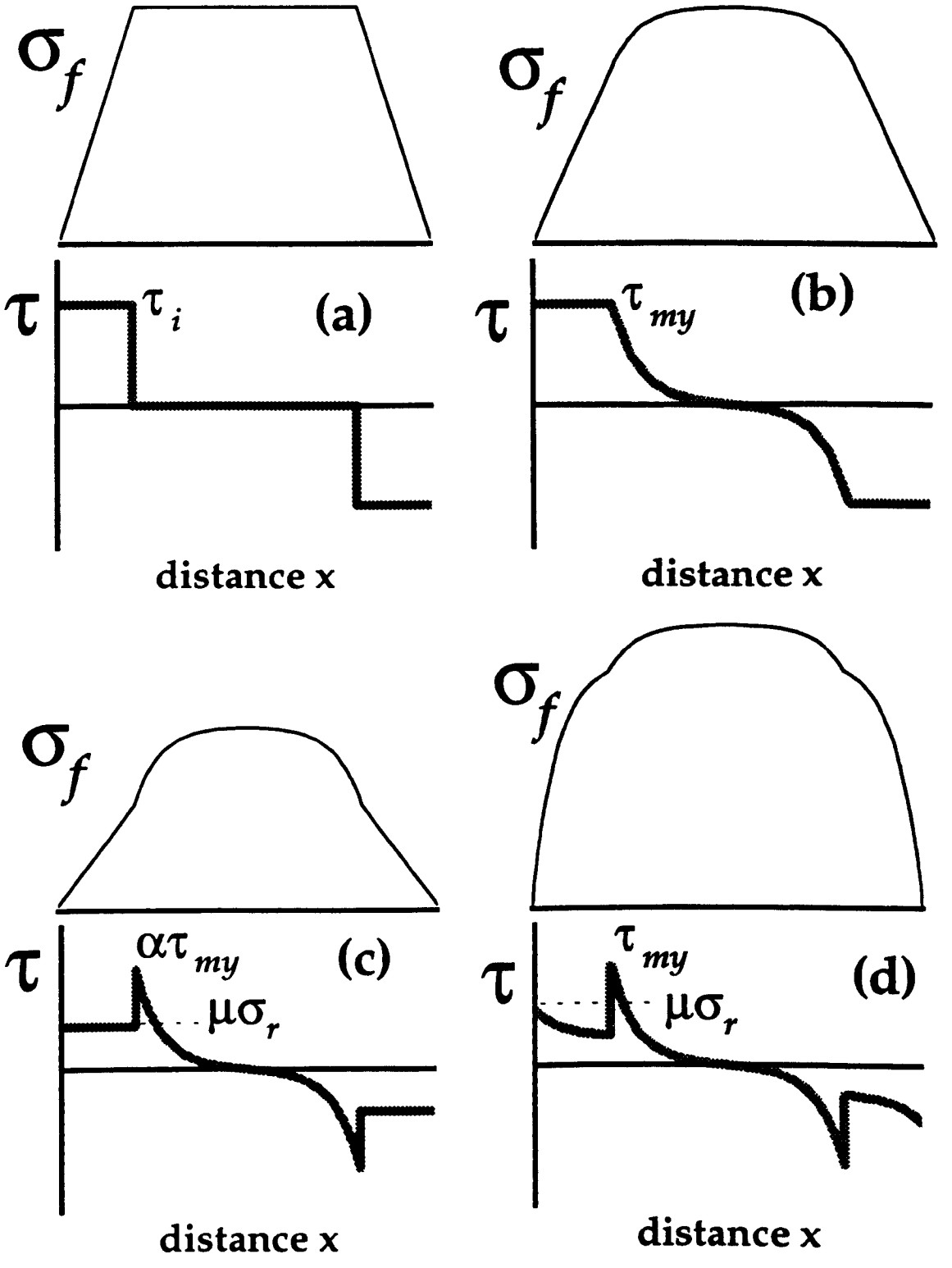

Figure 5.5. Treatments of stress transfer mechanisms for various materials [Kelly 1965], [Piggot 1966,1980].

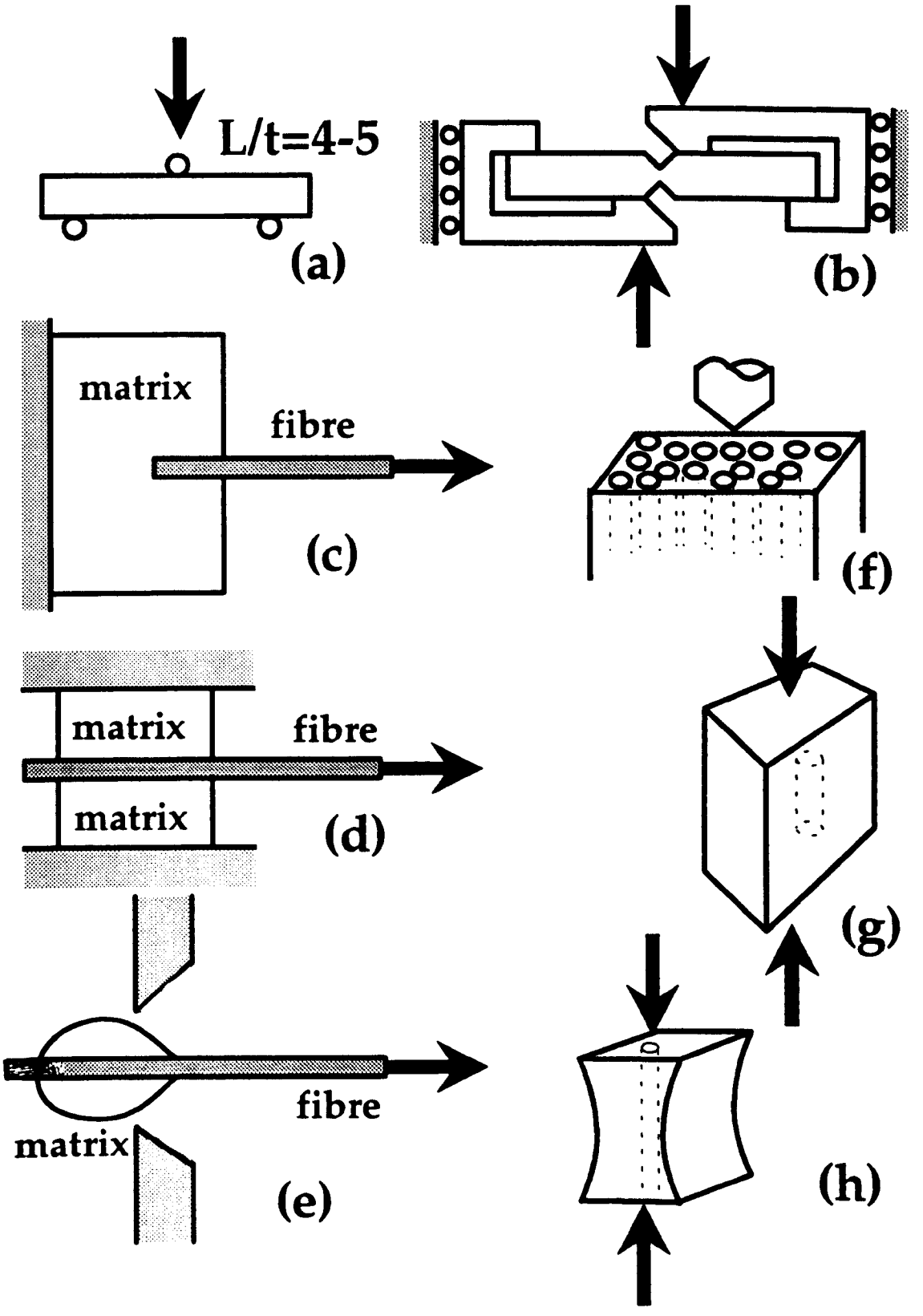

Figure 5.6. (a),(b) Indirect and (c)-(h) direct test methods for interfacial strength evaluation.

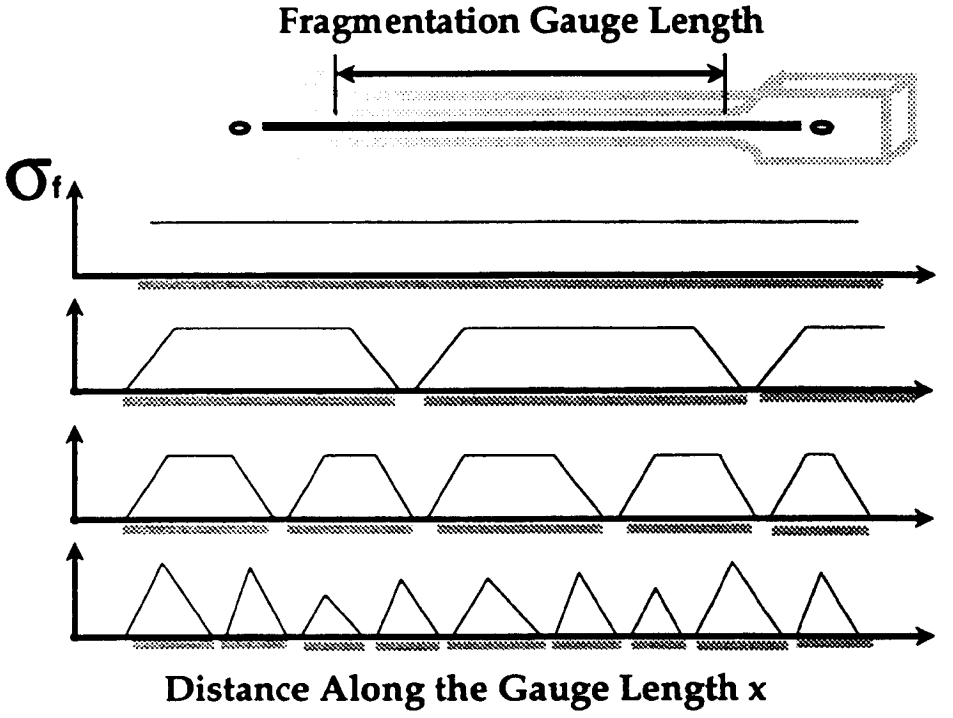

Figure 5.7. Classical fragmentation test.

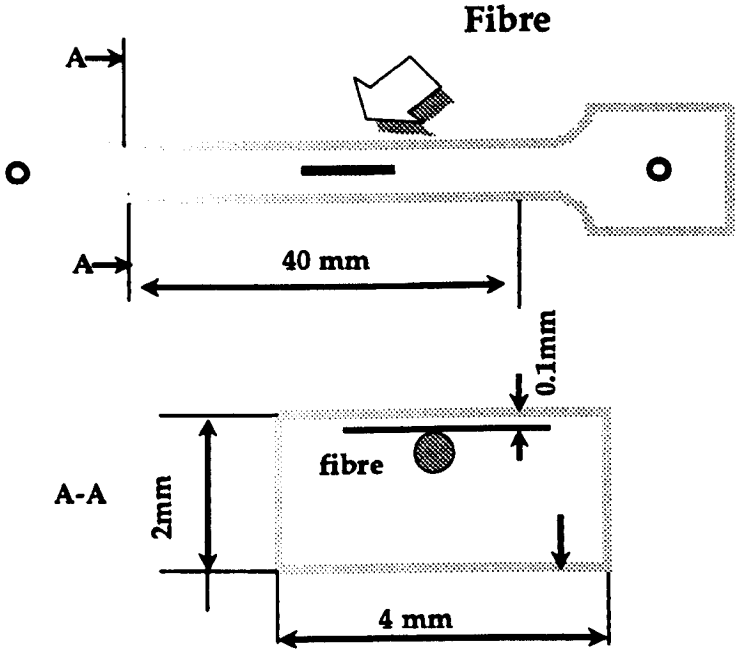

Figure 5.8. SSFC coupon geometry.

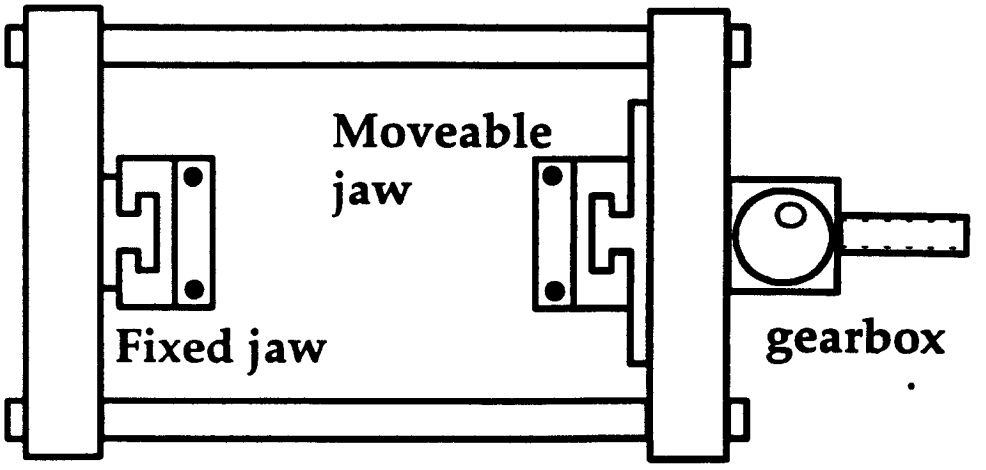

Figure 5.9. Schematic representation for microextensometer jig for IFSS testing.

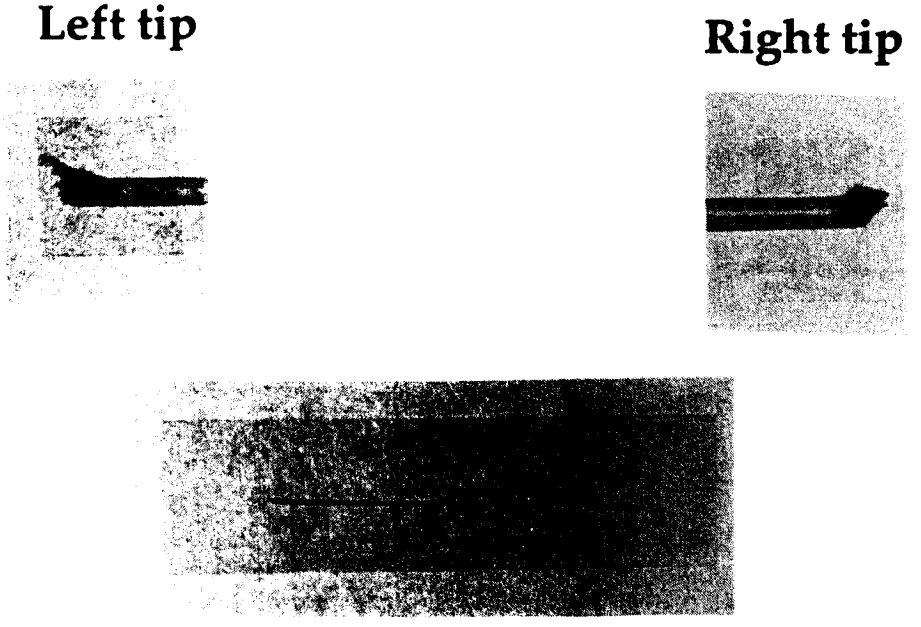

Figure 5.10. Microphotograph of short fibre embedded in epoxy resin with details of fibre tips (d=12μm).

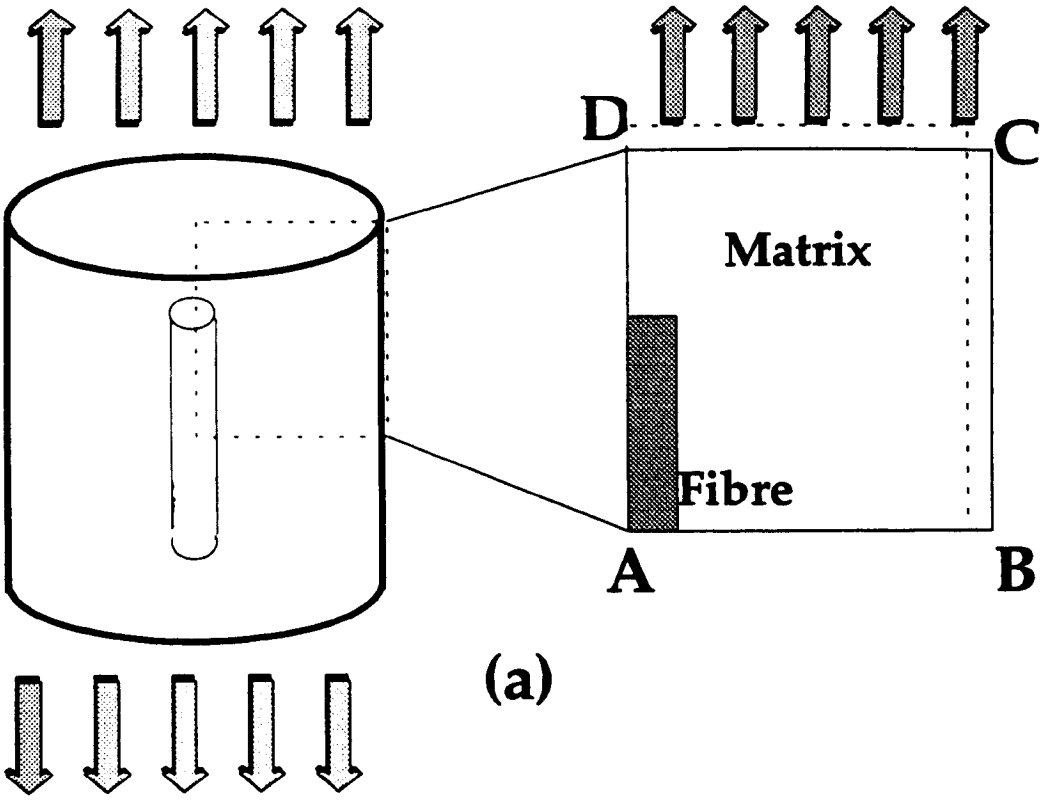

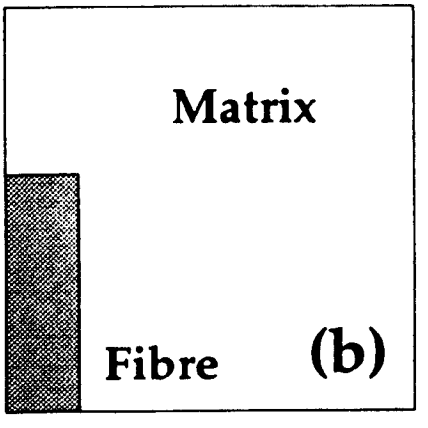

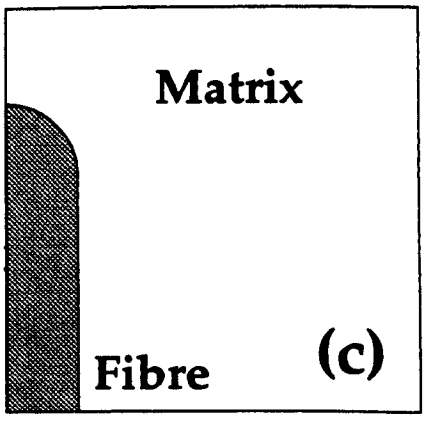

Figure 5.11. (a) The FEA model two geometries: (b) square and (c) round end [Guild 1994].

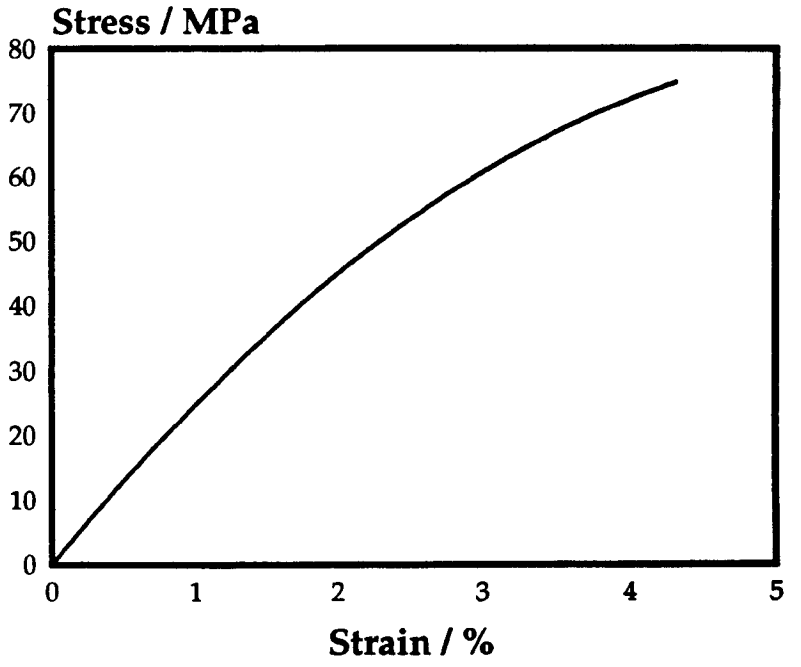

(a)

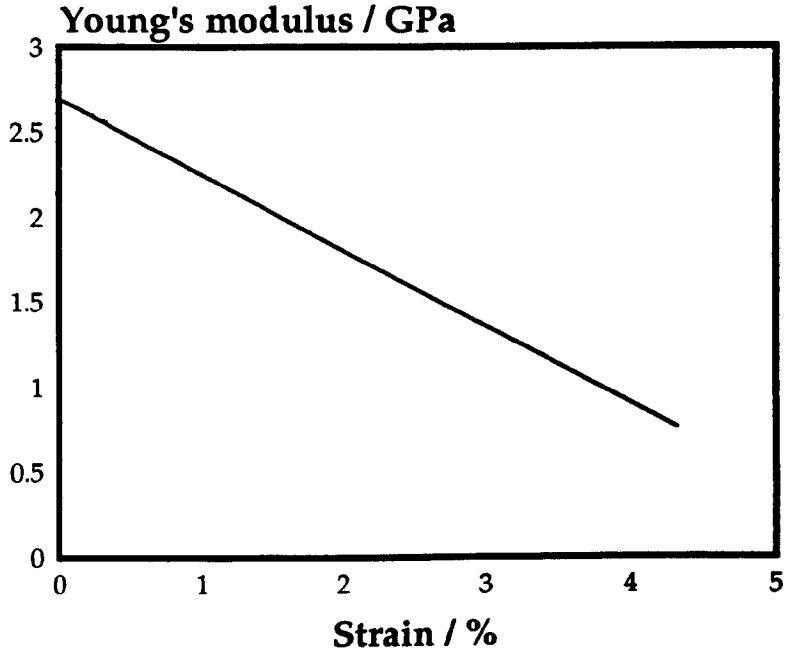

(b)

Figure 5.12. (a) Stress-strain and (b) Young's modulus-strain curves for the matrix material.

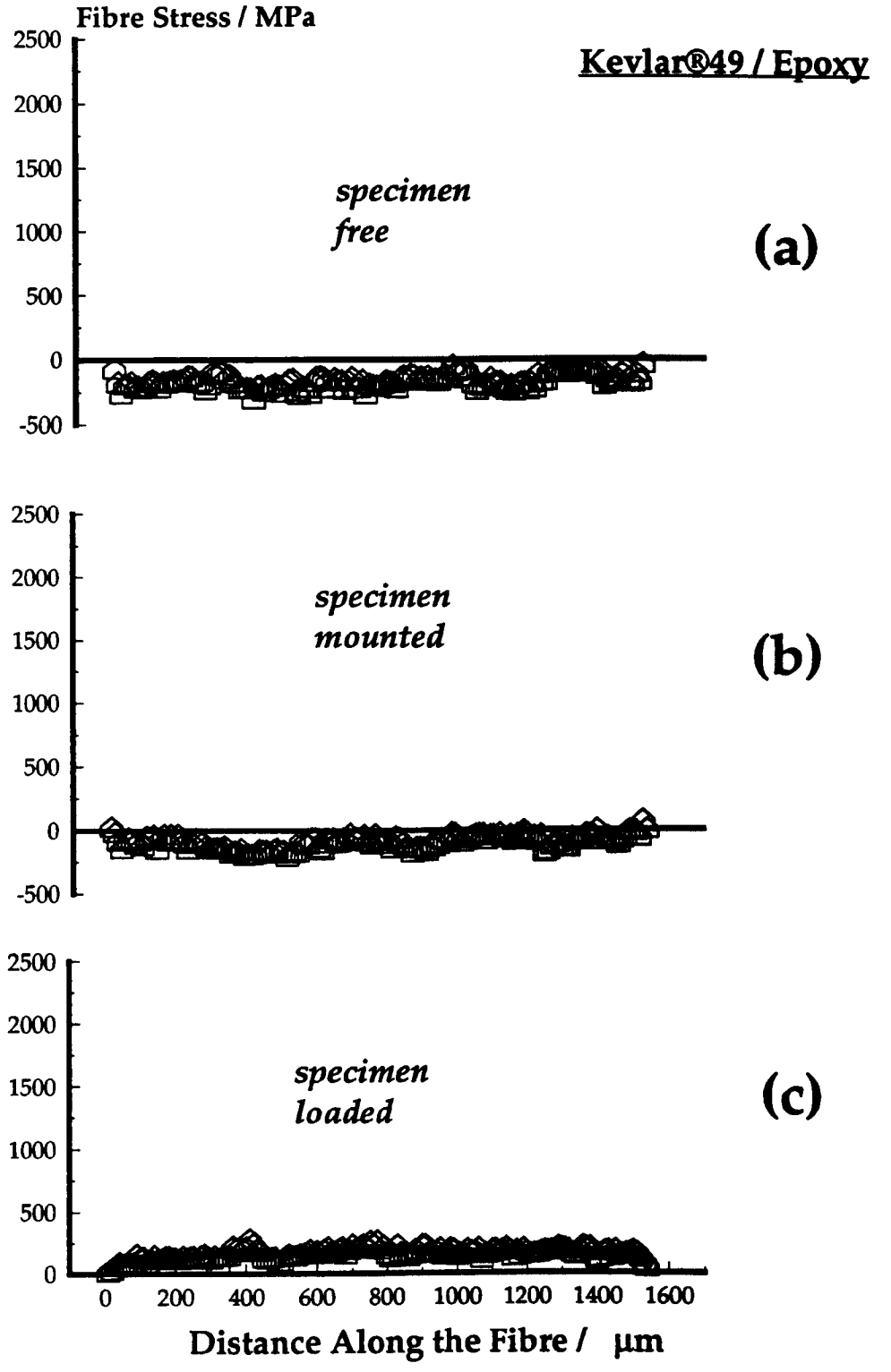

Figure 5.13. Fibre stress profiles for Kevlar®49/ epoxy system.

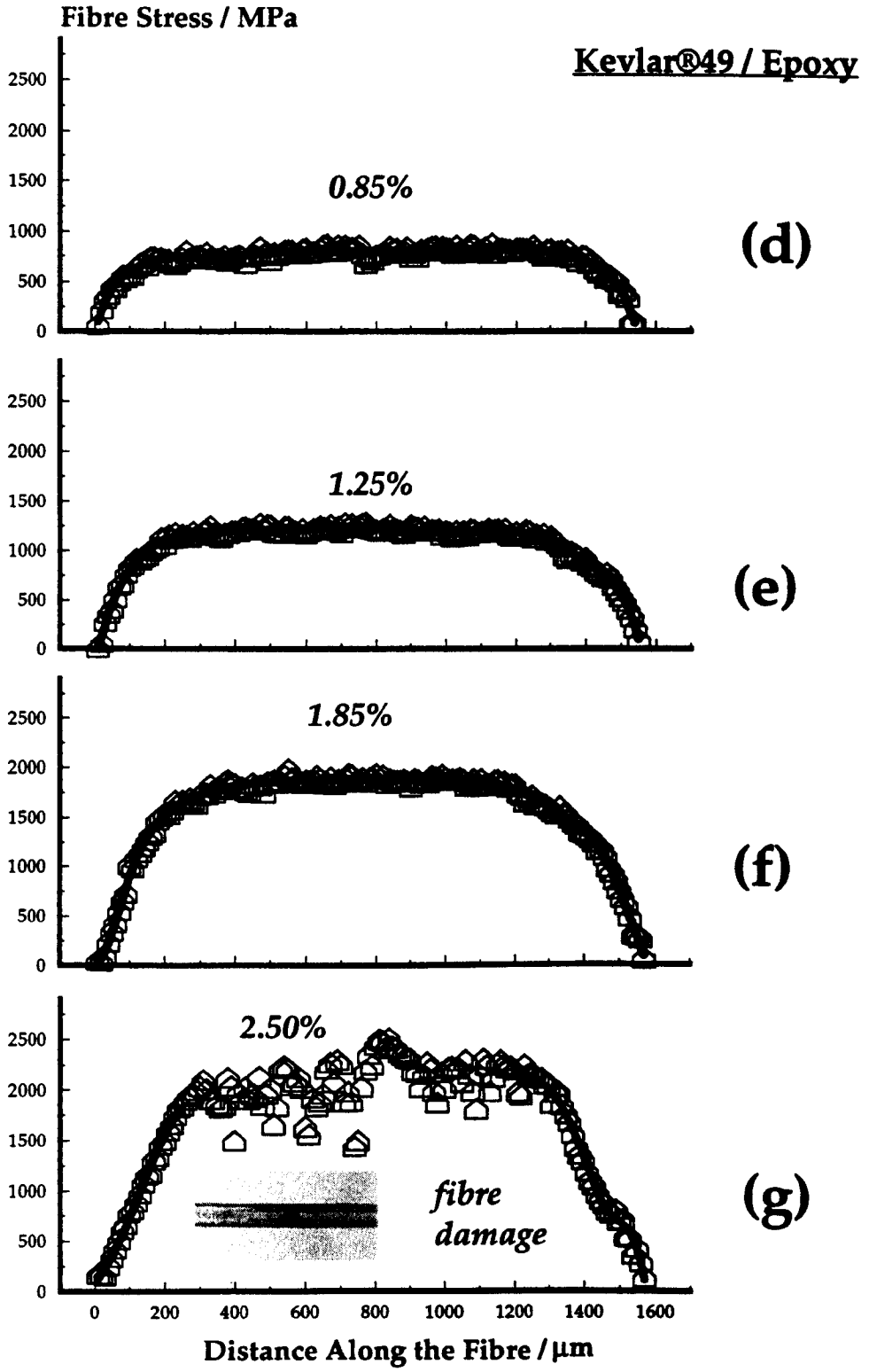

Figure 5.13. Fibre stress profiles for Kevlar®49/ epoxy system (continued).

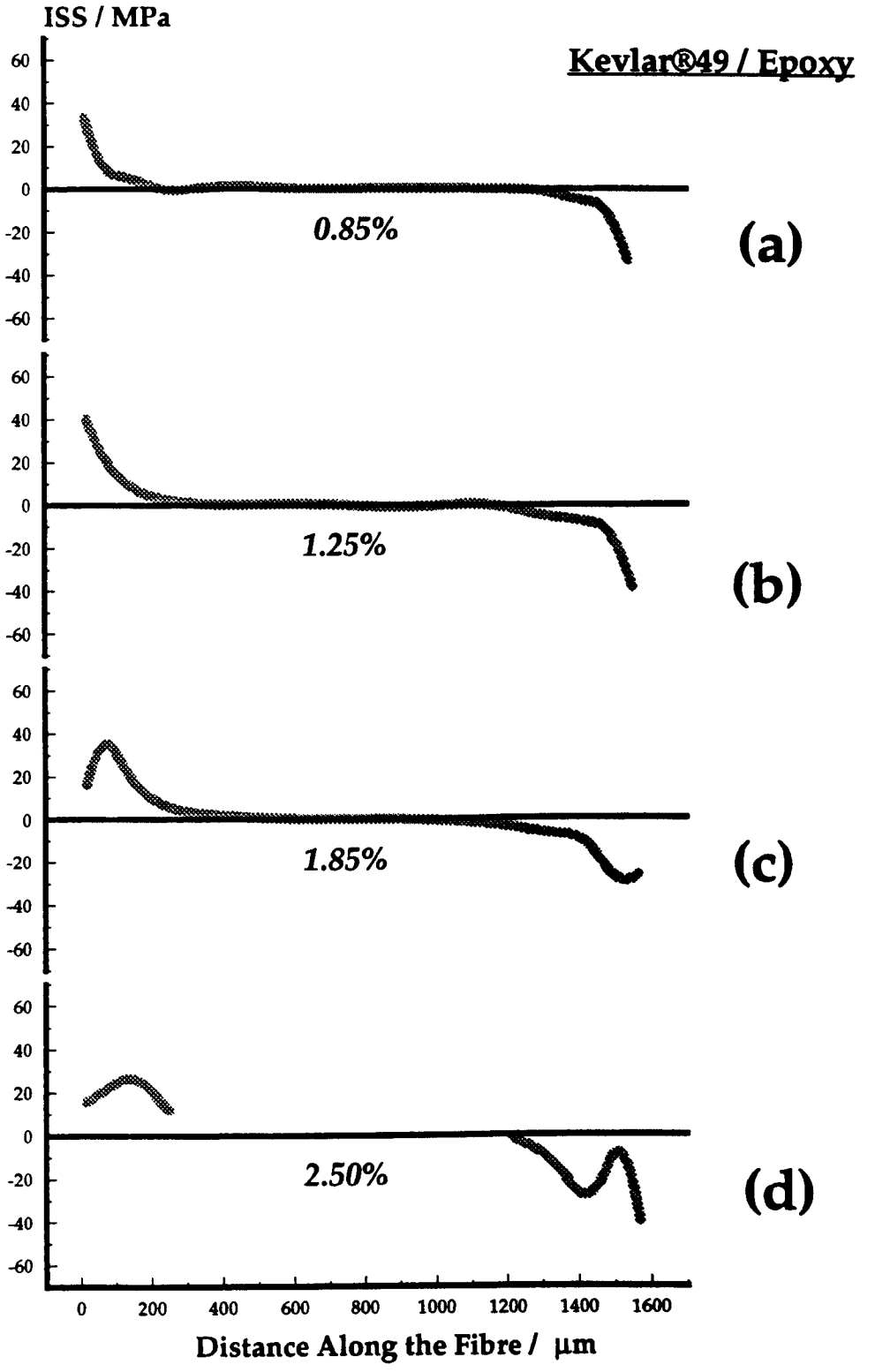

Figure 5.14. ISS profiles for Kevlar®49/ epoxy system.

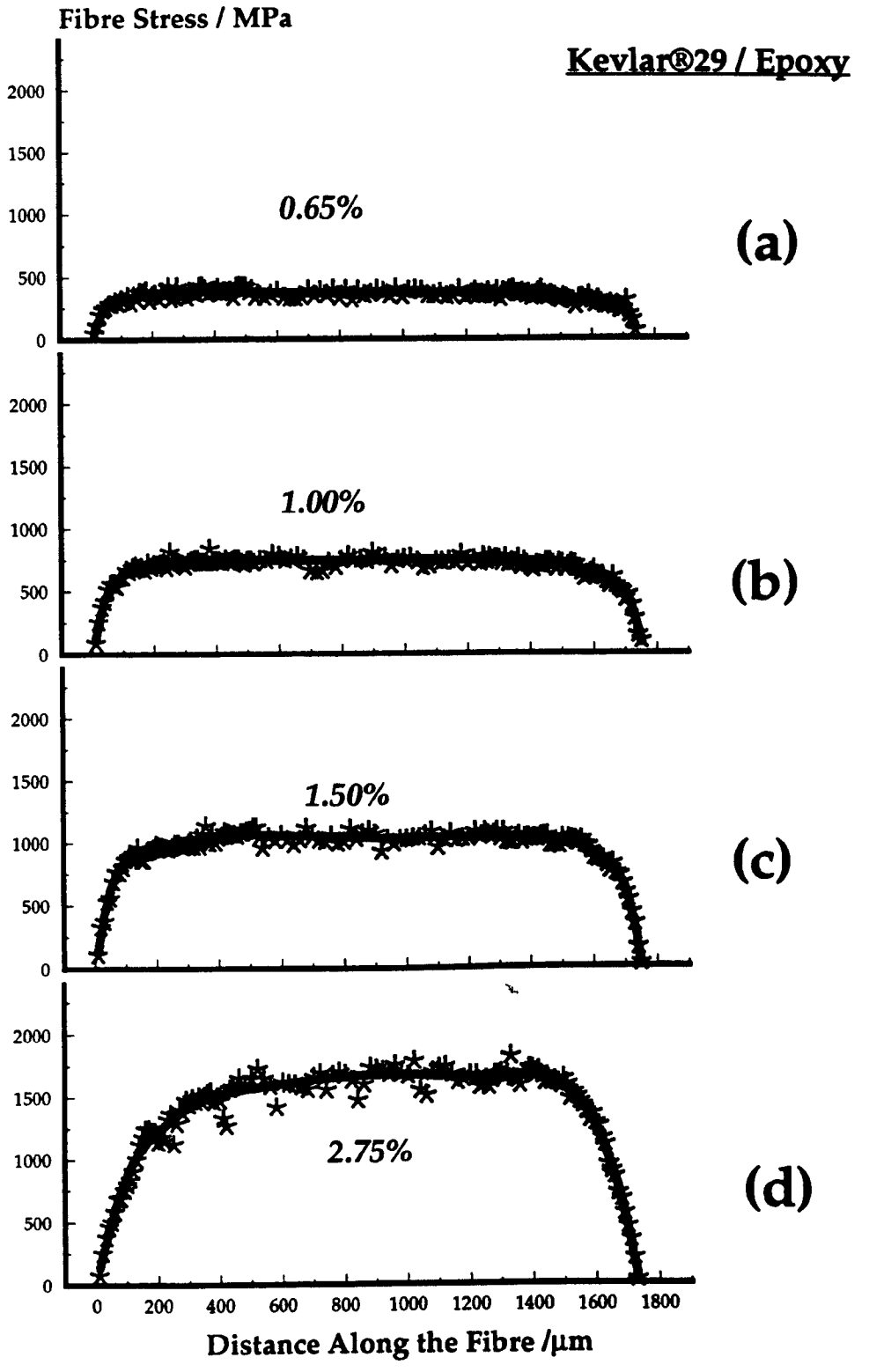

Figure 5.15. Fibre stress profiles for Kevlar®29/ epoxy system.

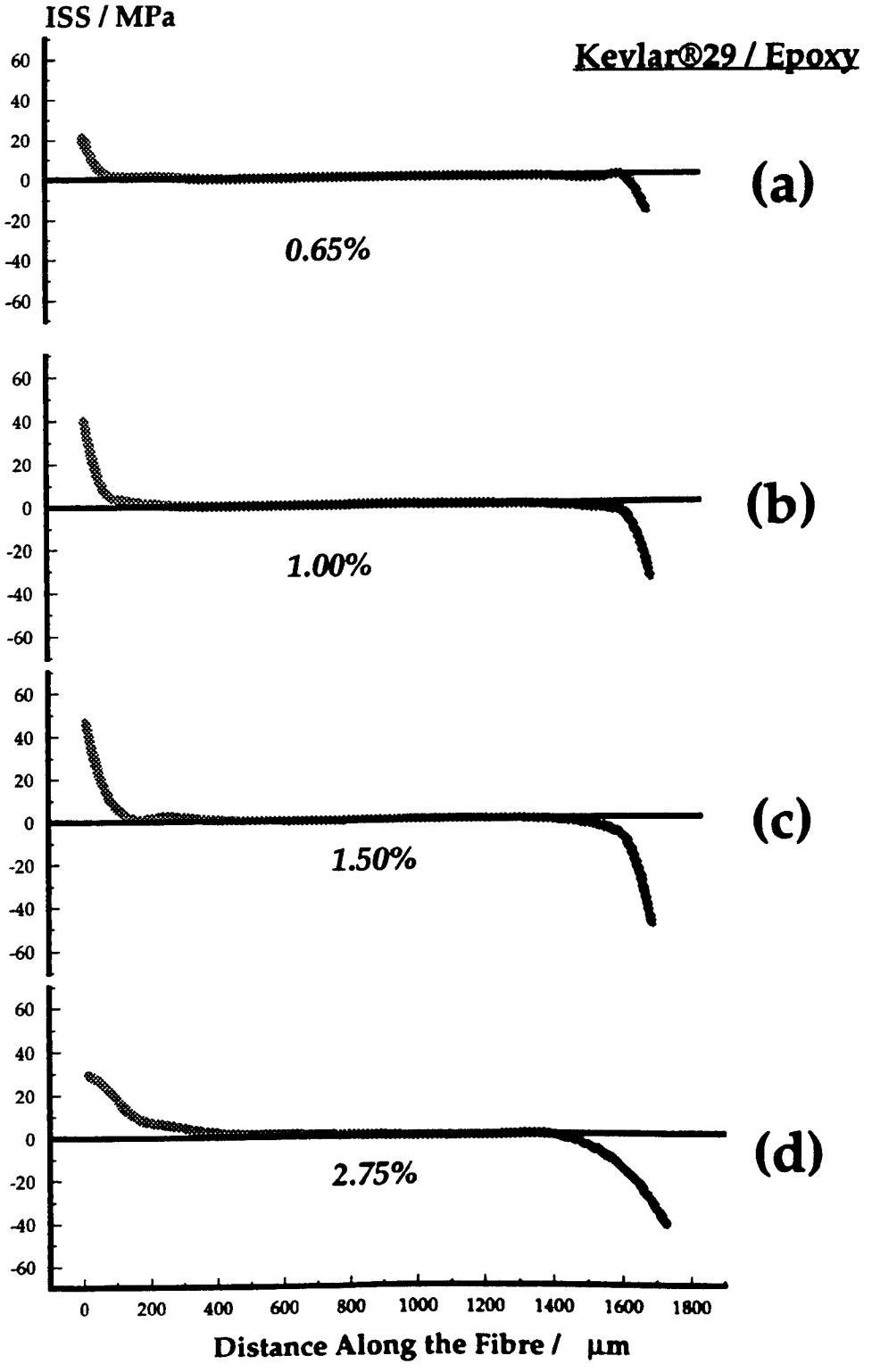

Figure 5.16. ISS profiles for Kevlar®29/ epoxy system.

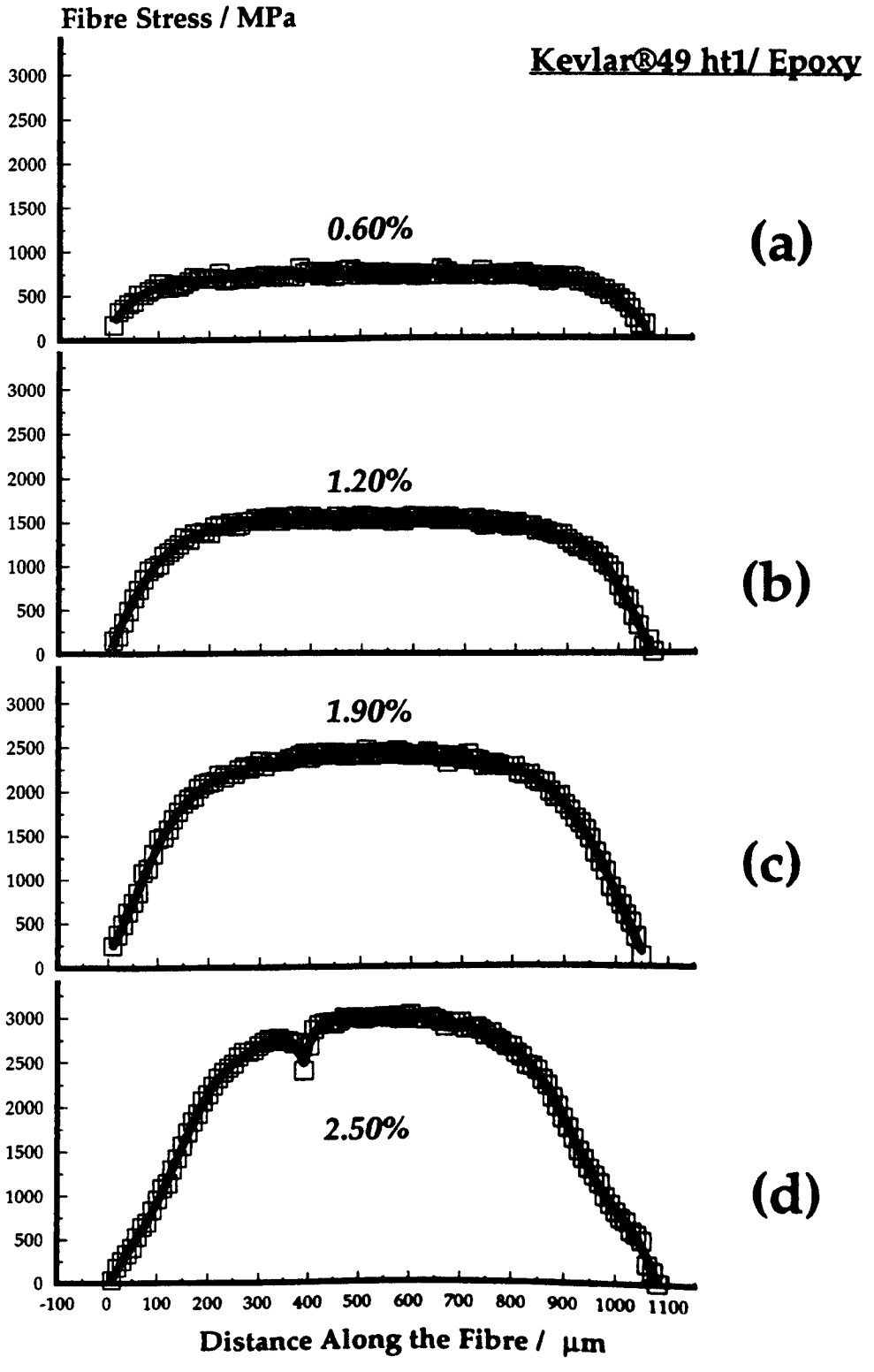

Figure 5.17. Fibre stress profiles for Kevlar®49 ht1 / epoxy system.

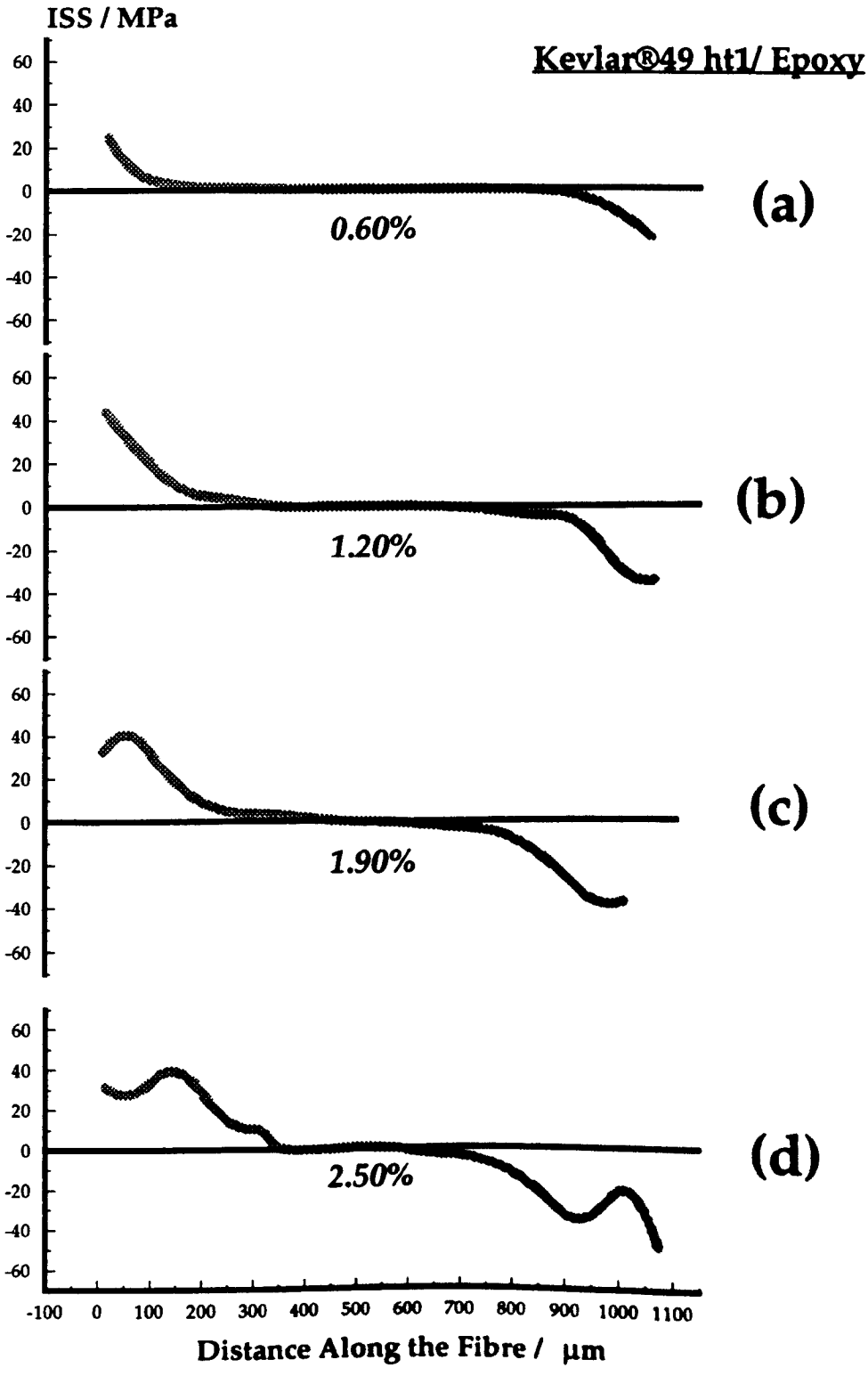

Figure 5.18. ISS profiles for Kevlar®49 ht1 / epoxy system.

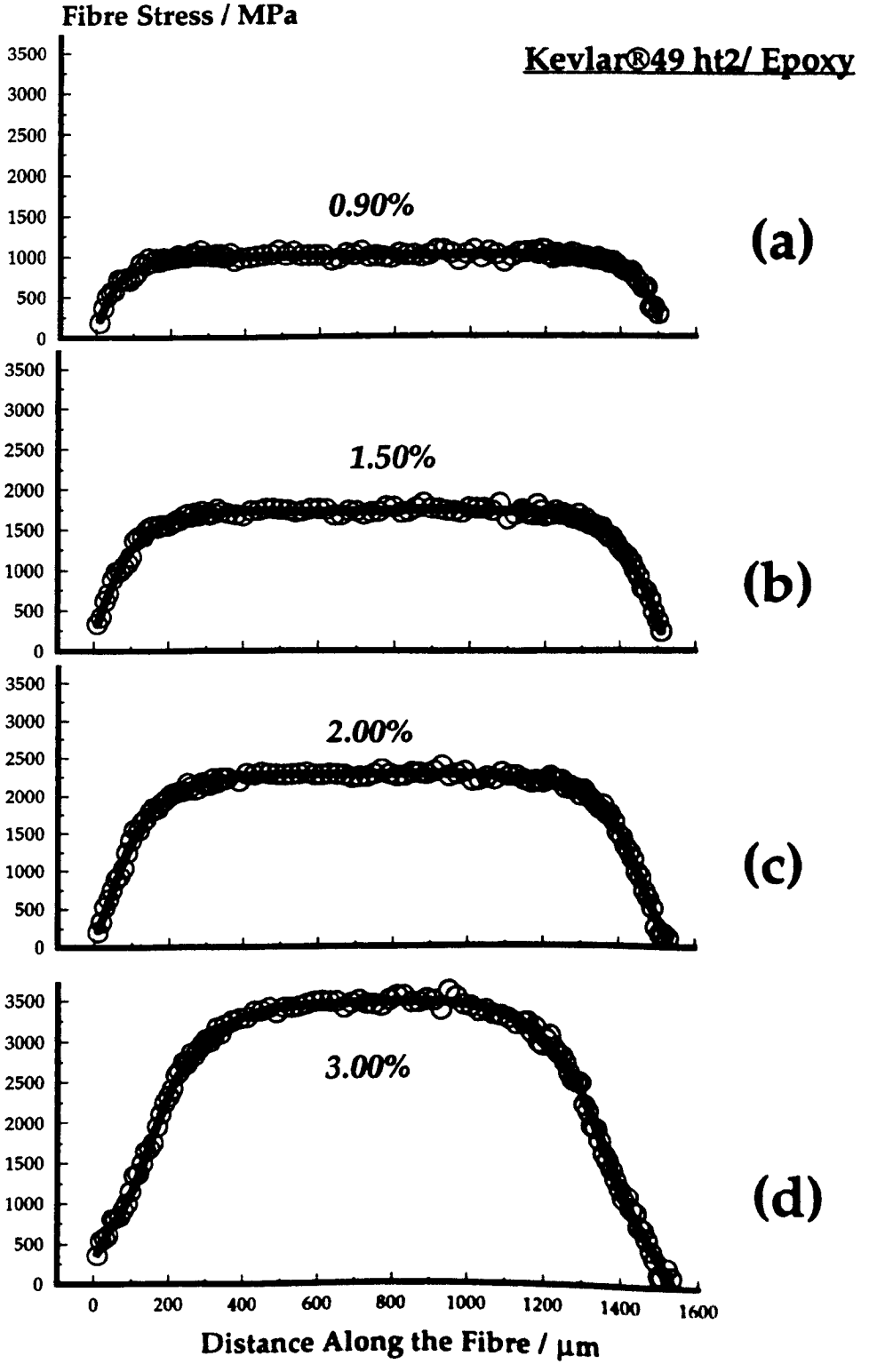

Figure 5.19. Fibre stress profiles for Kevlar®49 ht2 / epoxy system.

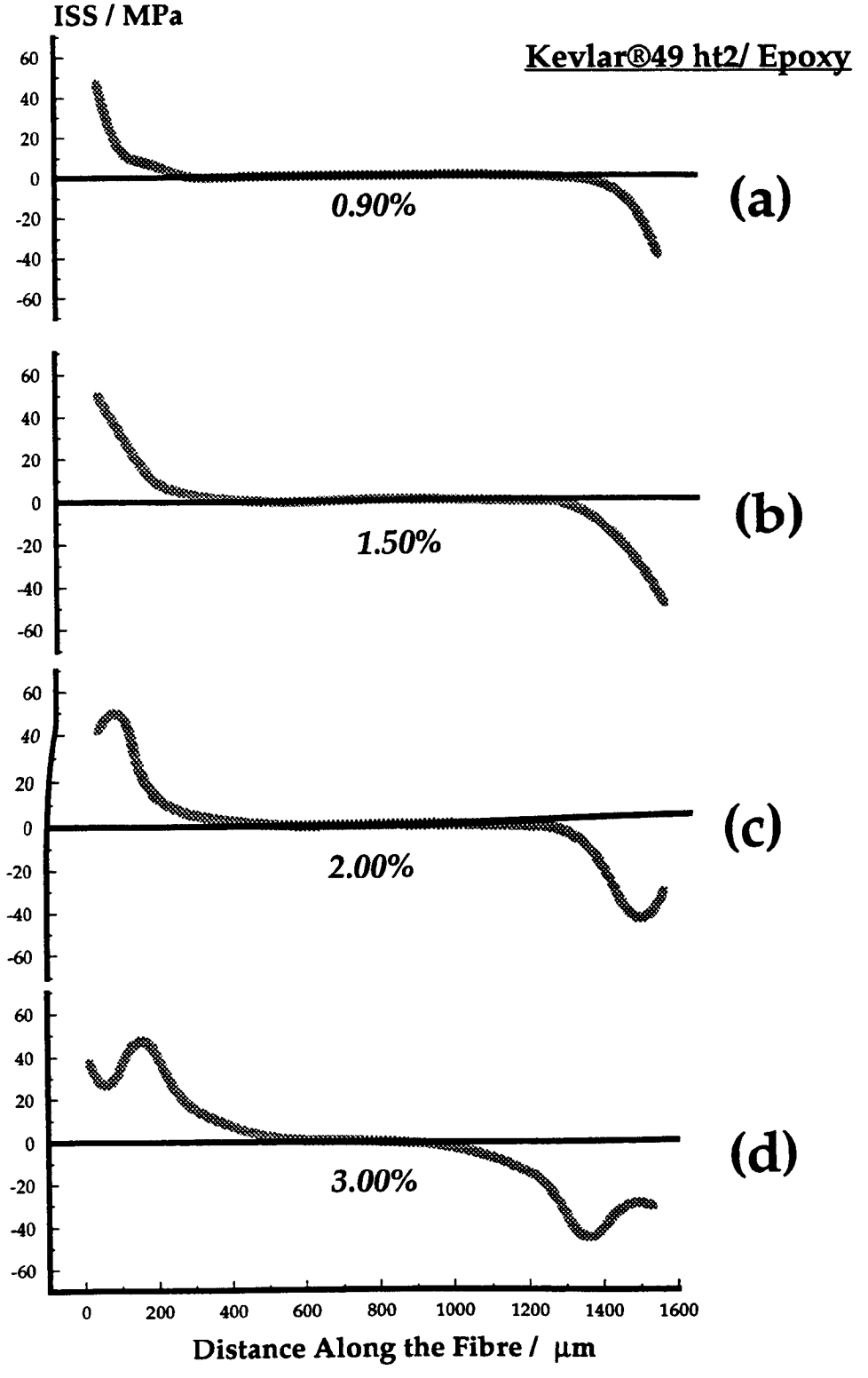

Figure 5.20. ISS profiles for Kevlar®49 ht2/ epoxy system.

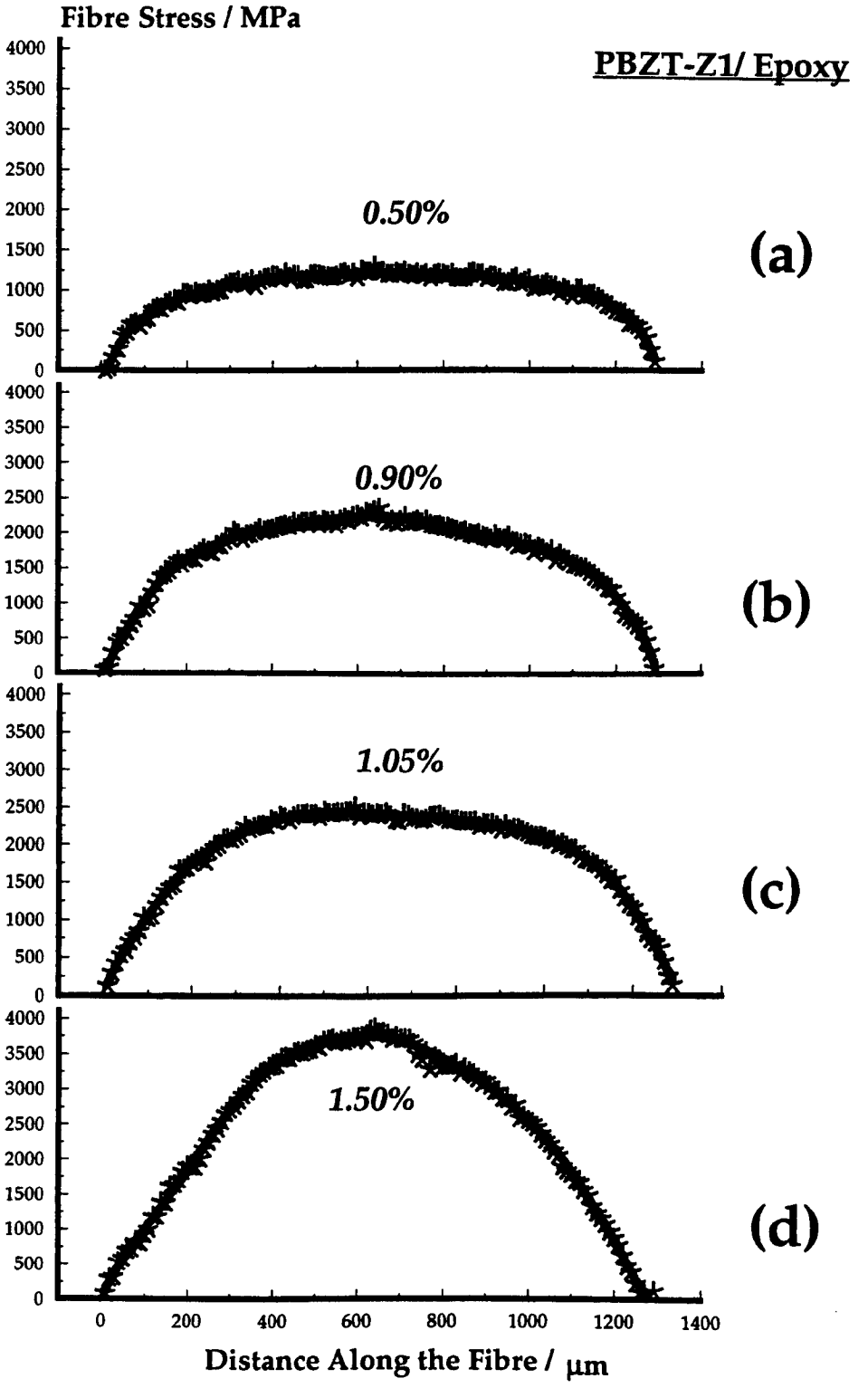

Figure 5.21. Fibre stress profiles for PBZT-Z1/ epoxy system.

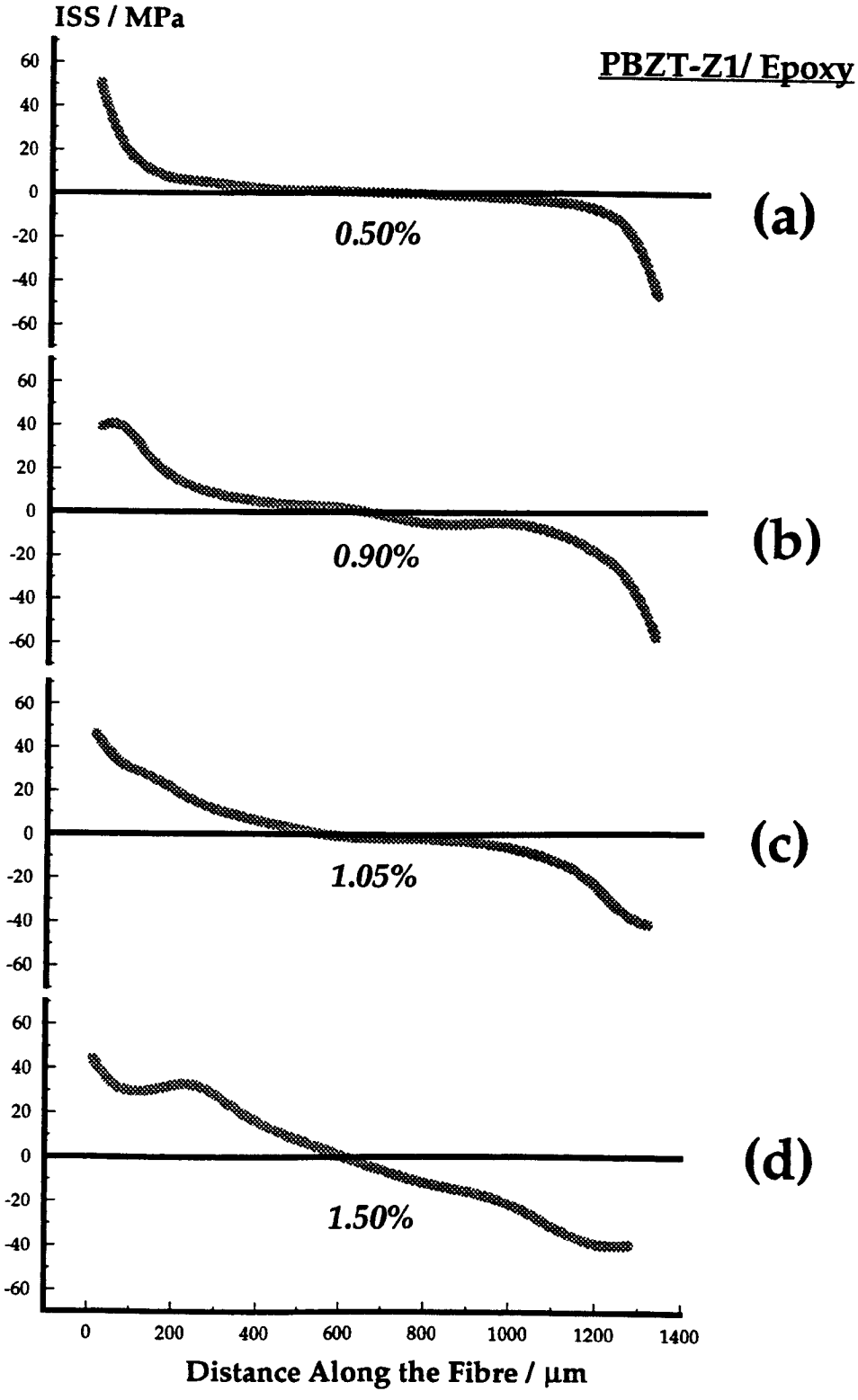

Figure 5.22. ISS profiles for PBZT-Z1 / epoxy system.

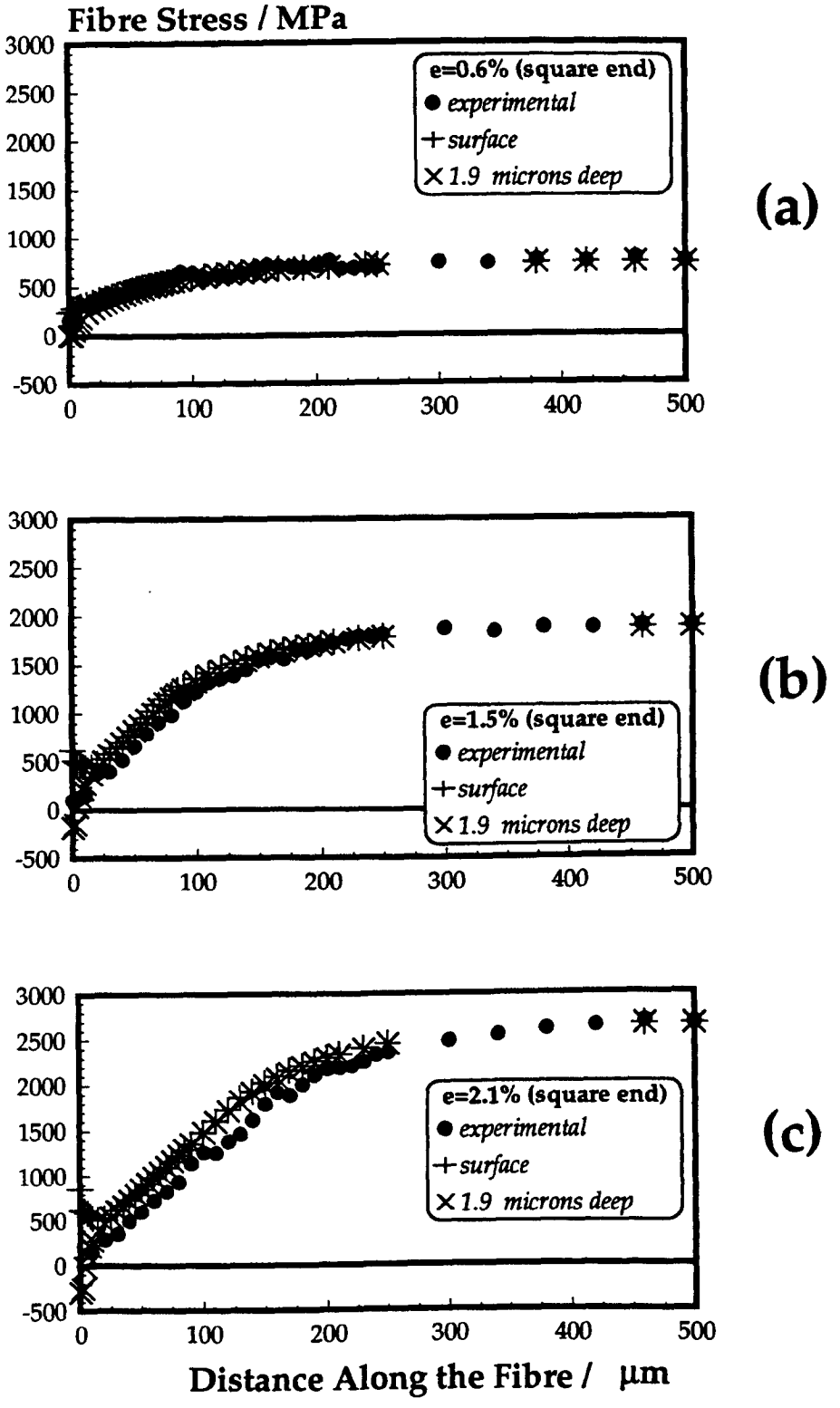

Figure 5.23. Comparison of experimental data and FEA predictions (square end) for fibre stress profiles along the fibre length.

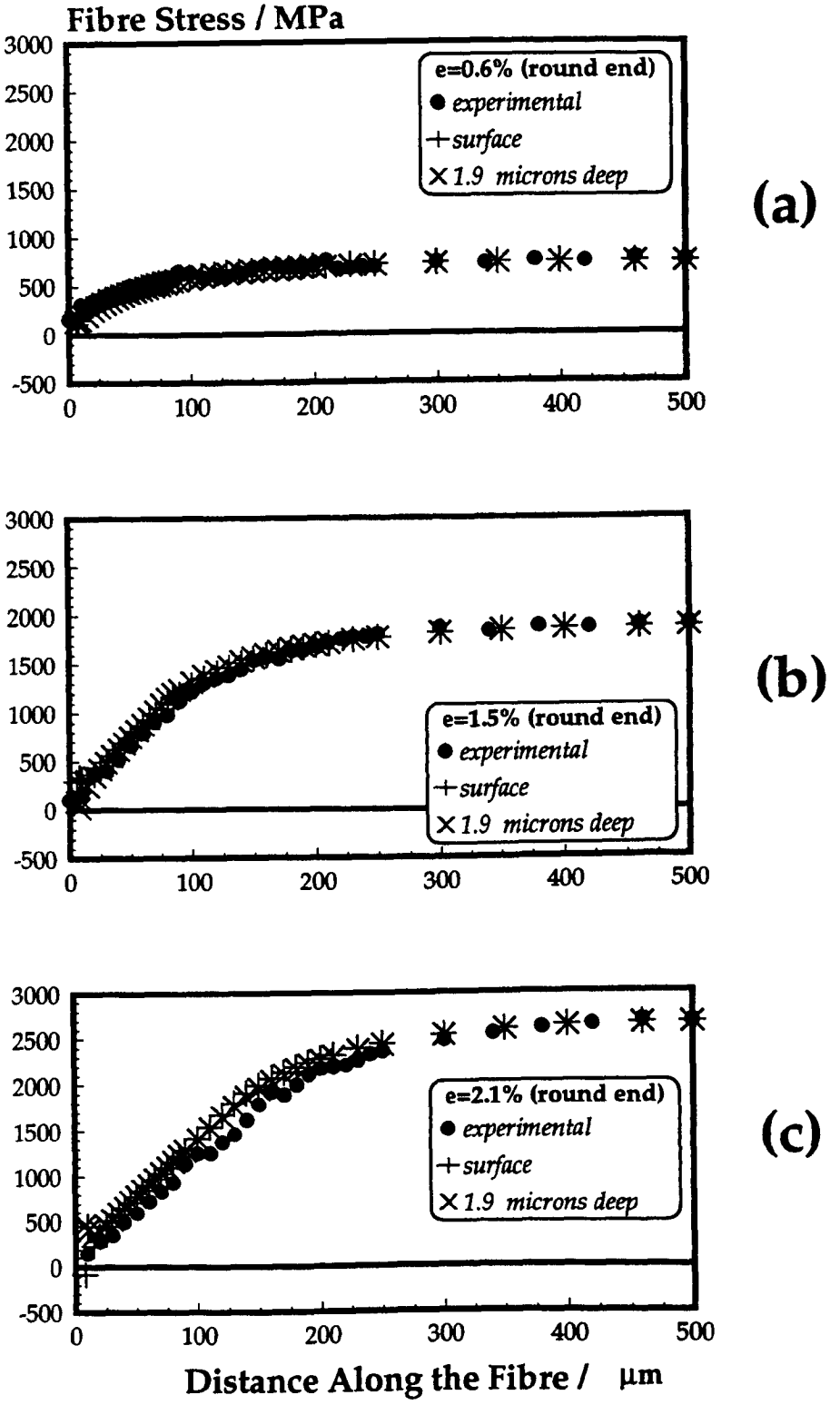

Figure 5.24. Comparison of experimental data and FEA predictions (round end) for fibre stress profiles along the fibre length.

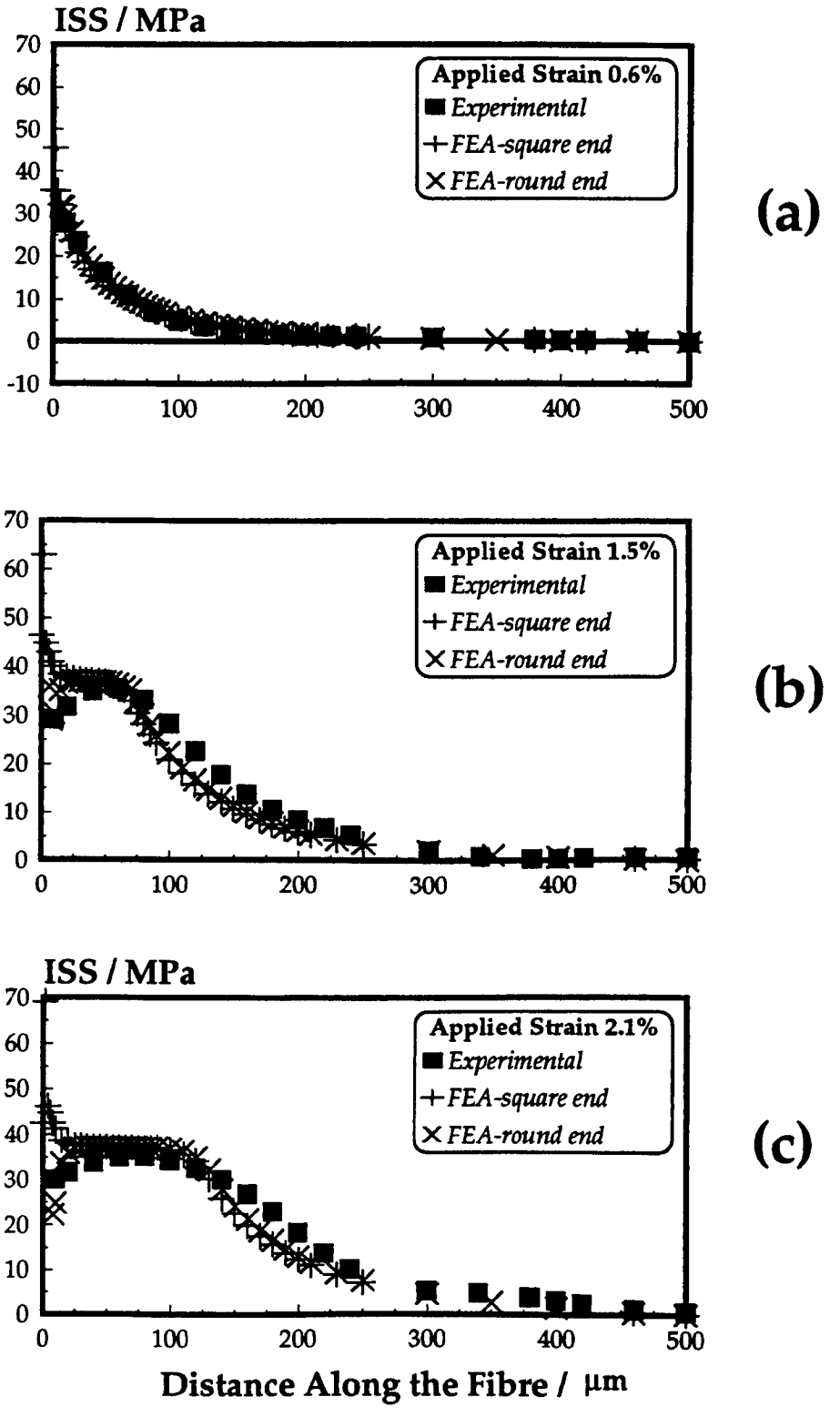

Figure 5.25. Comparison of experimental data and FEA predictions (square and round end) for ISS profiles along the fibre length.

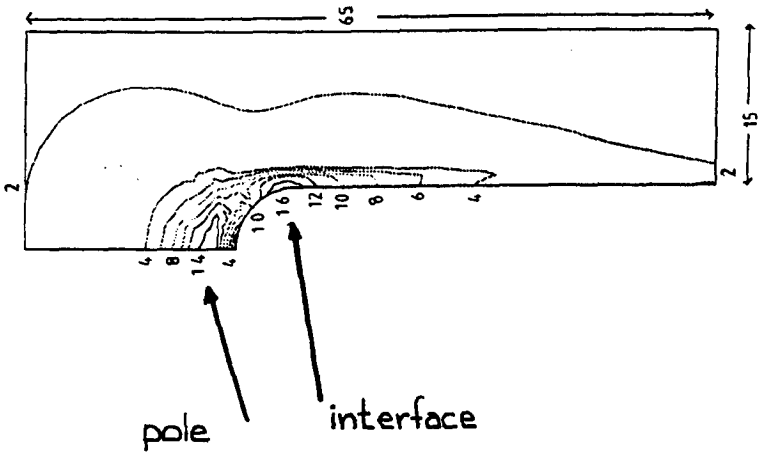

Figure 5.26. Von Mises strain contours in the matrix around the fibre end for applied strain 0.9% [**Guild 1994**].

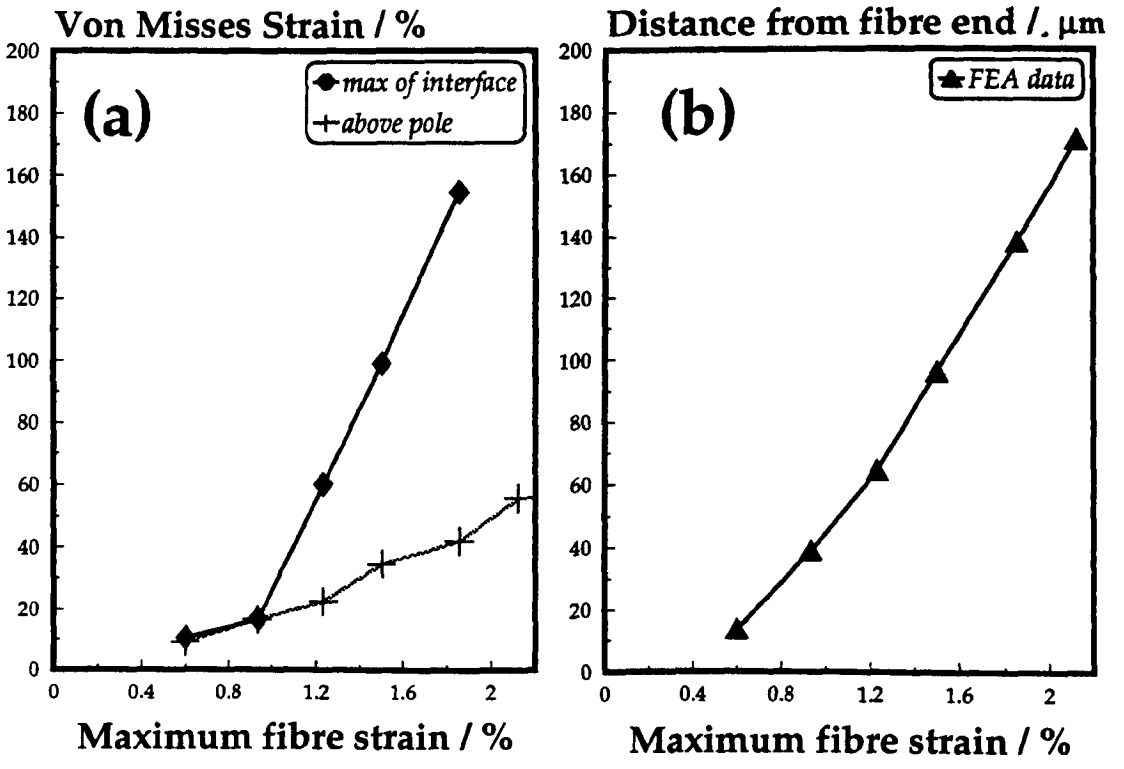

Figure 5.27. Maximum von Mises strain in the matrix vs applied strain [**Guild 1994**].

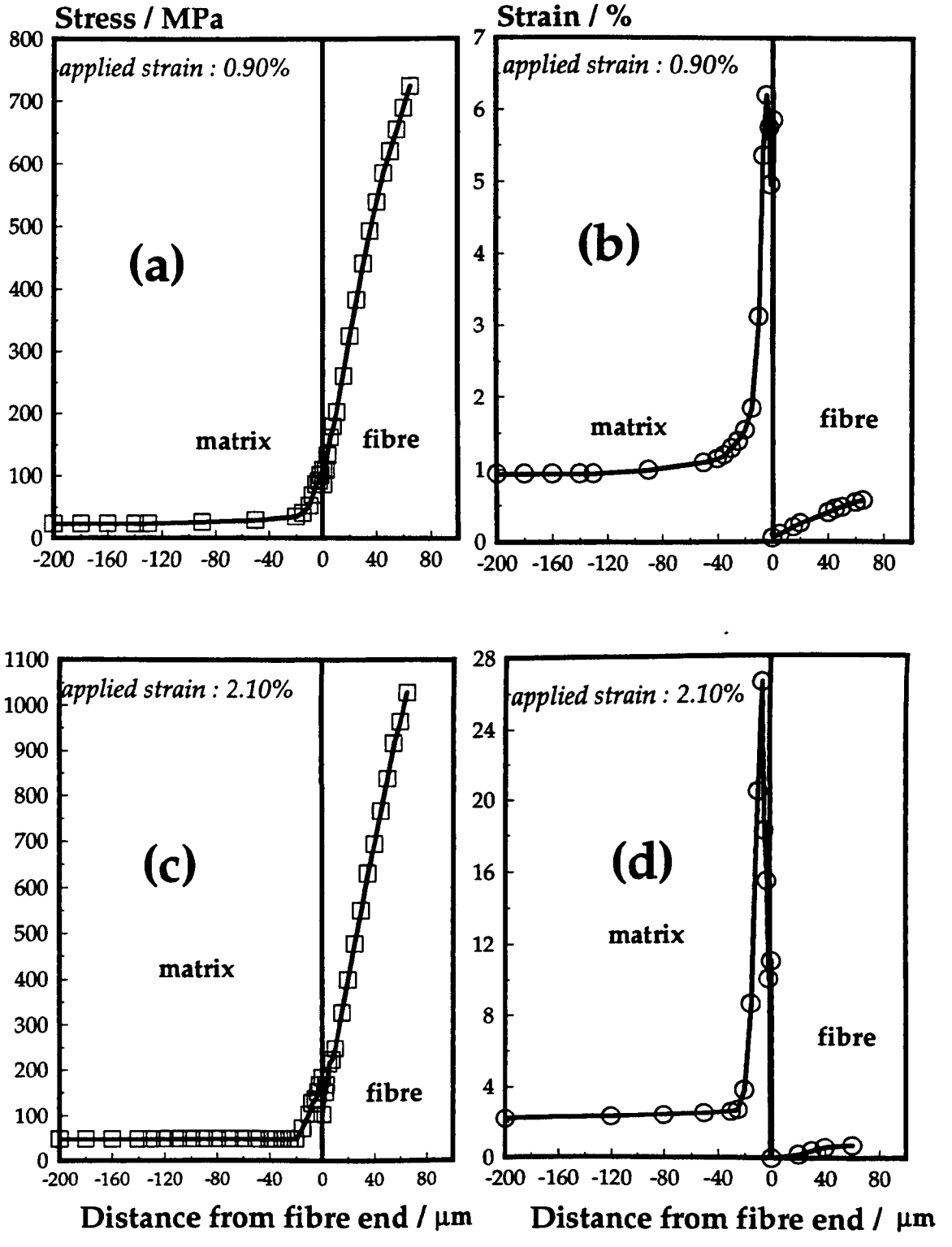

Figure 5.28. Stress and strain profiles through the matrix and the fibre for two different applied strains [Guild 1994].

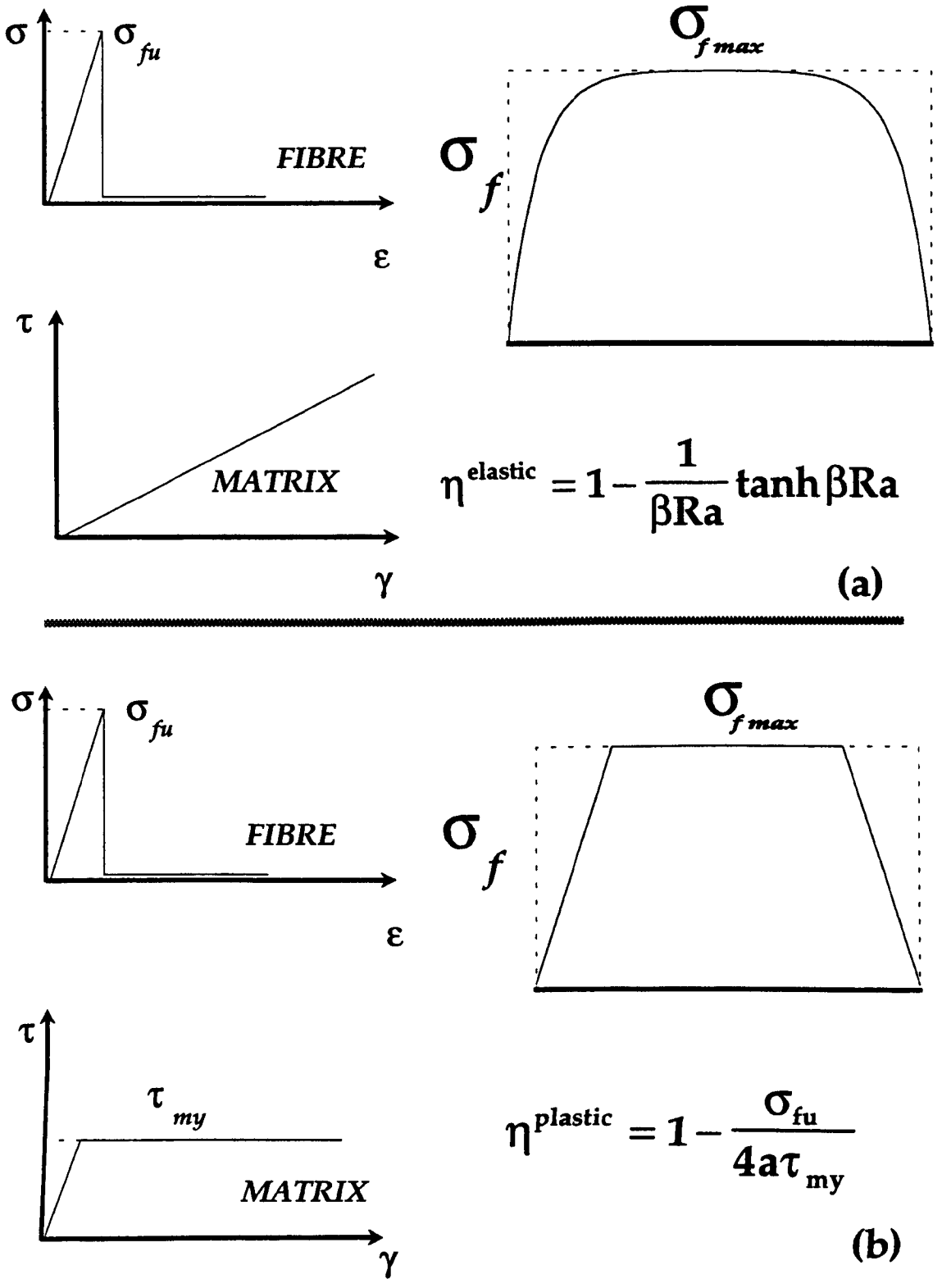

Figure 5.29. (a) FREF definition for elastic stress transfer model.
(b) FREF definition for plastic stress transfer model.

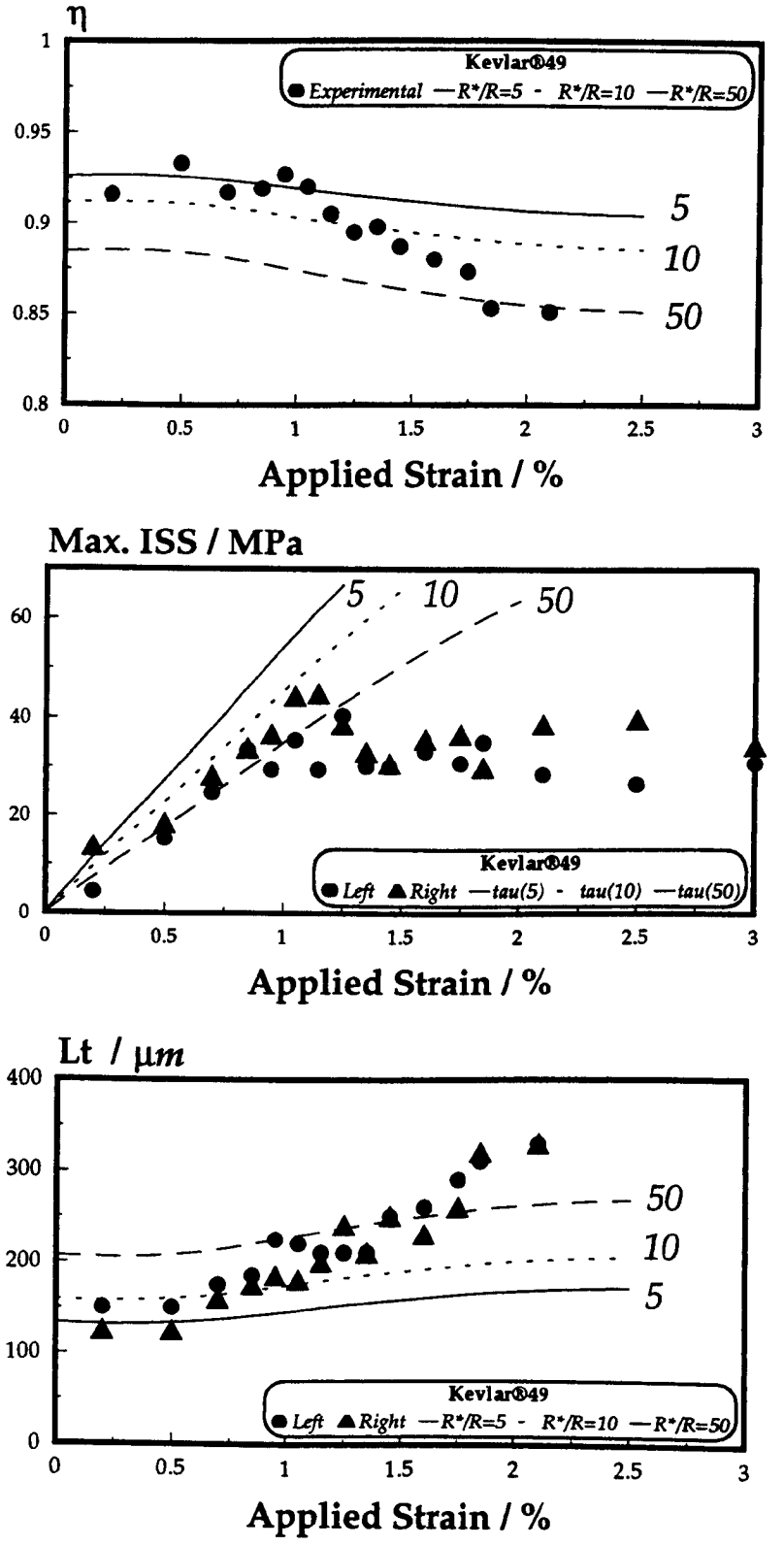

Figure 5.30. (a) FREF-applied strain data for Kevlar®49 / epoxy system.
(b) IFSS-applied strain data for Kevlar®49 / epoxy system.
(c) L_t-applied strain data for Kevlar®49 / epoxy system.

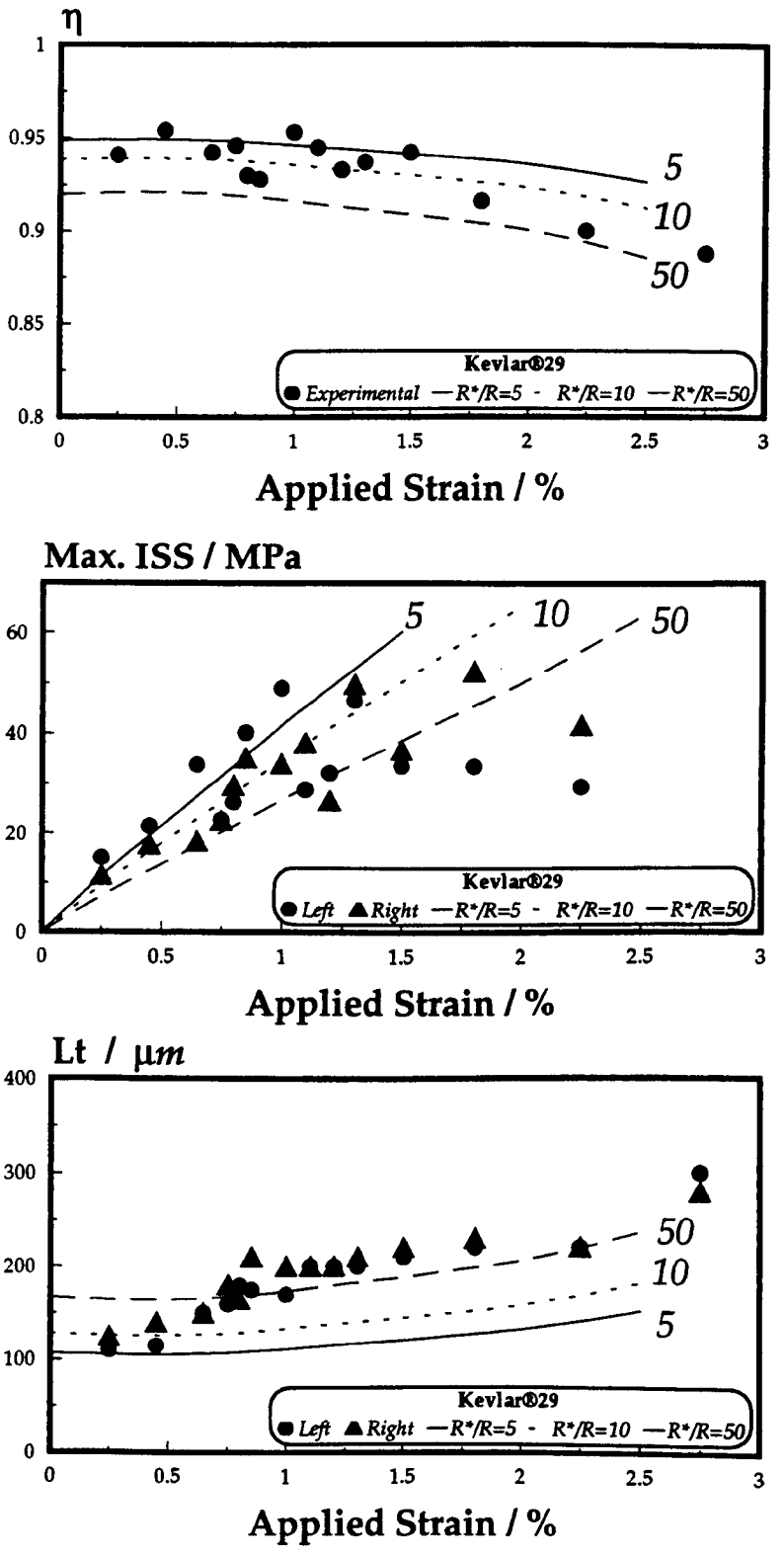

Figure 5.31. (a) FREF-applied strain data for Kevlar®29/ epoxy system.
(b) IFSS-applied strain data for Kevlar®29/ epoxy system.
(c) L_t-applied strain data for Kevlar®29/ epoxy system.

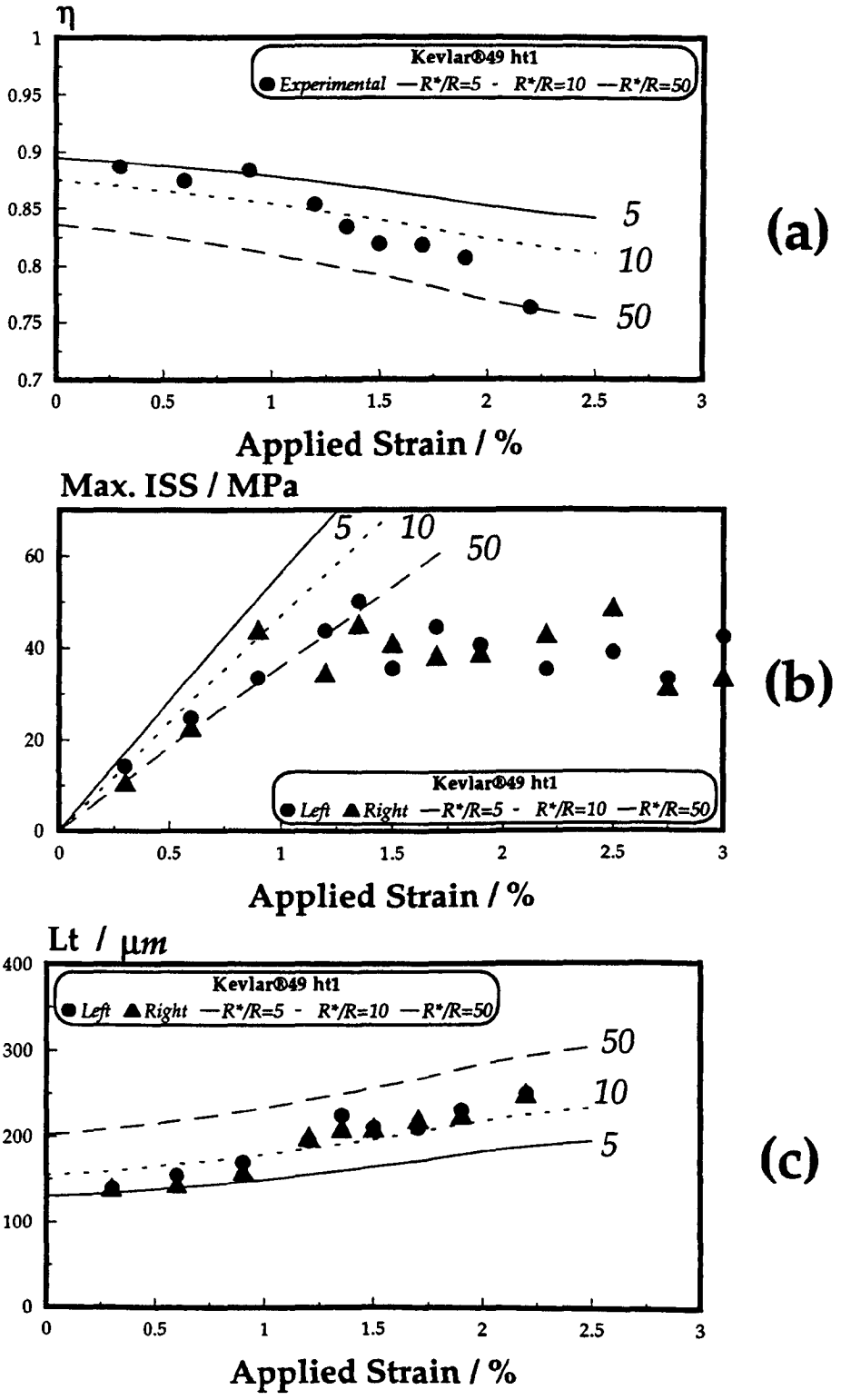

Figure 5.32. (a) FREF-applied strain data for Kevlar®49 ht1/ epoxy system.
(b) IFSS-applied strain data for Kevlar®49 ht1/ epoxy system.
(c) L_t-applied strain data for Kevlar®49 ht1/ epoxy system.

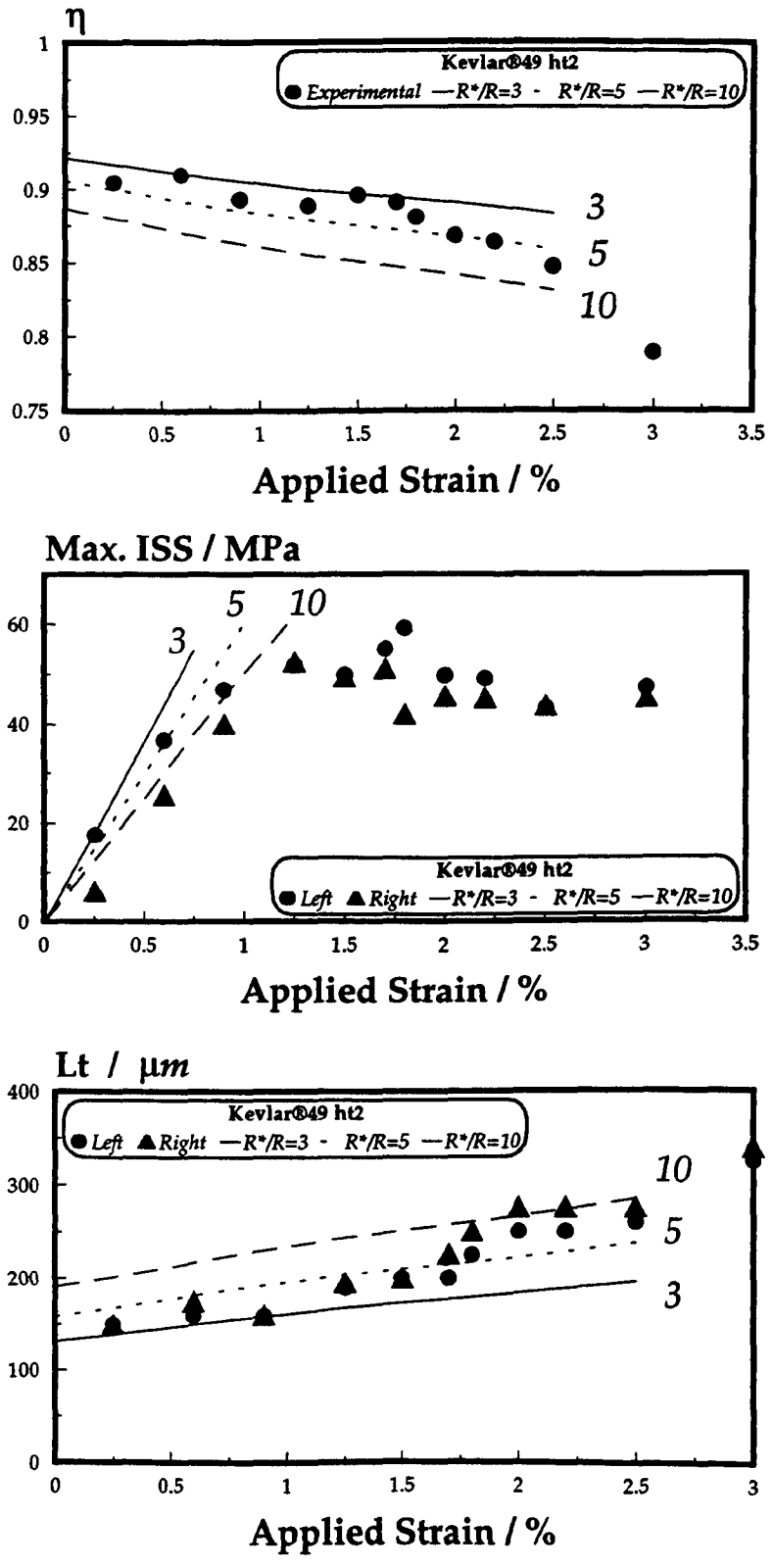

Figure 5.33. (a) FREF-applied strain data for Kevlar®49 ht2/ epoxy system.
(b) IFSS-applied strain data for Kevlar®49 ht2/ epoxy system.
(c) L_c-applied strain data for Kevlar®49 ht2/ epoxy system.

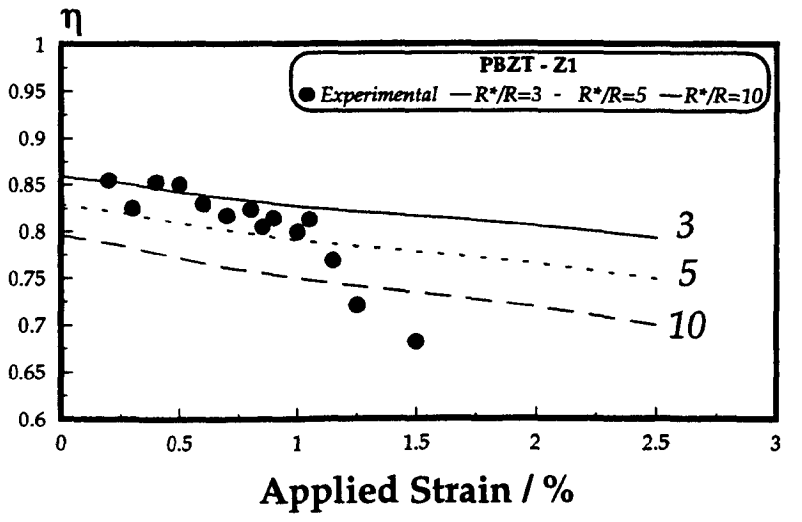

(a)

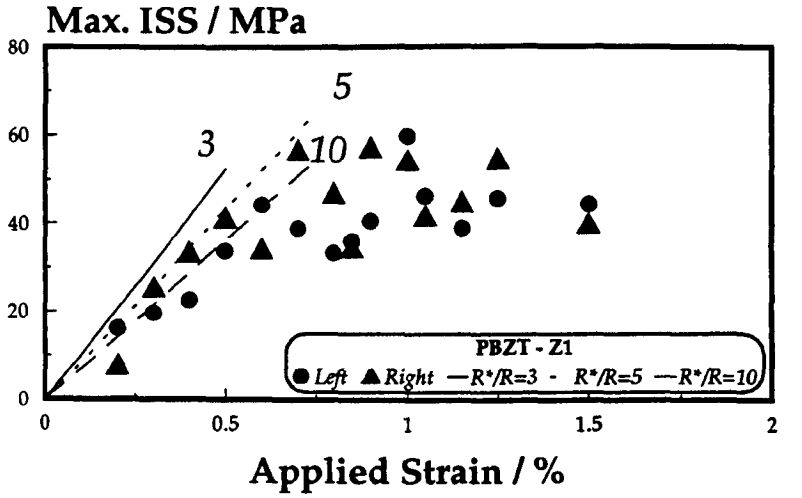

(b)

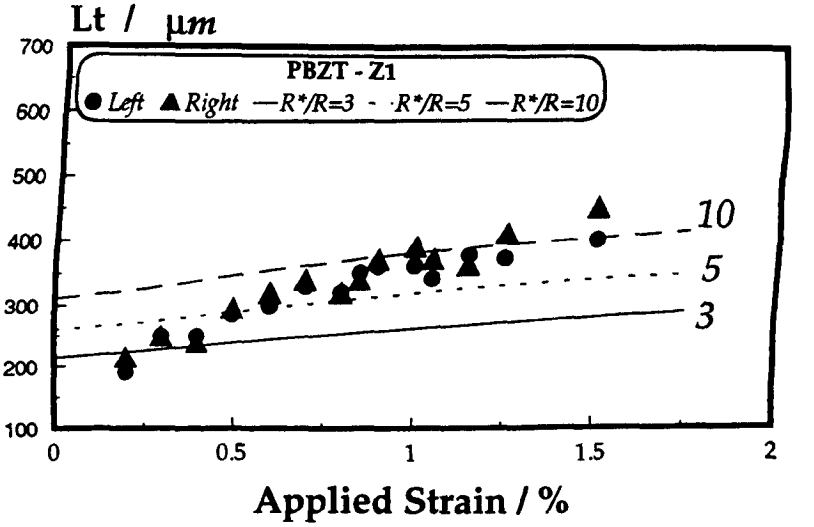

(c)

Figure 5.34. (a) FREF-applied strain data for PBZT-Z1/ epoxy system.
(b) IFSS-applied strain data for PBZT-Z1/ epoxy system.
(c) L_t-applied strain data for PBZT-Z1/ epoxy system.

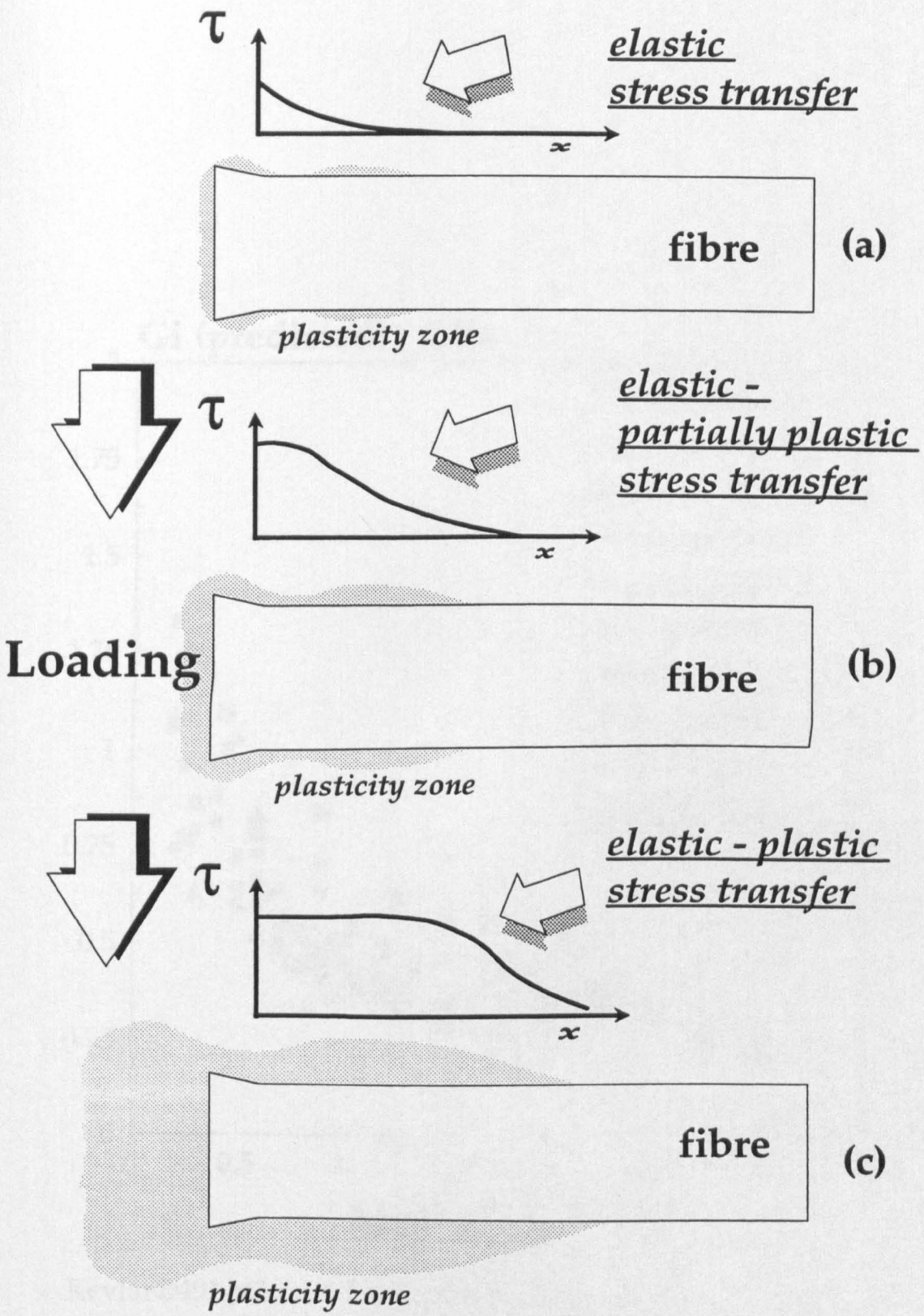

Figure 5.35. Schematic representation of the stress transfer mechanism in LCP fibre / epoxy resin systems.

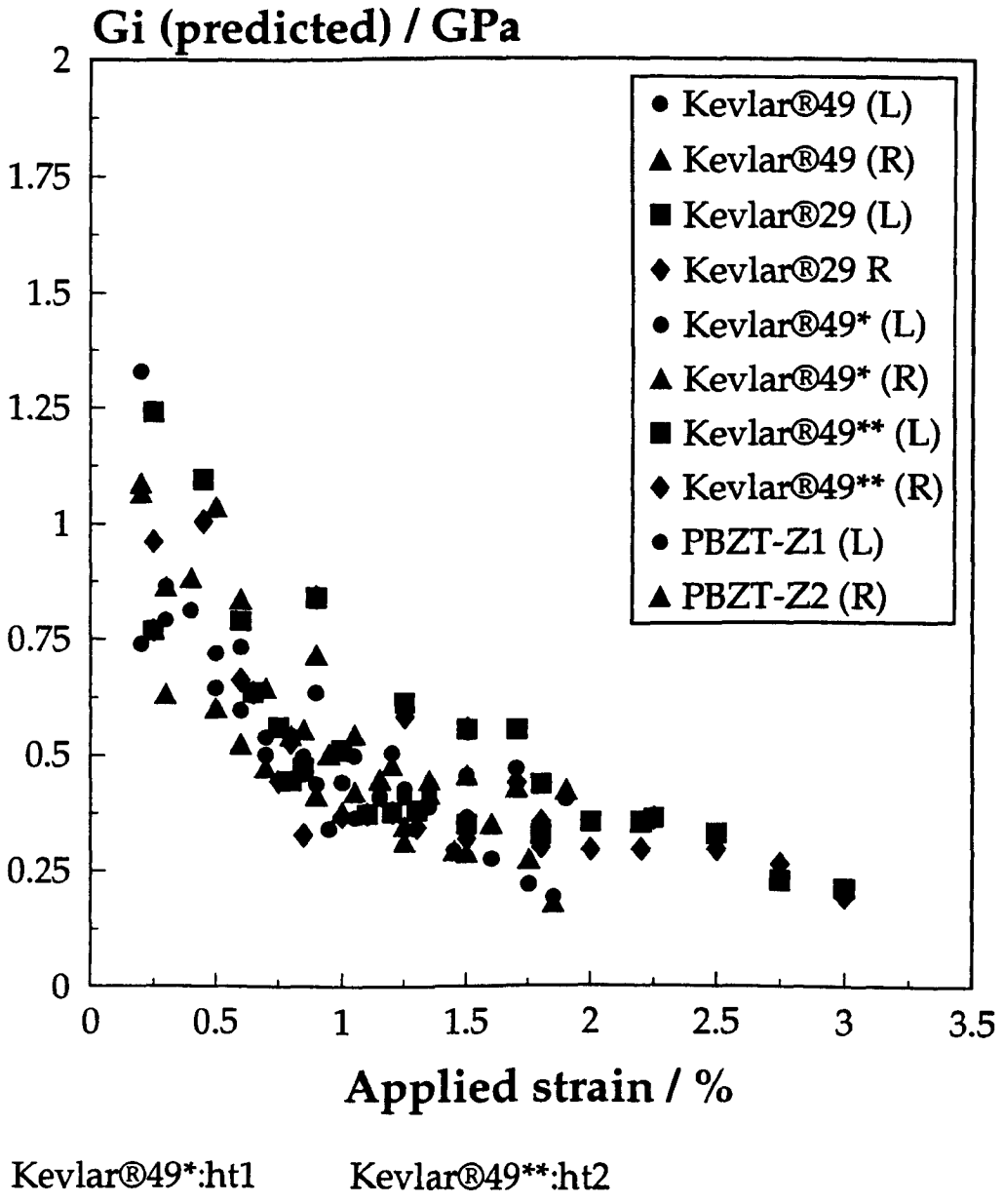

Figure 5.36. Stiffness prediction of the interphase for all LCP fibre / epoxy systems.

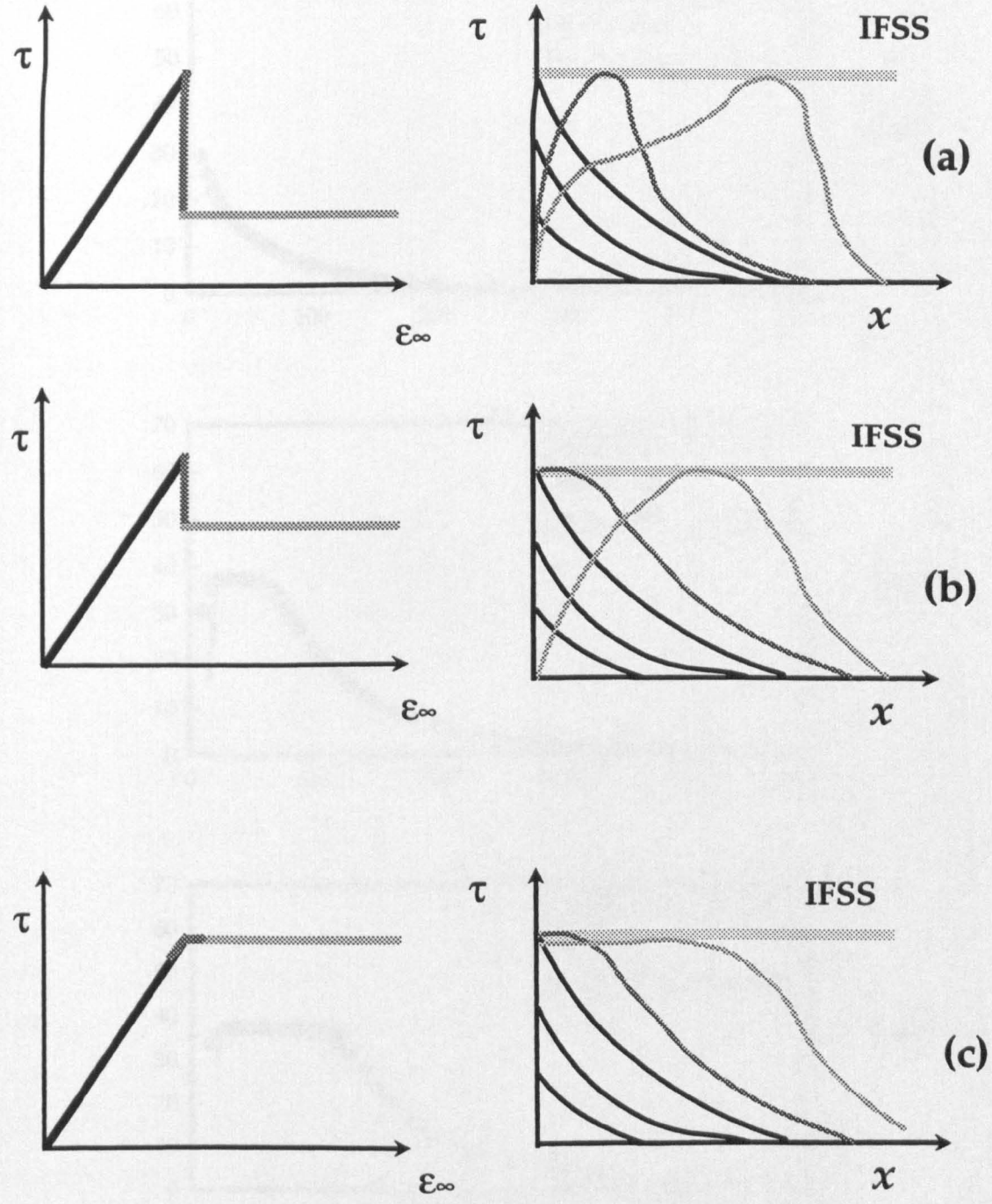

Figure 5.37. Mechanisms of stress transfer in various SFC systems.

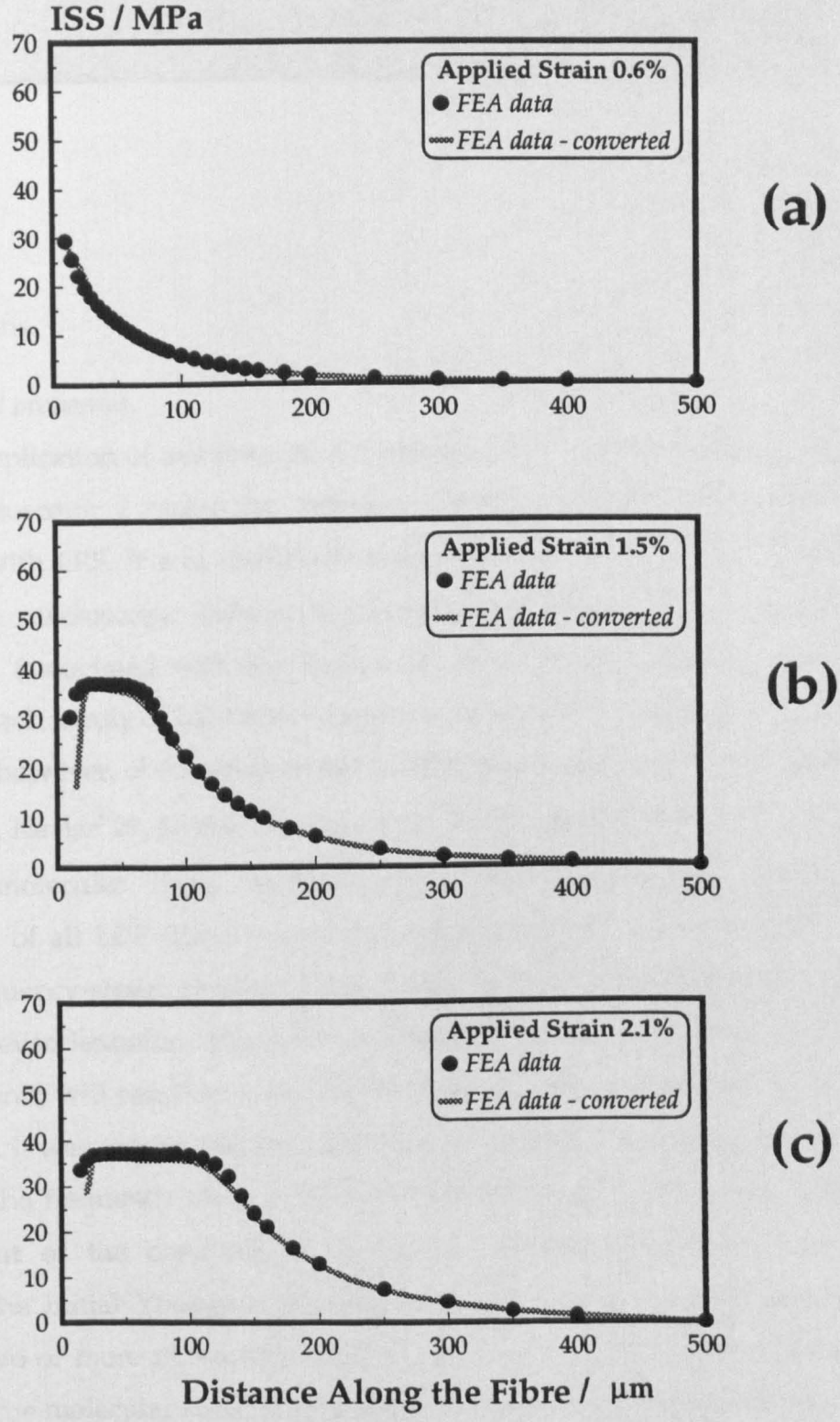

Figure 5.38. Comparison of direct FEA predictions and converted from stress profiles for ISS distributions along the fibre length.

CONCLUSIONS AND FURTHER WORK

1. Conclusions.

(i) Mechanical properties.

An application of macroscopic deformation in LCP fibres induces changes in their microscopic / molecular structure. These alterations can be accurately monitored with LRS. It was confirmed experimentally that a simple correlation between the macroscopic deformation (mechanical stress) and the molecular deformation (associated with the Raman frequency) exists. This correlation is unique for each family of LCP fibres and it was found to be linear. The difference in stiffness, however, obtained from fibres belonging in the same family (such as, for example, Kevlar®29, Kevlar®49 and Kevlar®149) is due to their different initial crystalline/molecular chain misorientation. The macroscopic stress-strain relationship of all LCP fibres examined in this work has a mirror image : the Raman frequency-strain response. Any procedure which will alter the initial crystallite misorientation characteristics of fibres derived from the same molecular unit, will result in a significant change of the mechanical response of these fibres. It was shown that the relationship between the macroscopic applied stress and the frequency shifts associated with 'backbone' vibrational modes is **independent** of the crystallite / molecular misorientation parameter (and therefore, the initial Young's modulus). In other words, the molecular chain bonds of two or more fibres with different initial molecular misorientation will 'feel' the same molecular stress if subjected to the same macroscopic stress.

It was also found that when LCP fibres are subjected to macroscopic deformations, the molecular misorientation parameter induces a gradient of stresses which act at microscopic / atomic level. Observed alterations in the

shape of the bands in the Raman spectra of LCP fibres ('broadening') confirmed this and a suitable model was developed for interpreting succesfully the mechanisms of band broadening.

The high anisotropy and the nematic crystalline character of LCP fibres upon which their superior tensile performance is based, are at the same time responsible for their compressive behaviour. Modified versions of the Cantilever Bending Beam (CBB) method and the Four-point Bending Beam (FBB) method combined with LRS were employed to study the behaviour of LCP fibres both in tension and compression. A method for converting spectroscopic data to stress-strain curves was proposed. It was found that in general, LCP fibres exhibit 'strain hardening' behaviour in tension and 'strain softening' behaviour in compression. The derived stress-strain and modulus-strain trends from the spectroscopic data are very similar to molecular chain stress-strain data reported in the literature. Further evidence that the molecular conformation / geometry of these materials is primarily responsible for bending/collapsing of the macromolecules encapsulated in the crystallites and consequently the macroscopic yielding of the fibres. These phenomena were attributed to axial-shear coupling and associated misorientation of crystallites/pleats in aramid fibres or fibrils in PBZT and PBO fibres (and thus molecular chain misorientation). In fact, the initial average misorientation distribution of the molecular chains induces shear instability which controls the mechanism of failure in compression. The compressive strength of LCP fibres was measured experimentally. It was found that LCP fibres are one order of magnitude weaker in compression compared with their superior tensile performance. From the whole range of fibres examined in this work, PBO fibres exhibit the most dramatic loss of strength in compression with the aramid and PBZT fibres slightly better.

(ii) Interfacial properties.

The existence of the interphase/mesophase and its properties is the major parameter controlling the stress transfer mechanisms in LCP fibre/ epoxy systems. The interfacial behaviour of LCP fibre/epoxy systems is very similar to

that proposed by the shear lag analysis up to a critical applied macroscopic strain. Maximum interfacial shear stresses (ISS) are located near the fibre end and increase gradually with the increase of the macroscopic applied strain. For applied strains higher than this critical value, mechanisms associated with the plastic behaviour of the matrix and/or the interphase take over. The stress transfer profile appears to be a 'trapezoid', the ISS fluctuates around a plateau value (plastic stress transfer) and then decays to zero towards the middle of the fibre (elastic stress transfer). The predominant mechanism of interfacial failure is, therefore, yielding in shear due to the high stresses developed near the fibre ends. The behaviour was satisfactorily confirmed by FEA analysis. The nature of this interfacial behaviour is different compared with sized carbon or other polymer fibre/epoxy sytems with 'finish' (sizing).

2. Future work.

In this work, an optical (spectroscopic) technique was used for investigating the mechanical properties of LCP fibres along with their adhesion to epoxy resins. The technique has the potential as an experimental method of stress analysis for a variety of modern reinforcing fibres and composites such as carbon fibres (PAN or pitch) **[Melanitis 1991]**, **[Filiou 1992]**, glass fibres with or without appropriate 'Raman active' coating **[Keneghan 1993]**, and others such as SiC fibres [**Bollet 1994**], providing that the fibres exhibit Raman activity which is dependent on the applied macroscopic deformation.

In this work, the simple 1-D coupon geometry shown in figure F.1a was employed for interfacial measurements in single fibre model composites based on a short fibre configuration. Stress transfer mechanisms investigation in single fibre model composites based on a continuous fibre configuration during classical fragmentation has also been achieved [**Melanitis 1991**]. The next natural step forward will be the application of the method to a more complex 2-D coupon geometry, shown in figure F.1b. This will enable us to investigate the effect of neighbouring fibres and the inter-fibre distance upon the stress transfer

characteristics prior to and after fibre fracture. Preliminary work [**Atallah 1993**] has shown the feasibility of the method in measuring stress concentration factors in the vicinity of a fibre fracture experimentally. To a stress analysis and composites design engineer, though, the ideal application of the method would be investigation and analysis of a full composite structure and integrity evaluation. Recent attempts in carbon fibre / epoxy [**Chohan 1995**] or even SiC fibre / glass matrix [**Bollet 1994**] involving a 3-D coupon geometry, have shown that the effect of the interface / interphase on the fracture characteristics of 'real' composites can be established and measured in a non-destructive manner by means of LRS.

One limitation of the conventional LRS technique is the fact that it is only applicable for surface studies and therefore a transparent matrix system is important for reliable and repeatable data acquisition. The improved remote LRS method (see chapter 2) provides us with the flexibility (separation between Laser Raman microprobe and spectrometer / detection unit) by the use of optical waveguides (fibre optics). This enable us to perform mechanical testing of the sample or structure under various environmental conditions in a universal mechanical tester and simultaneously obtain Raman spectra for further analysis. The remote LRS probe has also the potential for obtaining information from inside the 'heart' of a composite material by simply embedding optical waveguides between plies at 'strategic' points of the specimen or the composite structure and use these waveguides for Laser input / Raman output of the signal (figure F.2). Early attempts [**Arjyal 1995**] have shown that correlation between macroscopic mechanical stress (measured from the mechanical tester) and 'remote Raman stress' (measured by the remote Raman probe via the optical waveguides) can be obtained. To our knowledge, this is the only NDT (non-destructive technique) application which enables the user to measure in situ stress locally and precisely.

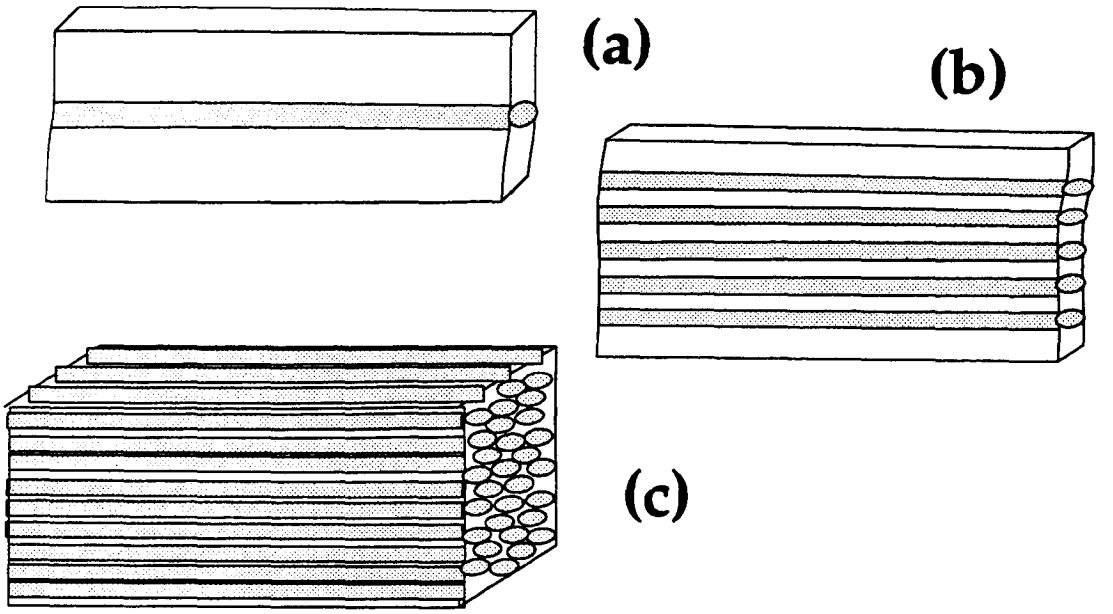

Figure F.1. (a) 1-D geometry, (b) 2-D geometry and (c) 3-D geometry in composites.

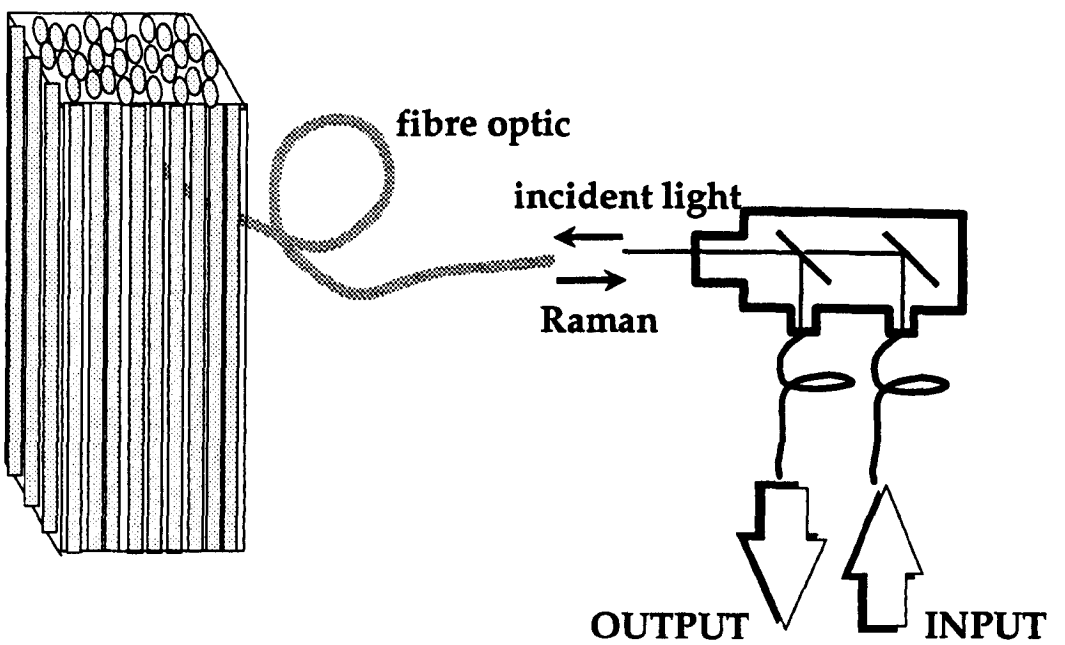

Figure F.2. In situ stress measurements in composites by means of Remote Raman Microprobe (ReRaM).

APPENDIX 1

In order to perform spectra analysis, the following functions were employed for baseline calculation and band intensity, position and width:

(i). A quadratic function for baseline calculations:

$$Q(x) = a_0 + a_1 x + a_2 x^2 \qquad \text{(Quadratic)} \qquad \text{(A1.1a)}$$

(ii). A Lorentzian or Gaussian (both symmetric) distributions for Raman band calculations:

$$C_n(x) = a_0 \frac{a_2^2}{(x - a_1)^2 + a_2^2} \qquad \text{(Lorentzian)} \qquad \text{(A1.1b)}$$

$$C_n(x) = a_0 \exp\left[-\left(\frac{x - a_1}{a_2}\right)^2\right] \qquad \text{(Gaussian)} \qquad \text{(A1.1c)}$$

In the following table the error due to symmetric distribution fit to the asymmetric peaks shown in figure 3.18 is calculated in absolute Delta Wavenumbers (cm^{-1}):

k	Position ν of Max. value / cm^{-1}	Error / cm^{-1}
low	1615 (arbitrary)	+0.10
medium	1620 (arbitrary)	+0.30
high	1480 (arbitrary)	+0.70

Table A1.1. *The effect of asymmetry to the spectroscopic calculations.*

In the following tables, the various combinations of symmetric distributions employed to fit spectra in the region of interest for each type of LCP

fibre are shown. The grey column represents the best fit (minimum R^2) for each fibre. Associated figures follow.

Fibre	R^2-LLLL	R^2-LLGL*	R^2-LGGL	R^2-GGGG
Kevlar49	99.96	27.60	31.08	35.59
Kevlar29	76.73	16.15	18.99	23.25
Kevlar149				
Kevlar49 ht1	113.98	29.64	33.82	47.28
Kevlar49 ht2	86.35	19.68	22.48	31.53

Table A1.2. *Evaluation of spectroscopic calculations for all Kevlar fibres. L: Lorentzian fit, G: Gaussian fit for 1520, 1570, 1615 and 1650cm^{-1} vibrational modes respectively.*

Fibre	R^2-L*	R^2-G
PBZT	56.55	72.84

Table A1.3. *Evaluation of spectroscopic calculations for PBZT fibre. L: Lorentzian fit, G: Gaussian fit for 1480cm-1 vibrational mode.*

Fibre	R^2-LLL*	R^2-LLG	R^2-GGG
PBO-B1	122.97	239.41	341.45
PBO-B2	33.84	88.83	145.56
PBO-B3	26.47	66.57	132.78
PBO-B4	45.06	133.89	221.54

Table A1.4. *Evaluation of spectroscopic calculations for all PBO fibres.*

L: Lorentzian fit, G: Gaussian fit for 1545, 1560 and 1620cm-1 vibrational modes respectively.

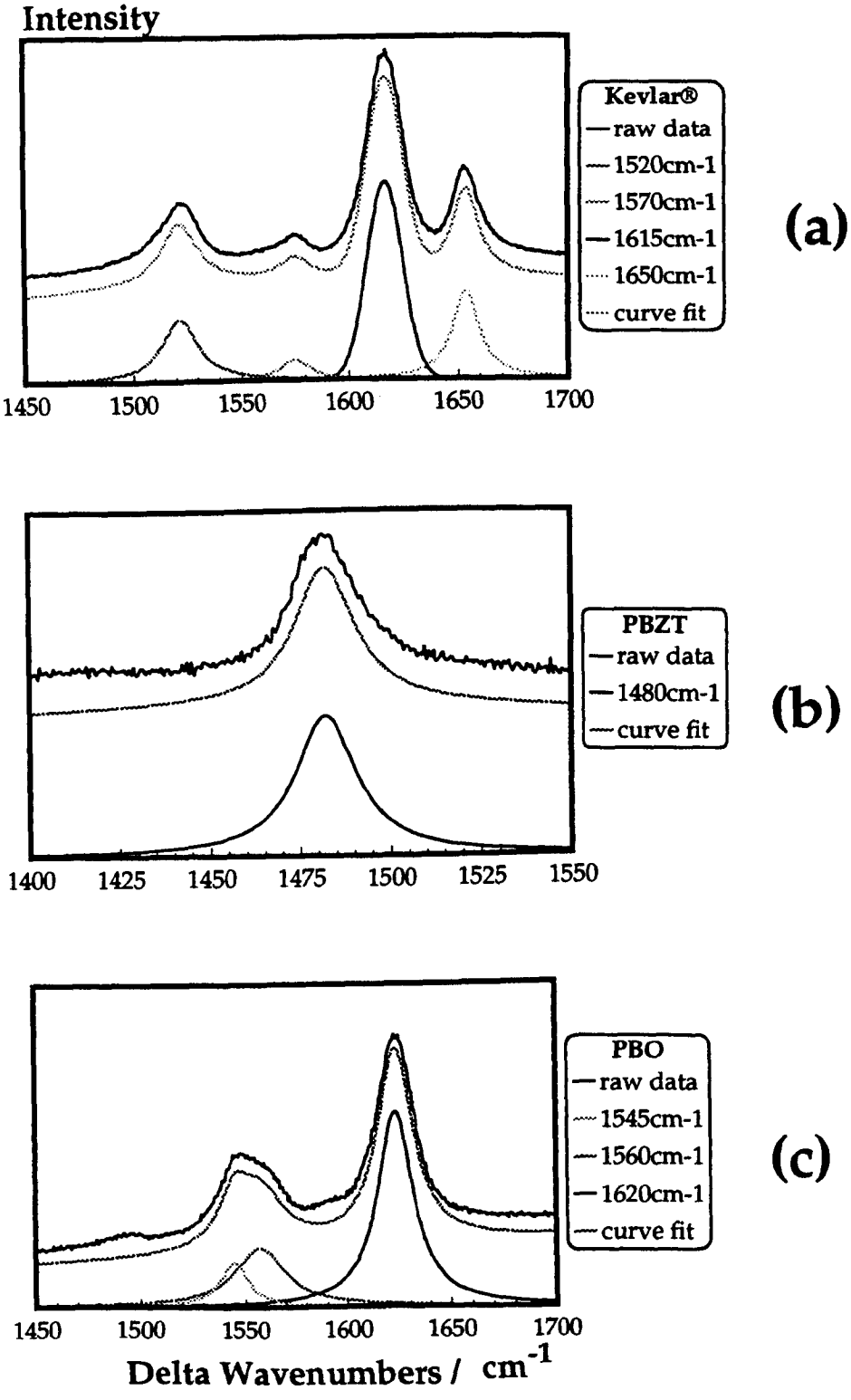

Figure A1.1. Optimum fit to Raman spectra of all fibres in the region of interest.

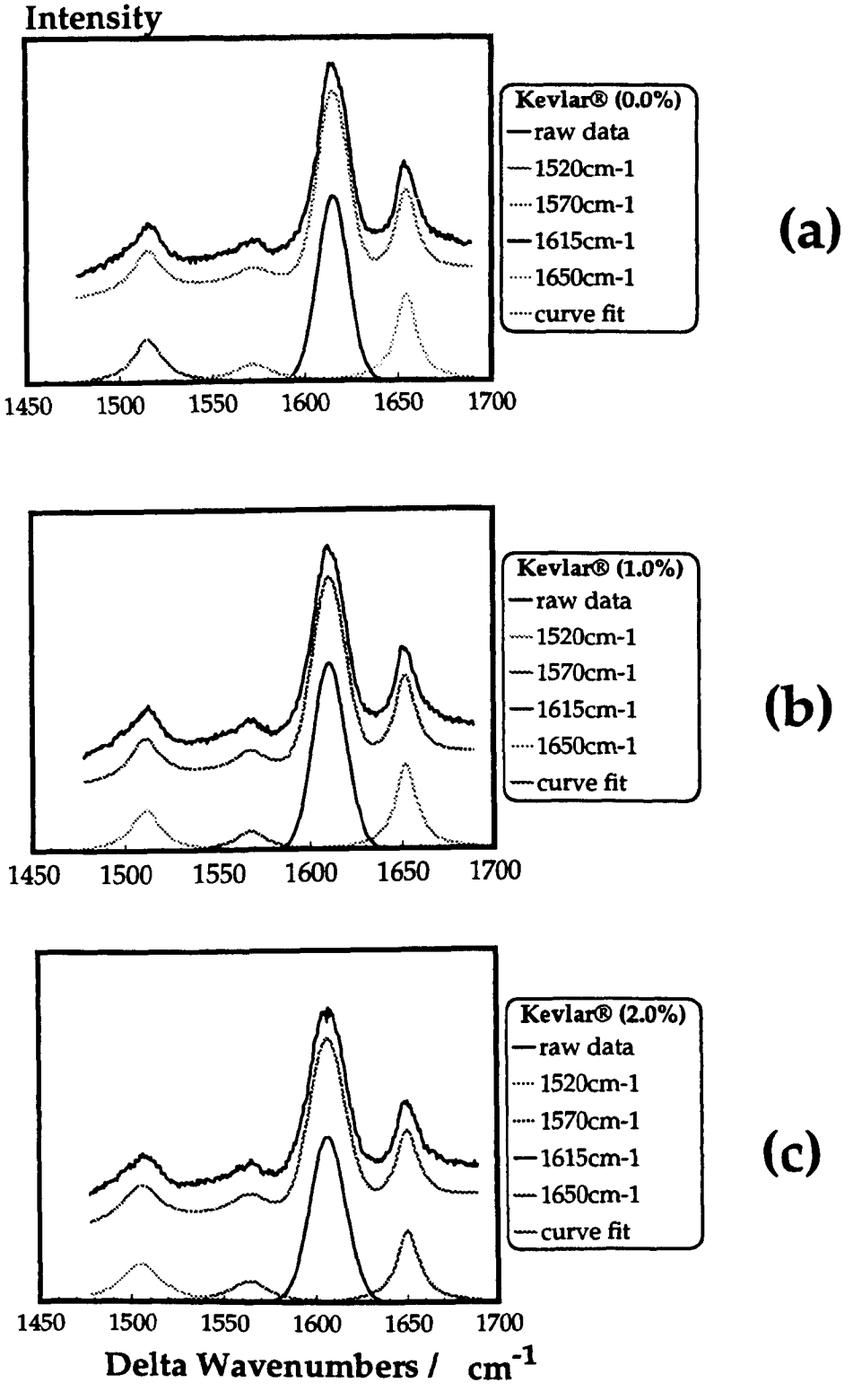

Figure A1.2. Optimum fit to Raman spectra of Kevlar® fibre at various tensile strain levels.

APPENDIX 2

In general, a set of data points which represent experimental measurements contains random errors. To seek a functional approximation to the data, it is first necessary to specify the mathematical form of the function. The two basic requirements for approximating experimental data are *smoothness* and *closeness*. In the case of polynomial fit the conflict of these two requirements is quite evident (figure A2.1). Keeping the degree of the polynomial at fairly low level, smoothness can be achieved but the fit may be poor (little closeness). On the other hand, if the degree of the polynomial is too high, the fit will be too close to the data, essentially following the random errors and tending to have unwanted fluctuations between the data points.

In this work, a *cubic spline function* was chosen **[Hayes 1974]** as the fitting function in two cases: (a) Raman frequency vs strain data (chapter 4) and (b) Fibre stress vs distance along the fibre (chapter 5). This function consists of a number of cubic polynomial segments joined end to end with continuity in first and second derivatives (unless otherwise stated). The x-values of the joints are called *knots*, or more precisely, *interior knots*. Their number determines the number of coefficients in the spline, just as the degree determines the number of coefficients in a polynomial **[Hayes 1974]**. The choise of these knots is a matter of trial and error.

Two examples are shown in figures A2.2 and A2.3 associated with the above two cases. In figure A2.2 the same set of experimental data has been fitted with two different numerical approximations, namely the polynomial and the cubic spline interpolations. As can be seen, the cubic spline interpolation gives a much more satisfactory fit to the experimental data. The polynomial fit is particularly poor in the area of compression failure where abrupt changes of the y-values occur. In figure A2.3, three different attempts at cubic spline interpolation to the same set of experimental data are shown. A different number of interior knots is used in each case. Quite clearly, poor fit is obtained for underestimation or overestimation of the number of knots and their position.

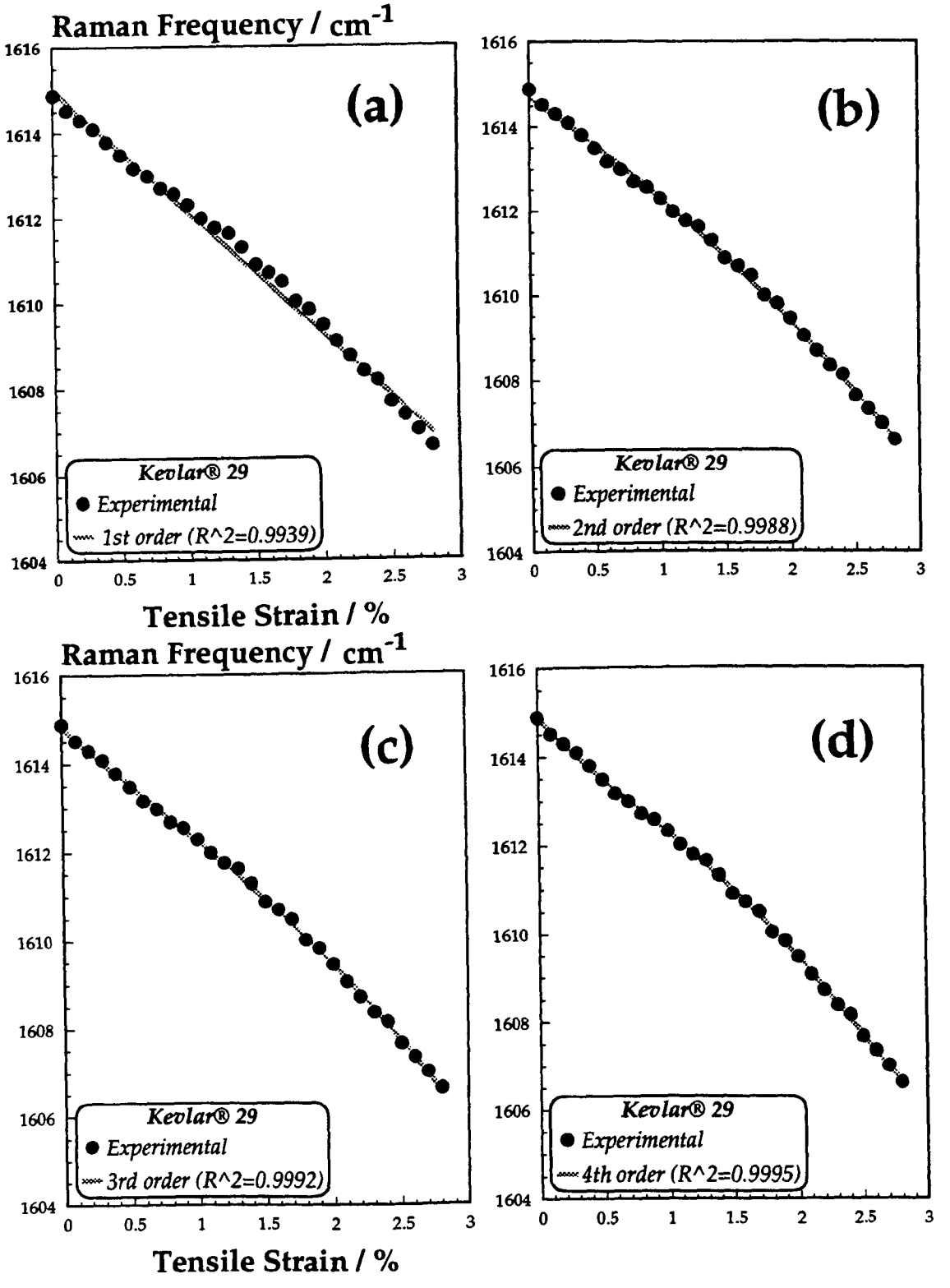

Figure A2.1. Polynomial interpolations to frequency vs strain data for Kevlar®29 fibre: (a) linear, (b) quadratic, (c) cubic and (d) fourth order interpolation.

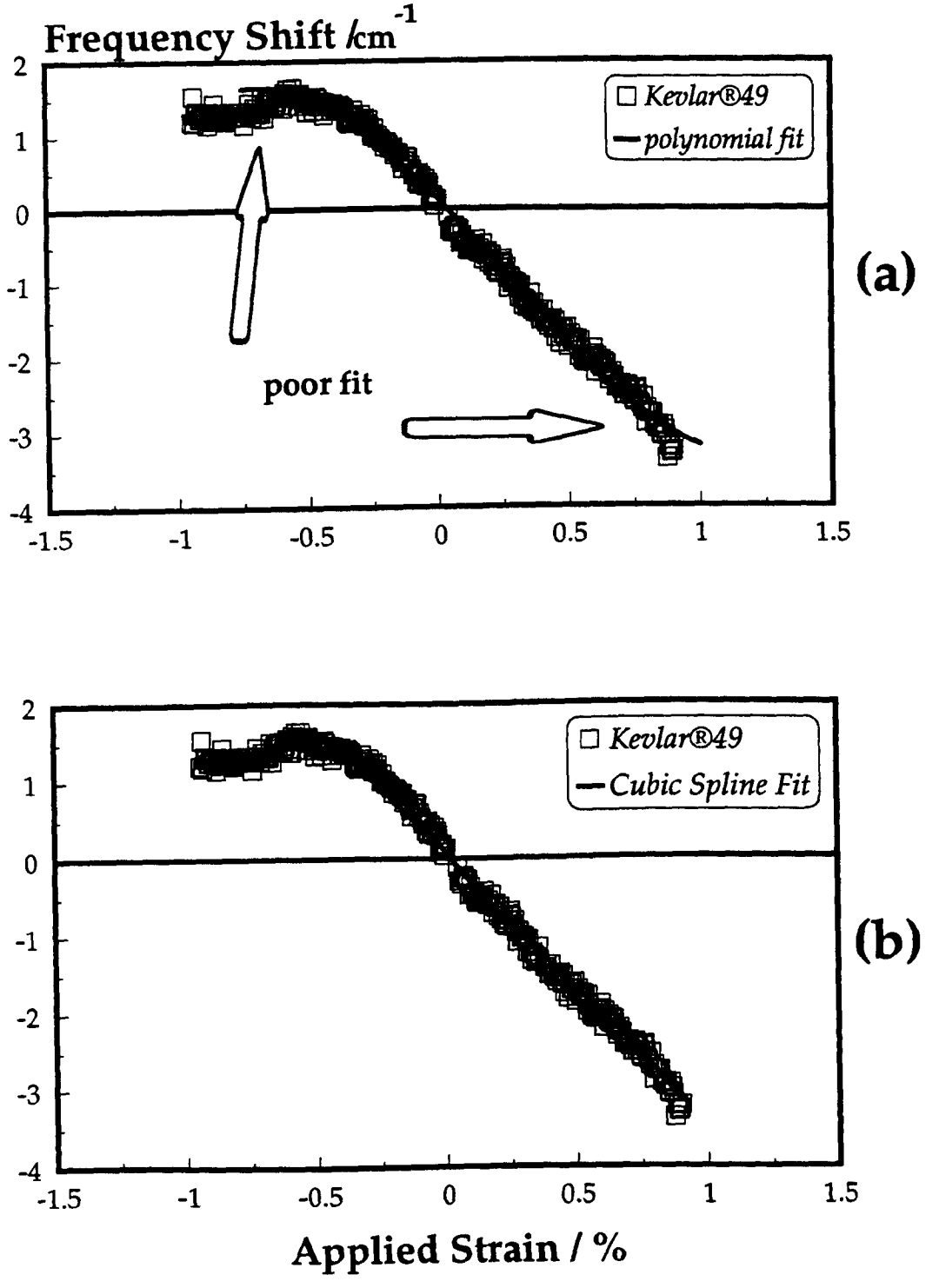

Figure A2.2. (a) polynomial and (b) cubic spline interpolation to frequency shift vs strain data for Kevlar®49 fibre.

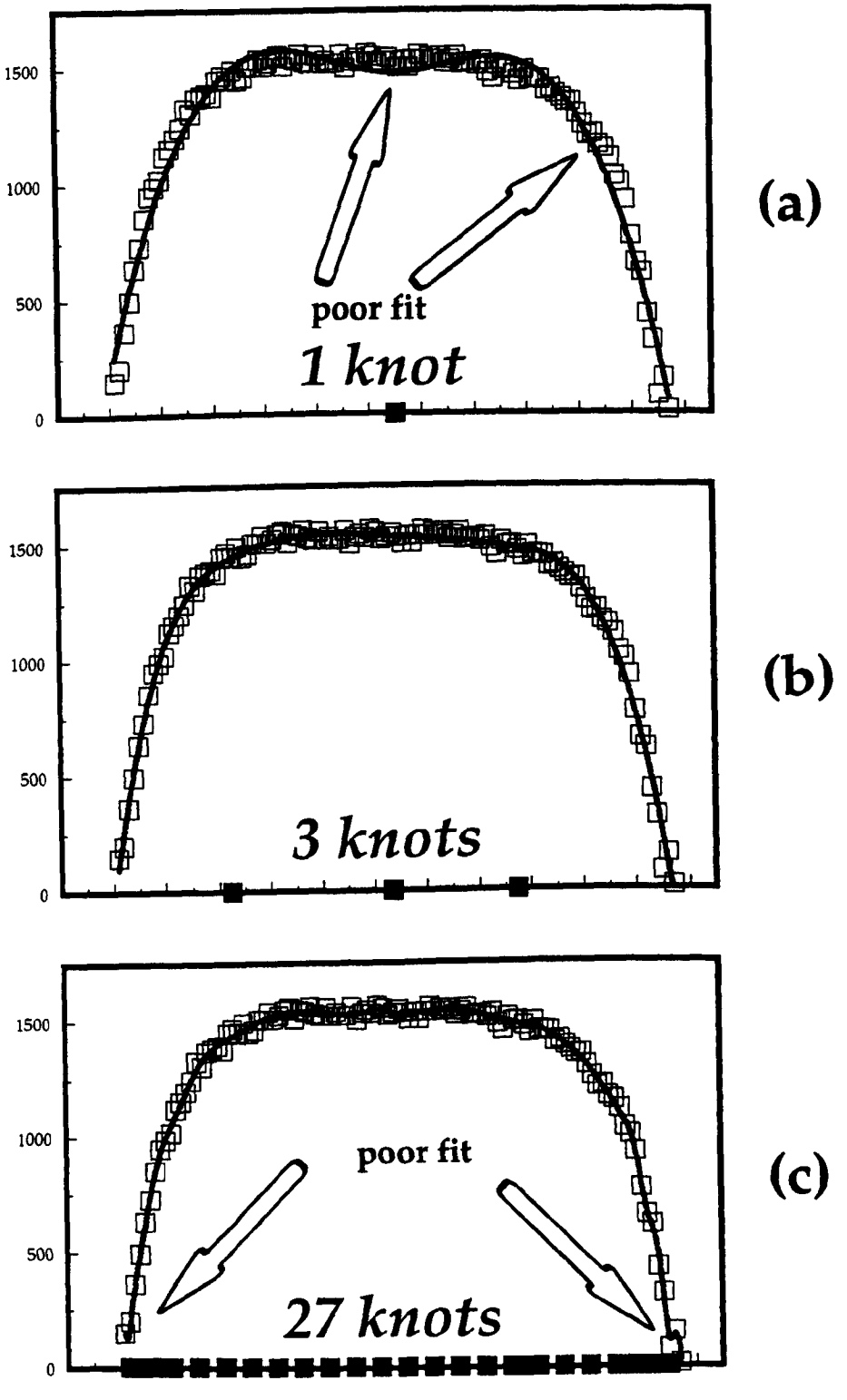

Figure A2.3. Cubic spline interpolation for various combinations of knots and knots position to fibre stress vs distance along the fibre data for Kevlar®49/ epoxy system.

APPENDIX 3

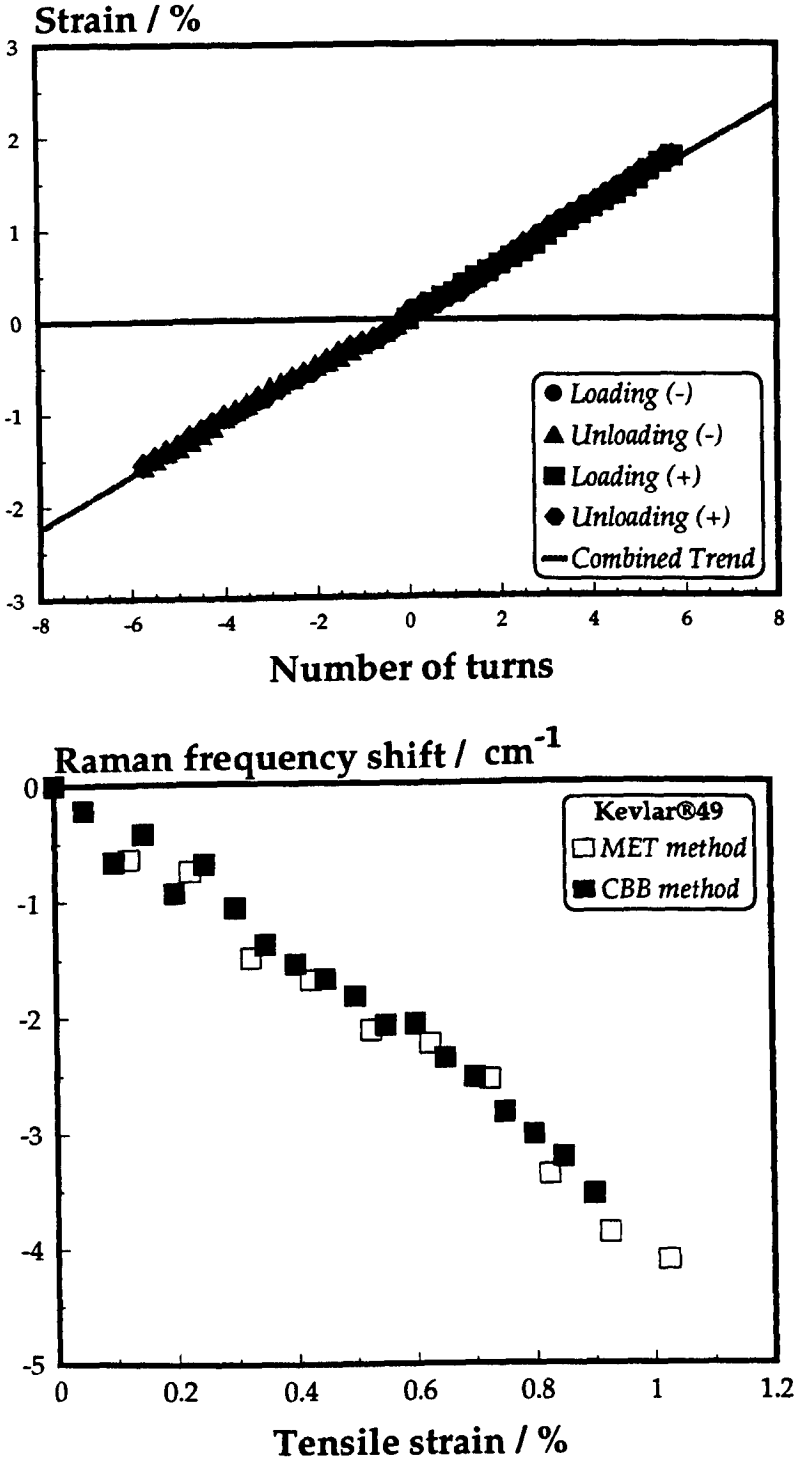

Figure A3.1. (a) Strain gauge measurement vs deflection for FBB tests.
(b) Comparison between MET and CBB data for Kevlar®49 fibre in tension.

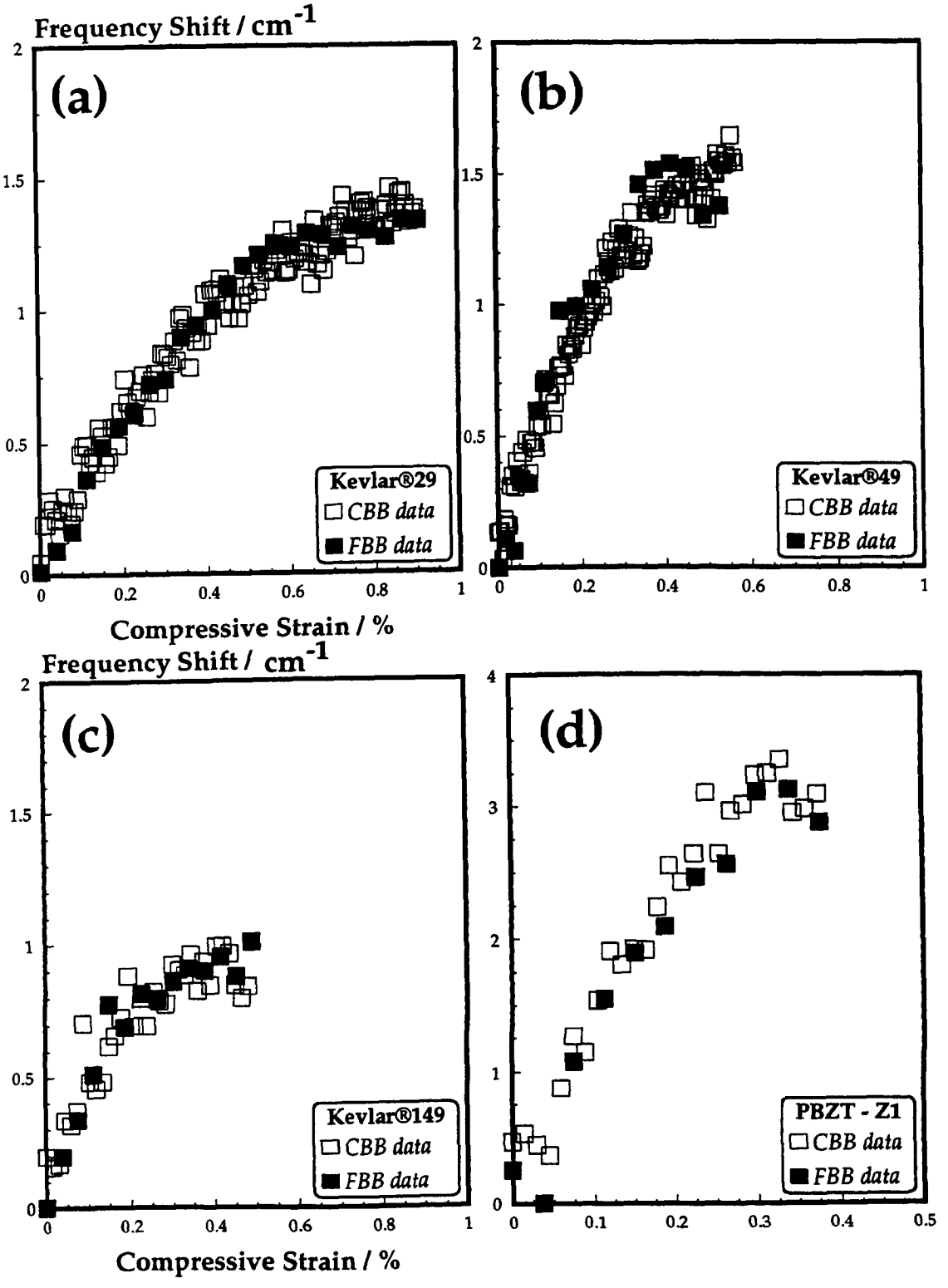

Figure A3.2. Comparison between CBB and FBB data in compression for : (a) Kevlar®29, (b) Kevlar®49, (c) Kevlar®149 and (d) PBZT-Z1 fibres.

REFERENCES

Adams, W.W., Azaroff, L.V. and Kulthreshna, Z. *Kristal*, **150**, p.321 (**1980**).

Agarwal, B.D. and Broutman, L.J. '*Analysis and Performance of Fiber Composites*', 2nd Ed., John Wiley & Sons, Inc., USA (**1990**).

Allen, S.R., Filippov, A.G., Farris, R.G. and Thomas, E.L., *J. Appl. Polym. Sci.*, **26**, p.291 (**1981a**).

Allen, S.R., Filippov, A.G., Farris, R.G., Thomas, E.L., Wang, C.P., Berry, G.C., and Chenevey, E.C., *Macromolecules*, **14**, p.1135 (**1981b**).

Allen, S.R. et al, '*The Strength and Stiffness of Polymers*', A. Zachariades and R. Porter (Eds.), Chapter 9, Dekker, New York (**1983**).

Allen, S.R., *J. Mater. Sci.*, **22**, p.853 (**1987**).

Allen, S.R., *Polymer*, **29**, p.1091 (**1988**).

Allen, S.R. and Roche, E.J., *Polymer*, **30**, p.996 (**1989**).

Allen, S.R. and Farris, R.J., *Polymer*, **31**, p.1467 (**1990**).

Allison, I.M. and Hollaway, L.C., Brit. *J. Appl. Phys.*, 18, p.979 (**1967**).

Allred, R.E., Street, H.K. and Martinez, R.J., *National SAMPE Symp.*, **24**, p.31 (**1979**).

Allred, R.E. and Roylance, D.K., *J. Mater. Sci.*, **18**, p.652 (**1983**).

Allred, R. E., *National SAMPE Tech. Conf.*, 16 (**1984**).

Allred, R.E., Merill E.W. and Roylance, D.K., '*Molecular Characterisation of of Composite Interfaces*', New York, Plenum Press, p.333 (**1985**).

Argon, A.S., '*Treatise of Materials Science and Technology*', 1, Academic Press, New York (**1972**).

Arjyal, B. and Galiotis, C., paper accepted in *EUROPT, Conference organised by Euoropean Optical Society & the International Society of Optical Engineering*, Munich, Germany (**1995**).

Asahi Chem. Ind. Co. Ltd., *Jap. Pat. Appl.* 12,325 & 12,326 (**1977**).

Ashbee, K.H.G. and Ashbee, E., *J. Comp. Mater.*, **22**, p.602 (**1988**).

Avakian, P., Blume, R.C., Gierke, T.D., Yang, H.H. and Panar, M., *Polym. Prepr. Am. Chem. Soc. Div. Polym. Chem.*, **21**, p.8 (**1980**).

Bader, M.G. '*Handbook of polymer-fibre composites*', Ed. F.R. Jones, Longman Scientific Technical, London (**1994**).

Bahl, S.K., Cornell, D.D. and Boerio, F.G., *J. Polym. Sci., Polym. Lett. Ed.*, **12**, p.13 (**1974**).

Baillie, C.A. and Bader, M.G., *Comp. Sci. & Technol.*, **48**, p.103 (**1993**).

Baillie, C.A. and Bader, M.G., *Composites*, **25**, No.6, p.401 (**1994**).

Bair, T.I. and Morgan, P.W., *U.S. Pat.* 3,673,143 (**1972**); 3,817,941 (**1974**).

Bair, T.I. and Morgan, P.W. and Killian, F.L., *Macromolecules*, 10(6), p.1396 (**1977**).

Ballou, J.W., *Polym. Prep.*, **17**, p.75 (**1976**).

Banwell, C.N., '*Fundamentals of Molecular Spectroscopy*', McGraw-Hill (**1983**).

Bascom, W.D. and Jensen, R.M., *J. Adhesion*, **19**, p.219 (**1986**).

Batchelder, D.N. and Bloor, D., *J. Polym. Sci., Polym. Phys. Ed.*, 17, p.569 (**1979**).

Bhaumik, D., Welsh, W.J. and Mark, J.E., *Macromolecules*, **14**, p.947 (**1981**).

Blades, H., *U.S. Pat.* 3,767,756 (**1973**); 3,869,429 (**1975**).

Boitsov, V.B. and Gotlib, Y.Y., *Opt. Spektrosk.*, **15**(2), p.216 (**1963**).

Bollet,F., Galiotis, C. and Reece, M.J., *Royal Microscopy Society Conference*, Oxford, UK (**1994**).

Born, M. and Huang, K., *'Dynamical Theory of Crystal Lattice'*, Oxford University Press, London (**1954**).

Bretzlaff, R.S. and Wool, *J. Appl. Phys.*, 52, p.5964 (**1981**).

Bretzlaff, R.S. and Wool, R.P., *Macromolecules*, **16**, p.1907 (**1983**).

Broutman, L.J., *Polym. Eng. Sci.*, **6**, p.263 (**1966**).

Broutman, L.J., *'Interfaces in Composites'*, ASTM STP 452, p.27 (**1969**).

Broutman, L.J., *Proc. 25th Annual Tech. Conf.*, Reinforced Plastics/Composites Division, The Society of Plastics Industry (**1970**).

Broutman, L.J. and Agarwal, B.D., *Polym. Eng. Sci.*, **14**(8), p.581 (**1974**).

Budiansky, B, *Comp. Struct.*, **16**, p.3 (**1983**).

Budiansky, B and Fleck, N.A., *J. Mech. Phys. Solids*, **41**(1), p.183 (**1993**).

Cansfield, D.L.M., Ward, I.M., Woods, D.W., Buckley, A., Pierce, J.M. and Wesley, J.L., *Polym. Commun.*, **24**, p.130 (**1983**).

Califano, S., 'Vibrational states', John Wiley & Sons Ltd., (**1976**).

Carrara, A.S. and McGarry, F.D., *J. Comp. Mater.*, **2**, p.222 (**1968**).

Chamis, C.C., *'Composite Materials'*, Academic Press, New York, **6**, p.31 (**1974**).

Chatzi, E.E. and Koenig, J.L., *Polym.-Plast. Technol. Eng.*, **26**(3&4), p.229 (**1987**).

Chiao, C.C., Moore, R.L. and Chiao, T.T., *Composites*, **8**, p.161 (**1977**).

Choe, E.W., *U.S. Pat.* 4,423,202 (**1983**).

Chohan V., Marston, C., Paipetis, A and Galiotis, C., submitted to *J. Mater. Sci.* (**1995**).

Chua, P.S. and Piggot, M.R., *Comp. Sci. Technol.*, **22**, p.33 (**1985**).

Chua, P.S. and Piggot, M.R., *Comp. Sci. Technol.*, **22**, p.107 (**1985b**).

Cohen., Y. and Thomas, E.L., *Macromolecules*, **21**, p.433 (**1988**).

Cox, H.L., Br. *J. Appl. Phys.*, **3**, p.72 (**1952**).

Daniel, I.M., 'Photoelastic Investigation of Composites', in *'Composite Materials'*, **2**, L.J. Broutman and R.H. Krock, eds., Academic Press, New York (**1974**).

Day, R.J., Robinson, I.M., Zakikhani, M. and Young, R.J., *Polymer*, 28, p.1833 (**1987**).

DeTeresa, S.J., Porter, R.S. and Farris, R.J., *J. Mater. Sci.*, **20**, p.1645 (**1985**).

DeTeresa, S.J., Porter, R.S. and Farris, R.J., *J. Mater. Sci.*, **23**, p.1886 (**1988**).

Dobb, M.G., Johnson, D.J. and Saville, B.P., *J. Polym. Sci., Polym. Phys. Ed.*, **15**, p.2201 (**1977**).

Dobb, M.G., Johnson, D.J. and Park, C.R., *J. Mater. Sci.*, **25**, p.829 (**1990**).

Dow, N.F., General Electric Co., Missiles and Space Div., Report No. R-635D61 (**1963**).

Drzal, L.T., Rich, M.J. and Loyd, P.F., *J. Adhesion*, **16**, p.1 (**1982**).

Drzal, L.T., Rich, M.J., Koenig, M.F. and Loyd, P.F., *J. Adhesion*, **16**, p.133 (**1983**).

E.I. du Pont de Nemours & Co., Inc., Technical Bulletins K-1 and K-2 (**1978**).

E.I. du Pont de Nemours & Co., Inc., Technical Bulletin H-05500 (**1989**).

Eagles, D.B., Blumentritt, B.F. and Cooper, S.L., *J. Appl. Polym. Sci.*, **20**, p.435 (**1976**).

Evans, R.A. and Hallam, H.E., *Polymer (Letter)*, 17 p.838 (**1976**).

Farmer, B.L., Chapman, B.R., Dudis, D.S. and Adams, W.W., *Polymer*, **34**(8) p.1588 (**1993**).

Favre, J.P., Sigety, P. and Jacques, D., *J. Mater. Sci.*, **26**, p.189 (**1991**).

Filliou, C., Galiotis, C. and Batchelder, D.N., *Composites*, **23**, p.28 (**1992**).

Fina, L.J., Bower, D.I. and Ward, I.M., *Polymer*, 29, p.2146 (**1988**).

Fratini, A.V. and Adams, W.W., *Am. Crystallog. Assoc. Abstract*, **13**, p.72 (**1985**).

Fratini, A.V., Cross, E.M., O'Brian, J.F. and Adams, W.W., *J. Macromol. Sci., Phys. Ed.*, **B24**, p.159 (**1985-1986**).

Frazer, W.A., Ancker, F.H. and DiBenedetto, A.T., *Proc. 30th Conf. on Reinf. Plastics*, The Society of Plastics Industry, New York, 22A (**1975**).

Frazer, W.A., Ancker, F.H., DiBenedetto, A.T. and Elbirli, B., *Polym. Comp.*, 4, p.238 (**1983**).

Galiotis, C., Young, R.J., Batchelder, D.N., *J. Mater. Sci.*, 2, p.263 (**1983**).

Galiotis, C., Young, R.J., Yeung, P.H.J. and Batchelder, D.N., *J. Mat. Sci.*, **19**, p.3640 (**1984**).

Galiotis, C., Vlattas, C. and Paipetis, A., *XIV International conference in Raman Spectroscopy*, Hong Kong, (**1994**).

Greenwood, J.M. and Rose, P.G., *J. Mater. Sci.*, **9**, p.1809 (**1974**).

Greszczuk, L.B., *'Interfaces in Composites'*, ASTM STP 452, p.42 (**1969**).

Gu, X.H., Young, R.J. and Day, R.J., *J. Mat. Sci.*, 30, p.1409 (**1995**).

Gubanov, A.I., *Mech. Polim.*, **5**, p.771 (**1967**).

Guild, F.J., Vlattas, C. and Galiotis, C., Comp. Sci. and Technol., 50, p.319 (**1994**).

Hagege, R., Jarrin, M. and Sutton, M., *J. Microscopy*, 115, p.65 (**1979**).

Haraguchi, K., Kajiyama, T. and Takayanagi, M., *J. Appl. Polym. Sci.*, **23**, p.915 (**1979**).

Harris B., *'Handbook of polymer-fibre composites'*, Ed. F.R. Jones, Longman Scientific Technical, London (**1994**).

Hasegawa, R.K., Chatani, Y. and Tadokoro, H., *Meeting of the Crystallographic Society of Japan*, p.21 (**1973**).

Hawthorne, H.M. and Teghtsoonian, E., *J. Adhesion*, 6, p.85 (**1974**).

Hawthorne, H.M. and Teghtsoonian, E., *J. Mater. Sci.*, **10**, p.41 (**1975**).

Helminiak, T.E. and Berry, G.C., *Polym. Preprints*, **18**, p.167 (**1977**).

Herglotz, H.K., in *'Structure of Crystalline Polymers'*, I.H. Hall (Ed.), Elsevier, (**1984**).

Hindeleh, A.M., Halin, N.A. and Zig, K.A., *J. Macromol. Sci., Phys.*, B23(3), p.289 (**1984**).

Hoffman, A.S., Keller, T.S., Miyake, A., Ratner, B.D. and McElroy, B.J., *Proc. Pac. Chem. Eng. Congr.*, Seoul, Korean Inst. Chem. Eng. (**1983**).

Hull, D., *'An Introduction to Composite Materials'*, Cambridge University Press, Cambridge, U.K., (**1981**).

Hunter, R.W., *J. Aust. Inst. Met.*, **18**, p.173 (**1973**).

Jacques, D., Ph.D. thesis, Institut Polytechnique de Lorraine, Nancy, France (**1989**).

Jahankhani, H. and Galiotis, C., *Interfaces in Polymer, Ceramic and Metal Matrix Composites*, Ed. H. Ishida, Elsevier, New York, p.107 (**1988**).

Jahankhani, H., *Ph.D. thesis*, University of London (**1990**).

Jahankhani, H. and Galiotis, C., *J. Comp. Mat.*, 25, p.609 (**1991**).

Jones, R.M., *'Mechanics of Composite Materials'*, Hemisphere Publising Co., New York (**1975**).

Jones, W.R. and Johnson, J.W., *Carbon*, **9**, p.645 (**1971**).

Kaneda, T., Ishikawa, S., Daimon, H., Katsura, T., Maeda, T. and Hondo, T., *U.S. Pat.* 4,178,431 (**1979**).

Kelly, A., *'Strong solids'*, Clarendon Press, Oxford (**1966**).

Keneghan, B. and Galiotis, C., *ICI technical report* (**1993**).

Kim, P.K., Chang, C. and Hsu, S.L., *Polymer*, **27**, (**1986**).

Knoff, E. F., *J. Mater. Sci.-Lett.*, **6**, p.1392 (**1987**).

Kovacs, A.J., Gonthier, A. and Straupe, C., *J. Polym. Sci.*, **50**, p.283 (**1975**).

Krause, S.J., Haddock, T.B., Vezie, D.L., Lenhert, P.G., Hwang, W.F., Price, G.E., Helminiak, T.E., O'Brien, J.F. and Adams W.W., *Polymer*, **29**, p.1354 (**1988**).

Krause, S.J., Vezie, D.L. and Adams, W.W., *Polym. Comm.*, 30, p.10 (**1989**).

Kumar, S. and Helminiak, T.E., MRS Symp., 134, p.363 (**1988**).

Kwolek, S.L., Morgan, P.W. and Sorenson, W.R., *U.S. Pat.* 3,063,966 (**1962**).

Kwolek, S.L., *U.S. Pat.* 3,671,542 (**1972**); *U.S. Pat.* 3,819,587 (**1974**).

Lawrence, P., *J. Mater. Sci.*, 7, p.1 (**1972**).

Liang, C.Y. and Krimm, S., *J. Mol. Spectrosc.*, **3**, p.554 (**1959**).

Long, D.A., *'Raman Spectroscopy'*, McGraw-Hill Inc. (**1977**).

Mandel, J.F., Chen, J.H. and McGarry, F.J., Intern. *J. Adhesion Adhesives*, **1**, p.40 (**1980**).

Mandel, J.F., Grande, D.H., Tsiang, T.H. and McGarry, F.J., *'Composite materials: testing and design' (7th Conf.)*, ed. J.M. Whitney, ASTM STP 893, p.87 (**1986**).

Marotzke, C., *Proc. 6th European Conf. on Comp. Mat.*, (ECCM6), Bunsell, A.R., Kelly, A. and Massiah, A. Editors, Woodhead Publishing Ltd., p.281 (**1993**).

Martin, D.C. and Thomas, E.L., *J. Mater. Sci.*, **26**, p.5171 (**1991**).

Macturk, K.S., Eby, R.K. and Adams, W.W., *Polymer*, 32, p.1782 (**1991**).

McCartney, L.N., *Proc. R. Soc. Lond.*, **A425**, p.215 (**1989**).

McGarry, F.J. and Fuhwara, M., *23rd Annual Technical Conference*, Reinforced Plastics Composites Division, The Society of the Plastics Industry, Section 9-B, p.1 (**1968**).

McGarry, F.J. and Moalli, J.E., *Polymer*, **32**, p.1811 (**1991**).

McLaughlin, T.F., *Experimental Mechanics*, 6(19), p.1 (**1966**).

McLaughlin, T.F., *J. Comp. Mater.*, 2(1), p.44 (**1968**).

Melanitis, N., Ph.D. thesis, University of London (**1990**).

Miller, B., Muri, P. and Rebenfeld, L., *Comp. Sci. Technol.*, **28**, p.17 (**1987**).

Morgan R.J., Mones, E.T., Steele, W.J. and Deutscher, *Proc. Of the National SAMPE Tech. Conf.*, **12**, p.368 (**1980**).

Morgan, R.J., Pruneda, C.O. and Steele, W.J., *J. Polym. Sci., Polym. Phys. Ed.*, **21**, p.1757, (**1983**).

Morgan, R.J. and Allred, R.E., *'Reference Book for Composites Technology'*, Ed. Lee, S.M., Technomic Publishing Co., (**1989**).

Nairn, J.A., *Mech. Mater.*, **13**, p.131 (**1992**).

Narkis, M., Chen, J.H. and Pipes, R.B., *Polym. Comp.*, 9(4), p.245 (**1988**).

Netravali, A.N., Henstenburg, R.B., Phoenix, S.L. and Schwartz, P., *Polym. Comp.*, **10(4)**, p.226 (**1989**).

Northolt, M.G. and van Aartsen, J.J., *J. Polym. Sci., Polym. Lett. Ed.*, **11**, p.333 (**1973**).

Northolt, M.G., *Eur. Polym. J.*, **10**, p.799, (**1974**).

Northolt, M.G. and van Aartsen, J.J., *J. Polym. Sci., Polym. Symp.*, **58**, p.283 (**1977**).

Northolt, M.G., *Polymer*, **21**, p.1199 (**1980**).

Northolt, M.G. and van der Hout, R., *Polymer*, **26**, p.310 (**1985**).

Ohsawa, T, Nakayama, A., Miwa, M. and Hasegawa, A., *J. Appl. Polym. Sci.*, **22**, p.3203 (**1978**).

Outwater, J.O., *Mod. Plast.*, **33**, p.56 (**1956**).

Paipetis, A., Vlattas, C. and Galiotis, C., submitted *to J. Raman Spectroscopy*.

Panar, M., Avakian, P., Blume, R.C., Gardner, K.H., Gierke, T.D. and Yang, H.H., J. *Polym. Sci., Polym. Phys. Ed.*, **21**, p.1955 (**1983**).

Penn, L. and Milanovich, F., *Polymer*, **20**, (**1979**).

Penn, L.S. and Miller, B., *J. Colloid and Interface Sci.*, 78, p.238 (**1980**).

Penn, L.S., Bystry, F.A. and Machioni, H.J., *Polymer Composites*, **4**, p.26 (**1983**).

Penn, L.S. and Liao, T.K., *Composites Tech.*, Rev.6, p.133 (**1984**).

Penn , L.S. and Lee, S.M., *J. Composites Tech. Res.*, **12**, p164 (**1990**).

Piggot, M.R., *Acta Metallurgica*, **14**, p.1429 (**1966**).

Piggot, M.R.,*'Load-Bearing Fibres'*, Pergamon Press (**1980**).

Provost, R.L., *U.S. Pat.* 4,144,023 (**1977**).

Pruneda, C.O., Steele, W.J., Kershaw, R.P., Morgan, R.J., *Polym. Prepr., Am. Chem. Soc., Div. Polym. Chem.*, **22**, p.216 (**1981**).

Raman, C.V. and Krishnan, K.S., *Nature*, 121, p.501 (**1928**).

Robinson, I.M., *Ph.D. thesis*, University of London (**1987**).

Robinson, I.M. and Robinson, J.M., *J. Mat. Sci.*, 29, p.4663 (**1994**).

Roche, E.J., Takahashi, T. and Thomas, E.L., *Fiber Diffraction Methods (ACS Symposium 141), Am. Chem. Soc.*, p.303 (**1980**).

Roche, E.J., Allen, S.R., Fincher, C.R. and Paulson, C., *Mol. Cryst. Liq. Cryst.*, 153, p.547 (**1987**).

Rosen, B.W. *'Mechanics of Composite Strengthening'*, ASM Seminar, Amer. Soc. of Metals, Philadelphia, Pennsylvania, USA (**1964**).

Schaefgen, J.R., Bair, T.I., Ballou, J.W., Kwolek, S.L., Morgan, P.W., Panar, M. and Zimmerman, J., *'Ultra-High Modulus Polymers'*, A. Ciferri and J.M. Ward (Eds.), Applied Science Publishers, London (**1979**)

Schuster, D.M. and Scala, E., *Trans. Metallurgical Society AIME*, **230**, p.1635 (**1964**).

Shen, D.Y. and Hsu, S.L., *Polymer*, **23**, p.969 (**1982a**)

Shen, D.Y., Venkatesh, G.M., Burchell, D.J., Shu, P.H.C. and Hsu, S.L., *J. Polym. Sci., Polym. Phys. Ed.*, **20**, p.509 (**1982b**)

Shiryaeva G.V. and Andreevska, G.D., *'The Plastics'*, (USSR), **4**, p.40 (**1962**).

Sinclair, D., *J. Appl. Phys.*, **21**, p.380 (**1950**).

Starikovskii, G.P. and Shcherbakov, V.T., *Mekhanika Kompozitnykh Materialov*, **4**, p.719 (**1984**).

Szymanski, H.A., *'Raman Spectroscopy / Theory and Practice'*, Plenum Press (**1967**).

Takahashi, T., Miura, M. and Sakuri, K., *J.Appl. Polym. Sci.*, **28**, p.579 (**1983**).

Takaku, A. and Arridge, R.G.C., *J. Phys. D: Appl. Phys.*, **6**, p.2038 (**1973**).

Tashiro, K., Kobayashi, M. and Tadokoro, H., *Macromolecules*, **10**(2), p.413, (**1977**).

Tashiro, K., Wu, G., and Kobayashi, M., *J. Polym. Sci., Part B: Polym. Phys.*, **28**, p.2527 (**1990**).

Tashiro, K., Minami, S., Wu, G., and Kobayashi, M., *J. Polym. Sci., Part B: Polym. Phys.*, **30**, p.1143 (**1992**).

Tashiro, K., *Prog. Polym. Sci.*, Vol.18, p377 (**1993**).

Termonia, Y., *J. Mater. Sci.*, 22, p.504 (**1987**).

Termonia, Y., Personnal Communication with Galiotis, C. (**1989**).

Tetlow, P.L., Personal Communication (**1990**).

Theocaris, P.S., *'The mesophase concept in composites'*, ed. by G.Henrici-Olive & S. Olive, Springer-Verlag Berlin Heidelberg, GDR (**1987**).

Thomas, E.L., Farris, R.J., Hsu, S.L., Allen, S., Filippov, A., Minter, J., Roche, E., Shimamura, K., Takahashi, T. and Venkatesh, G., *US Air Force Technical Report AFWAL-TR-80-4045*, vol.III, Part I, (**1982**).

Timoshenko, S.P. and Gere, J.M., *'Theory of Elastic Stability'*, McGraw-Hill (**1961**).

Tse, M.K., *SAMPE J.*, p.11 (**1985**).

Tyson, W.R. and Davies, G.J., *Brit. J. Appl. Phys.*, **16**, p.199 (**1965**).

Uy, W.C., Mammone, J.F., *33rd IUPAC International Symposium on Macromolecules*, Montreal, Canada (**1990**).

Van der Zwaag, S. and Kampschoer, G. *Integration of Fundamental Polymer Science & Technology*, 2nd Edn by P.J. Lemstra and L. Kleintjens, Elsevier Applied Science, Oxford, p.545 (**1988**).

Venkatesh, G.M., Shen, D.Y. and Hsu, S.L. *J Polym. Sci., Polym. Phys. Ed.*, **19**, p.1475 (**1981**).

Vettegren, V.I. and Novak, I.I., *J. Polym. Sci., Polym. Phys. Ed.*, 11, p.2135 (**1973**).

Wagner, H.D. and Eitan, A., *Appl. Phys. Lett.*, 56(20), p.1965 (**1990**).

Ward, I.M., *Chem. Ind.* (London), p.905 (**1956**); *Chem. Ind.* (London), p.1102 (**1957**).

Ward, I.M., *Proc. Phys. Soc.*, **80**, p.1176 (**1962**)

Wellman, M.W., Adams, W.W., Wolff, R.A., Dudis, D.S., Wiff, D.R. and Fratini, A.V., *Macromolecules*, **14**, p.935 (**1981**).

Wertheimer, M.R. and Schreiber, H.P., *J. Appl. Polym. Sci.*, **26**, p.2087 (**1981**).

Wesson, S.P. and Allred, R.E., *Proc. of 7th Annual Meeting of The Adhesion Society*, Jacksonville, FL, p.27 (**1984**).

Whitney, J.M. and Drzal, L.T., *Toughened Composites*, ASTM STP 937, Ed. by N.J. Johnston, Philadelphia, p.179 (**1987**).

Whitney, J.M., Daniel, I.M. and Pipes, B.R., *'Experimental Mechanics of Fiber Reinforced Composite Materials'*, The Society for Experimental Mechanics (**1984**).

Wierschke, S.G., Shoemaker, J.R., Haaland, P.D, Pachter, R. and Adams, W.W., *Polymer*, 33(16), p.3357 (**1992**).

Wolfe, J.F., Loo, B.H. and Arnold, F.E., *Polym. Prepr.*, **19**(2), p.1, (**1978**).

Wolfe, J.F. and Loo, B.H., *U.S. Pat.* 4,225,700 (**1980**).

Wolfe, J.F. and Sybert, P.D., *U.S.Pat.* 4,533,693 (**1985**); 4,703,103 (**1987**).

Wool, R.P., *J. Polym. Sci., Polym. Phys. Ed.*, 13, p.1795 (**1975**).

Wool. R.P. and Bretzlaff, R.S., *J. Polym. Sci., Part B: Polym. Phys.*, 24, p.1039 **(1986)**.

Yang, H.H., *'Aromatic High Strength Fibers'*, John Wiley & Sons, New York, USA **(1989)**.

Yang, H.H., *'Kevlar Aramid Fiber'*, John Wiley & Sons, Chichester, UK **(1993)**.

Young, R.J., Day, R.J. and Zakikhani, J. *Mater. Sci.*, **25**, p.127, **(1990)**.

Young, R.J. and Ang, P.P., *Polymer*, **33**, p.975 **(1992)**.

Zhurkov, S.N., Vettegren, V.I., Korsukov, V.E. and Novak, I.I., *'Fracture 1969', Proc. of the Second International Conference on Fracture*, p.545 **(1969)**.